THE UNIVERSITY *of* EDINBURGH

THE UNIVERSITY *of* EDINBURGH

Development of a fluidic platform for studying cancer cells under physiologically relevant oxygen conditions

Ailsa Jane Golightly Lamb

Thesis submitted for the degree of

Doctor of Philosophy

The University of Edinburgh

School of Chemistry

2022

Declaration

I declare that this thesis has been composed solely by myself and that it has not been submitted, in whole or in part, in any previous application for a degree. Except where stated otherwise by reference or acknowledgment, the work presented is entirely my own.

29 October 2022

Ailsa Jane Golightly Lamb

Lay Summary

In 2020, almost 10 million people died from cancer worldwide. Cancer is a complex disease that can start in almost any part of the human body. When normal healthy cells turn into cancer cells, they can multiply extremely fast to form tissue masses called tumours. As the tumours grow, the dynamics within the tissue change and the environment becomes very harsh. Under such conditions, most normal healthy cells would not be able to survive, but cancer cells are able to change their cell chemistry to adapt to the conditions around them.

In healthy tissue, cells get oxygen from the surrounding blood supply and use it to make energy. However, because tumour tissue grows so fast, the oxygen demand from the cells quickly surpasses the oxygen supply from surrounding blood vessels. This leads to the formation of oxygen gradients through the tumour tissue. Cells on the tumour surface that are close to a blood supply receive some oxygen, but oxygen concentration gradually reduces towards the core of the tumour. When there is very little or no oxygen – a state called hypoxia – the cells become reliant on glucose, rather than oxygen, to make energy. Hypoxia is associated with aggressive cancer growth, spreading of cancer cells to other parts of the body and resistance to treatments including radiotherapy and chemotherapy. Therefore, it is a very important feature of cancer that has to be considered when researching new cancer treatments.

Traditional cancer research models include 2D cultures of human cancer cells and animal models. Cell cultures are a cost effective and easy-to-use method to study human cells, but as the cells are grown in 2D layers, it is not very representative of the dynamic and complex 3D tumour environment in real tumours. Animal models do capture the 3D tumour environment, but there are many fundamental biological differences between animals and humans. Often, drugs that are found to treat cancer in mice do not effectively treat human disease. Also, the use of animals in research is strictly controlled by ethics policies and researchers and pharmaceutical companies are trying to replace and reduce animal testing as much as possible.

Emerging technologies are making it possible to build new models to study human cancer cells in more realistic environments. Microfluidics are small devices – sometimes called chips and usually made from plastic – which contain a series of channels on the micrometre scale. The aim of this project was to design a chip that could be used to grow human cancer cells under a range of physiologically relevant oxygen concentrations at the same time. In the longer term, the chip could then be used to investigate the relationship between hypoxia and treatment resistance.

An image of a chip produced using a novel fabrication technique is shown in Figure 1. The channel design is based on combining two solutions; one with a high oxygen concentration and one with a low oxygen concentration. These two solutions flow into the chip and mix through the network, producing a range of oxygen concentrations. This is illustrated in Figure 2. After making the chip and demonstrating that the oxygen gradient across the chip was stable, the model was tested with liver cancer cells.

Under low oxygen concentration, cells express hypoxia dependent proteins (HDP). Liver cancer cells were seeded throughout the channel network, it was expected that higher concentrations of HDP would be detected in cells in the low oxygen channels compared to cells in the channels with more oxygen. Unexpectedly, similar levels of HDP were observed across all cells in the chip. This means that further development of the model is required to optimise the conditions for cell culture.

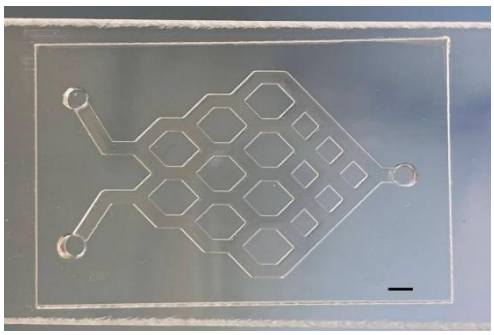

Figure 1: Image of a fluidic chip made from acrylic. Scale bar is 2 mm

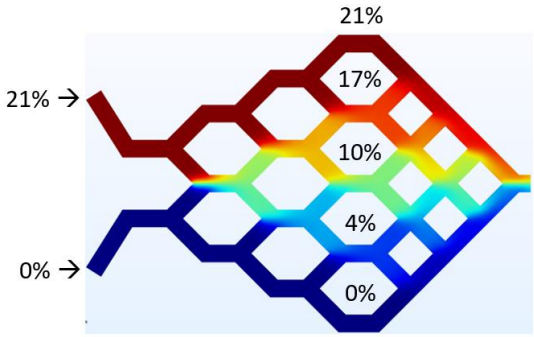

Figure 2: Oxygen distribution in the chip simulated in COMSOL Multiphysics®.

Abstract

In solid cancer tumours the oxygen concentration can be lower than in the corresponding healthy tissue. This condition, known as hypoxia, impacts the behaviour and characteristics of the cancer cells and can result in tumour growth and resistance to treatment. Therefore, it is important to consider oxygen concentration when studying cancer cells in a research environment. Fluidics and organ-on-a-chip systems are popular and widely researched tools for representing organs and their microenvironments *in vitro*. This work presents development and fabrication of a novel system for studying cancer cells under a range of oxygen concentrations on the same fluidic chip.

The fabrication method developed in this project uses low-cost, biocompatible materials to rapidly prototype fluidic chips in a reproducible manner. An example chip is shown in Figure 1. Oxygen distribution in the channel network was investigated using computational simulations in COMSOL Multiphysics® 5.6 (Figure 2) and fluorescence microscopy experiments using $Ru(BPY)_3$ (an oxygen sensitive fluorophore). Both methods confirmed the channel network supports a gradient across the chip based on two media inputs of different oxygen concentrations.

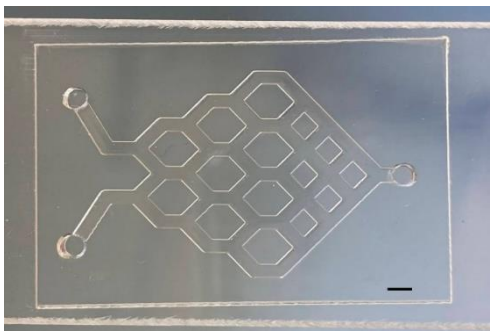

Figure 1: Image of a fluidic chip made from acrylic. Scale bar is 2 mm

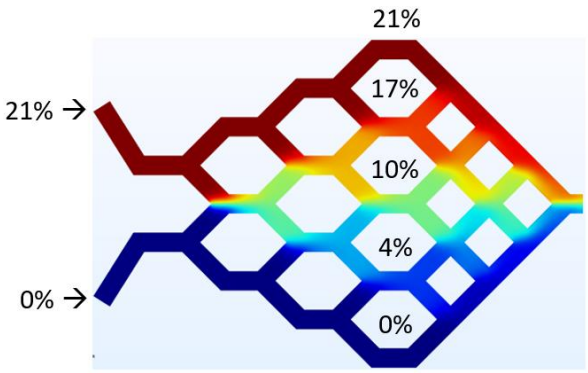

Figure 2: Oxygen distribution in the chip simulated in COMSOL Multiphysics®.

Operation and function of the platform was tested with liver carcinoma cell line HepG2/C3A. Cells were seeded throughout the channel network and responses to the different oxygen conditions were investigated via immunofluorescence staining. It was expected that cells in areas of the chip with lower oxygen concentration would show higher expression of the hypoxia inducible factor, HIF-1α, however, no significant differences in HIF-1α were observed. The results from the cell culture experiments indicate that further work is required to optimise the conditions for cancer cells.

Acknowledgments

I would like to thank my supervisors Professor Colin Campbell, Professor Adam Stokes, Dr Bill Nailon and Dr Duncan McClaren for giving me the opportunity to work on this project. Your support, advice and expertise has been invaluable throughout.

Thank you to the Jamie King Urological Cancers Research Fund, the Engineering and Physical Sciences and Research Council (EPSRC), and OPTIMA for funding this project. Many thanks to the Neil Campbell Fund for contributing to funds for my research trip to Colorado.

Thank you to past and present members of the Campbell group (Will, Ailsa, Heather, Shannon, Bilgi and Angus). Working alongside you was an amazing experience. You are incredibly talented and I have learned from you all.

Thank you to the following people for providing your specialist knowledge, skills and advice; George Steedman, Lloyd Mitchell, David Kelly, John White, Richard Brewster, Stephen Mahon, Anthony Buchoux, Maks Gepner, John Skottis and James Meehan.

Many thanks to OPTIMA for allowing me onto the programme last minute. Thank you to everyone involved, especially the 2018 cohort, for making all the courses and events into valuable and memorable occasions. Thank you to Ishani Malhotra and Carcinotech for hosting my placement.

I would like to thank my nearest and dearest family and friends, especially Mum, Dad, Ross and Thomas. Your encouragement, support and friendship gets me through everyday. Thank you for being there for the big moments and helping me find joy in the little things. I wouldn't be where I am today without all of you. Thank you.

Contents

Abbreviations

Abbreviation	Word or Phrase
ADP	Adenosine diphosphate
AMP	Adenosine monophosphate
ANOVA	Analysis of variance
ATP	Adenosine triphosphate
AU	Arbitrary units
BPY	2,2'-Bipyridine
CAIX	Carbonic anhydrase IX
CBP	CREB binding protein
CF	Cofactor
CHO	Chinese hamster ovary cells
CNC	Computerized numerical control
CO_2-Ind	Carbon dioxide independent medium
CREB	Cyclic AMP response element binding
DFO	Deferoxamine
DMEM	Dulbecco's modified eagle medium
DNA	Deoxyribonucleic acid
DU145	Human prostate cancer cell line
$FADH_2$	Flavin adenine dinucleotide
FAL	Femoral artery ligation
FDA	Food and Drug Administration

Abbreviation	Word or Phrase
GLUT	Glucose transporter
HAP	Hypoxia activated prodrug
HEK293T	Human kidney cells
HeLa	Henrietta Lacks, cervical cancer cell line
HepG2/C3A	Human hepatocellular (liver) cancer cell line
HIF	Hypoxia inducible factor
HRE	Hypoxia response element
L-15	Leibovitz-15 medium
LDO	Luminescent dissolved oxygen
MCF-7	Michigan Cancer Foundation-7, human breast cancer cell line
MGV	Mean gray value
NAD(P)H	Nicotinamide adenine dinucleotide (phosphate)
NS	Navier-Stokes
ODDD	Oxygen dependent degradation domain
PBS	Phosphate buffered saline
PC3	Human prostate cancer cell line
PDMS	Polydimethylsiloxane
Pen-strep	Penicillin-streptomycin
PHD	Prolyl hydroxylase
PMMA	Polymethyl methacrylate

Abbreviation	Word or Phrase
RBF	Round bottom flask
RPMI	Roswell Park Memorial Institute 1640 medium
SCLC	Small cell lung carcinoma
SCC-7	Squamous cell carcinoma-7, mouse cell line
U251	Human brain cancer cell line
Ub	Ubiquitin
VEGF	Vascular endothelial growth factor
VHL	von Hippel-Lindau protein

Chapter 1: Introduction

1.1 Hypoxia in Solid Cancer Tumours

1.1.1 Cancer and Hypoxia – Definition and Statistics

In 2020, almost 10 million people died of cancer worldwide.[1] In the same year, 18 million people were diagnosed with cancer and this number is expected to continue rising, with an estimated 27.5 million new cases per year predicted by 2040.[1,2] Graphs showing the most common cancers worldwide and in the UK are displayed in Figure 1.1 and Figure 1.2 respectively. These figures highlight the global persistence of cancer and the necessity of quality cancer research.

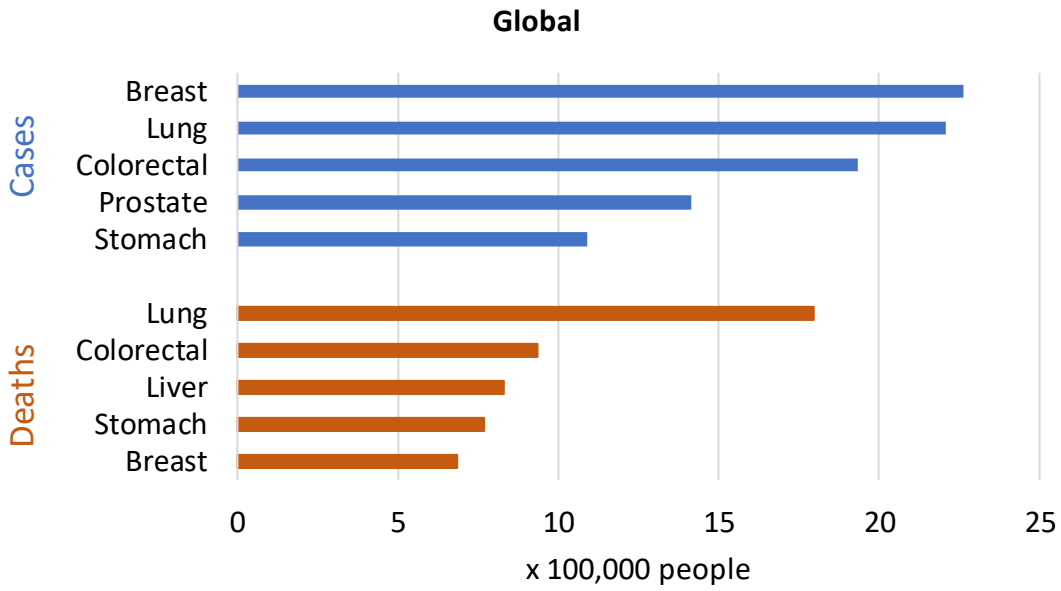

Figure 1.1: Five most common cancers in terms of new cases and deaths in the world in 2020.[1]

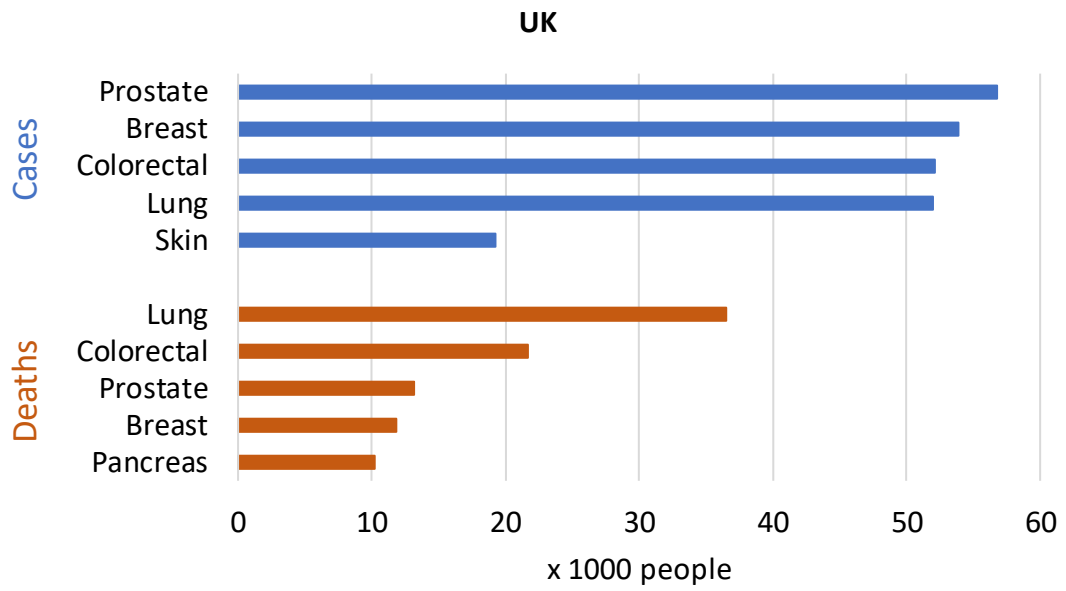

Figure 1.2: Five most common cancers in terms of new cases and deaths in the UK in 2020.[1]

Cancer research is challenging because there are over 200 different types of cancer, each with its own complexities.[3] Cancer originates from normal healthy cells in almost any part of the body which go through a series of changes to develop into cancer cells. The cancer cells can then grow uncontrollably to form tumours and spread to other organs and tissues in the body.[3]

In normal healthy tissues, oxygen is delivered to the cells for essential metabolism via the blood supply. The oxygen concentration varies depending on the tissue, but is usually around 3 – 7%.[4] However, solid cancer tumours can grow so quickly that eventually the blood supply cannot meet the oxygen demand.[5,6] The tumour releases signals to promote growth of new blood vessels around the tissue, but often the vasculature ends up dysfunctional and prone to leaking. The oxygen supply to the tumour tissue becomes inconsistent and the oxygen concentration in regions of the tissue that are further away from the blood supply can become very low, either temporarily or consistently.[5–7] Low oxygen concentration (<2%) is referred to as hypoxia and is observed in most types of solid tumour.[4,8] It is a key focus of the work in this project.

In 2000, Hanahan and Weinberg created a list of characteristics that are common to all types of cancer, known as the hallmarks of cancer.[9] Their aim was to summarise the complexity of cancer into key concepts to provide a useful framework for research and understanding. The most recent version of the list was published in 2022 and includes 12 characteristics as shown in Figure 1.3.[10] Generally, they describe the essential mechanisms that allow tumours to survive, grow and spread.

As discussed earlier in this section, hypoxia is related to inducing or accessing vasculature and it is also related to many other hallmarks including proliferative signalling, activating invasion and metastasis and deregulating cellular metabolism.[11] The following section, Section 1.1.2, will explore the relationship between hypoxia, deregulation of cellular metabolism and tumour invasion in more detail.

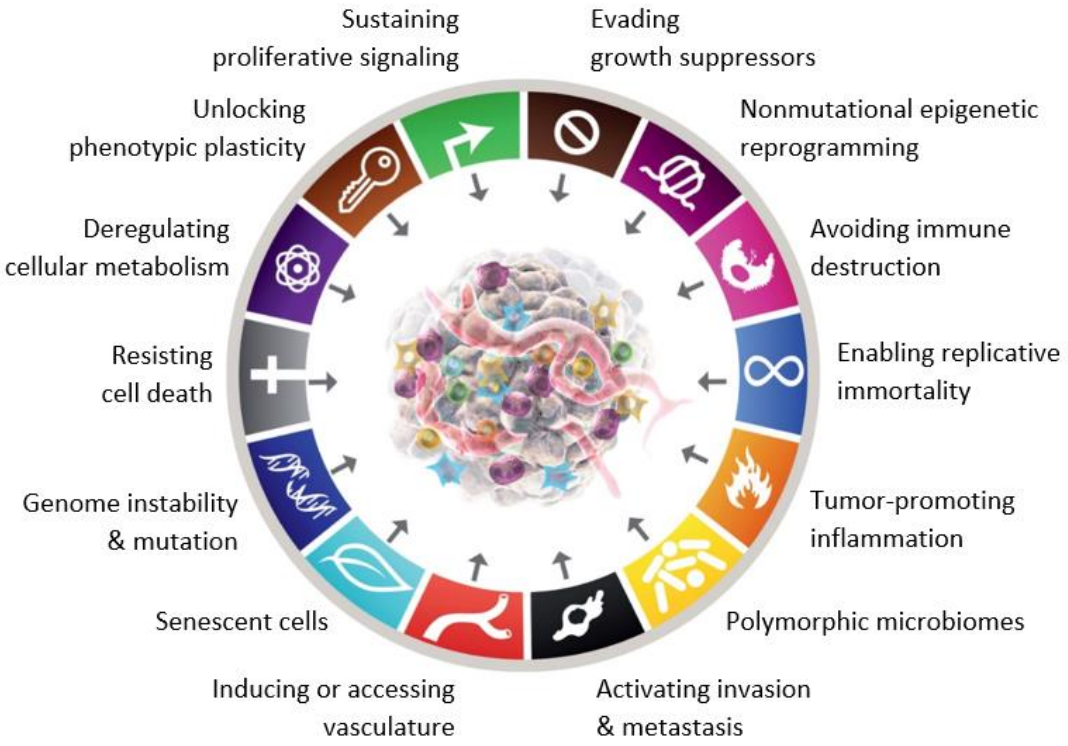

Figure 1.3: The hallmarks of cancer, 2022. Reprinted from Hanahan with permission from the American Association for Cancer Research.[10]

1.1.2 Cancer Cell Metabolism

The purpose of metabolism in mammalian cells is to break down glucose molecules for the production of energy in the form of molecules of adenosine triphosphate (ATP).[12] The processes involved in metabolism in mammalian cells are outlined in Figure 1.4.

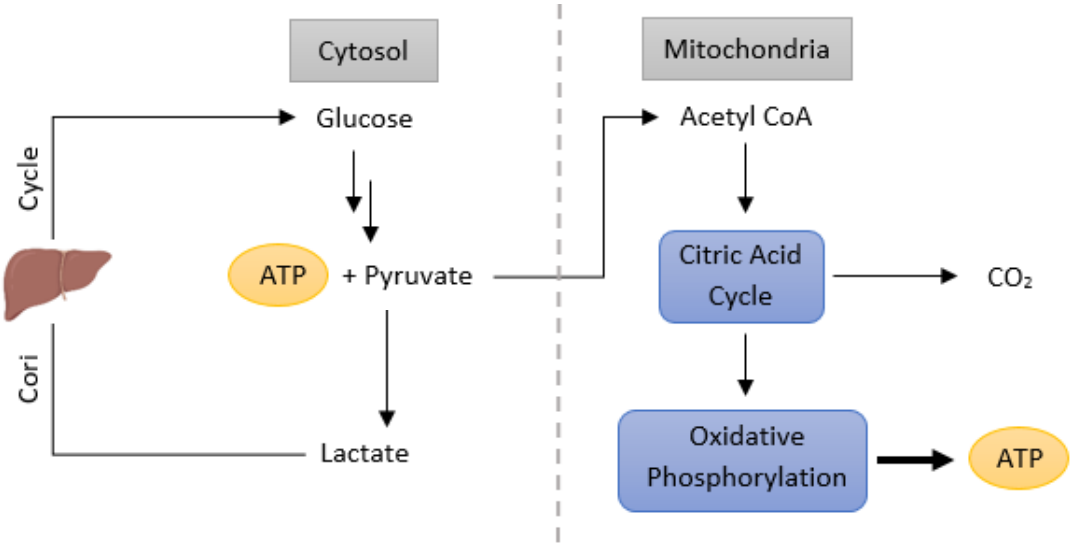

Figure 1.4: Schematic of glucose metabolism in cells. In the cytosol, glucose is converted into 2 molecules of pyruvate and 2 molecules of adenosine triphosphate (ATP) are produced in the process. Pyruvate can be further metabolised in the cytosol to produce lactate, which can be converted back to glucose via the Cori cycle in the liver. The main metabolic pathway in aerobic conditions is for pyruvate to be converted into acetyl coenzyme A (CoA) and processed in the mitochondria, where CO_2 and ATP (approximately 36 molecules) are produced via the citric acid cycle and oxidative phosphorylation.[13–15]

The first step in metabolism is the conversion of glucose to pyruvate in the cytosol, which produces a net gain of 2 ATP molecules.[13,14] This process is referred to as aerobic glycolysis in the presence of oxygen and anaerobic glycolysis in the absence of oxygen.[12] Following aerobic glycolysis, pyruvate is converted into acetyl coenzyme A (CoA), which then enters the citric acid cycle in the mitochondria, releasing carbon dioxide as a product. Coenzymes nicotinamide adenine dinucleotide

(NADH) and flavin adenine dinucleotide ($FADH_2$) are produced throughout the metabolic process. Oxidative phosphorylation is the final step in which oxygen and coenzymes NADH and $FADH_2$ are processed in the electron transport chain to phosphorylate adenosine diphosphate (ADP) to ATP.[13,15] This is the main source of energy for cells in the presence of oxygen.[13,15]

In the absence of oxygen, oxidative phosphorylation cannot proceed and so the main source of energy for the cells is glycolysis. Glycolysis becomes upregulated to try to produce enough ATP to keep the cell alive and excess pyruvate is converted into lactate.[12,13] In the Cori cycle, lactate is transported to the liver via the blood circulation and converted back into glucose, which can be delivered back to the cells and reused as an energy source.[14]

The conversion of glucose to pyruvate produces protons, so an increase in glycolysis results in an increase in acidity.[12,16] In healthy cells, this increase in acidity is sensed by regulators of cellular metabolism, such as p53 (tumour suppressor), which can either initiate corrective measures or cell death. However, in cancer cells, the increase in glycolysis is allowed to proceed and actually provides survival advantages.[12,16]

In cancer cells, the intracellular pH is tightly regulated and excess protons are pumped into the extracellular space.[16] Acidification of the extracellular environment increases the invasive potential of tumours because it is not tolerable for surrounding healthy tissue. Depletion of the extracellular matrix and cell death in the healthy tissue provides more space for the cancer tissue to grow into.[16]

Glycolysis is also linked to synthesis of biomass for the production of new cells, which helps support the rapidly growing tumour tissue.[12,15] Due to the benefits for tumour survival, growth and invasion, glycolysis can also be upregulated in cancer cells even in the presence of oxygen. This is known as the Warburg Effect.[12–16]

Although oxidative phosphorylation is reduced, some pyruvate is still processed in the mitochondria to produce CO_2 as the citric acid cycle can proceed without oxygen.[15,16] CO_2 can be converted into bicarbonate ions and protons (equation *1.1*) by carbonic anhydrase enzymes, and this is a second source of extracellular acidification in hypoxic cancer cells.[16,17] Carbonic anhydrase IX (CAIX) is found in the cell membrane, and is upregulated in hypoxic cancer cells where it plays a significant role in regulating the intracellular pH. Upregulation in expression of CAIX is controlled by the hypoxia inducible factor, as explained in the following section (Section 1.1.3).[16,17]

$$CO_2 + H_2O \leftrightharpoons HCO_3^- + H^+ \qquad 1.1$$

1.1.3 Hypoxia Inducible Factor

A significant part of the hypoxic response of a cancer cell is regulated by the hypoxia inducible factor, HIF-1α.[18] In the presence of oxygen, HIF-1α has a short half-life of around 5 minutes or less.[18] However, in the absence of oxygen, HIF-1α is stabilised and can cause transcriptional activation of hundreds to thousands of downstream genes related to tumour growth and metastasis.[18–21]

The oxygen dependent regulation of HIF-1α is described by Figure 1.5. HIF-1α contains an oxygen dependent degradation domain (ODDD) with proline residues that are hydroxylated by prolyl hydroxylases (PHDs), which rely on oxygen and iron as cofactors.[18,22] The hydroxylated HIF-1α is then tagged with ubiquitin by the von Hippel-Lindau protein (VHL), enabling the protein to be recognised and degraded by the proteasome.[18,22]

However, if oxygen concentration falls below 2%, PHD becomes inactive and the HIF-1α protein is stabilised.[8] It can then form a protein complex with its counterpart, HIF-1β, and other cofactor enzymes such as CBP/p300 (CBP: CREB binding protein, CREB: cyclic AMP response element binding, AMP: adenosine monophosphate).[18,21,23] This complex then binds to sequences of DNA known as

hypoxia response elements (HREs) which are responsible for protein transcription.[18,21]

Hypoxia *in vitro* can also be mimicked by adding agents such as cobalt chloride or deferoxamine (DFO) to the cell culture media.[24–26] These agents stabilise HIF-1α by interfering in the degradation pathway, even in the presence of oxygen. Both agents can competitively bind to iron, which is the cofactor for PHD, hence the activity of PHD is inhibited and HIF-1α can accumulate and become transcriptionally active.[24–26]

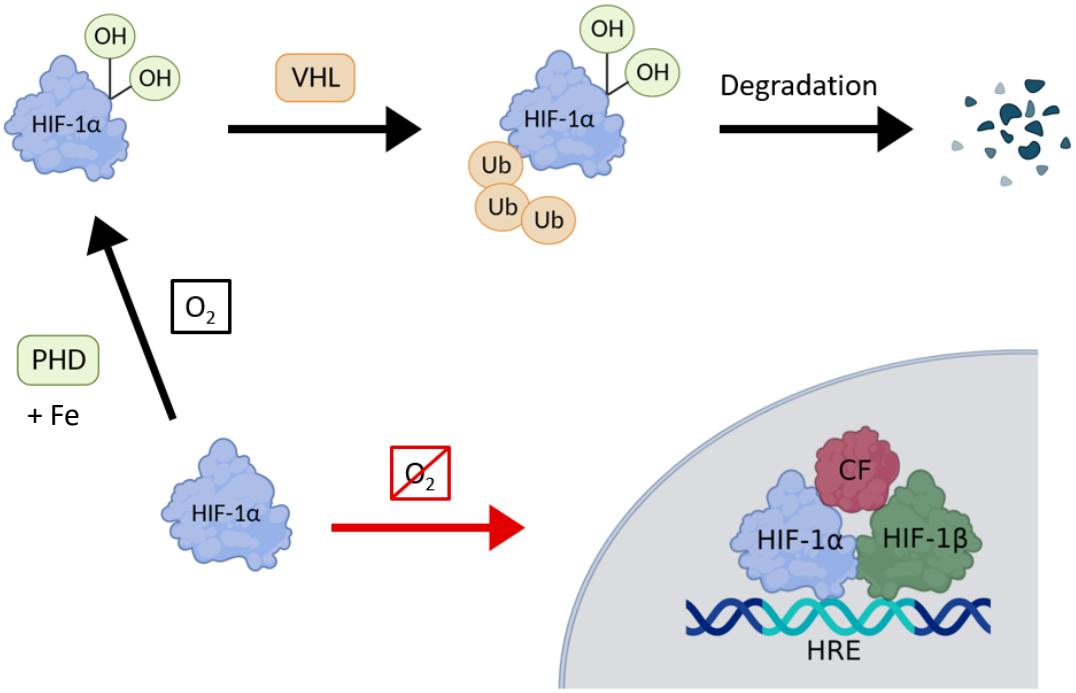

Figure 1.5: HIF-1α pathway in the presence and absence of oxygen. HIF: hypoxia inducible factor, PHD: prolyl-4-hydroxylase, VHL: von Hippel-Lindau protein, Ub: ubiquitin, HRE: hypoxia response element, CF: cofactor. Figure created in BioRender.com.

Examples of downstream proteins that are regulated by HIF-1α include glucose transporters (GLUTs), vascular endothelial growth factor (VEGF) and CAIX.[18,19] GLUTs are responsible for bringing glucose molecules into the cell.[18] This is particularly important in hypoxic cells, where the cell is reliant on glycolysis to produce energy.[18]

VEGF stimulates the production of new blood vessels (angiogenesis), which increases the supply of oxygen and nutrients to the tumour.[18] CAIX is a membrane associated protein involved in pH regulation, as discussed in Section 1.1.2.[16,17]

1.1.4 Effect of Hypoxia on Cancer Treatment

Ultimately, understanding hypoxia in cancer tumours is important because it is associated with aggressive tumour growth, resistance to treatments and poorer clinical outcome. There are many different types of cancer treatment and the treatment that a patient receives will depend on which type of cancer they have and how advanced it is.[27] Generally, the most common treatments in the UK are surgery, radiotherapy and chemotherapy.[28,29] Between 2013 and 2016 in England, 46% of patients had surgery, 31% received radiotherapy and 27% received chemotherapy either on its own or in combination with other therapy.[29] Some statistics state that more than half of cancer patients will receive radiotherapy at some point during their care.[30,31] Yet both radiotherapy and chemotherapy are less effective on hypoxic cancer cells.[7,8]

In radiotherapy, ionising radiation is directed at the tumour site to damage and kill the cancer cells.[32,33] DNA is initially damaged as a direct consequence of radiation and by hydroxide radicals produced by the hydrolysis of water. Additionally, radiation causes reduction of molecular oxygen to produce superoxide radicals, which propagate to produce reactive oxygen and nitrogen species (ROS and RNS) and radical organic molecules.[32] High concentrations of these species are very destructive in the cell and can cause further damage to DNA, proteins, enzymes and lipids eventually leading to cell death.[32,33] However, in hypoxic cells, there are very low levels of molecular oxygen, therefore less ROS and RNS are produced by radiotherapy, less damage is inflicted and the cells have a better chance of recovery.[32,33]

In chemotherapy, cytotoxic drugs are delivered to the cancer site via the bloodstream.[34] There are hundreds of different chemotherapy drugs that can be used

to kill cancer cells at different stages of the cell cycle by causing genetic damage.[34,35] However, delivery of chemotherapeutic agents to hypoxic regions of tumours via the bloodstream is often not that effective because of the disrupted and inefficient vasculature around the tumour site.[4,7]

Cancer therapies are under constant development and improvement and there are several approaches to target hypoxia in solid tumours. Some methods are based around direct targeting of hypoxic cells and others are based on trying to increase tumour oxygenation (reduce hypoxia) to increase sensitivity to other treatments such as radiotherapy, as summarised in Table 1.1. There are many radiosensitisers undergoing clinical trials, but other approaches have been less successful so far.[7,8,31,36]

For example, tirapazamine is a hypoxia activated prodrug (HAP) that looked very promising in preclinical studies. When the drug enters hypoxic cells, it is reduced to a highly reactive radical form that causes damage to DNA.[37,38] Preclinical studies on animals and cell culture suggested that tirapazamine could be an effective agent to enhance the effects of radiotherapy and other chemotherapy drugs such as cisplatin. However, success in human clinical trials was limited and some trials concluded that tirapazamine did not offer additional clinical benefit compared to existing treatments.[37,38]

Table 1.1: Approaches to improving therapy against hypoxic cancer cells.

Approach	Treatment	Description
Directly targeting hypoxic cells	Radiosensitisers	Chemicals that accumulate in hypoxic cells and enhance radiation induced DNA damage in the absence of oxygen or prevent DNA repair.[7,31]
	Hypoxia activated prodrugs	Drugs that are administered in an inactive form and accumulate in hypoxic cells, where they then become activated and cytotoxic.[7,36]
Decreasing hypoxia by increasing oxygen concentration	Hyperbaric oxygen breathing	Breathing high concentrations of oxygen before and during treatment to increase blood oxygen levels.[36]
	Vascular-targeting agents	Agents that stabilise tumour vasculature to increase oxygen delivery to the tumour.[8]
	Oxygen diffusion and transport agents	Agents that increase the amount of oxygen that can be carried in the blood or improve oxygen diffusion in blood plasma or tissue.[7]

1.2 Research Models of Hypoxia

1.2.1 Research Models in the Drug Discovery Process

The development of a new drug or therapeutic treatment can be summarised in four broad stages; discovery, preclinical research, human clinical trials and regulatory approval and marketing.[39] Overall, the process is time consuming and expensive, often taking over 12 years and $1 – 2 billion.[39,40] It is also very inefficient, with only around 12% of drugs entered into clinical trials being approved by the United States Food and Drug Administration (FDA).[39]

In the preclinical research phase, drugs are tested on animal models to estimate their stability, efficacy and toxicity before being allowed into human clinical trials.[39] However, animal models have been shown to be poor predictors of drug toxicity in humans and this is likely to be an important reason as to why so many drugs fail in human clinical trials.[39,41]

There are also significant objections to animal testing for ethical reasons.[42] The 3Rs approach - replacement, reduction and refinement - was first outlined by Russell and Birch in the 1950s and has since been widely adopted by the pharmaceutical industry.[42,43] It recommends that animal models should be replaced with non-animal models where possible. When animals are required, the study should be carefully designed to minimise the number of animals needed and minimise pain and suffering of the animals.[42,43]

Recent advancements in technology have enabled the development of research models that are based on human-biology, such as human cell based assays, organ-on-chip models and computer modelling.[44] These technologies offer viable alternatives to animal models in preclinical testing. The FDA Modernisation Act 2.0 was signed into United States law in December 2022.[45,46] It states that there is no longer a legal requirement for testing on animal models before human clinical trials for all drugs and that testing on appropriate human-based biological models may be used instead.[45–47] This recent action is a massive step forward for the pharmaceutical

and biotechnology industries and puts innovation and development of human-based biological models in the limelight.

The following sections will describe some examples of how animal models and human-based alternatives have been used to research hypoxia in human cancers.

1.2.2 Animal Models

Cancer tumours in animals are considered good research models because they contain many of the same physiological properties as human cancer tumours; they are 3-dimensional, are composed of different cell types and extra-cellular matrix, have vasculature, can interact with other tissues and organs and experience hypoxia.[48] Mice are the most popular animal model for oncology research, and are used in over 95% of *in vivo* studies.[48,49]

One of the drawbacks of animal models is that results often don't translate to produce similar results in humans due in part to fundamental differences in the biology of animals and humans. In cancer tumour models, this has been partially improved by xenograft models, which enable human cancer cells to be implanted in the mice. Tumours based on the human cells then develop in the mice, providing a potentially more clinically relevant research model.[48,49]

Even though hypoxia occurs naturally in the tumours, it is beneficial to be able to control the extent of hypoxia across populations when investigating the effects on tumour biology and cancer treatments. Methods of regulating hypoxia in mouse models have been recently reviewed by Bruycker *et al*.[50] One of the most common methods is to change levels of oxygen in the air that the mice breathe. Increased oxygen content of the air increases oxygen levels in the blood which increases oxygenation of the tumour and oppositely, decreased oxygen content of the air decreases oxygenation of the tumour.[50]

This method was utilised by Mortensen *et al*. who showed that mammary mouse tumours were less hypoxic in populations of mice breathing carbogen (95% oxygen,

5% CO_2) compared to mice breathing normal air. The tumours were treated with radiotherapy, which was more effective at reducing tumours in the carbogen breathing population than the population breathing normal air.[51]

Alternatively, more extreme measures can be taken to increase tumour hypoxia. Hong *et al*. studied metastasis of human Ewing sarcoma (cancer in bones or tissue around the bones) tumours in mice.[52] They used femoral artery ligation (FAL) to surgically restrict the blood supply to the tumour site, resulting in hypoxia throughout the majority of the tumour tissue. In the control population without FAL, only a small proportion of the tumour tissue that was positioned further away from the vasculature was hypoxic. The primary tumours were surgically removed and the occurrence of tumour metastasis were monitored over a few weeks. The mice with FAL experienced more metastatic tumours with larger volume compared to the mice without FAL.[52]

1.2.3 Basic 2D-Culture Models

Standard monolayer cell cultures provide a much simpler and less expensive way to study human cells, however, they lack the biological complexity and dynamic environment that animal models have.[53] Traditionally, hypoxia has been studied on monolayer cultures using hypoxic chambers, incubators or gloveboxes, where the cell culture is placed in an enclosed container and the air in the container is replaced with the desired concentration of oxygen.[54–56] One key disadvantage of this method is that the cells can only be studied under one oxygen concentration at a time.[55,56]

Strese *et al*. used hypoxic incubation to study the effects of different drugs on monolayer cell cultures at different oxygen concentrations. Populations of 5 different cell lines (ovarian, renal, breast, small-cell lung carcinoma (SCLC) and lymphoma) were grown in 96-well plates at oxygen concentrations of 20%, 1% and 0.1% oxygen. Each population of cells was treated with 15 different chemotherapy drugs for 72 hours and then cell viability was assessed.[54]

As expected, the efficacy of each drug was dependent on the cell line and level of oxygenation. For example tirapazamine was more effective under 0.1% oxygen than 21% oxygen for renal and SCLC cells. Docetaxel had a stronger effect on renal cells at 21% oxygen than renal cells at 0.1% oxygen, but the effect was similar on SCLC cells regardless of oxygen concentration. The simple experimental model and refined experimental protocol make for clear and comparable results. However, the authors also acknowledge that that there are many variables of an *in vivo* environment that are excluded from the model including 3D structure and gradients in nutrient and oxygen supply such that clinical translation of the results is limited.[54]

1.2.4 Microfluidics and 2D-Culture

Microfluidics can help to overcome some of the issues with standard 2D culture models. For example, systems have been developed that allow cells to be studied under multiple oxygen concentrations at the same time, which is more experimentally efficient compared to looking at only one concentration at a time in hypoxic incubators. These systems can be used to create more physiologically relevant environments by incorporating oxygen gradients and fluctuating oxygen concentrations.

The following examples include integration of microfluidics with a 96-well plate to create different oxygen concentrations in different wells, a compact oxygen gradient over a single microfluidic channel and a device to study interactions between hypoxic cancer cells and non-hypoxic non-cancerous cells. Further examples of microfluidic oxygen gradients created using gas flows, oxygen scavenging chemicals and cellular consumption of oxygen will be discussed throughout the introductory sections to Chapters 2, 3 and 4.

<u>Example: Combining microfluidics with a standard well plate</u>

Yao *et al*. have developed devices based on the standard 96-well plate format. By utilising microfluidics, they can expose cells in different wells to different oxygen concentrations at the same time.[56–58] The device design is shown in Figure 1.6. The

bottom layer of the device contains a microfluidic network, which allows input gases to mix and flow through into the gasket layer. The gasket layer has channels directing the output gas from the manifold to areas under each row of the well plate. The bottom surface of the well plate is permeable, which allows molecules to diffuse between the gas layer and liquid layer of the cell culture, resulting in control of the oxygen concentration in each row of the well plate.[58] The authors tested the device by growing breast, pancreatic and colorectal cancer cells under 8 different oxygen concentrations at the same time. Each cell line was responsive to the hypoxic conditions, with cells in rows with lower oxygen concentration showing higher expression of characteristic hypoxic markers HIF-1α and CAIX.[58]

In further iterations of the device, it was shown that the oxygen can be cycled between high and low concentration by controlling the gas inputs, creating a dynamic environment in the wells.[57,58] In pancreatic and colorectal cancer cells cycling hypoxia over 24 hours resulted in higher expression of HIF-1α compared to static hypoxic conditions.[57] This experiment further highlighted that the oxygen environment has significant effects on cell behaviour. The device was also demonstrated as a drug testing platform. It was found that tirapazamine was more effective on cells with lower oxygen concentrations, and was equally effective under static and cycling hypoxia.[56] The authors intend to continue developing the device and exploring the effects of dynamic hypoxic conditions on cancer cells.[56]

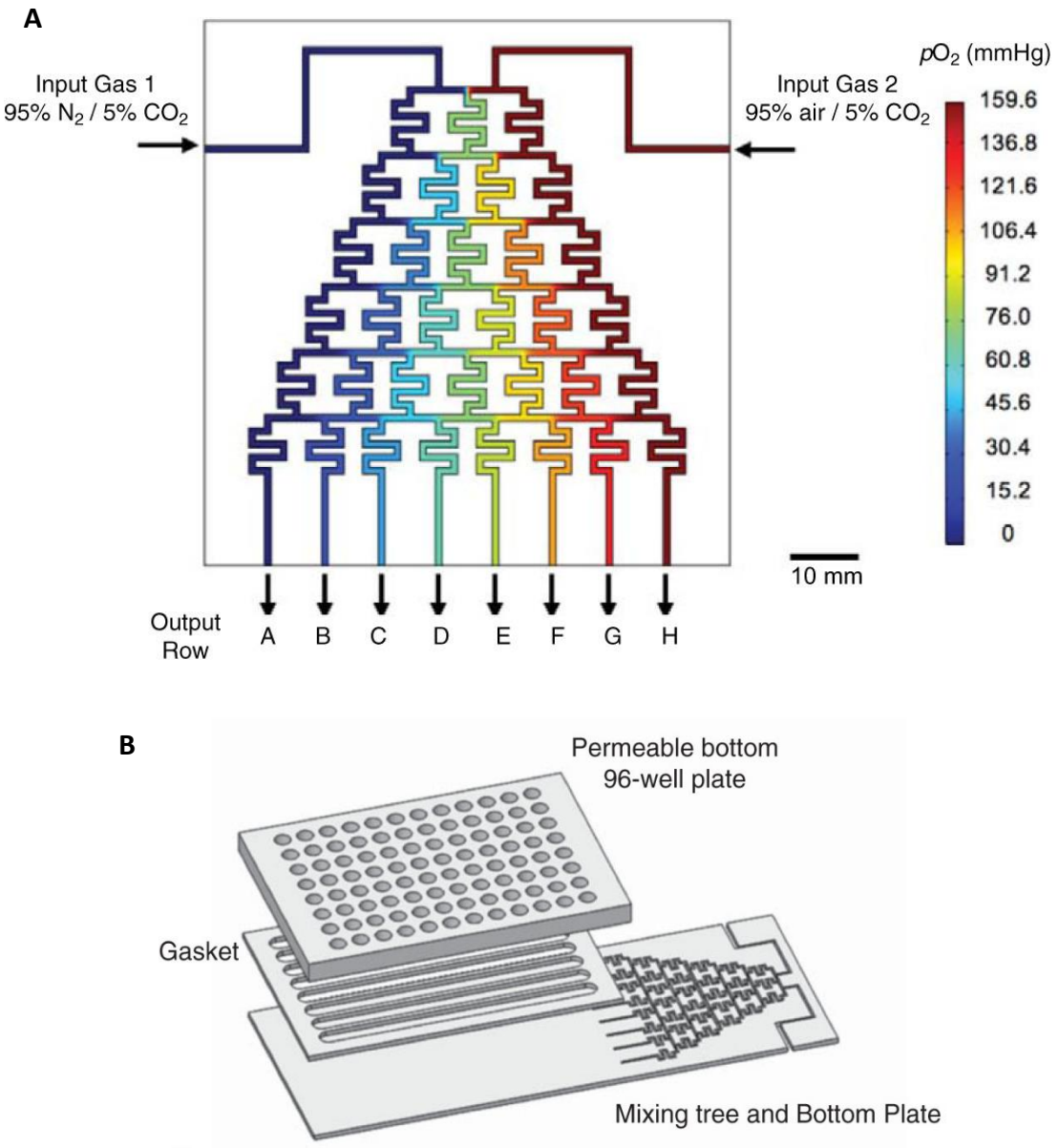

Figure 1.6: Device by Yao et al. for controlled oxygen delivery to wells of a 96-well plate.[58] ***A*** *Example of gas control to deliver a different oxygen concentration to each row of a well plate.* ***B*** *Layers of the device. Gases flow through the mixing tree and into the gasket channels. Diffusion through the permeable well plate surface results in control of the oxygen concentration in the well. Reprinted from Yao et al. with permission from The American Physiological Society.*[58]

Example: Oxygen gradient in a single fluidic channel

Orcheston-Findlay *et al*. demonstrated a microfluidic device that could be used to grow cancer cells under a physiologically relevant oxygen gradient in a single channel, as shown in Figure 1.7.[59] Cells are seeded into the main channel then two solutions of cell culture media with different oxygen concentrations flow in. The streams of media flow down the channel to create a gradient of oxygen across the surface of the cells. The aim is to have a gradient of oxygen that represents a cross section of a tumour from the oxygenated areas close to the vasculature to hypoxic areas further away from vasculature.[59]

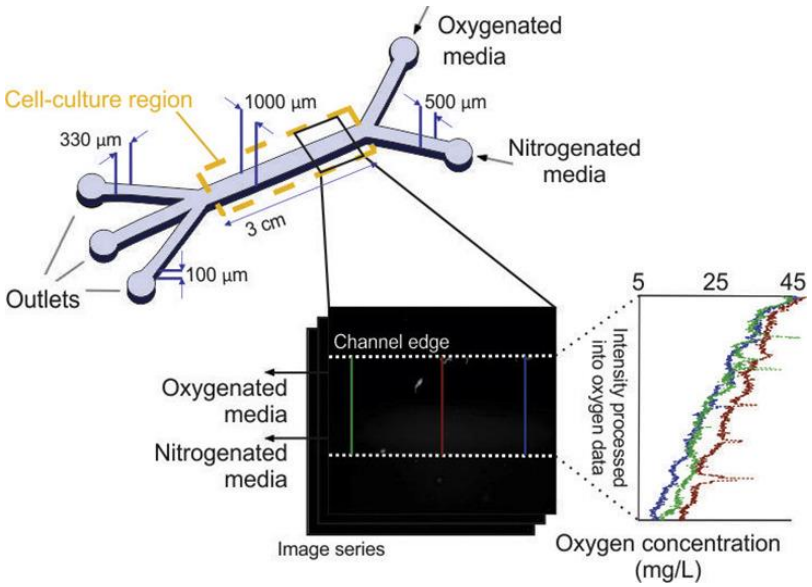

Figure 1.7: Device by Orcheston-Findlay et al. for formation of an oxygen gradient across a single microfluidic channel.[59] Cells are seeded in the chip and then solutions of cell culture media saturated with nitrogen and oxygen flow through the two inlets. As the streams of media come together, they flow parallel to one another down the length of the channel and oxygen diffuses between the streams to make an oxygen gradient across the cells. The graph shows measurements of oxygen concentration across the width of the channel. Reprinted from Orcheston-Findlay et al. with permission from Elsevier.[59]

Operation of the device was shown to be effective with endometrial cancer cells and a media flow rate of 5 – 10 µL/hour. Cells in the device have not yet been tested for markers of hypoxia or response to drug treatments. Further development of the device is required to optimise the range of the oxygen gradient.[59] However, the device represents a more compact approach compared to the 96-well plate style device described above.

Example: Microfluidic oxygen gradient with co-culture

In both of the microfluidic examples discussed so far, the studies have only considered one cell type at a time. Sun *et al.* have designed a device which can be used to study hypoxia and the interaction between two different cell types at the same time.[60] The authors used the device to study the interaction between mouse skin cancer cells (B16) and non-cancerous mouse fibroblasts (L929), which are commonly found in the stroma surrounding the tumour.[60] This device is interesting because it enables study of how cancer cells interact with the local non-cancerous cells and how these interactions are influenced by tumour hypoxia.

As shown in Figure 1.8, the cancer cells are cultured adjacent to the chemical reaction channel, where sodium hydroxide and pyrogallol are purged through to create an oxygen scavenging reaction. These two channels are separated by a thin permeable wall such that depletion of oxygen in the environment surrounding the chemical reaction channel results in a gradient of oxygen forming across the cancer cells. The cells closest to the chemical reaction channel experience hypoxia and the oxygen concentration gradually increases across the width of the cancer cell culture channel.

In the channel on the opposite side of the chip, fibroblasts can be cultured without experiencing hypoxia. The two cell culture channels are separated by another channel which contains only cell culture media. The barriers between these three channels are made of micropillars which allow the two cell types to communicate through chemical signals released into the media. Both cell types can also migrate

into the middle channel over time; hence this device is also a model to study cancer cell migration.[60]

In a series of experiments conducted by the authors in the presence of oxygen (no oxygen scavenging reaction), the skin cancer cells migrated further into the media channel when they were co-cultured with fibroblasts in the device. The migration was increased further when the cancer cells were cultured under the hypoxic gradient.[60] This study is a good demonstration of how microfluidics can be used to create more dynamic, complex and physiologically relevant cancer models compared to standard 2D cultures.

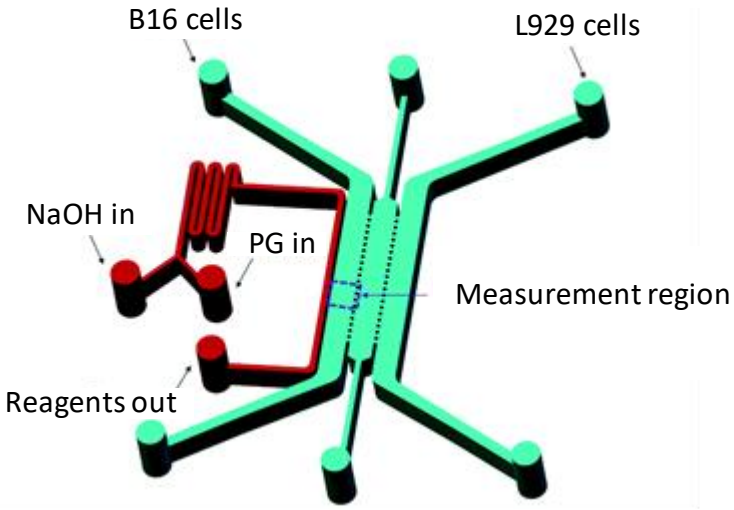

Figure 1.8: Device by Sun et al for culture of cancer cells under an oxygen gradient with co-culture of non-cancerous cells.[60] Mouse skin cancer cells (B16) and mouse fibroblasts (L929) are cultured in the outer channels, separated by a channel which is filled with cell culture media as a space for the cell lines to migrate into. In the red channel on the left, pyrogallol (PG) and NaOH are mixed to make an oxygen scavenging reaction. The reaction channel and B16 culture channel are separated by a permeable barrier such that oxygen depletion in the reaction channel produces an oxygen gradient across the width of the B16 culture channel. The channel wall closest to the reaction channel is hypoxic and oxygen concentration gradually increases

towards the opposite side of the channel. Reprinted from Sun et al. with permission from the Royal Society of Chemistry.[60]

1.2.5 3D-Culture Models

3D culture models give rise to further opportunities to increase the complexity of *in vitro* cancer models. Different types of 3D models have been developed including spheroids, scaffolds and hydrogels. These models can offer naturally occurring gradients in oxygen and nutrient availability and are also more physiologically relevant from the perspective of cell organisation. In 3D models, cells have the opportunity to maximise cell-cell contact and cell-extra cellular matrix contact which is much more representative of the *in vivo* tissue environment compared to 2D monolayer cultures.[53,61,62] Using 3D culture models to study tumour hypoxia has been recently reviewed by Bhattacharya *et al*.[61]

Example: Comparison of drug toxicity of 3D spheroids and 2D cultures

As shown by the transmitted light images in Figure 1.9, spheroids are 3D spherical aggregates of cells. Close and Johnston grew spheroids of human head and neck cancer and monitored how hypoxia developed in the core of the spheroids over four days of growth.[63] The authors demonstrated that the core of the tumour was hypoxic by staining with fluorescent probes that selectively stain hypoxic cells and showing that HIF-1α expression was increased in cells at the core (hypoxia probes are further reviewed in Chapter 6).[63]

The limited diffusion of oxygen and nutrients from the spheroid surface to the core of the spheroid is similar to the limited diffusion in an *in vivo* tumour as distance from the vasculature increases. Hence, spheroids represent a more physiologically relevant model for drug testing compared to 2D cultures where all cells have equal availability of oxygen, nutrients and drug dosage. To demonstrate this, Close and Johnston tested HAPs on spheroid cultures and monolayer cultures of head and neck cancer cells.[63]

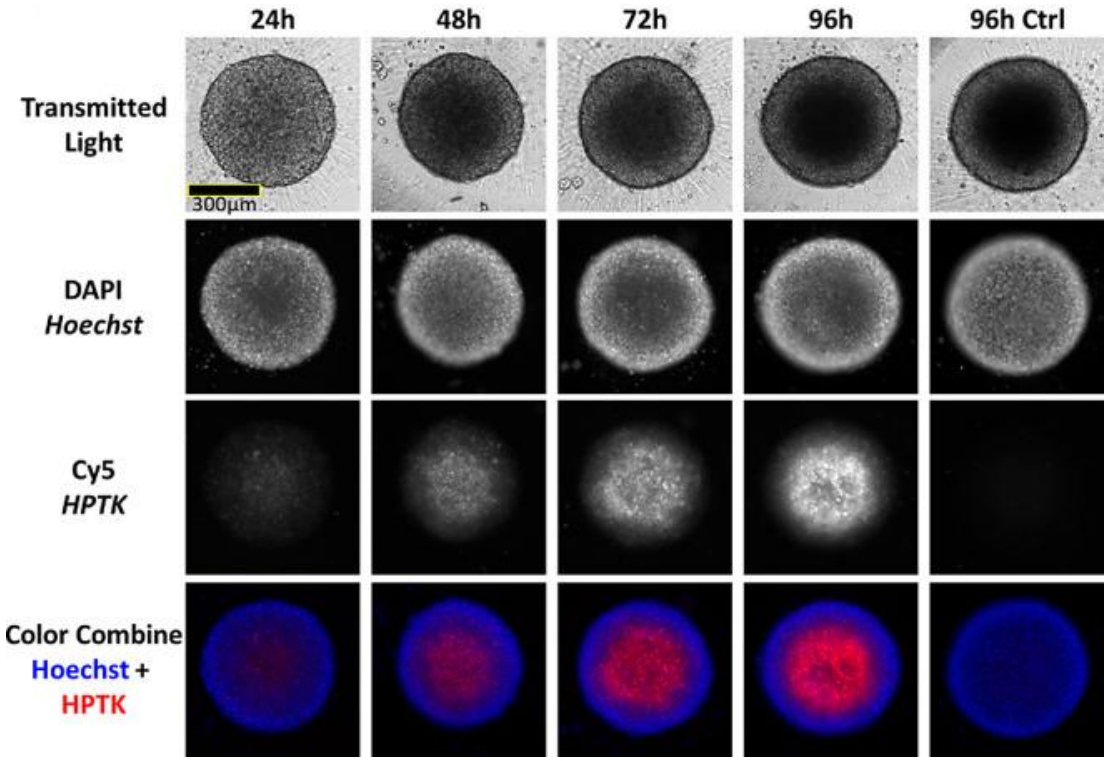

Figure 1.9: Hypoxia staining of live head and neck squamous cell carcinoma multicellular tumour spheroids by the HypoxiTRAK™ (HPTK) probe by Close and Johnston.[63] DAPI and Cy5 are the fluorescence imaging channels used to image Hoechst nuclear stain and HPTK respectively. Images of the spheroids were acquired over 4 days and the control (Ctrl) was not stained with HPTK. Reprinted from Open Access article (Creative Commons CC BY) by Close and Johnston.[63]

Tirapazamine and evofosfamide are HAPs that were shown to be effective on hypoxic cancer cells in monolayer cultures, but had a much lower impact on the spheroids. There were still many live cells remaining after treating spheroids with each drug. This highlights that the physiological parameters represented in spheroids, namely 3D structure, oxygen and nutrient gradients and cell-cell contact, can significantly improve cell survival during cancer treatments. The results of the spheroid drug testing experiments were more aligned with the real clinical outcomes of tirapazamine and evofosfamide. Although both showed promising results in preclinical testing, they both failed in human clinical trials.[63]

Spheroids can be cultured in well plates, making high throughput analysis possible, but adoption of spheroid culture has been slow because not all cell types can grow as spheroids, the 3D nature can make standard analysis more challenging and sample inhomogeneity can make interpretation of the data more difficult. However, spheroids could become increasingly important if growth and analysis can be standardised and they continue to provide better predictive capabilities compared to monolayer culture.[64]

Example: Combined scaffold and hydrogel model

Simon *et al.* used a scaffold design to make stacks of human lung cancer cells that experienced vertical gradients of oxygen, as shown in Figure 1.10.[65] Each layer of the scaffold had 10 cell culture zones, where cells were suspended in 3D in Matrigel, which is a popular hydrogel consisting of proteins commonly is found in the extra cellular matrix such as collagen and laminin. The model had a total of six cell culture layers which were stacked on top of each other and secured in an acrylic frame. Media was supplied from the top of the scaffold so oxygen and nutrients were readily available to cells in the top layers of the scaffold. However, oxygen diffusion through the hydrogel was limited and cells in the bottom layers became increasingly hypoxic as oxygen in the local environment was depleted through metabolism.[65]

After an experiment, the individual layers of the scaffold were separated and the cells were harvested for analysis. The authors demonstrated that the cells cultured in the lower layer of the scaffold expressed higher levels of hypoxia markers HIF-1α and CAIX. They also treated models with doses of radiotherapy and found that cells in the deeper, more hypoxic layers of the scaffold were more resistant to radiotherapy.[65]

The authors acknowledge that further development could involve co-culture of different cell types in different scaffold layers to increase physiological relevance and complexity.[65,66] Additionally, sensors could be embedded into the scaffold framework to allow cellular analysis *in situ* without having to separate the scaffold layers.[65]

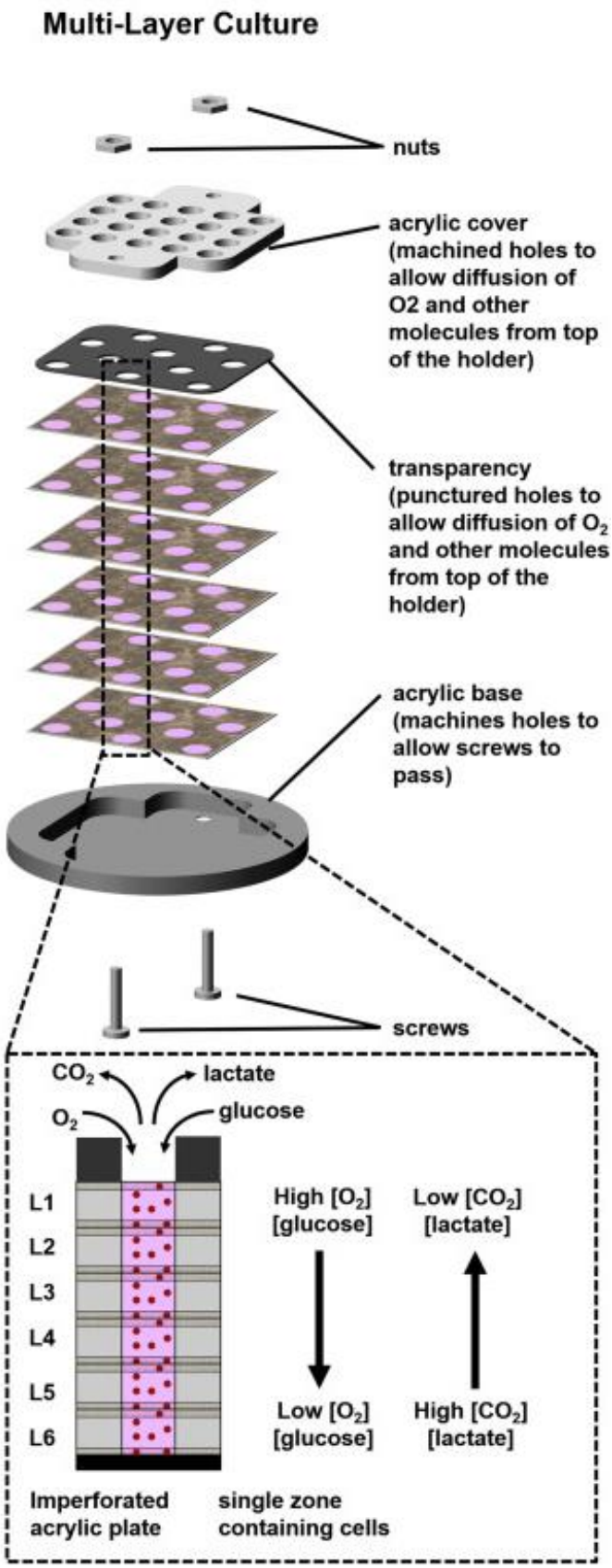

Figure 1.10: 3D culture system by Simon et al.[65] The scaffold contains six layers of paper-plastic composite sheets (approximately 130 µm thick), each containing 10 aligned cell culture zones. Cell suspensions in Matrigel are seeded into each zone in each composite sheet before stacking to form the scaffold. The layers at the top of the scaffold are close to the cell culture medium so they have access to oxygen and nutrients and metabolic waste products, CO_2 and lactate, can diffuse out. However, access to media progressively decreases down the layers of the scaffold where access to oxygen and nutrients is limited and metabolic waste products can accumulate. Reprinted from Simon et al. with permission from Elsevier.[65]

Example: Spheroids On-A-Chip

Refet-Mollof *et al*. created a device to culture 240 spheroids at the same time, as shown in Figure 1.11.[67] The authors used the chip to grow human smooth muscle cancer (leiomyosarcoma) and human soft tissue sarcoma cells into large spheroids. They demonstrated that the spheroids had to be grown to a size of 750 µm in diameter in order to exhibit a significant proportion of hypoxic cells at the core.[67]

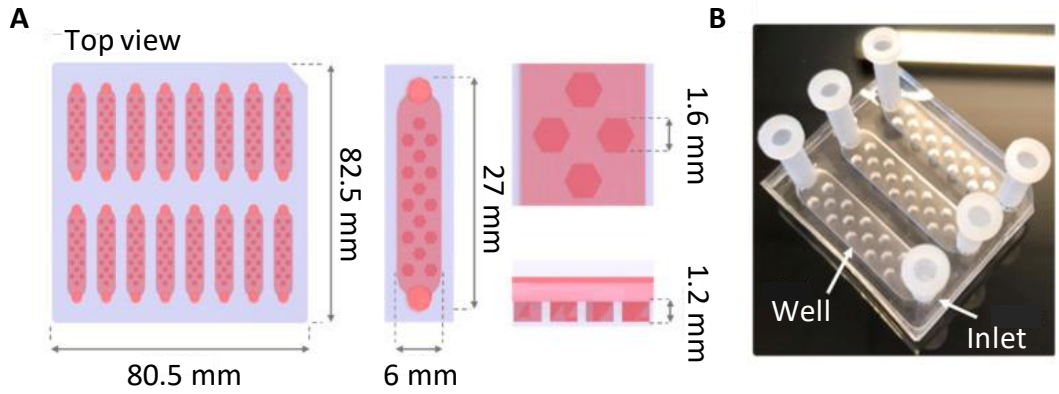

Figure 1.11: Chip made by Refet-Mollof et al. for culture of large spheroids.[67] ***A*** *Chip design with 16 channels, each with 15 wells, 1 spheroid is cultured in each well giving the device a capacity of 240 spheroids.* ***B*** *Image of device with 3 channels. Reprinted from Open Access article (Creative Commons CC BY) by Refet-Mollof et al.[67]*

Spheroids from both cell lines were stained for the hypoxia markers HIF-1α and CAIX. As expected, the soft tissue cell spheroids showed increased expression of both HIF-1α and CAIX in the hypoxic core. However, smooth muscle cell spheroids showed increased expression of CAIX in the hypoxic core but a more uniform distribution of HIF-1α throughout the spheroid. The authors suggested that this unexpected observation was due to abnormal basal levels of HIF-1α in this cell line due to a mutation which enables stabilisation of HIF-1α even in the presence of oxygen.[67]

The spheroids were then treated with tirapazamine and radiotherapy independently and as expected, tirapazamine targeted the cells in the hypoxic core of the spheroid. However, an unexpected result was that the hypoxic core was not found to be less

susceptible to radiotherapy compared to the non-hypoxic cells on the spheroid surface. This result is not well understood, but it was suggested that the spheroids may need to be even larger to increase the proportion of hypoxic cells at the core of spheroid to increase the potential of observing radioresistance.[67]

The main advantages of this chip over standard well-plate culture of spheroids is that the size of spheroid growth is controlled and consistent, more spheroids can be cultured per unit area and the culture requires less media and reagents. The chip provides a useful platform for studying effects of drugs, radiotherapy and combination treatments on hypoxic spheroids.[67] The results also highlight the importance of investigating different models of hypoxia with different cell lines to further understand the relationship between hypoxia and the efficacy of radiotherapy.

1.3 Project Outline and Objectives

Hypoxia in solid cancer tumours is a critical physiological parameter that is correlated with aggressive tumour growth, metastasis and resistance to treatments. Traditionally, preclinical research on hypoxic cancer cells has been done using monolayer cultures of human cancer cells or 3D tumours in animal models. However, these models are not representative of the *in vivo* human tumour environment and have been shown to be poor predictors of clinical success.

New and innovative models of cancer tumours are being developed to try to improve physiological relevance of *in vitro* studies by incorporating more characteristics of the human tumour environment. One approach is to use microfluidic technology, however, as highlighted in a recent review by Chermat *et al*., the use of microfluidics to study the relationship between tumour hypoxia and radiotherapy has been underexplored.[68]

Therefore, the goal for this project was to work towards the development of a microfluidic model of tumour hypoxia to study the impact of radiotherapy and combined treatments on human cancer cells. Initially, the aim was to use prostate

cancer cells, as prostate cancer tumours are known to experience severe hypoxia and around 30% of prostate cancer patients in the UK receive radiotherapy during their care.[4,69] It was hypothesised that if a working device could be demonstrated with prostate cancer, the same technology could then be applied to other cancer types.

To start the project, the first objective was to make a simple device for culturing monolayer cells under a range of oxygen concentrations at the same time. The design and fabrication of the microfluidic device is presented in Chapter 2. After fabricating the device, computational and physical experiments were used to characterise the oxygen profiles in the chip, as discussed in Chapters 3 and 4 respectively. A method to culture cells in the device was established in Chapter 5, then the response to hypoxic oxygen conditions was investigated in Chapter 6.

Chapter 2: Design and Fabrication of Fluidic Chip

2.1 Introduction

Since the 1990's, microfluidic devices have become increasingly popular and have found many applications in synthesis, bioanalysis and drug testing.[70] A whole host of materials and fabrication methods have been utilised and developed to suit a range of applications, as summarised in recent review papers by Niculescu *et al.* and Nielsen *et al*.[70,71]

The aim of the experimental work presented in this chapter was to design and make a chip that could be used for culturing cells under an oxygen gradient without using clean room facilities. First, a design and fabrication method for a PDMS chip is presented and the technical and usability challenges faced are discussed (Section 2.2.1). Following this, a second chip design and the fabrication method for making the chip from acrylic is presented (Sections 2.2.2 and 2.2.3). The components used to complete the set-up for the acrylic chip are discussed and a full picture of the complete system is presented in Section 2.2.4.

2.1.1 Fabrication Methods for PDMS Chips

Soft lithography is one of the most well established methods for making devices from PDMS for biological applications.[72] The soft lithography process is briefly explained in Figure 2.1. PDMS is a silicon polymer that is popular due to its many favourable properties; biocompatible, optically transparent, mouldable, permeable to gas. It is an ideal material for rapid prototyping and produces high quality devices, however, soft lithography techniques generally require use of clean room facilities which can be expensive and time consuming.[72]

Soft lithography is based on making a mould for PDMS, so other methods for making the moulds have been investigated. Less expensive techniques to make moulds that do not require clean room facilities include 3D-printing and micromachining

acrylic.[72–75] Although these techniques may be more accessible, the resolution is lower which limits the applicability of these methods for making microfluidics.[72]

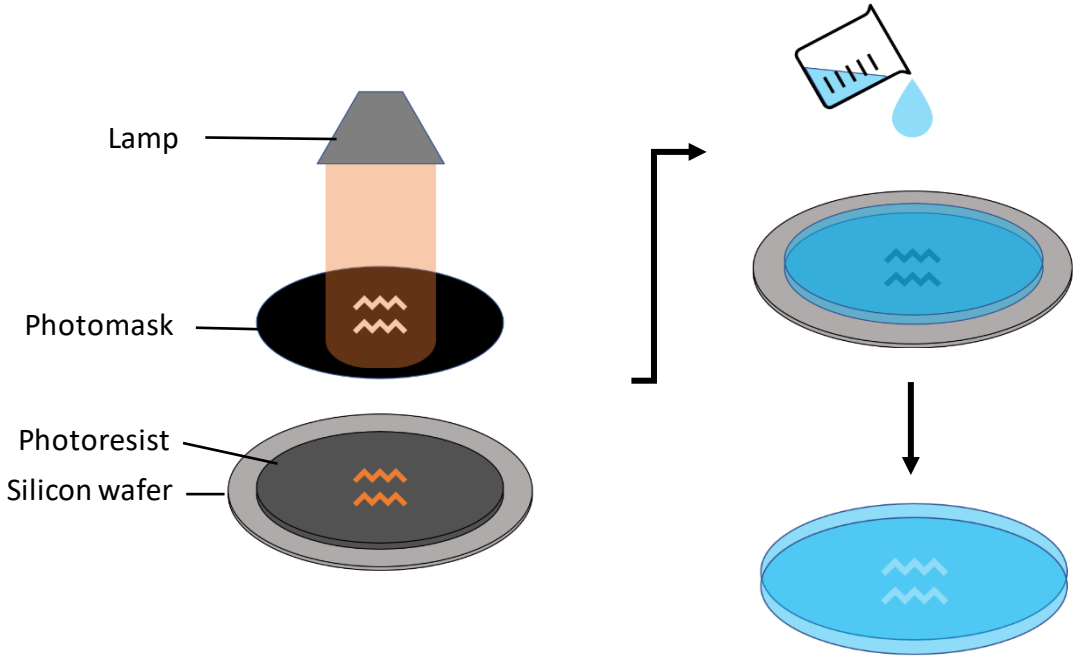

Figure 2.1: Summary of soft lithography process. Photoresist (light sensitive polymer) is spin coated onto a silicon wafer. The desired pattern is set into the photoresist (orange) by projecting light onto the surface through a mask. The mould is developed and excess photoresist (grey) is removed, leaving a positive footprint of the design. Liquid PDMS is then poured into the mould, set and removed to produce a PDMS part with an inset pattern.[76,77]

Rexius-Hall *et al*. used soft lithography techniques to fabricate a PDMS device for studying cells under oxygen gradients, as shown in Figure 2.2.[78] The device has a glass base, then two gas flow channels in PDMS. The gas channels are separated from the open cell culture channel by a thin PDMS membrane. Flow of nitrogen and oxygen rich gases through the gas channels generates an oxygen gradient through the cell culture.[78]

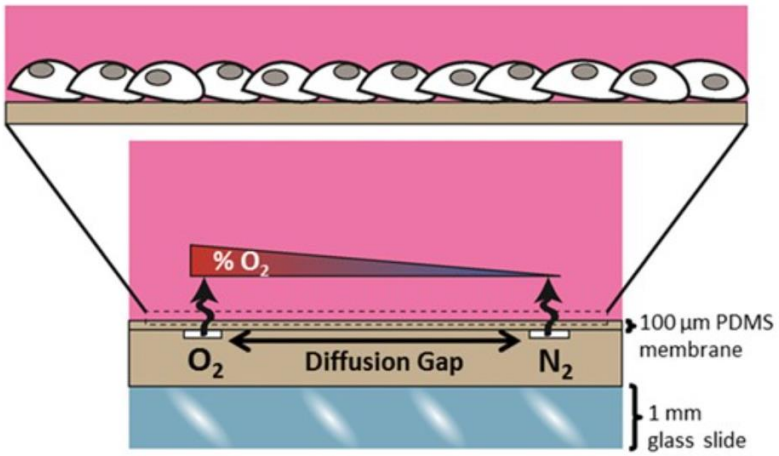

Figure 2.2: Microfluidic device with open culture area separated from gas channels by a thin PDMS membrane. There is a glass slide on the bottom of the device. Reprinted from Rexius-Hall et al. with permission from Oxford University Press.[78]

A similar device was presented by Menolascina *et al*., however, it was fabricated using an alternative method to soft lithography. The device consisted of 3 channels; one central channel for cell culture and 2 adjacent channels for gas flow, as shown in Figure 2.3.[79] The channels were separated by thin PDMS walls such that the gasses in the outer channels permeate through the walls and produce an oxygen gradient across the cell culture channel. The device was fabricated by using a precision cutting technique to cut and remove the channel segments from a thin PDMS sheet. The remaining PMDS formed the channel walls which were irreversibly bonded between two glass slides (Figure 2.3).

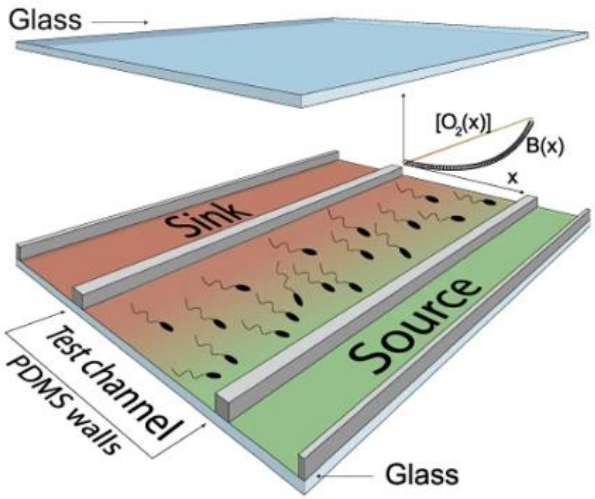

Figure 2.3: Microfluidic device with 3 parallel channels separated by PDMS walls and with top and bottom glass surfaces. Reprinted from Open Access article (Creative Commons CC BY) by Menolascina et al.[79]

2.1.2 Fabrication Methods for Acrylic Chips

An alternative to PDMS is PMMA (acrylic), which is a rigid plastic that still offers biocompatibility and optical transparency.[80–82] It can be processed using techniques including milling, hot embossing and injection moulding without the need for a clean room.[82,83] For example, Peñaherrera *et al.* made an acrylic device for studying human kidney cells (HEK293T).[84] The channels in the acrylic device were formed by etching with a CO_2 laser.[84]

Guzzi *et al.* made a multilayer acrylic device for culturing cell lines.[81] Channels and wells were micro-milled into the acrylic, then the acrylic layers were bonded together with a heated pneumatic press. The device was shown to be compatible with cultures of multiple human cell lines; cervical cancer (HeLa) cells, lymphoblast cells (Jurkat), lung cancer (A549) and kidney cells (HEK293T).[81]

2.2 Results

2.2.1 PDMS Chip

The design for the PDMS chip discussed here was inspired by the chip presented by Menolascina *et al*. in Section 2.1.1.[79] It consisted of 3 channels: one central channel for cell culture and 2 adjacent channels for gas flow. The channels were separated by thin PDMS walls such that the gasses in the outer channels permeate through the walls and produce an oxygen gradient across the cell culture channel, as illustrated in Figure 2.4. In theory, it would then be possible to analyse the cells in the culture channel at various points across the gradient and study the different characteristics and behaviours of the cells under different oxygen concentrations.

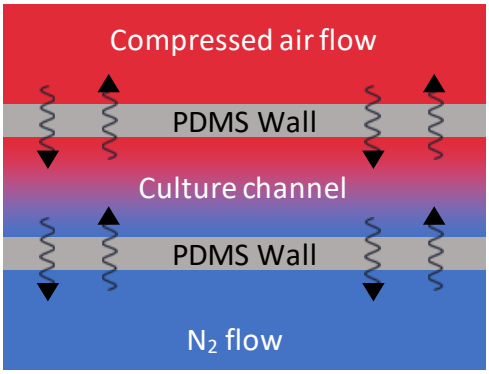

Figure 2.4: Illustration showing 3 channel design of PDMS chip. Black arrows indicate movement of oxygen and nitrogen molecules through the PDMS walls. Red indicates high oxygen concentration and blue indicates low oxygen concentration.

As previously mentioned, the chip by Menolascina *et al*. (Figure 2.3) had glass surfaces and was made using a precision cutting technique.[79] For the chip discussed here, it was attempted to make the whole chip from PDMS, using a method that was more suitable for batch production and without using standard soft lithography techniques.

The method for creating the PDMS mould was based on using stickers and laser cutters, similar to work presented by Samuel *et al*.[85] A vinyl sticker sheet was stuck to a piece of acrylic, then the chip design was cut into the vinyl layer using a UV laser

(LPKF ProtoLaser U3). The calibrated UV laser allowed the thin vinyl sticker to be cut without damaging the underlying acrylic. The unwanted sections of vinyl sticker were peeled off leaving the design footprint and the acrylic was cut to fit a large petri dish (14 cm). This formed the mould as shown in Figure 2.5 (A).

Safety Note: In general, laser cutting of vinyl is not recommended. Heating or burning of materials containing polyvinyl chloride can lead to the production of hydrochloric acid and toxic fumes, which can be hazardous to the operator and damage the laser cutter.[86] *However, when used appropriately, UV lasers result in minimal heat deposition into the material during cutting (unlike CO_2 lasers) and so avoid thermal damage to the material and production of toxic chemicals.*[87–89]

The mould was filled with liquid PDMS (Sylgard 184 elastomer and curing agent, 1:10 w/w, mixed and degassed) which was cured at 60° C for 2 hours. A scalpel was used to cut out the individual PDMS parts and inlets and outlets were formed with a biopsy punch. The PDMS parts were plasma bonded to glass cover slips forming the chips as shown in Figure 2.5 (B) and (C).

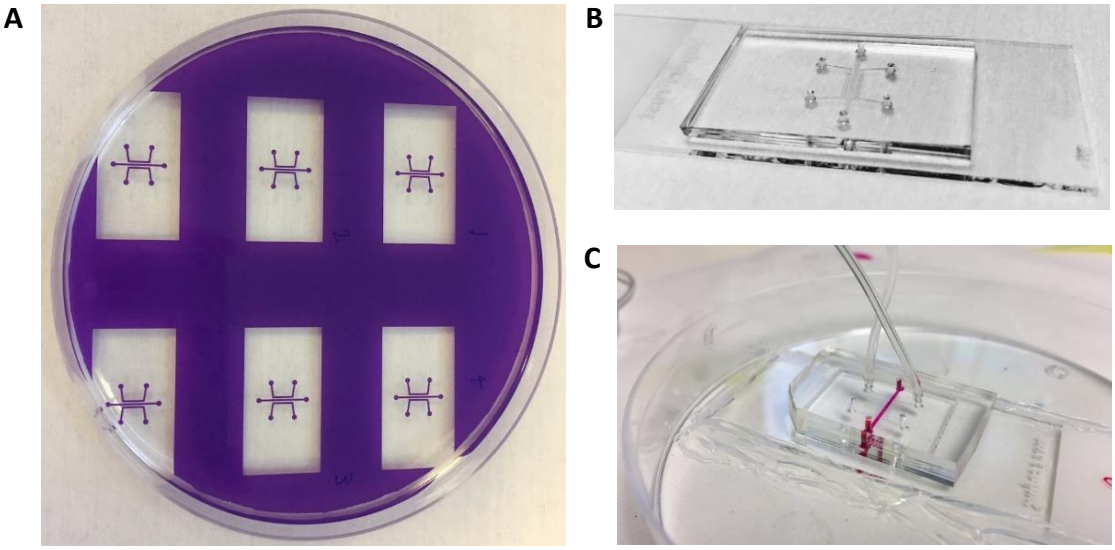

Figure 2.5: PDMS chips. ***A*** *PDMS mould made from petri dish and vinyl stickers.* ***B*** *PDMS chip cut from mould and bonded to glass slide.* ***C*** *PDMS chip with tubing fitted for gas supply and pink dye in the central channel.*

Advantages of this approach are that it was low cost, did not require clean room facilities, the moulds were reusable and the materials were biocompatible. The developed fabrication method successfully produced suitable chips, however, the main difficulty with the surrounding set up was found to be the gas supply. Compressed air and nitrogen were supplied by gas cylinders and the flow rate (approximately 10 mL/min) was controlled by flowmeters (Cole Parmer Masterflex), as shown in Figure 2.6. It was essential that the system was portable so that the chip system could be moved between instruments, laboratories and buildings. The gas cylinders were stored on a trolley with wheels, however, transport was still challenging due to the combined weight of the cylinders.

Figure 2.6: Image of compressed air and nitrogen gas cylinders with regulators and flowmeters in a portable trolley.

It was also challenging to achieve a stable gas flow with the flowmeters. The flow was set by turning on the cylinder, controlling the output pressure with the regulator and then setting the flow rate to the chip with the flowmeter. The flow rate was checked routinely (every 5 – 10 minutes) during tests and often had to be corrected back to

the desired rate. The connections between the cylinder, regulator and flow meter were tested and found not to be leaking, so the reason for the unstable flow rate remained unclear. Higher precision flowmeter systems that can be controlled electronically are available, however, they are expensive and do not remove the need for the gas cylinders.[79,90]

Additionally, the gas flow often resulted in bubble formation in the liquid in the central channel, as shown in Figure 2.7. This was potentially due to imperfect bonding at the glass – PDMS interface at the walls, or evaporation from the liquid channel.

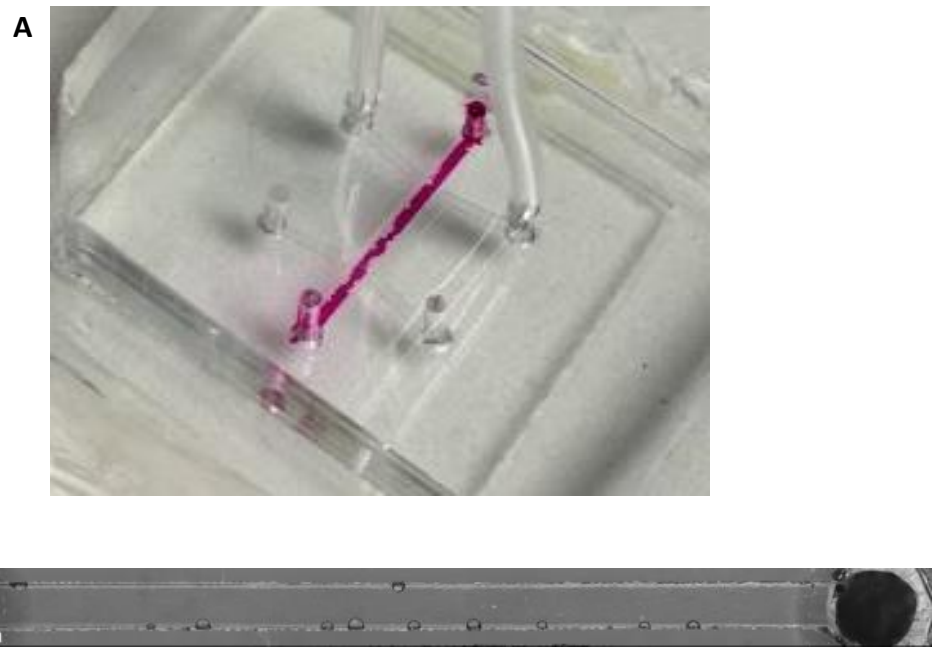

Figure 2.7: Images showing bubble formation in the liquid channel whilst gas was flowing through the gas channels. ***A*** *Bubble formation is visible in the pink dye.* ***B*** *Bubble formation is visible at the channel walls. Image taken on Nikon-TiE microscope, scale bar in 300 µm.*

Bubble formation is a well-recognised problem with PDMS devices, particularly for cell culture applications.[91,92] Many approaches have been taken in literature to solve this, including incorporation of bubble traps into the microfluidic system and active removal of bubbles by suction through the gas permeable PDMS.[93–95] Wood *et al*. and Grist *et al*. both made devices with a liquid cell culture channel and gas flow channels,

similar to the design described here.[96,97] They avoided bubble formation in the cell culture channel by adding an additional liquid channel between the culture and gas flow channels, termed a hydration layer.[96,97]

Further iterations of this device could have been developed to incorporate hydration channels and minimise bubble formation. However, it was decided to investigate alternative materials and fabrication methods to develop a more novel and simple system that did not require gas flow, as discussed through the rest of this chapter.

2.2.2 Acrylic Chip Design

Section 2.2.1 presented a method for creating an oxygen gradient in a PDMS chip, however the requirement for gas flow made the system difficult to use. Following this, a new approach was taken to try to eliminate the need for *in situ* gas cylinders, and to make the chips and associated set-up more user friendly.

The hypothesis was that an oxygen gradient could be generated in a chip by mixing two input solutions of different oxygen concentrations (0% and 21%), removing the need for gas flow. A channel pattern was designed, as shown in Figure 2.8 with dimensions detailed in Figure 2.9. The channel design starts with two inlet channels which combine and split multiple times to form a series of isolated segments with oxygen concentrations between 0 – 21%.

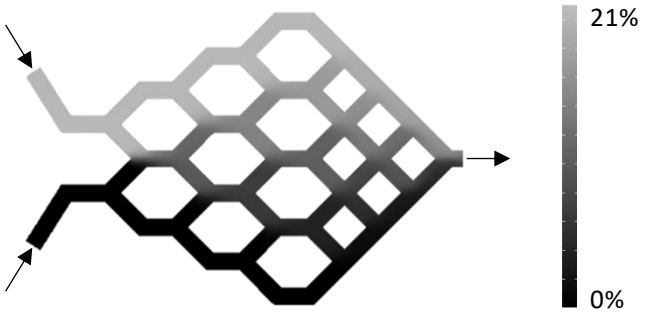

Figure 2.8: Designed channel network for making an oxygen gradient from two input solutions, one with 0% oxygen and one with 21% oxygen. Legend shows oxygen concentration in partial pressure and arrows indicate direction of fluid flow.

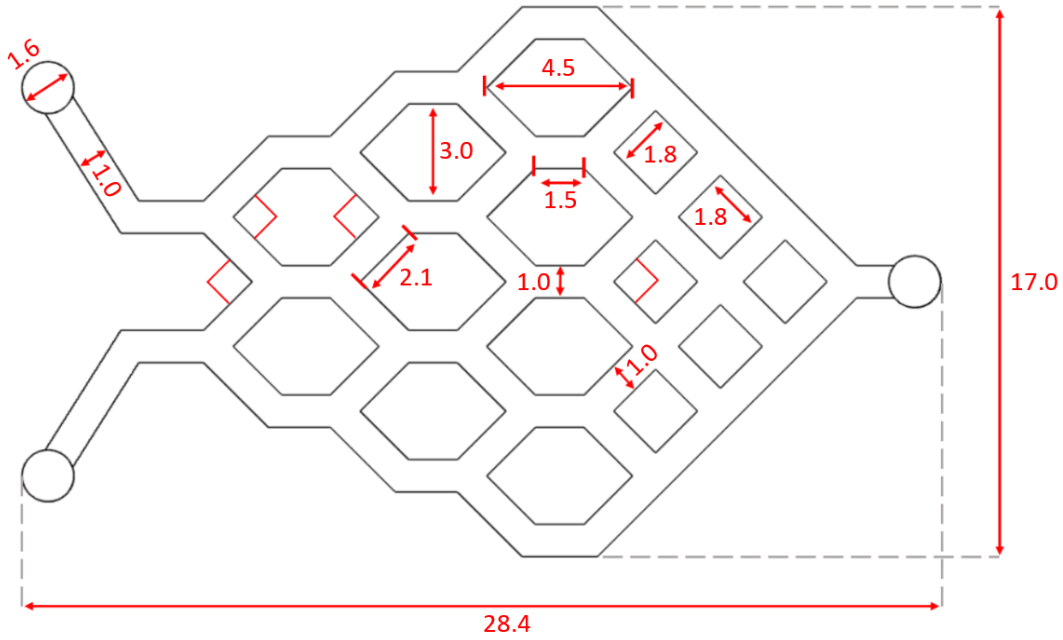

Figure 2.9: Dimensions of channel design, all values in mm. Channel depth was 0.3 mm.

The design includes only 2 inlets and 1 outlet, which helps to keep the experimental set-up relatively simple whilst allowing multiple oxygen concentrations to be studied at the same time. There are 5 different channel segments with different oxygen concentrations at the widest part of the design; the bottom channel segment represents hypoxic tissue, the middle channels represent tissue with varying levels of oxygenation and the top channel represents the oxygen concentration used in traditional cell culture methods. Depending on the aim of specific experiments and oxygen concentration range of interest, the number of channel segments and oxygen concentrations of input solutions could be altered accordingly.

The channel pattern was produced using a CNC milling machine where the minimum drill bit size available was 0.5 mm, this limited the channel width to 1 mm. Each channel segment is 1.5 mm long and 1 mm wide to allow space for many cells to be studied in each area. The length of the channels is also important to allow full mixing of the solutions to establish a constant oxygen concentration in each channel segment (discussed further in Chapter 3). Following the 5 main channel segments, mixing of solutions and even oxygen concentration is not important, so these channels converge over a shorter distance to reach the outlet.

To make this design work, the channels had to be isolated from atmospheric oxygen, otherwise oxygen would be able to diffuse form the air into the areas of the device with lower oxygen concentration. Therefore, the material selection for making the chip was important. Acrylic was selected (instead of PDMS as previously used) as it is a hard plastic with low gas permeability that is readily available, low-cost and biocompatible.[80,98] The change of material also resulted in the need for a new fabrication method and set-up. There were two main iterations of the set-up, which are described in Sections 2.2.3 and 2.2.4.

2.2.3 Acrylic Chip Fabrication and System Assembly – Iteration 1

Chip Fabrication

To create the channel pattern discussed in Section 2.2.2, a CNC milling machine (Modela or Tormach) was used (detailed settings given in Section 2.4.2). Designs were cut out 3 at a time into a single sheet of 1.5 mm acrylic using a 0.5 mm end mill. The individual chips were then cut to the size of a microscope slide (75 mm × 25 mm) using a CO_2 laser cutter (Epilog Fusion, 60 watt).

It was considered important to seal the channels using a biocompatible material that cells can attach to and grow on. Additionally, the depth of the material used to seal the channels had to be kept to a minimum so that the contents of the channels remained visible under a microscope. Initially, a glass cover slip (32 × 22 × 0.15 mm) was bonded onto the acrylic part using a medical grade epoxy resin (EpoTek 301-2, 1 g Part A: 0.35 g Part B). The glue was applied to the acrylic surface (avoiding the channels) using a cotton bud, the glass slide was placed gently on top and the glue was cured at room temperature for 48 hours. This resulted in a strong and secure bond between the acrylic and glass, however, there were some disadvantages to this approach. It was difficult to manually apply the right amount of glue; too little and there would not be a good bond between the acrylic islands and the glass, too much and the glue would get into the channels resulting in channel blockage or asymmetric channels. Images of these problems are shown in Figure 2.10. The long curing time of the glue was also not ideal. The glue can be cured faster at 80° C for 2 hours, however, initial warming of the glue reduced the viscosity and increased leakage of glue into the channels before it fully cured.

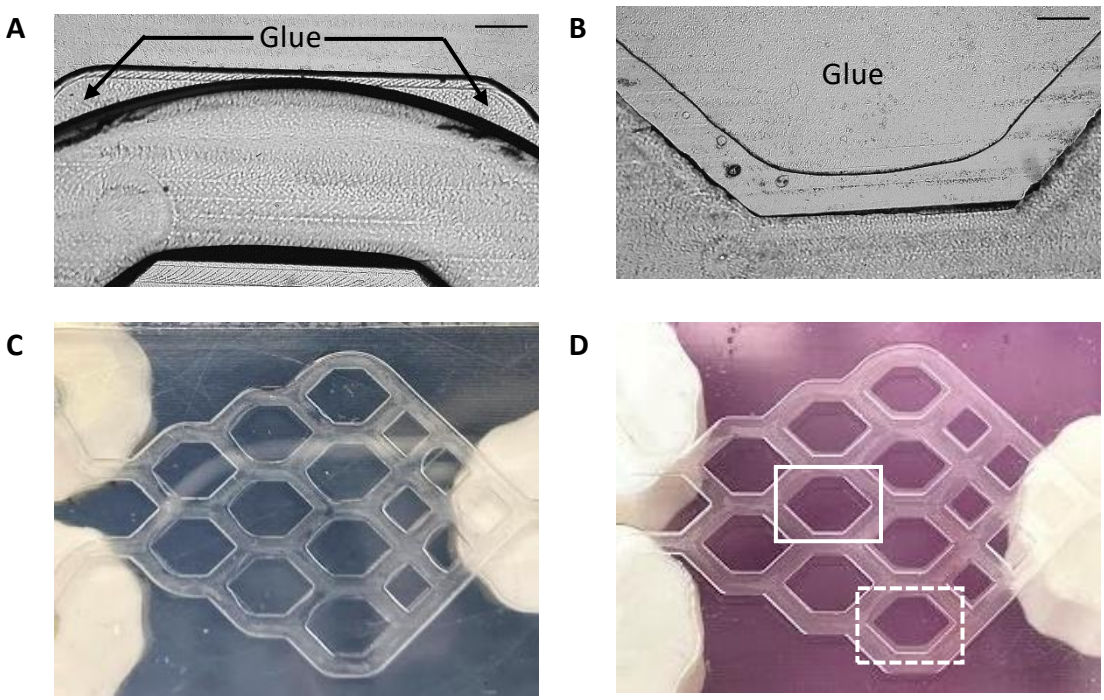

*Figure 2.10: Images of glass slides glued onto acrylic chips. Panels **A** and **B** are images taken on Motic AE200 microscope with x4 objective, scale bar is 300 µm. **A** Glue that leaked into a channel during bonding. **B** Incomplete bonding between the island and glass due to insufficient application of glue. **C** Glue leaked into the channels around the corners and around most of the islands. **D** An example with some glue leaked into the channels, some islands with complete glue coverage (solid white rectangle) and some islands with incomplete glue coverage (dashed white rectangle).*

Chip Connections

Male luer connectors were glued over the chip ports (Figure 2.11) to allow tubing to be reversibly connected to the chip. The glue used was the same biocompatible epoxy resin mentioned in Section 2.2.3 (EpoTek 301-2, 1 g Part A: 0.35 g Part B), which was cured at 80° C for 2 hours.

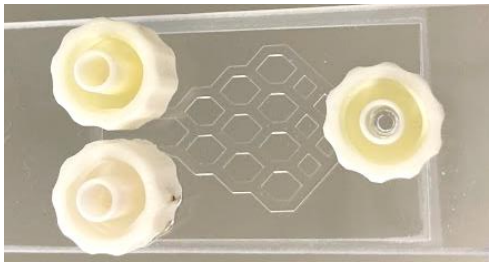

Figure 2.11: Image of chip with luer connectors.

Materials for System Set-Up

As discussed in Section 2.2.2, the chip has been designed such that a gradient is generated across the channels by providing media flow of 2 solutions with different oxygen concentrations through separate inlets. Therefore, it was important that the materials used to provide and collect media from the system had low oxygen permeability. Otherwise, atmospheric oxygen would be able to diffuse into the system, potentially changing the oxygen concentration in the starting solutions.

The components required to complete the system included syringes to store the different media solutions, a container (pouch) to collect outflow and tubing to connect everything together. Generally, plastic syringes are used because they are readily accessible, sterile and single use. Tygon® microbore tubing is a popular choice for biological microfluidic applications due to its biocompatibility, flexibility and very small inner diameter which makes it ideal for delivering small volumes of fluid.[99,100] However, plastics are often permeable to oxygen so may not be the best choice for this application.[98]

An experiment was conducted to compare the commonly used plastic materials to alternatives; plastic syringe vs glass syringe, plastic pouch vs aluminium foil pouch, stainless steel tubing vs Tygon® tubing. Water was deoxygenated by bubbling with nitrogen gas then stored in the different vessels for 24 hours. A glass round bottom flask (RBF) sealed with a septum was used as a control and to determine how much atmospheric oxygen diffused into the water as a result of transferring into and out of the vessels. To test the tubing, deoxygenated water was drawn from an aluminium

pouch through the different types of tubing and collected in a glass syringe. The water was collected at a slow flow rate over 24 hours. The oxygen concentration was then measured using a Hach HQ40d multimeter luminescent dissolved oxygen (LDO) probe. Further details of the experiment are given in Section 2.4.3 and results are shown in Table 2.1.

Table 2.1: Oxygen concentration of deoxygenated water after 24 hours storage in or flow through different vessels. Results are given as an average and standard deviation of 3 samples. PP: polypropylene, PE: polyethylene, PA: polyamide.

Vessel	**Material**	**Oxygen Concentration (mg/L)**
Round bottom flask	Glass	1.5 ± 0.1
Syringe	Glass	1.3 ± 0.2
	Plastic (PP/PE)	4.8 ± 0.1
Pouch	Aluminium foil	1.6 ± 0.2
	Plastic (PE/PA)	6.5 ± 0.1
Tubing	Stainless steel	1.3 ± 0.3
	Plastic (Tygon)	4.2 ± 0.3

The results in Table 2.1 clearly demonstrate that more oxygen got into all of the plastic vessels compared to the alternatives. The measured oxygen concentrations for the glass syringes, foil pouches and stainless steel tubing are all very close to the glass RBF control, indicating that very little oxygen gets through these materials over 24 hours. Hence, these materials were selected and taken forward to assemble the system around the chip.

First Iteration of Full System

The first version of the full system is shown in images in Figure 2.12. Stainless steel needles were used to connect the chip to pouches containing solutions and the outlet was connected to a syringe with stainless steel tubing. The fluid from the pouches could then be drawn through the chip at a constant flow rate controlled by the syringe pump.

The pouches were inverted and attached to an acrylic frame. This helped prevent the formation of air bubbles, as liquid was drawn through the needles from the bottom of the liquid volume whilst any air present would rise to the top. It also enabled the pouches and chip to fit neatly into a small cell culture incubator, so both cells in the chip and media supply could be maintained at 37° C (the standard temperature for cell culture).

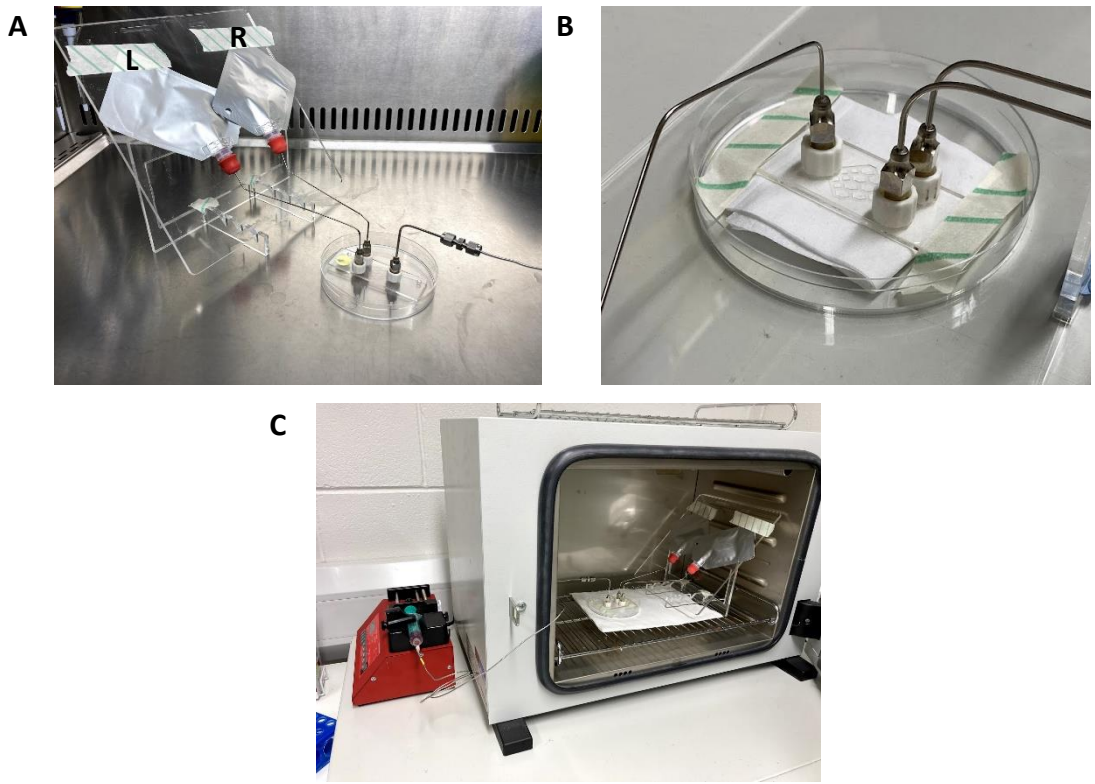

Figure 2.12: Images of first iteration of full chip system. ***A*** *Chip connected to two stainless steel needles which are inserted into pouches (L: left pouch, R: right pouch) via a septum. Pouches are secured onto an acrylic frame with tape.* ***B*** *Close up image of chip – tubing connections.* ***C*** *Chip and pouches inside the incubator connected to syringe on a syringe pump outside the incubator.*

The system was tested to investigate if it was water-tight, if flow could be maintained without the formation of air bubbles and if the supply of solution from each pouch was even. Experiments were set up to draw water through the system from the two pouches containing equal volumes of water. The pouches were weighed before and after the period of flow to see if fluid was being drawn evenly from both sources. This experiment was repeated multiple times in two different chips (A and B) and the results are presented in Table 2.2. The system was visually observed throughout the experiments and there were no issues with leaks or air bubbles.

Table 2.2: Results of testing fluid flow from two pouches in first iteration of full system with two chips, A and B. Left and right pouches were assigned as shown in Figure 2.12. The pouches were filled with the same volume of water, and then the water was drawn through the system at 250 µL/hour overnight (19 – 30 hours). Pouches were weighed before and after the flow test and the weight difference for each pouch is reported. The value for the pouch which supplied the most water is highlighted in bold.

Chip	Experiment #	Volume (mL)	Left pouch (g)	Right pouch (g)
A	1	10	1.5	**4.1**
	2	10	2.0	**3.7**
	3	10	**4.2**	2.1
	4	10	**3.4**	3.2
	5	10	**3.3**	2.9
B	1	30	2.4	**5.2**
	2	25	1.4	**3.4**
	3	25	**4.2**	2.3

The hypothesis behind this set up is that one pouch will contain deoxygenated media and the other will contain oxygenated media. The solutions will then flow evenly through the chip to form an oxygen gradient. Therefore, it is important that the flow from pouches A and B is equal and consistent, so that the oxygen gradients produced in the chip are consistent and reproducible. However, the results in Table 2.2 show that the flow from the pouches A and B is inconsistent.

The difference in the amount of water removed from each pouch varies, for example in chip A experiment 1 the difference between pouches A and B is 2.6 g, whereas, in chip A experiment 4 the difference is 0.2 g. The pouch from which most water is taken also changes between the experiments, for some it is the left pouch and for others is

it the right pouch. The majority of the system i.e. the chips, tubing and outlet syringes, are consistent across the experiments. Therefore, the variations are unlikely to be due to a problem with the fluidic channels themselves but possibly related to inherent differences between the two pouches.

Since the pouches are malleable, it is not realistically possible to get the two to sit in exactly the same way. In the initial experiments with chip A, the volume of water used was 10 mL, which did not fill the pouch. So, for experiment with chip B, larger volumes of water were used to see if fuller pouches were more consistent, however, this did not result in more even flow from the two pouches.

2.2.4 Acrylic Chip Fabrication and System Assembly – Iteration 2

The main challenges with the first iteration of the acrylic chip system were that gluing the glass slide to the acrylic chip was fiddly and it was challenging to produce consistent chips. The method for supplying media solutions from pouches was also inconsistent. For the second iteration of the system, it was attempted to address these issues by altering the fabrication method and media supply method.

Chip Fabrication

The fabrication method was altered by using a heated hydraulic press (Carver 4386) to seal the channels with a thinner piece of acrylic (34 × 22 × 0.2 mm) instead of sealing with glass cover slips. Ethanol was applied between the two acrylic parts, which were placed between two heated plates (70° C) and 1000 pound-force (2372 kPa) applied for 2 minutes.[83,101] This method was reliable, produced chips with consistent channels and was easier and faster than gluing on the glass cover slips.

However, during fabrication of the first few devices using this method of CNC milling, laser cutting and thermal bonding, cracks through the acrylic pieces were occasionally observed at various points through process. Representative images are shown in Figure 2.13. Occasionally cracks would appear when depositing ethanol on the acrylic surface during the thermal bonding procedure and sometimes cracks would appear

on the internal surfaces of the channels whilst using the devices after thermal bonding. This was due to residual stress in the acrylic structure as a result of the machining processes.[102] It was resolved by introducing annealing steps between each step of the overall fabrication process. To anneal the acrylic parts they were placed in an oven preheated to 80° C for 2 hours, the oven was then turned off and the acrylic parts were left inside with the door closed until the oven had reached room temperature.[101,102]

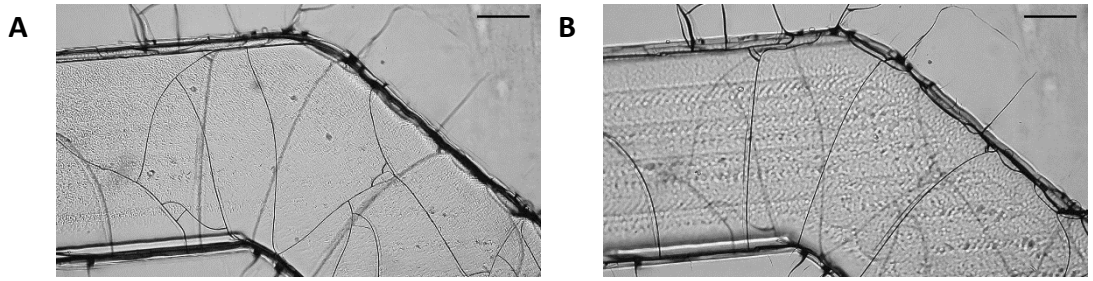

*Figure 2.13: Stress cracking observed on **A** top and **B** bottom of acrylic channels. Images taken on Motic AE200 microscope with x4 objective, scale bar is 300 µm.*

The final production process for producing the acrylic chips is summarised in the following points:

(1) Use CNC milling to cut three channel designs into a piece of 1.5 mm acrylic
(2) Laser cut individual chip pieces to 75 × 25 mm
(3) Laser cut 34 × 22 mm rectangles from 0.2 mm acrylic
(4) Anneal all laser cut parts
(5) Use thermal bonding to bond acrylic rectangles over channel design on the chips
(6) Anneal completed chips

The method was relatively fast and produced chips that were consistent and robust. An image of a representative chip produced using this process is shown in Figure 2.14.

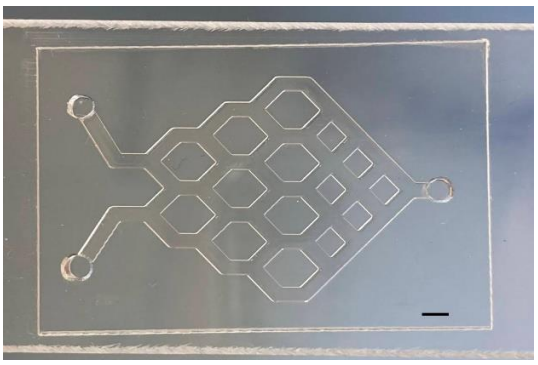

Figure 2.14: Image of chip produced by CNC milling and thermal bonding. Scale bar is 2 mm.

Second Iteration of Full System

Images of the fully assembled system are shown in Figure 2.15. Media supply is contained in two glass syringes, which are connected to the chip via stainless steel tubing. The chip is held in a petri dish and connected to an outflow liquid pouch via a stainless steel needle. To produce a gradient, the syringes (containing solutions with different oxygen concentrations) are connected to a dual syringe pump. This ensures that the chip receives the same amount of liquid from each media source. When culturing cells inside the chip, the chip system can be maintained at 37° C by placing the chip and outflow pouch inside an incubator, whilst keeping the syringes and syringe pump outside the incubator (Figure 2.15 C).

The device was tested for leaks and bubble formation by flowing water through the system from the syringes. The system was found to be water tight and bubbles were much less of a problem compared to the PDMS device (Section 2.2.1). Occasionally bubbles did get in during assembly of the system, however, they were easily removed by flowing extra liquid through the channels. Since the system is not permeable to gas, no additional bubble formation was observed.

A

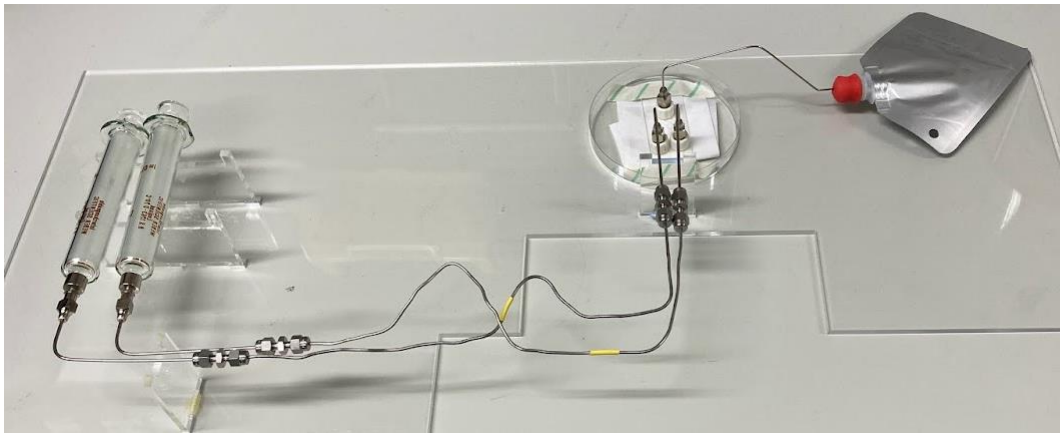

B

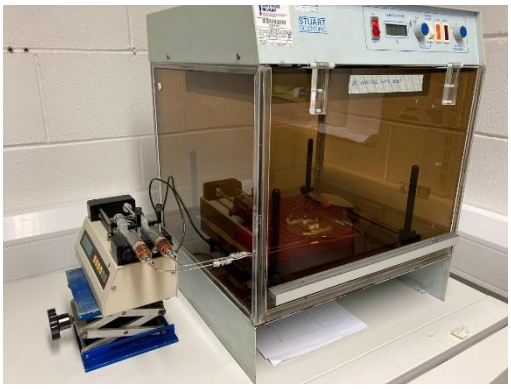

Figure 2.15: Images of full chip system. ***A*** *Two glass syringes connected to chip inlets via stainless steel tubing, chip outlet connected to outflow liquid pouch via stainless steel needle.* ***B*** *Chip in incubator. Syringes sit on syringe pump on outside of the incubator, with chip and outflow pouch inside the incubator.*

2.3 Summary

This chapter has explored techniques for making fluidic devices from PDMS and acrylic. The fabrication method for the PDMS devices was suitable, however, the device design required gas flow to generate the oxygen gradient. Gas components (cylinders and flowmeters) made the system bulky, difficult to transport and it was not easy to achieve a stable flow.

Moving on, the design and fabrication of the acrylic chip were more successful. After testing different sealing processes and materials for the external set-up, the acrylic chip was finalised. The chip itself was made using CNC milling and thermal bonding, and luer lock connections were used to connect the chip to stainless steel tubes. Flow

of media was provided by two glass syringes connected to a syringe pump and outflow liquid was collected in an aluminium pouch.

With the device design and fabrication method in place, the next step was to further study the oxygen gradient in the chip. The next chapter will discuss simulations in COMSOL Multiphysics® which demonstrate how the two inlet solutions come together and how oxygen diffuses to create a gradient across the channel network.

2.4 Materials and Methods

2.4.1 Materials for Device Fabrication and System Assembly

Acrylic chips were made from 1.5 mm acrylic and 0.2 mm Clarex Optical Grade Cast Acrylic (Weatherall Equipment and Instruments Ltd.). Epoxy resin (EpoTek 301-2, 1 g Part A: 0.35 g Part B) was used to attach nylon male luer lock connectors to the chip. Inlet tubing was assembled from stainless steel capillary tubing (1/16") connected to one stainless steel needle (16G, blunt, luer lock fitting) at each end using a twin ferrule compression fitting. A stainless steel needle (19G) was used to connect the chip outlet to an aluminium pouch fitted with a Suba-Seal® septum (size 13). Glass syringes were fitted to a dual syringe pump (Harvard Apparatus, 11 Plus, 70-2212). An incubator shaker (Stuart Scientific) was used to incubate the chip at 37° C (no shaking) during cell culture experiments.

2.4.2 CNC Milling Machines

Modela MDX-20 3D Milling Machine

Designs were created in Fusion360 then saved as mpj files for loading into MODELA player 4 software. A carbide 0.5 mm 2 flute end mill was used for all steps. Surfacing, roughing and finishing cut settings were manually defined in MODELA player 4, details of settings used are given in Table 2.3.

Table 2.3: Settings used for cutting steps on Modela MDX-20.

Parameter	Step		
	Surfacing	**Roughing**	**Finishing**
XY Speed (mm/sec)	10.2	10.2	7.6
Cutting feedrate (mm/sec)	0.1	0.1	1.0
Spidle rotation speed (rpm)	6500	6500	6500
Cutting in depth (mm)	0.05	0.05	0.1
Path interval (mm)	0.23	0.23	0.1

Tormach PCNC 440

Designs and cutting profiles were created in Fusion360 then saved as GCode for loading into PathPilot software. A carbide 0.5 mm single flute end mill was used. Details of settings used are given in Table 2.4.

Table 2.4: Settings used for cutting steps on Tormach PCNC 440.

Parameter	Step	
	Cutting	**Bore**
XY Speed (mm/sec)	10.2	10.2
Cutting feedrate (mm/sec)	7.6	7.6
Spidle rotation speed (rpm)	6500	6500
Cutting in depth (mm)	0.05	0.01
Path interval (mm)	0.2	NA

2.4.3 Testing Materials with the Hach HQ40d Multimeter LDO Probe

Materials

List of materials tested:

- Glass syringes, Samco, 20 mL capacity
- Plastic syringes (polypropylene/polyethylene), Braun, 20 mL capacity
- RBF, Pyrex, 50 mL capacity
- Aluminium foil pouches, Hemoton, 50 mL capacity
- Plastic pouches (polyethylene/polyamide), Hemoton, 100 mL capacity
- Stainless steel needle, Merck, 12", 19G
- Tygon® ND-100-80 tubing, 0.02" inner diameter, 0.06" outer diameter, 12" length. One female and one male Luer lock superglued onto each end of the tubing. A needle (2", 21G) was attached to the male Luer lock.

Probe Set-Up and Calibration

The LDO probe was calibrated in water-saturated air and at 0% oxygen using sodium sulphite solution (50 mg/mL in water).

To take sample measurements, the probe was inserted into a 250 mL beaker through an acrylic lid, as shown in Figure 2.16. The lid was laser cut and contained two holes: one for the probe and another for a Suba-Seal® septum. This allowed samples to be injected into the bottom of the beaker via a needle and glass syringe whilst minimising mixing with air. Due to the surface area of the beaker and the depth of the probe, the minimum sample volume was 20 mL.

Figure 2.16: Image of oxygen probe in sealed beaker.

Sample Preparation

Water was deoxygenated by bubbling with nitrogen gas for 1.5 hours. A sample of deoxygenated water was tested with the probe before using (1.0 – 1.5 mg/L).

RBFs were fitted with a Suba-Seal® septum, purged with nitrogen for 3 minutes then filled with 30 mL deoxygenated water. Pouches were fitted with a Suba-Seal® septum, purged with nitrogen 3 times then filled with 30 mL deoxygenated water. Syringes were purged with nitrogen 3 times then filled with 20 mL water. They were sealed with a luer lock cap and parafilm. Three samples were prepared for each vessel. All samples were left at room temperature for 24 hours. Oxygen concentration was then measured in each of the solutions.

Deoxygenated water was drawn through plastic tubing (Tygon®) and stainless steel tubing. Three experiments were set-up for each tubing type. Foil pouches were filled with 30 mL deoxygenated water as above. A glass syringe was purged with nitrogen 3 times and filled with a small amount of deoxygenated water. Tubing was connected to the syringe, washed through with the deoxygenated water, then the needle end was inserted through the septum into the pouch. The syringe was connected to a syringe pump which was set to withdraw at 0.75 mL/hour for 24 hours. Oxygen concentration was then measured in each of the solutions.

Chapter 3: COMSOL Multiphysics® Simulation of Oxygen Gradient

3.1 Introduction

Computational fluid dynamics (CFD) is a field of research based on modelling fluid flow, heat transfer and mass transfer in natural environments and engineered systems.[103] The simulations are based on calculations of numerical solutions to the equations that govern the physical laws for conservation of mass, momentum and energy.[103] CFD calculations can be performed on bespoke, specially written codes or on commercially available platforms, for example COMSOL, Autodesk and Flow-3D among others.[104]

COMSOL Multiphysics® is a CFD simulation platform used for applications in scientific research and manufacturing, including fluid flow and chemical transport within microfluidic devices.[105] The programme can run specialised interfaces designed to require only basic input from the user. For example, the fluidics interface runs on physical parameters including pressure, flow rate, viscosity and density.[105]

COMSOL Multiphysics® has been used to simulate diffusion of oxygen in microfluidic devices in a variety of contexts including in gradients generated by gas flow,[79,97] chemical reactions,[106] oxygen scavenging chemicals,[107,108] and consumption of oxygen by cell culture.[109,110] An example of a simulation of oxygen concentration in a device based on oxygen scavenging is described in Figure 3.1 and an example based on cellular oxygen consumption is described in Figure 3.2. Both examples show different methods of oxygen gradient generation and effective modelling of the gradients in COMSOL Multiphysics®.[108,109] In both cases, the simulated results correlated well with experimental optical sensing measurements of oxygen concentration.[108,109] Optical sensing techniques are discussed further in Chapter 4, Section 4.1 and the example by Ando *et al.* is discussed further in Figure 4.3.

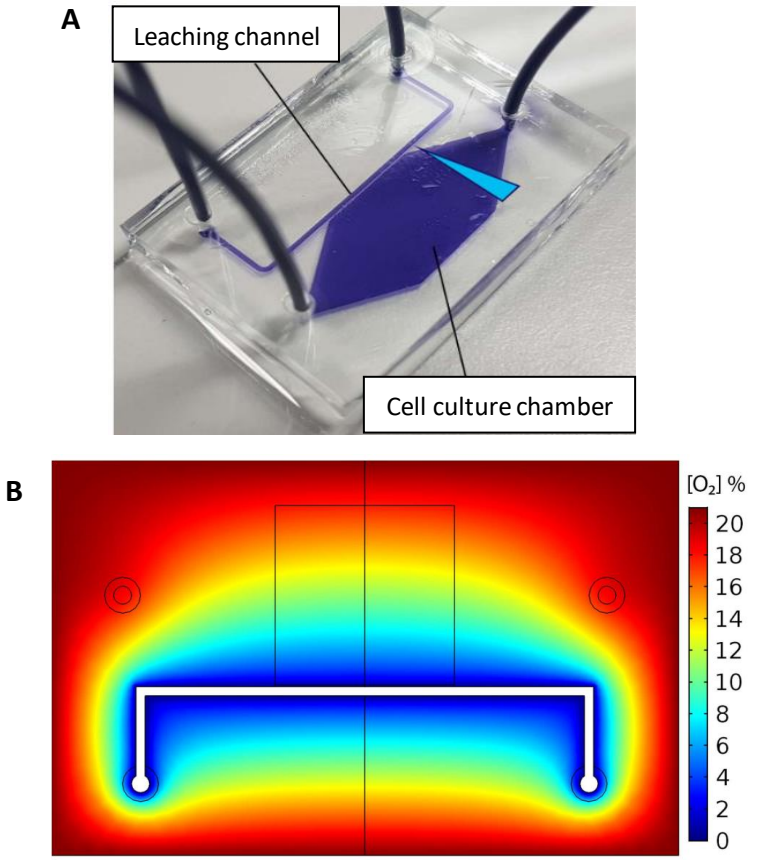

Figure 3.1: COMSOL Multiphysics® simulation of oxygen concentration by Sleeboom et al. ***A*** *The microfluidic device made from PDMS. A solution of oxygen scavenger (sodium sulfite, 50 mg/mL) flows through the leaching channel, which is separated from the cell culture chamber by a thin PDMS wall.* ***B*** *Results of simulation of steady-state oxygen concentration, black lines indicate position of the culture chamber. Oxygen concentration in the bulk solution was calculated based on oxygen diffusion through the bulk PDMS and oxygen consumption in the leaching channel. Reprinted from Open Access article (Creative Commons CC BY) by Sleeboom et al.*[108]

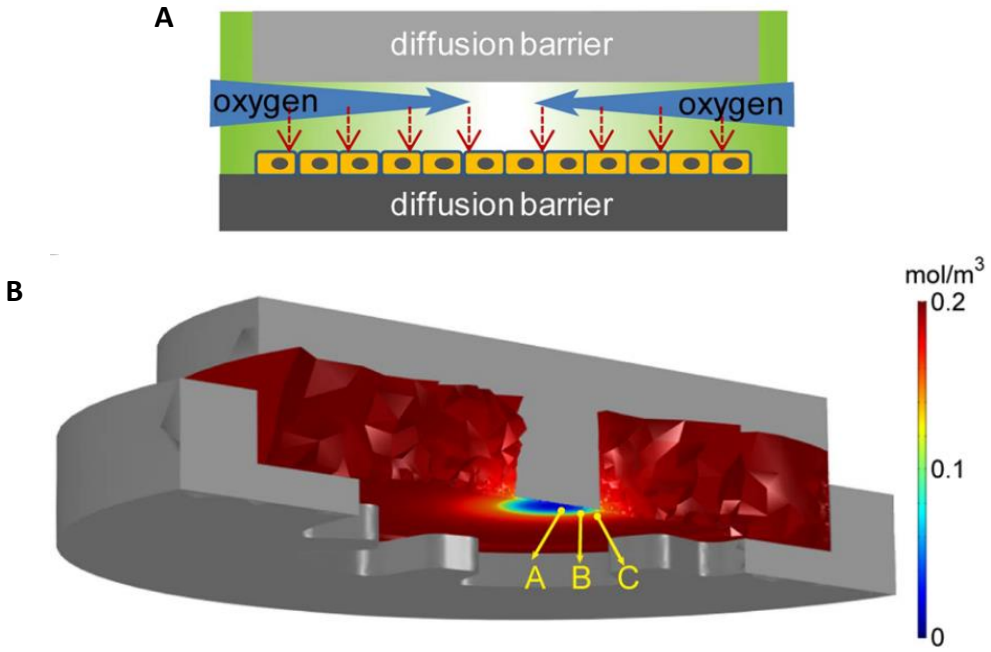

Figure 3.2: COMSOL Multiphysics® simulation of oxygen concentration by Ando et al. ***A*** *The device concept. The base of the device is made from Delrin (polyoxymethylene), cells are cultured on glass cover slips and the top of the device is made from polycarbonate.* ***B*** *Results of simulation of steady-state oxygen concentration. Oxygen concentration in the bulk solution was modelled considering oxygen consumption by the cells and oxygen diffusion from the bulk media. Reprinted from Open Access article (Creative Commons CC BY) by Ando et al.*[109]

In Chapter 2, a design for making an oxygen gradient on a chip was discussed. The design was based on two inlet solutions mixing through a series of channels to create isolated areas with a range of oxygen concentrations. Some of these areas, referred to as channels 1 – 5, are highlighted with red boxes in Figure 3.3 (copied and slightly altered from Figure 2.8). It is important to understand how the fluids behave in the chip and how the oxygen is distributed in order to achieve a uniform oxygen concentration in each area.

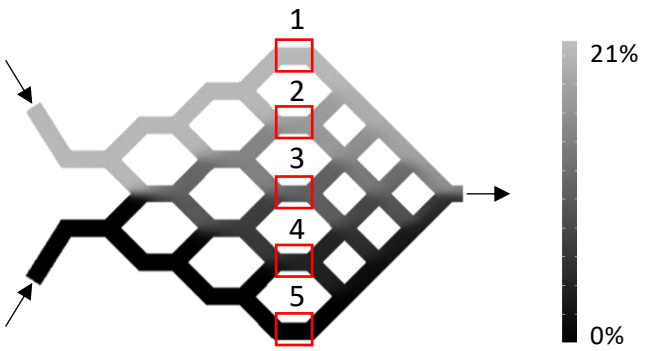

Figure 3.3: Designed channel network for oxygen gradient development from two input solutions, one with 0% oxygen and one with 21% oxygen. Legend shows oxygen concentration in partial pressure and arrows indicate direction of fluid flow. Red boxes highlight areas referred to as channels 1 – 5.

For the work in this chapter, COMSOL Multiphysics® simulations were used to investigate the behaviour of fluids and oxygen in the chip. The aim of the simulation was to explore how flow rate altered oxygen distribution in the chip. The Creeping Flow interface was used to model fluid flow, then the Transport of Dilute Species interface was used to calculate oxygen concentration within the modelled fluid.

A background theory section is included in this chapter to cover key concepts for understanding what the simulation software is calculating and how it is doing so. A brief summary of laminar fluid flow and oxygen diffusion is given in Section 3.2.1. The Navier-Stokes equations, as used by the Creeping Flow interface, are discussed in Section 3.2.2 and the mass-balance equation, as used by the Transport of Dilute Species interface, is discussed in Section 3.2.3.

3.2 Background Theory

3.2.1 Laminar Flow and Oxygen Diffusion

The motion of fluid particles can be defined by two regimes: laminar or turbulent flow (Figure 3.4).[111] In laminar flow, fluid particles move in parallel streamlines. Motion is controlled by frictional forces between the fluid particles (viscous forces) due to high viscosity and/or low velocity.[111,112] Turbulent flow occurs when a fluid has low viscosity and/or high velocity. Forces which cause the fluid to move (inertia forces) overpower the viscous forces that dominate in the laminar regime.[111,112] The fluid no longer moves in parallel streamlines and the motion of the fluid particles is more random and chaotic.[111]

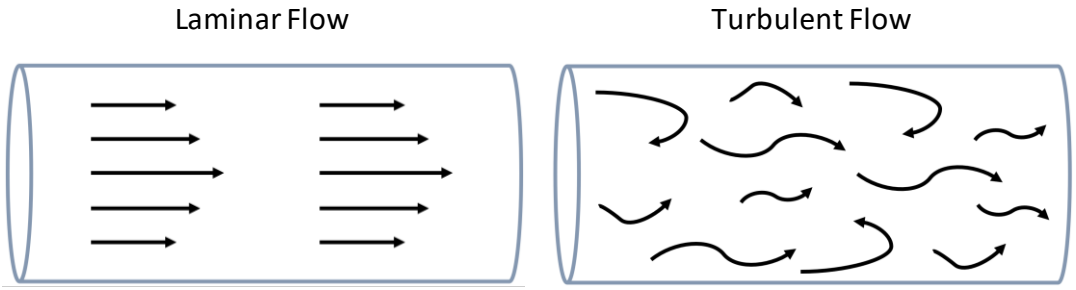

Figure 3.4: Illustration of fluid motion in laminar flow and turbulent flow.

These concepts are concisely expressed by the equation defining the Reynolds number, R_e (equation *3.1*), where ρ is density, $\boldsymbol{u}$ is velocity, L is a characteristic length of the system and μ is viscosity.[105,112] Flow is generally considered to be laminar when $R_e < 1000$ and for most microfluidic applications $R_e \ll 1$.[105]

The characteristic length of a rectangular channel is the hydraulic diameter, D_H, which is expressed in terms of channel width, w, and height, h, as shown in equation *3.2*.[113] At the beginning of an experiment, the velocity may not be known. However, it can be calculated from the applied flow rate, Q, and A using the relationship defined in equation 3.3. The full calculation of R_e for the chip is presented at the beginning of Section 3.3.

$$R_e = \frac{\rho \boldsymbol{u} L}{\mu} = \frac{\rho \boldsymbol{u} D_H}{\mu} \qquad 3.1$$

$$D_H = \frac{2(w \times h)}{(w + h)} \qquad 3.2$$

$$\boldsymbol{u} = \frac{Q}{A} \qquad 3.3$$

Fluid flow in the chip is expected to be laminar, including at junctions in the chip where two channels merge into one channel (Figure 3.5 A). So if the solutions in the inlet channels have different oxygen concentrations, a uniform concentration of oxygen in the new channel will not be achieved by turbulent mixing of the two fluid streams. A uniform concentration of oxygen in the new channel can therefore only be achieved by molecular diffusion of oxygen down the concentration gradient from the stream with high oxygen concentration to the stream with low oxygen concentration (Figure 3.5 B).[114] Figure 3.5 C and D show that the flow rate has to be carefully controlled to allow enough time for oxygen to diffuse across the width of the channel. If oxygen diffusion in the chosen medium is slow or the fluid flow is too fast, an oxygen gradient may be observed in the new channel.

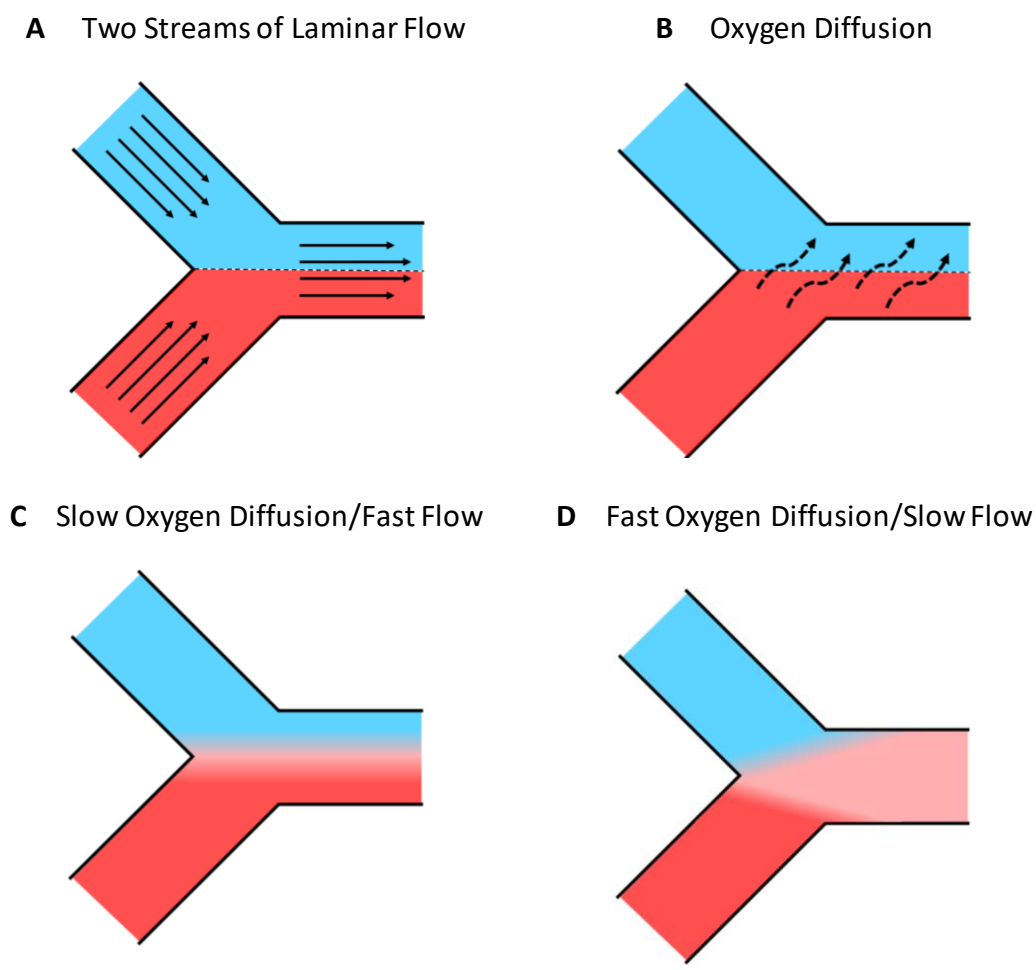

Figure 3.5: Oxygen diffusion in two streams of laminar flow. ***A*** *Streams of laminar flow from two channels, one blue and one red, merge into one channel. Arrows indicate the direction of fluid flow.* ***B*** *Red indicates fluid with high oxygen concentration and blue indicates fluid with low oxygen concentration. Oxygen can move from one laminar stream to the other by diffusion down the concentration gradient, indicated by dashed arrows.* ***C*** *If oxygen does not diffuse the width of the channel, due to slow diffusion in the medium or fast flow conditions, a gradient of oxygen concentration will be observed for the length of the channel.* ***D*** *If oxygen does diffuse the width of the channel, due to fast diffusion in the medium or slow flow conditions, the oxygen concentration will be consistent across the channel. The oxygen concentration in the channel will be the average of the two input solutions (pink colour).*

3.2.2 Equations for Fluid Flow

Newton's second law of motion famously describes that acceleration of an object is dependent on how heavy that object is and what forces are being applied to it; force = mass × acceleration. This theory is utilised in the Navier-Stokes equation, (*3.4*), to describe the motion of compressible Newtonian fluids, replacing mass with density.[112] On the left side of the equation, density is multiplied by the term in brackets that represents acceleration to give term 1 which represents inertial forces. Terms 2 and 3 on the right side of the equation represent pressure and viscous forces respectively.[112] Definitions of the terms in equation *3.4* are given in Table 3.1.

$$\underbrace{\rho\left(\frac{\partial \boldsymbol{u}}{\partial t} + \boldsymbol{u}\cdot\nabla\boldsymbol{u}\right)}_{1} = \underbrace{-\nabla p}_{2} + \underbrace{\nabla\cdot\left(\mu(\nabla\boldsymbol{u} + (\nabla\boldsymbol{u})^{T}) - \frac{2}{3}\mu(\nabla\cdot\boldsymbol{u})I\right)}_{3} + F \qquad 3.4$$

Table 3.1: Definition of terms in the Navier-Stokes equation.[112]

Term	Definition	Term	Definition
ρ	Density	I	Identity tensor
$\boldsymbol{u}$	Velocity	T	Transpose matrix operator
p	Pressure	1	Inertial forces
μ	Viscosity	2	Pressure forces
t	Time	3	Viscous forces
F	External forces		

The NS equation can be simplified for incompressible fluids (e.g. water). The equation that describes the conservation of mass (mass continuity equation, *3.5*) indicates that velocity is dependent on density and time. However, for an incompressible fluid, density can be considered constant and independent of space and time

(equation *3.6*).[115] This reduces equation *3.5* to equation *3.7* and removes $\frac{2}{3}\mu(\nabla \cdot \boldsymbol{u})I$ from the NS equation.[112,115]

$$\frac{\partial \rho}{\partial t} + \nabla \cdot (\rho \boldsymbol{u}) = 0 \qquad 3.5$$

$$\frac{\partial \rho}{\partial t} = 0 \qquad 3.6$$

$$\nabla \cdot \boldsymbol{u} = 0 \qquad 3.7$$

In microfluidic devices, fluids are generally moving very slowly in small channels which leads to a very small Reynolds number ($R_e \ll 1$).[105] This means that inertial forces are insignificant compared to the dominant viscous forces, and inertial forces can be removed from the NS equation.[112] External forces, such as gravity, are neglected and overall the NS equation (*3.4*) is reduced to equation *3.8*.[112] This NS equation is used to solve flow velocity for fluids in the COMSOL Multiphysics® Creeping Flow interface.[105,112,115]

$$0 = -\nabla p + \nabla \cdot \left(\mu(\nabla \boldsymbol{u} + (\nabla \boldsymbol{u})^T)\right) \qquad 3.8$$

3.2.3 Equations for Diffusion of a Dilute Species

The Transport of Dilute Species interface is used to simulate movement of a species within a solute based on Fick's first law and the mass conservation equation. The mass conservation equation (*3.9*) describes that concentration of a species in a solute at a given time is dependent on flux (J), velocity, concentration gradients in the solute (∇c) and sources/sinks (e.g. chemical reactions) of the species (R).[116] Term 1 in equation *3.9* represents transport due to diffusion, and term 2 represents transport due to convection.[116]

Fick's first law (equation *3.10*) explains that when a concentration gradient is present, a species will diffuse from an area of high concentration to an area of low

concentration.[117] The rate of diffusion is defined by the diffusion coefficient, D, which is unique to the particular species and solvent of interest.[117]

$$\frac{\partial c}{\partial t} + \underbrace{\nabla \cdot J}_{1} + \underbrace{\boldsymbol{u} \cdot \nabla c}_{2} = R \qquad 3.9$$

$$J = -D\nabla c \qquad 3.10$$

The stationary simulations carried out in this chapter were completed at a single time point with fully developed flow. This allows the time dependent term $\frac{\partial c}{\partial t}$ to be removed from equation *3.9*. The simulation investigates movement of oxygen in a closed system, so no oxygen can be created or destroyed and $R = 0$. Hence, COMSOL Multiphysics® uses equation *3.11* to calculate oxygen concentration in the fluids modelled by the Creeping Flow interface.[105]

$$\nabla \cdot J + \boldsymbol{u} \cdot \nabla c = 0 \qquad 3.11$$

3.3 Results

First, the Reynolds number for fluid flow in the channels was calculated using equations *3.1 – 3.3*. The working shown below is based on the channel dimensions specified in Chapter 1 (Figure 2.9), a flow rate of 100 µL/hour and the density and viscosity of water as defined in the COMSOL Multiphysics® Material Library.[118]

$$D_H = \frac{2(w \times h)}{(w + h)} = 2\left(\frac{0.3\ mm \times 1\ mm}{0.3\ mm + 1\ mm}\right) = 0.5\ mm = 5 \times 10^{-4}\ m$$

$$\boldsymbol{u} = \frac{Q}{A} = \frac{100\ \mu L\ hour^{-1}}{0.3\ mm^2} = \frac{2.8\ \times 10^{-11}\ m^3\ s^{-1}}{3 \times 10^{-7}\ m^2} = 9.3 \times 10^{-5}\ m\ s^{-1}$$

$$R_e = \frac{\rho \boldsymbol{u} D_H}{\mu} = \frac{998.2\ kg\ m^{-3} \times 9.3 \times 10^{-5}\ m\ s^{-1} \times 5 \times 10^{-4}\ m}{0.001\ kg\ m^{-1}\ s^{-1}} = 0.05$$

When the chip is used for cell culture applications, the solution flowing through the system will be a cell culture medium. For the purposes of this simulation, it was assumed that the properties of the media are approximately the same as those of water. The simulation was set up with water flowing through the channel network. The oxygen concentration in the water was set to 0% at one inlet and 21% at the other inlet. Flow rates of 25, 50, 100 and 500 µL/hour were applied at both inlets and the oxygen concentration throughout the channels was calculated. Further details on the settings and parameters used are given in Section 3.5.

Figure 3.6 shows plots of the oxygen concentration throughout the channels at various flow rates, with red indicating higher oxygen concentration and blue indicating lower oxygen concentration. From examining the images, it is observed that slower flow rates result in more uniform oxygen concentrations in individual channels. For example, at 25 µL/hour the zoomed in image over channel 3 in Figure 3.6 A displays an even green colour across the bulk of the channel. Whereas at 500 µL/hour (panel D), the same area shows a gradient of oxygen across the channel, with red at the top transitioning into blue at the bottom. At 100 µL/hour (panel C), channel 3 shows a slight oxygen gradient with an orange/yellow colour towards the top of the channel and a blue/green colour towards the bottom of the channel. At 50 µL/hour (panel B), there is a slight gradient at the left side of the channel that evens out towards the right of the channel.

The profiles at 25 µL/hour and 50 µL/hour are discussed here in more detail since the data presented in Figure 3.6 suggested more uniform oxygen concentrations across channels 1 – 5 compared to the higher flow rates. Figure 3.7 shows the channel positions that were studied to produce graphs in Figure 3.8 - Figure 3.11. Similar graphs were also produced for data at 100 µL/hour and 500 µL/hour which are provided in Appendix 1.

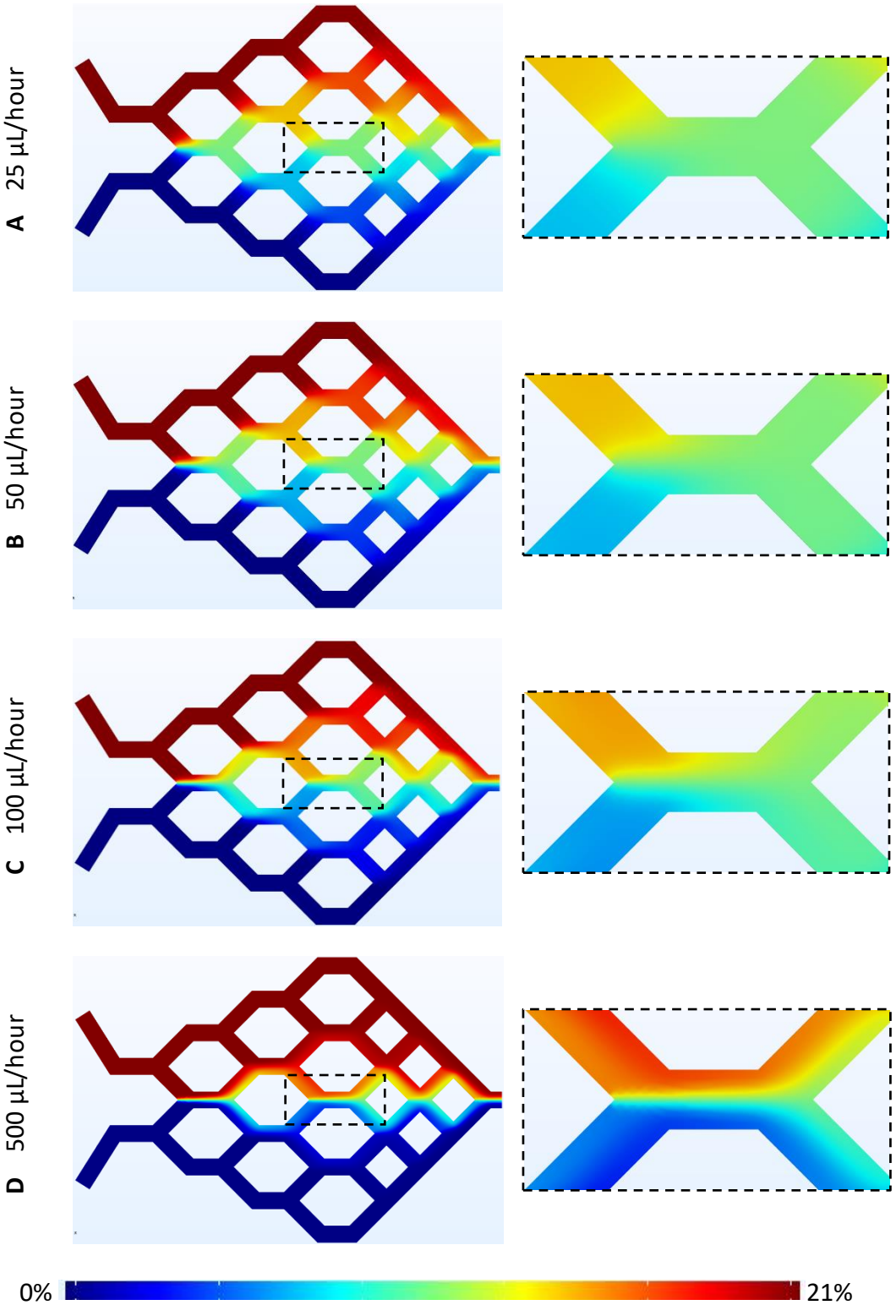

Figure 3.6: Plots of oxygen concentration through the channel network calculated using COMSOL Multiphysics® 5.6. ***A, B, C*** *and* ***D*** *show plots at inlet flow rates of 25, 50, 100 and 500 µL/hour respectively with a zoomed in image over channel 3.*

Figure 3.8 and Figure 3.10 show the calculated oxygen concentrations in channels 1 – 5 at 25 µL/hour and 50 µL/hour respectively. The data indicates that the solutions mix in the chip at each flow rate to produce oxygen concentrations of approximately 0, 4, 10, 17 and 21% oxygen in channels 1 – 5 respectively. There are some concentration gradients present in the channels, with channel 3 experiencing the largest gradient, followed by channels 2 and 4, then no gradient in channels 1 and 5. The gradients are larger at 50 µL/hour compared to 25 µL/hour.

This trend is further emphasised by looking at the gradients across the beginning, middle and end of channel 3 (left to right as displayed in Figure 3.7), as shown in Figure 3.9 for 25 µL/hour and Figure 3.11 for 50 µL/hour. For each flow rate, the gradient is largest at the entrance to the channel and as the laminar streams progress through the channel, oxygen diffuses down the concentration gradient and the gradients become smaller.

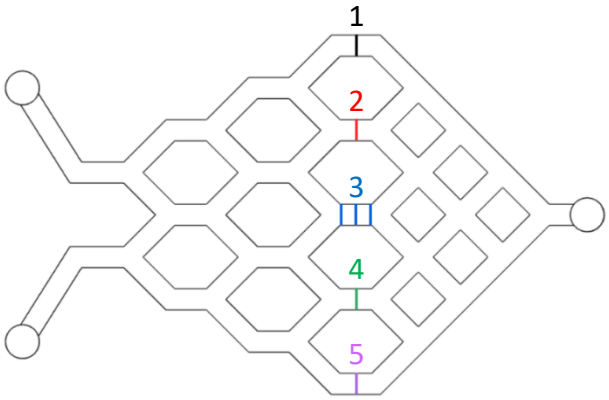

Figure 3.7: Coloured lines show positions where data was collected from computation results. Lines in the middle of each channel were used to produce the graphs in Figure 3.8 and Figure 3.10. The three lines across the channel 3 were used to produce the graphs in Figure 3.9 and Figure 3.11.

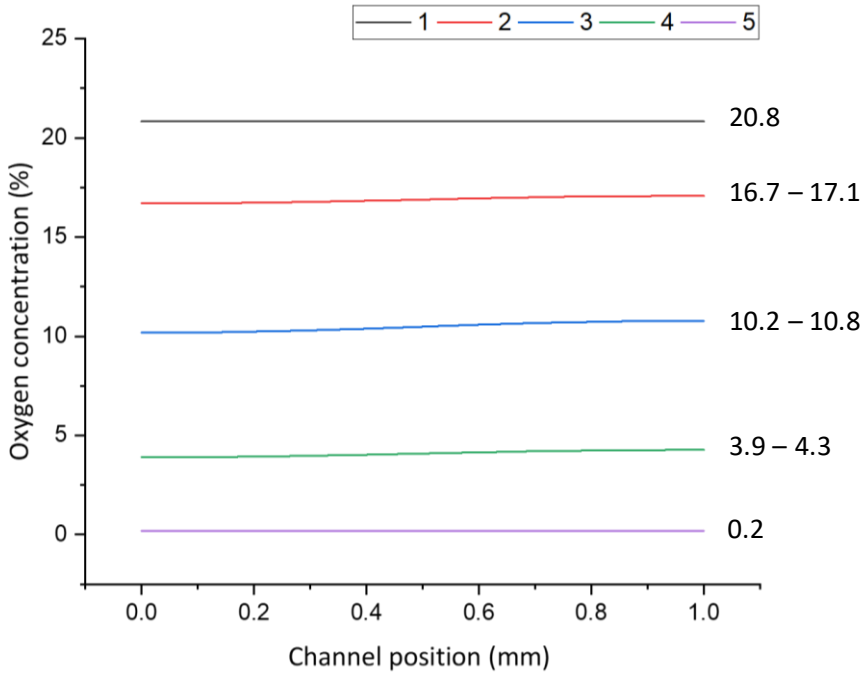

Figure 3.8: Oxygen concentrations in the centre of channels 1 – 5 with 25 µL/hour flow rate at both inlets. Channel coordinates go from the bottom, 0 mm, to the top, 1 mm, of each channel as displayed in Figure 3.7.

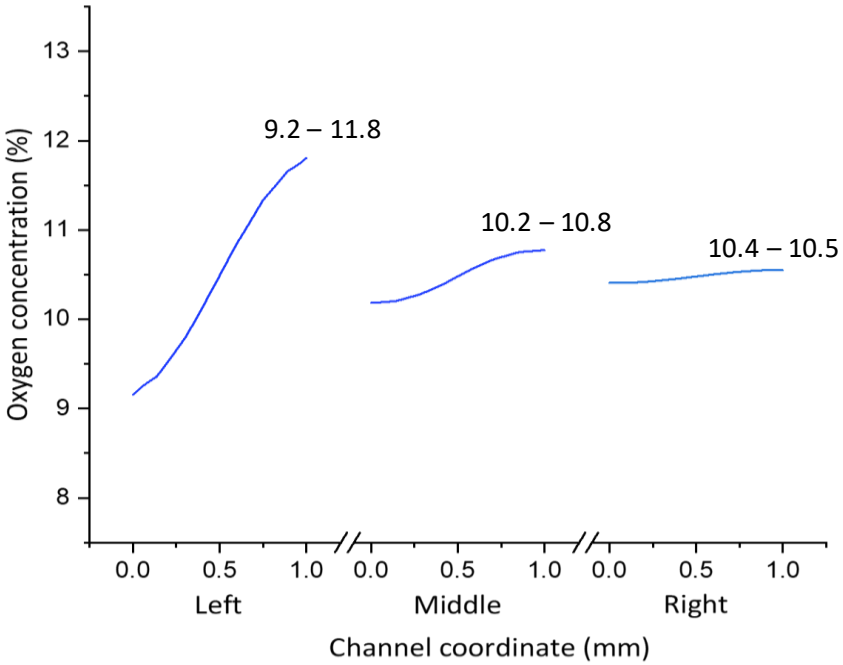

Figure 3.9: Oxygen concentrations at the left, middle and right of channel 3 with 25 µL/hour flow rate at both inlets. Channel coordinates go from the bottom, 0 mm, to the top, 1 mm, of each channel as displayed in Figure 3.7.

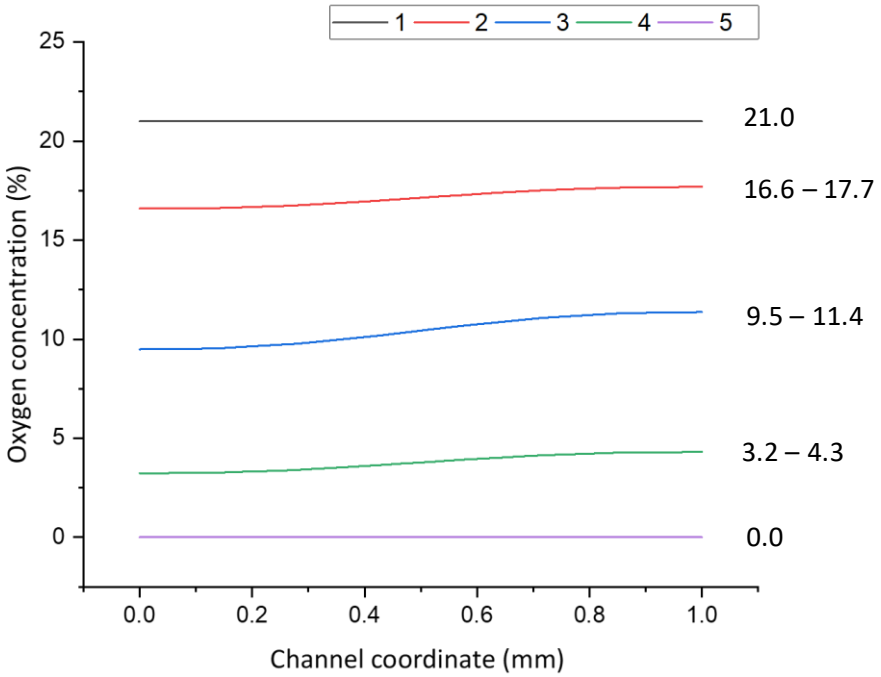

Figure 3.10: Oxygen concentrations in the centre of channels 1 – 5 with 50 µL/hour flow rate at both inlets. Channel coordinates go from the bottom, 0 mm, to the top, 1 mm, of each channel as displayed in Figure 3.7.

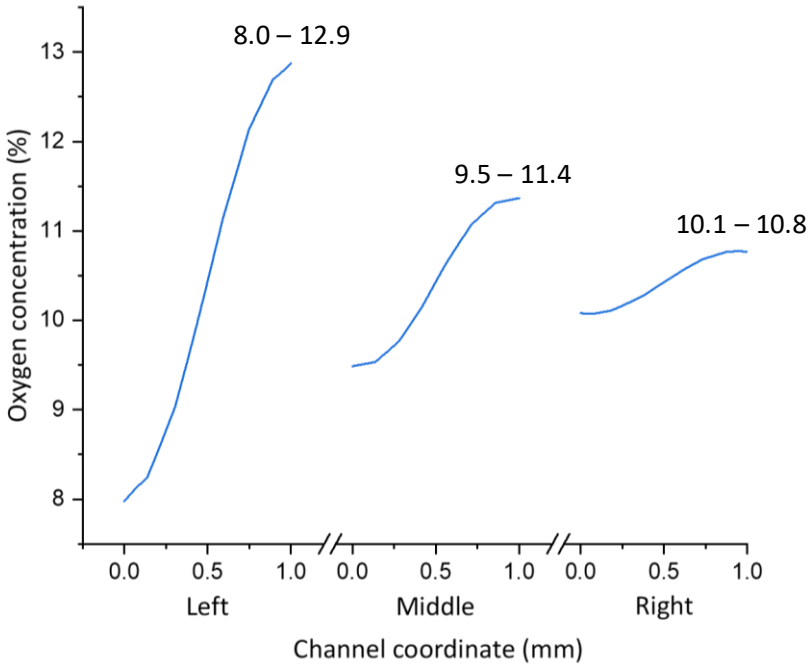

Figure 3.11: Oxygen concentrations at the left, middle and right of channel 3 with 50 µL/hour flow rate at both inlets. Channel coordinates go from the bottom, 0 mm, to the top, 1 mm, of each channel as displayed in Figure 3.7.

The results in Figure 3.6 show that faster flow means less time for oxygen diffusion and steeper oxygen gradients. The same logic can be applied here; there is a larger gradient in the middle channels because the flow through the middle of the chip is faster than flow through the outer channels. This is confirmed by the velocity plot calculated in COMSOL Multiphysics® and shown in Figure 3.12. Selected values from the velocity plot are reported in Table 3.2. These results are from the simulation with a flow rate of 50 µL/hour at each inlet, however the trends in velocity are the same for all flow rates studied.

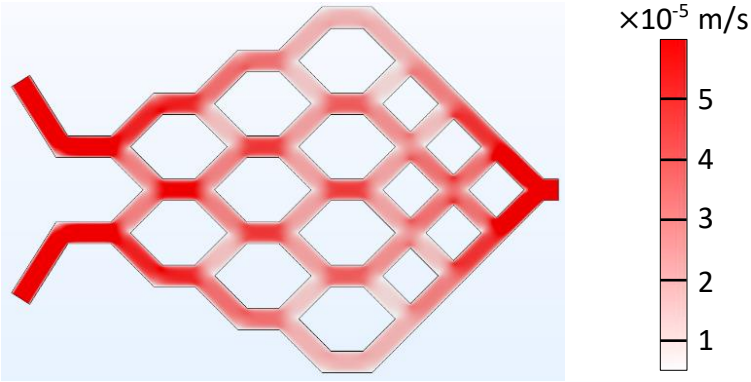

Figure 3.12: Plot of velocity through the channel network calculated using COMSOL Multiphysics® 5.6. Flow rate was 50 µL/hour at each inlet.

Table 3.2: Velocity in channels 1 – 5 and in the diagonal channels leading in to channels 1 – 5 (top/bottom inlet channels). Flow rate was 50 µL/hour at each inlet.

Channel	**Velocity** (m/s)		
	Top inlet channel	Bottom inlet channel	Main channel
1	NA	2.1	2.1
2	1.6	2.5	4.0
3	2.4	2.4	4.8
4	2.5	1.6	4.0
5	2.1	NA	2.1

In the computation the flow rate at each inlet was set to 50 µL/hour, hence the flow rate at the outlet is constant at 100 µL/hour. Equation *3.3* shows that flow rate, Q, is dependent on velocity, $\boldsymbol{u}$, and area, A.[111] When two channels merge into one, the cross sectional area of the output channel is half the size of the two input channels combined. So in order to maintain a constant flow rate across the chip, velocity must increase. The inverse is true when one channel splits into two. In this case the cross sectional area of the output channels is double the size of the input channel and velocity must decrease.

Following different paths from the inlets to the outlet, the fluid can encounter different numbers of channel splitting and merging events. For example, Figure 3.13 shows paths from an inlet to channel 1 (panel A) and channel 3 (panel B). Fluid following the path to channel 1 goes through three channel splitting events and so experiences deceleration. Fluid following the path to channel 3 goes through 3 splits and 3 merges, so the deceleration is less severe. Hence, the velocity is slower in channel 1 than channel 3.

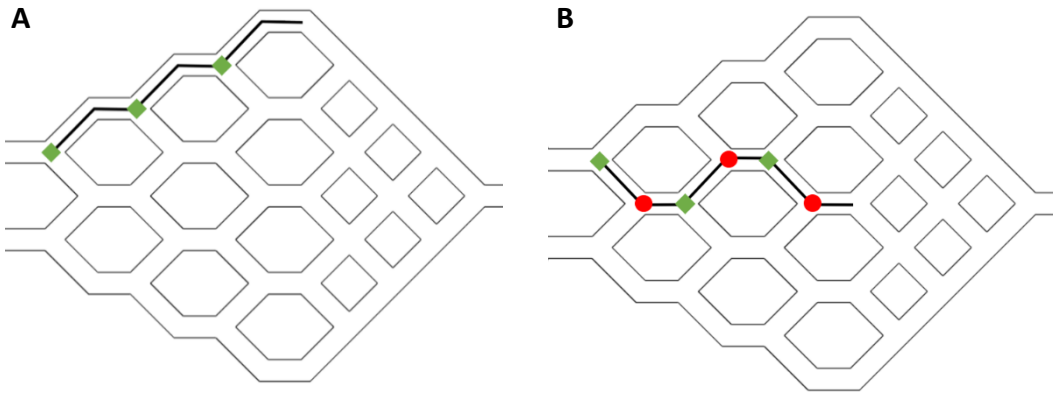

*Figure 3.13: Paths of fluid flow from an inlet to channel 1 (**A**) and channel 3 (**B**). Green diamonds indicate where a channel splits and red circles indicate where two channels merge.*

Another observation from the velocity plot (Figure 3.12) is that when the outer channels split, fluid prefers to continue flowing through the outer channel rather than flowing towards the centre of the channel network. This trend has been observed in other microfluidic devices with branched networks for generating oxygen gradients.[119] For channels 2 and 4, there is more fluid supplied from the inlet channel coming from the middle of the network (velocity of 2.5 m/s) than the inlet channel coming from the outside of the network (velocity of 1.6 m/s).

The variation in velocity also correlates with variation in shear stress, which is defined as the mechanical stress caused by the horizontal movement of fluid parallel to the cell surface.[111,120] Shear stress, τ, is a function of the dynamic viscosity, μ, velocity, $\boldsymbol{u}$, and distance between the surface and point of interest in the fluid, y, as described in Equation *3.12*.[121] The values of shear stress in each channel are provided in Appendix 2. The variation in shear stress has potential consequences for the cell culture, as discussed more thoroughly in Chapter 5.

$$\tau = \mu \frac{\partial \boldsymbol{u}}{\partial y} \qquad 3.12$$

The trend in velocty has an influence on oxygen concentrations in channels 2 and 4, where supply of fluid from the inlet channels is not 1:1. Figure 3.14 shows the expected oxygen concentrations throughout the channel network if splitting and mixing of fluid at each node was 1:1. It is observed that the concentrations in channels 2 and 4 are different to those calculated in the simulation. The simulation results showed oxygen concentrations of approximately 17% and 4%, whereas Figure 3.14 gives concentrations of 18% and 3% for channels 2 and 4 respectively.

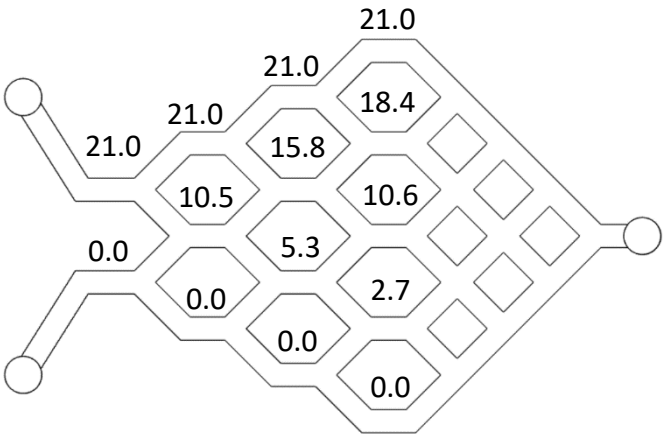

Figure 3.14: Oxygen concentrations (%) in channels with 1:1 mixing of solutions at each junction. Concentration values correspond to the channel below.

Even though the fluid flow through the network is not as even as initially expected, the results show that the device can generate a range of defined oxygen concentrations in 5 different channels. In future work, the channel geometry could be altered according to Murray's Laws to produce even velocity and shear stress throughout the channel network.[122] For example, increasing the width of channels where velocity is currently observed to be high will reduce the flow rate and shear stress in those areas.

3.4 Summary

COMSOL Multiphysics® was used to study how flow rate influenced oxygen concentration in the channel network designed in Chapter 2. First, the Creeping Flow interface was used to model fluid flow through the channels. Then, the Transport of Dilute Species interface was used to calculate oxygen concentration throughout the modelled fluid.

Calculations were performed with flow rates of 25, 50, 100 and 500 µL/hour applied at both inlets. Results showed that higher flow rates resulted in steeper gradients of oxygen concentration, particularly in the central channels. At 50 µL/hour, a gradient was observed at the entrance to channel 3, which becomes more uniform towards

the end of the channel. Channels 2 and 4 experience smaller oxygen gradients and channels 1 and 5 display a uniform oxygen concentration.

The larger gradients in the central channels compared to the outer channels was found to be a result of higher fluid velocity through these areas. The variation in velocity through the channels is a consequence of the way in which the channel network was designed. Different paths of fluid flow experience different sequences of channel merging and splitting events that have an impact on velocity.

Going forward, the next chapter will build on these computational results by measuring oxygen concentration in the chip system fabricated in Chapter 2 using fluorescence microscopy techniques.

3.5 Methods – COMSOL Multiphysics® 5.6 Settings

Materials

Water was selected from the COMSOL Multiphysics® materials library. At 293.15 K, the density was 998.2 kg/m^3 and the dynamic viscosity was 0.001 Pa s.[118]

Creeping Flow

The boundary conditions were defined as 'fully developed flow' for both inlets, 'pressure' for the outlet and 'no slip' for all channel walls. Flow rates of 25, 50, 100 and 500 µL/hour were applied at both inlets.

Transport of Diluted Species

The oxygen concentration of the solution at one inlet was 0.21×10^{-4} mol/m^3 (21% partial pressure) and 0 mol/m^3 (0% partial pressure) at the other inlet. The diffusion coefficient used for oxygen in water at 293.15 K was 3.2×10^{-9} m^2/s.[108,123]

Mesh

A fine size free quad mesh calibrated for fluid dynamics was created on the bottom x,y face of the geometry then swept through the z height. Convergence tolerance was 0.001.

Chapter 4: Fluorescence Measurements of Oxygen Gradient

4.1 Introduction

The aim of the work in this chapter was to measure the oxygen concentration in the fluidic device designed and fabricated in Chapter 2, and compare the results to those obtained by computational methods in Chapter 3.

There are many techniques for measuring oxygen concentration in microfluidic devices presented in literature, as discussed in recent reviews by Grist *et al.*, Azimzadeh *et al.* and Brennan *et al.*[124–126] A brief summary of key techniques including electrochemical and optical sensing are given in Sections 4.1.1 - 4.1.3.

The technique selected for the work in this chapter was fluorescence imaging of an oxygen sensitive dye, $Ru(BPY)_3$. Gradients between 0 – 21% oxygen were set up in the chip at flow rates of 25 µL/hour and 50 µL/hour. The oxygen concentrations were calculated, analysed and compared to the computational results (Chapter 3), as discussed in Section 4.2.

4.1.1 Electrochemical Sensor Example

Electrochemical approaches generally employ versions of a Clark-style electrode, where reduction of oxygen at a working electrode produces a measurable current.[127–129] Luo *et al*. presented a chip with a built in Clark-style electrode positioned below a microfluidic channel, as shown in Figure 4.1.[129] This allowed measurements of dissolved oxygen (0 – 8.1 mg/L) in the microfluidic channel in real time.[129]

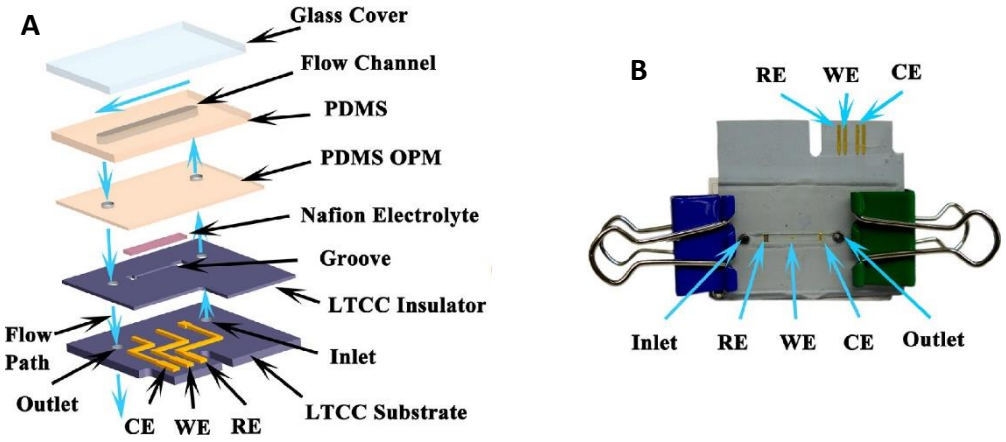

Figure 4.1: Device made by Luo et al. for measurement of dissolved oxygen in a microchannel using a Clark-style electrode.[129] ***A*** *Schematic representation of the layers and materials used to make the device.* ***B*** *Image of the chip held together with clamps. CE: counter electrode (gold), WE: working electrode (gold), RE: reference electrode (Ag/AgCl), LTCC: low temperature co-fired ceramic, OPM: oxygen permeable matrix. Reprinted from Luo et al. with permission from Elsevier.*

4.1.2 Optical Sensing Techniques

Optical sensing methods involve measuring fluorescence of a dye (fluorophore), usually a ruthenium or platinum based complex, that is oxygen sensitive.[124,130] In the presence of oxygen, the fluorescence of the fluorophore decreases due to collisional quenching, as summarised in Figure 4.2.[131] When a fluorophore collides with an oxygen molecule, the energy involved in the relaxation of an electron from the excited state to the ground state is not emitted as a visible photon but instead transferred to the oxygen molecule.[131]

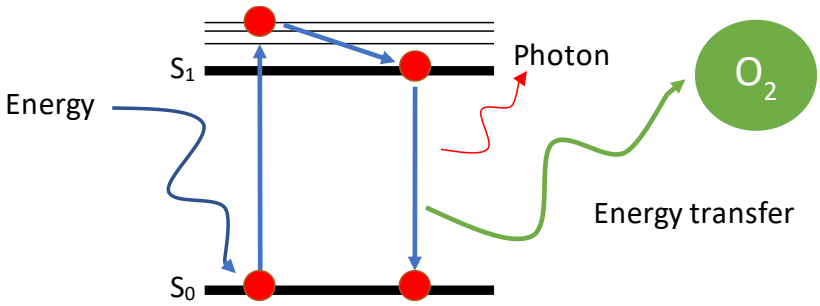

Figure 4.2: Diagram of fluorescence and collisional quenching. An electron is promoted from the ground state (S_0) to the excited state (S_1) of a fluorophore by energy (light source of appropriate wavelength). As the electron transitions back to the ground state, energy is emitted as a visible photon (red arrow). Alternatively, in the presence of a quencher, for example oxygen, the energy is transferred to the oxygen molecule upon collision and no visible photons are produced (green arrow).[131]

The relationship between fluorescence and oxygen concentration is described by the Stern-Volmer equation (*4.1*, terms defined in Table 4.1).[130] The equation can be expressed in terms of fluorescence lifetime, τ, or fluorescence intensity, I.

$$\frac{\tau_0}{\tau_{[O_2]}} = \frac{I_0}{I_{[O_2]}} = 1 + k_q\tau_0[O_2] = 1 + K_q[O_2] \qquad 4.1$$

Table 4.1: Definition of terms in the Stern-Volmer Equation.[130]

Term	Definition
$[O_2]$	Oxygen concentration
τ_0	Lifetime of the excited state when no oxygen is present
$\tau_{[O_2]}$	Lifetime of the excited state at a specified oxygen concentration
I_0	Fluorescence intensity when no oxygen is present
$I_{[O_2]}$	Fluorescence intensity at a specified oxygen concentration
k_q	Quenching rate coefficient
K_q	Quenching constant equal to $k_q \times \tau_0$

Lifetime is the length of time that a fluorophore spends in the excited state and intensity is the total amount of light emitted by a fluorescent sample.[131] Both are dependent on oxygen concentration as when more oxygen is present, the likelihood of collision between the fluorophore and oxygen molecule increases. This reduces the amount of time that a fluorophore will spend in the excited state and reduces the overall amount of light emitted by a sample.[131]

Intensity measurements can be collected from standard fluorescence microscope set-ups. The fluorophore is excited by a light source, and light emitted from the sample is collected at a detector. The image produced is an array of pixels, where brighter pixels represent higher fluorescence intensity.[131] Measurements are dependent on fluorophore concentration, as a higher concentration of fluorophore means more light emitted by the sample as a whole. This can result in inconsistencies in intensity measurements due to background effects and non-uniformities in the sample.[125]

One approach to improve reliability of intensity measurements is ratiometric fluorescence. In this technique, intensity measurements from two (or more) fluorophores in the same environment are collected, where one fluorophore is oxygen sensitive and the other is not.[125] Variation in intensity measurements for the oxygen-insensitive fluorophore can then be used to correct for variation in the background and other sample non-uniformities.[125]

Measurements of fluorescent lifetime can be achieved by different methods including fluorescence lifetime imaging microscopy (FLIM) and time-correlated single-photon counting (TCSPC).[125] FLIM is based on measuring the rate of decay of fluorescence intensity over very short time scales, which can in turn be used to calculate the average length of time that the excited state was populated.[131] TCSPC is based on measuring the time between excitation of the sample with a light source and emission of individual photons.[131] Lifetime measurements are independent of fluorophore concentration and fluorescence intensity which helps to achieve more

consistent measurements throughout a sample compared to intensity measurements.[132] Techniques to measure fluorescent lifetime are more accurate and more robust than intensity measurements, however, they require expensive and advanced equipment.[125]

4.1.3 Integration of Optical Sensors into Microfluidics

Literature examples show optical sensors being incorporated into microfluidic chips as micro/nanoparticles, fluorescent films and liquid solutions.[124–126] Ando *et al*. described a technique to incorporate microparticles loaded with an oxygen sensitive ruthenium dye and a reference dye into a microfluidic cell culture system, as illustrated in Figure 4.3.[109] Ratiometric fluorescence imaging was then used to measure oxygen concentration in solution during cell culture experiments.[109] Ungerbröck *et al*. and Grist *et al*. presented a similar concept, but instead of using microparticles an oxygen sensitive platinum based dye and reference dye were incorporated in a polystyrene sensor layer at a cell culture interface, as illustrated in Figure 4.4.[97,133]

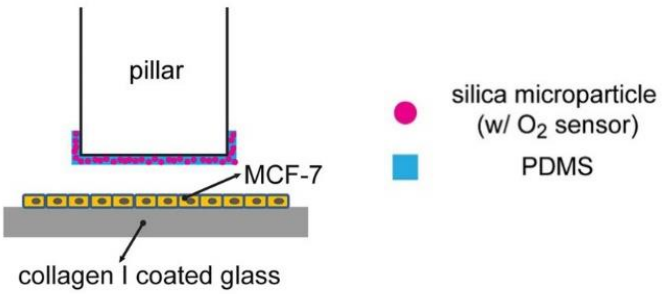

Figure 4.3: Silica microparticles loaded with Ru dye and Nile blue dye (reference) are embedded in PDMS layer on the pillar. Oxygen concentration in solution over the area of the pillar can be measured with ratiometric fluorescence. Reprinted from Open Access article (Creative Commons CC BY) by Ando et al.[109]

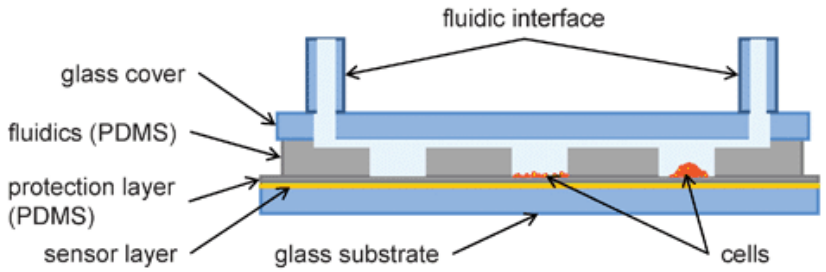

Figure 4.4: PtTFPP dye and Macrolex Fluorescent Yellow dye (reference) incorporated in polystyrene to form sensor layer. Oxygen concentration was measured by ratiometric fluorescence. Reprinted from Open Access article (Creative Commons CC BY) by Ungerbröck et al.[133]

Zirath *et al*. also used optical sensing to measure oxygen concentrations inside a microfluidic chip, shown in Figure 4.5.[134] The authors coated microparticles in an oxygen sensitive platinum-based fluorophore and the sensors were dried in small spots within the device. Instead of microscopy, the sensor spots were monitored with fibreoptic probes and an optical oxygen meter.[134] This technique requires precise positioning of the delicate fibreoptic probes and may not be compatible with all styles of device. However, the equipment is smaller and more portable than a microscope and can be used for long term *in situ* monitoring of oxygen concentration.

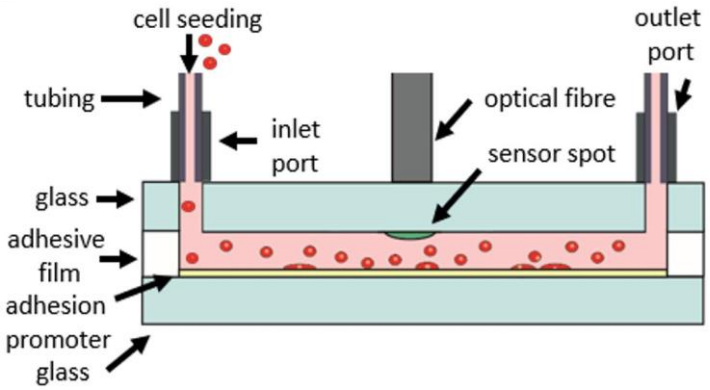

Figure 4.5: Sensor spots made from dried microparticles coated in a platinum based, oxygen sensitive fluorophore. Oxygen concentration was measured by optical sensing by the optical fibre and read out system. Reprinted from Open Access article (Creative Commons CC BY) by Zirath et al.[134]

A popular and simple approach to measuring oxygen in microfluidic channels is to fill the device with an oxygen sensitive ruthenium based dye, such as $Ru(BPY)_3$ (Figure 4.6), and measure the fluorescence intensity. This has been carried out in a number of different devices where oxygen has been controlled by gas flow, cellular oxygen consumption or chemical oxygen scavenging.[108,126,135–139] Although the literature lists disadvantages to this technique (discussed in Section 4.1.2), it also suggests that it is versatile and capable of measuring oxygen concentration in the range of interest (0 – 21%). The key advantage compared to electrochemical, optical nano/microparticles and optical films, is that it requires no special adaptation or modification to the device itself. Hence, this is the technique that was utilised for the work in this chapter.

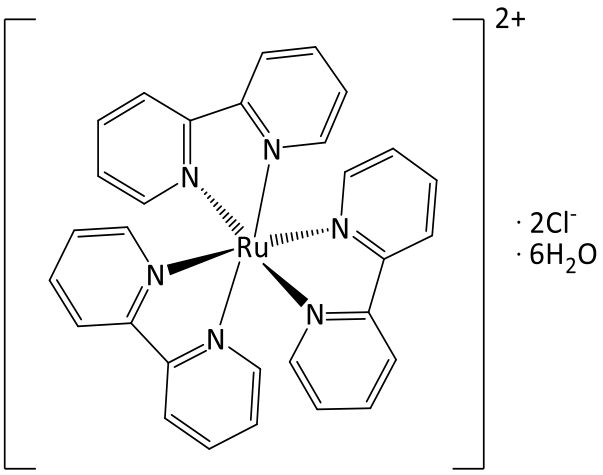

Figure 4.6: Structure of ruthenium tris(2,2'-bipyridyl) dichloride hexahydrate, $Ru(BPY)_3$.

4.2 Results

Results from the computational experiments in Chapter 3 showed that slower flow rates produced more uniform oxygen concentrations in channels 1 – 5. In this chapter, fluorescence experiments were carried out at flow rates of 25 µL/hour and 50 µL/hour at both channel inlets. Oxygen gradients were set up with 21% oxygen solution in the top inlet (channel 1 side) and 0% oxygen solution in the bottom inlet (channel 5 side) (more detail in Section 4.4). The experiment at 50 µL/hour was repeated twice, and the two sets of results are referred to as data set 1 and data set 2.

Before conducting any gradient measurements, the quenching constant, K_q, in the Stern-Volmer equation was calculated from control measurements, as described in Section 4.4. The chip system was assembled as shown in Chapter 2, Figure 2.15 and the chip was secured onto the microscope stage with magnetic clips. The chip was purged with solutions of $Ru(BPY)_3$ control solutions at 0% and 21% oxygen to measure I_0 and $I_{[O_2]}$ respectively before each experiment. The flow rate of solutions at each inlet was 25 µL/hour or 50 µL/hour to match the flow rate used in the experiment.

The fluorescence intensity – reported as mean gray value (MGV) – of each solution flowing through the chip was measured in multiple fluorescence images of channels 1 – 5 over 30 minutes. The measurements for each channel were used to calculate an average MGV across the chip at multiple time points, as shown in Figure 4.7 for the experiment at 50 µL/hour (data set 1). The graph highlights that there is a difference of approximately 10,000 units between the solutions at 21% and 0% oxygen. An average of all MGV measurements recorded for each solution were used as I_0 and $I_{[O_2]}$ to calculate K_q for each experiment, as reported in Table 4.2.

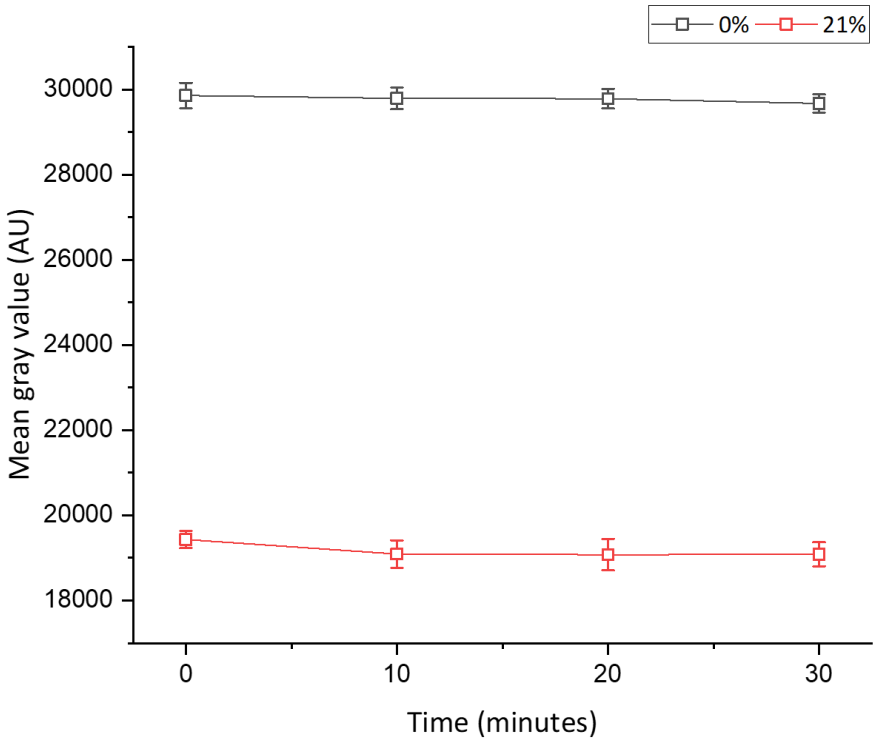

Figure 4.7: Average mean gray value of 0% and 21% oxygen control solutions over channels 1 – 5 at 50 µL/hour (data set 1). Plotted points are average and standard deviation of 45 measurements (9 measurements for each of 5 channels).

Table 4.2: Average I_0, $I_{[O_2]}$ and K_q values for each experiment. Averages and standard deviations included measurements from all time points in channels 1 – 5. Errors for K_q were calculated by error propagation from standard deviation values for I_0 and $I_{[O_2]}$.

Experiment	**Average I_0**	**Average $I_{[O_2]}$**	**Calculated K_q**
25 µL/hour	28175 ± 303	18693 ± 333	0.024 ± 0.001
50 µL/hour data set 1	29540 ± 454	18998 ± 244	0.026 ± 0.002
50 µL/hour data set 2	28912 ± 351	19985 ± 281	0.021 ± 0.001

After measuring fluorescence of control solutions and calculating K_q, the chip was set up with an oxygen gradient. Graphs showing MGVs in channels 1 – 5 over time at 25 µL/hour, 50 µL/hour data set 1 and data set 2 are shown in Figure 4.8, Figure 4.9 and Figure 4.10 respectively. At 25 µL/hour and 0 minutes, there is a large standard deviation for the value reported for channel 3 because there was still an oxygen gradient present in the channel from flushing the solutions through at a higher flow rate. As time progresses and the flow rate stabilises, the MGV in channel 3 becomes more uniform, however the MGV in channels 3 – 5 decreases (oxygen concentration appears to increase).

At 50 µL/hour, the MGVs show some variation over time in each channel, however the trends are different compared to 25 µL/hour. In data set 1 (Figure 4.9), the MGVs in channels 3 – 5 initially decrease as the flow rate stabilises, but then gradually increase again over time. In data set 2 (Figure 4.10), the MGVs in channel 5 are relatively stable but the values in channels 1 – 3 increase over time. The increasing MGVs implied that the oxygen concentration was decreasing, however, it is unlikely that oxygen is leaving the system.

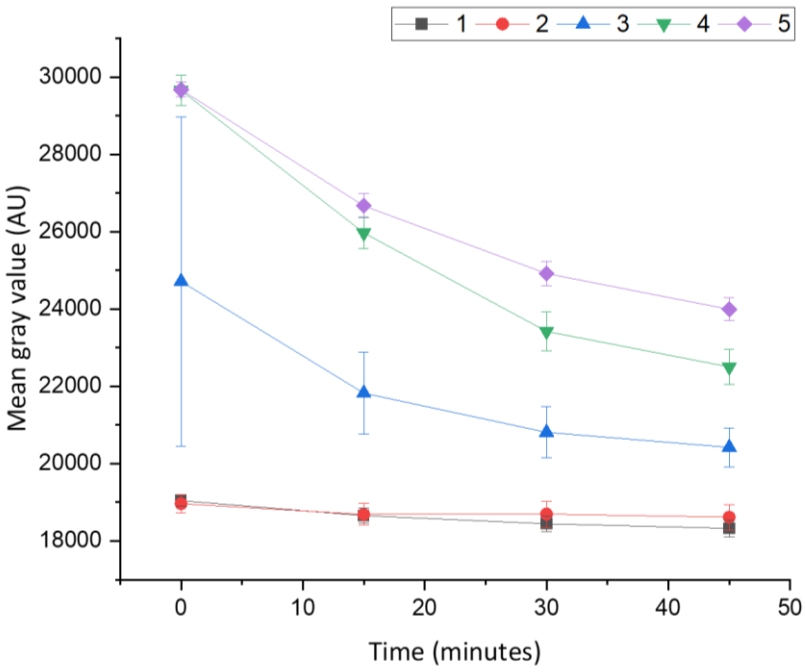

Figure 4.8: Mean gray value (AU, arbitrary units) in solution in channels 1 – 5 at 25 µL/hour (both inlets) over 45 minutes. Data points show average and standard deviation of 9 measurements per channel.

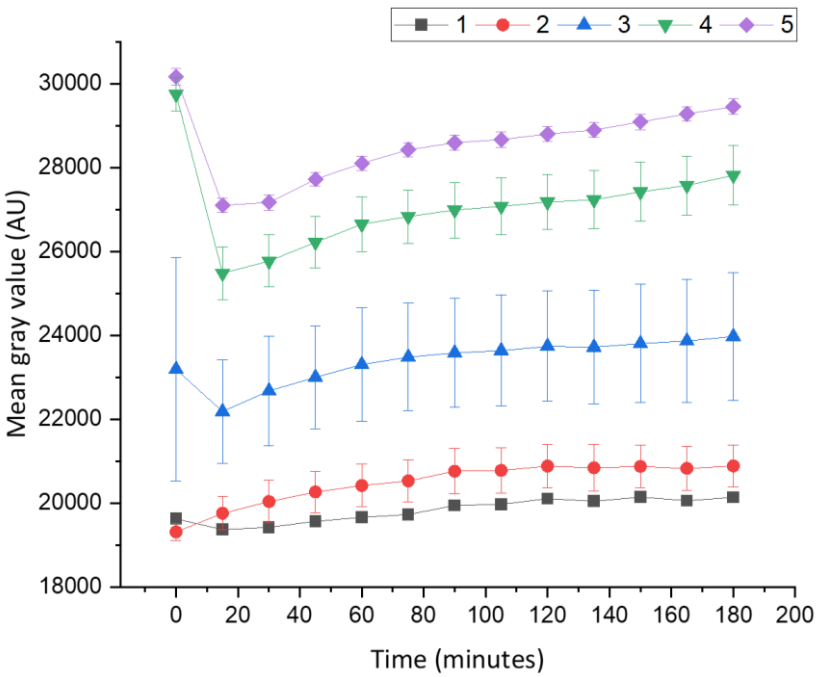

Figure 4.9: Data set 1. Mean gray value (AU, arbitrary units) in solution in channels 1 – 5 at 50 µL/hour (both inlets) over 180 minutes. Data points show average and standard deviation of 9 measurements per channel.

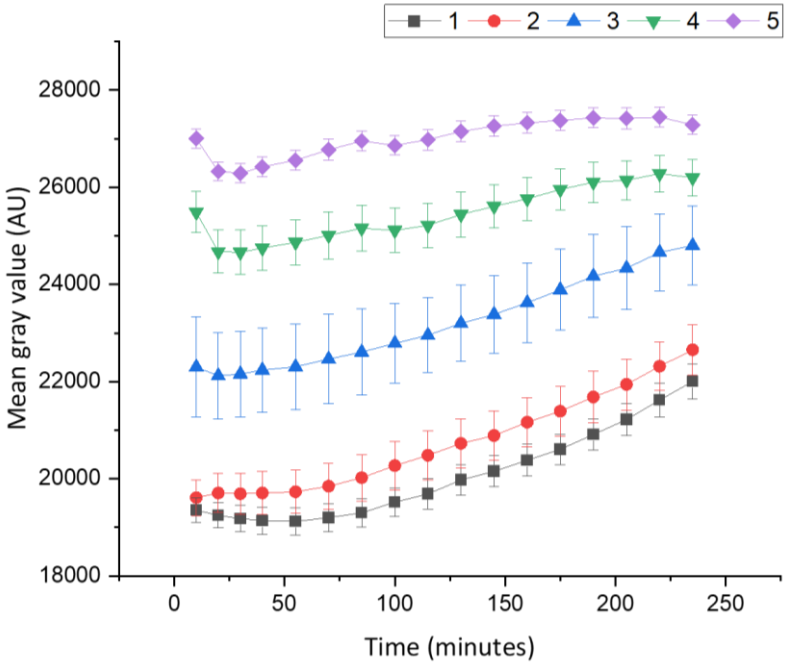

Figure 4.10: Data set 2. Mean gray value (AU, arbitrary units) in solution in channels 1 – 5 at 50 µL/hour (both inlets) over 240 minutes. Data points show average and standard deviation of 9 measurements per channel.

The differences in trends between data set 1 and data set 2 suggest that there may be other factors causing variation in the MGVs. It is possible that the chip position changed as a result of the moving microscope stage. The chip was secured into a microscope slide sized slot, however the chip did not fit tightly so there could have been slight movements in the x, y direction over time. The stainless steel tubes also made the set up very rigid. It is possible that the rigid tubing was forcing the chip to tilt slightly as the stage moved backwards and forwards between channels despite securing with magnetic clips, which could have caused inconsistency in the imaging depth.

Normalisation was used on the data set to remove fluctuations in the trends potentially caused by experimental factors. Normalisation was also required to remove negative values which could arise when the average I_0 from the 0% control solution was lower than intensity values measured in the gradient set-up. In theory, the control I_0 is measured at 0% oxygen and should have the highest MGV. However,

because it was an averaged value, it was possible for measurements taken during the gradient set-up to have higher MGV than the control solution. Using these values in the Stern-Volmer equation resulted in negative oxygen concentration, which is not realistically possible.

There were two potential approaches to normalising the data. One approach was to normalise over the whole data set. In this case data from all time points would be normalised with respect to one maximum and one minimum value for the whole date set. Alternatively, the subsets of data at each time point could be normalised independently of the rest of the data set. In this case the data for channels 1 – 5 would be normalised with respect to the maximum and minimum values recorded at the same time point, regardless of the values recorded at other time points.

Figure 4.11 shows oxygen concentrations in channels 1 – 5 at 25 µL/hour normalised over the whole data set and Figure 4.12 shows the concentrations normalised at each time point. Figure 4.13 and Figure 4.14 show oxygen concentrations normalised per time point in channels 1 – 5 at 50 µL/hour in data sets 1 and 2 respectively. For the data sets at 50 µL/hour, the data was normalised from 30 minutes onwards to focus on the results after the flow rate was stable.

Normalising the data removed fluctuations potentially caused by experimental factors. However, Figure 4.11 and Figure 4.12 show that the approach used to normalise the data has a big influence on the results at 25 µL/hour. When normalised over the whole data set, the oxygen concentration in channels 4 and 5 increases over the 45 minutes window, suggesting a potential leak of oxygen into the system. However, when normalised over the whole data set, the distribution of oxygen is as expected and there is no evidence of oxygen getting into the system.

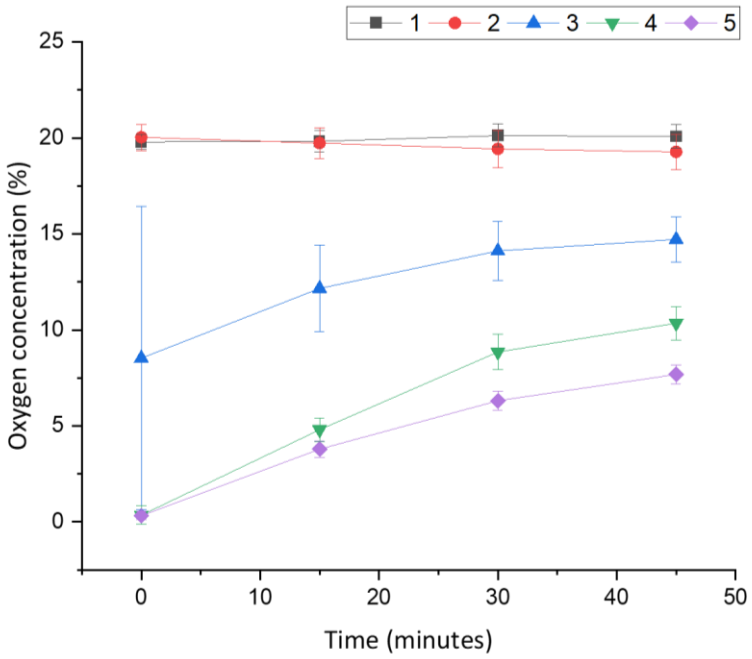

Figure 4.11: Oxygen concentrations in channels 1 – 5 at 25 µL/hour (both inlets). Data points show average and standard deviation of 9 measurements per channel. Concentration was normalised over all time points.

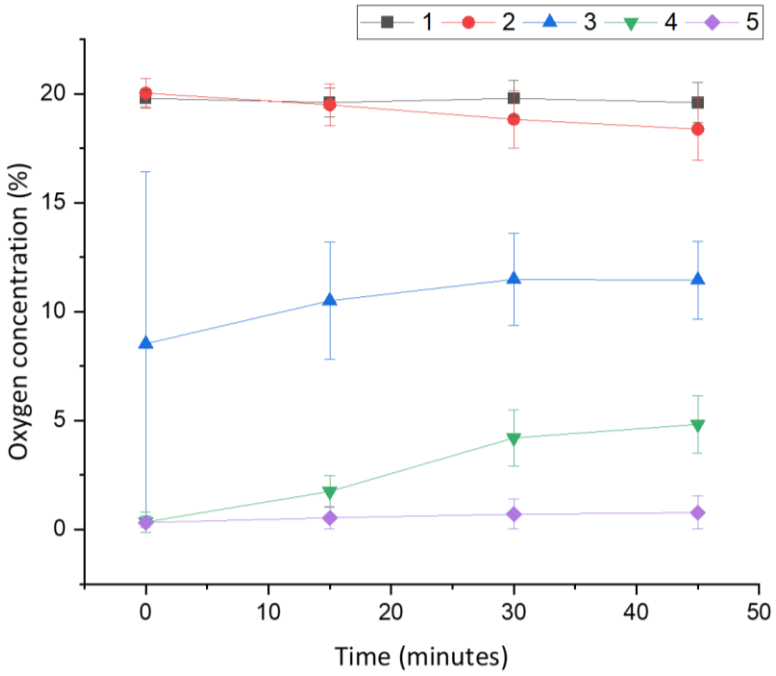

Figure 4.12: Oxygen concentrations in channels 1 – 5 at 25 µL/hour (both inlets). Data points show average and standard deviation of 9 measurements per channel. Concentration was normalised at each time point.

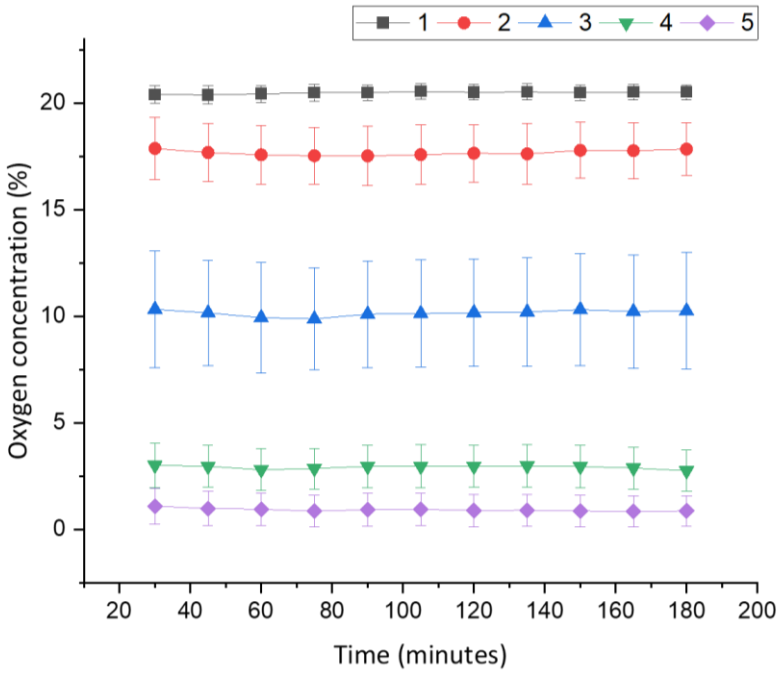

Figure 4.13: Data set 1. Oxygen concentrations in channels 1 – 5 at 50 µL/hour (both inlets). Data points show average and standard deviation of 9 measurements per channel. Concentration was normalised at each time point.

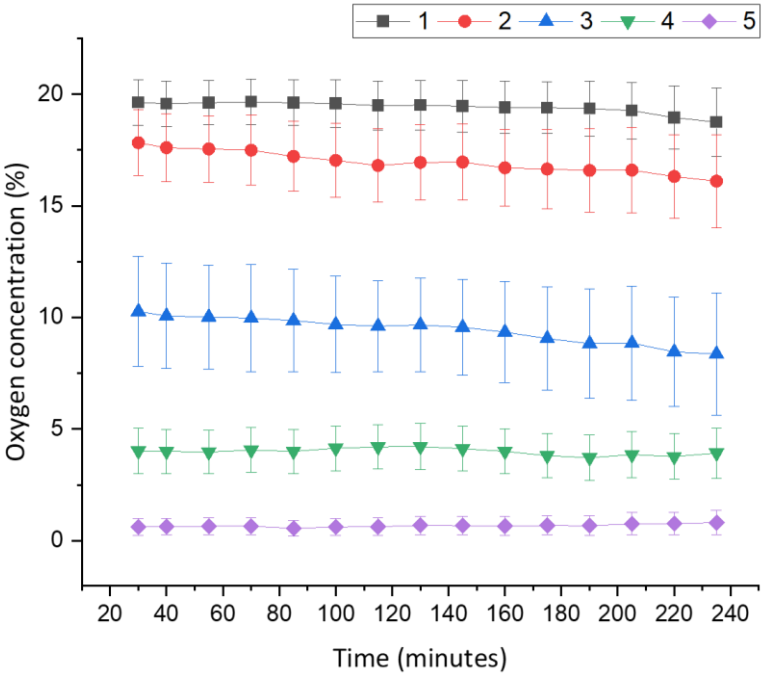

Figure 4.14: Data set 2. Oxygen concentrations in channels 1 – 5 at 50 µL/hour (both inlets). Data points show average and standard deviation of 9 measurements per channel. Concentration was normalised at each time point.

Since the variation in MGVs for both raw data sets at 50 µL/hour don't indicate oxygen getting into the system, it seems reasonable to assign the fluctuations in these results to experimental factors as discussed above. However, for the data set at 25 µL/hour it is plausible that there was a slow oxygen leak into the system and the flow rate was slow enough to allow oxygen to accumulate in the solution. Whereas doubling the flow rate to 50 µL/hour allowed the fluid to move faster, preventing any accumulation of oxygen.

A possible source of the suspected oxygen leak is the acrylic material used to make the chip. Although the oxygen permeability of PMMA is low (5 cc - mm/m^2 - 24 hr - Bar) compared to other materials such as PDMS (4500 cc - mm/m^2 - 24 hr - Bar) and polycarbonate (117 cc - mm/m^2 - 24 hr - Bar), it is still slightly permeable.[98,125,140] Oxygen is also soluble in PMMA to a degree, so oxygen can be stored in the bulk PMMA and leach out over time, especially in the presence of a concentration gradient.[125]

Table 4.3 provides a summary of the oxygen concentrations in each channel for each data set alongside the computational data obtained in Chapter 3. When normalised at each time point, the three data sets show a consistent range of oxygen concentrations in each channel. Comparing the computational and normalised fluorescence data, there is clear agreement between the predicted and measured values of oxygen concentration in each channel.

Table 4.3: Average oxygen concentration per channel at 25 µL/hour and 50 µL/hour (data sets 1, 2 and computational results). Average and standard deviation for fluorescence experiments taken over all time points greater than 20 minutes for each channel. Average and standard deviation for computational results taken over all values from the middle of each channel (Figure 3.7 and Figure 3.10).

Channel	**Oxygen Concentration (%)**			
	25 µL/hour	50 µL/hour Data Set 1	50 µL/hour Data Set 2	Computational 50 µL/hour
1	19.7 ± 0.9	20.4 ± 0.5	19.5 ± 1.1	21.0 ± 0.0
2	18.6 ± 1.4	17.9 ± 1.4	17.1 ± 1.7	17.1 ± 0.4
3	11.5 ± 1.9	10.3 ± 2.6	9.6 ± 2.4	10.4 ± 0.7
4	4.5 ± 1.3	2.8 ± 1.1	4.0 ± 1.0	3.8 ± 0.4
5	0.7 ± 0.7	0.9 ± 0.7	0.7 ± 0.4	0.0 ± 0.0

The computational results discussed in Chapter 3 showed that at 50 µL/hour, oxygen gradients were present in channels 2 – 4. The gradient was steepest at the entrance to channel 3, but reduced down the length of the channel (Figure 3.10 and Figure 3.11). The data is presented again here in a slightly different way. Instead of plotting concentration across the width of the channel as in Chapter 3, it is plotted down the length of the channel as shown in Figure 4.15 and Figure 4.16.

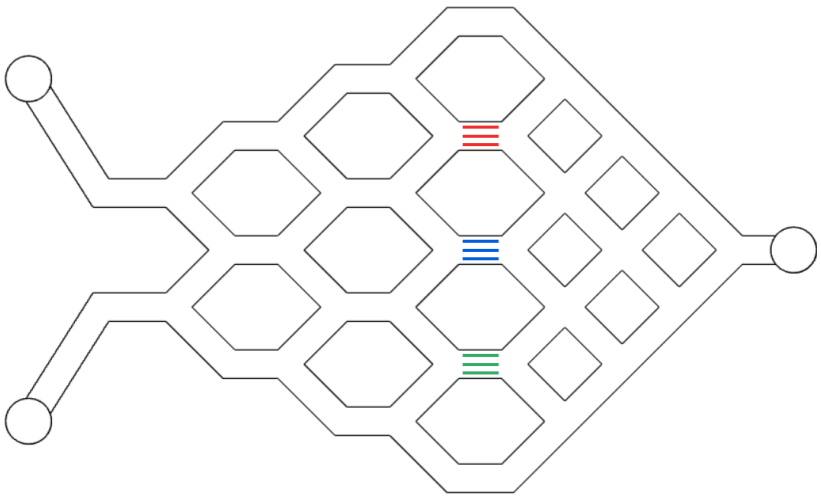

Figure 4.15: Coloured lines show positions where data was collected from computation results. The three lines in the middle channels 2 – 4 were used to produce the graph in Figure 4.16.

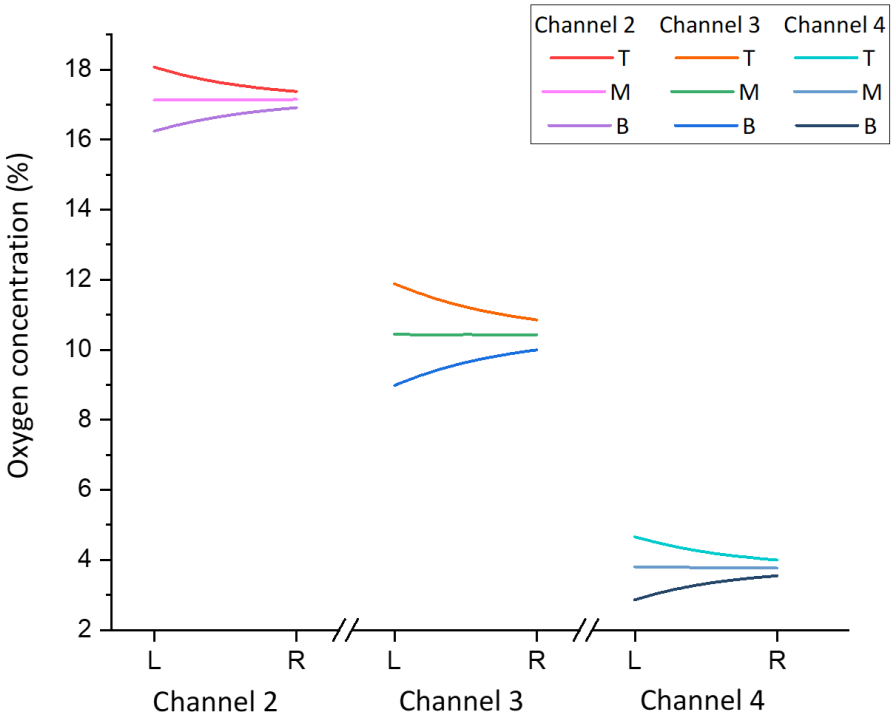

Figure 4.16: Oxygen concentration down the length of channels 2, 3 and 4 from simulations in COMSOL Multiphysics® with flow rate at 50 µL/hour. Lines are plotted from the top (T), middle (M) and bottom (B) of each channel as shown in Figure 4.15.

The gradients in channels 2 – 4 were also studied using the data collected from the fluorescence experiments, to compare to the computation results in Figure 4.16. The 9 individual measurements of MGV in each channel were labelled A – I as shown in Figure 4.17, so that changes in oxygen concentration between the top and bottom and left and right of the channel could be studied. Results for channels 2, 3 and 4 (data set 1) are shown in Figure 4.18, Figure 4.19 and Figure 4.20 respectively. The discussion below focusses on data set 1, but similar values and trends were observed in data set 2. Tabulated results for channels 1 – 5 from both data sets 1 and 2 are given in Appendix 3.

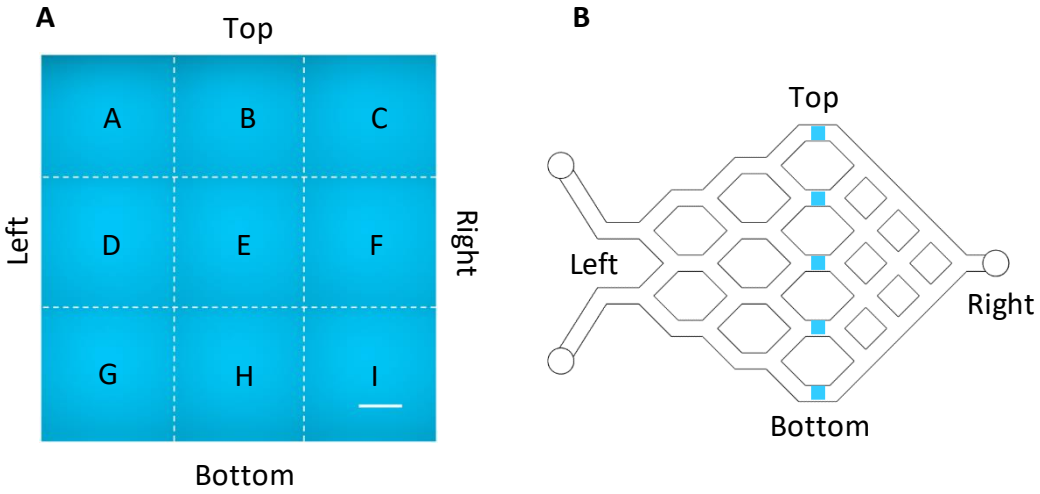

Figure 4.17: ***A*** *3 × 3 image with each individual image labelled A – I. White dashed lines indicate the outline of each image and the solid white scale bar is 100 µm.* ***B*** *Image of channels indicating orientation and position of images within the channel network.*

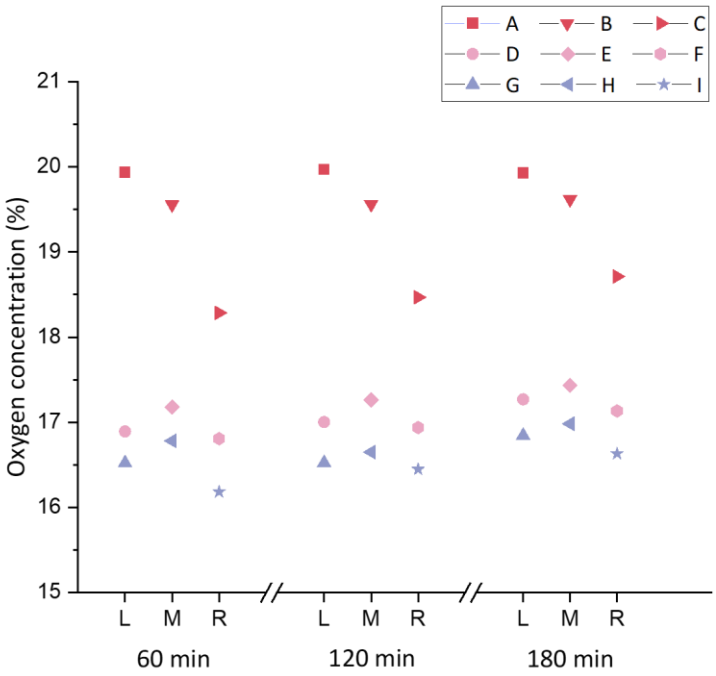

Figure 4.18: Oxygen concentrations in panels A – I for channel 2 from 50 µL/hour, data set 1, at 60, 120 and 180 minutes. L, M and R refer to the left, middle and right of the channel.

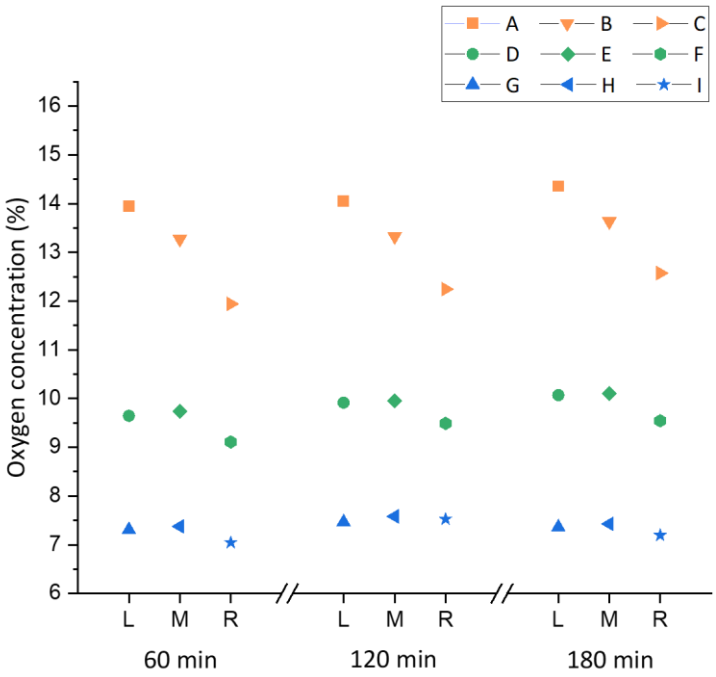

Figure 4.19: Oxygen concentrations in panels A – I for channel 3 from 50 µL/hour, data set 1, at 60, 120 and 180 minutes. L, M and R refer to the left, middle and right of the channel.

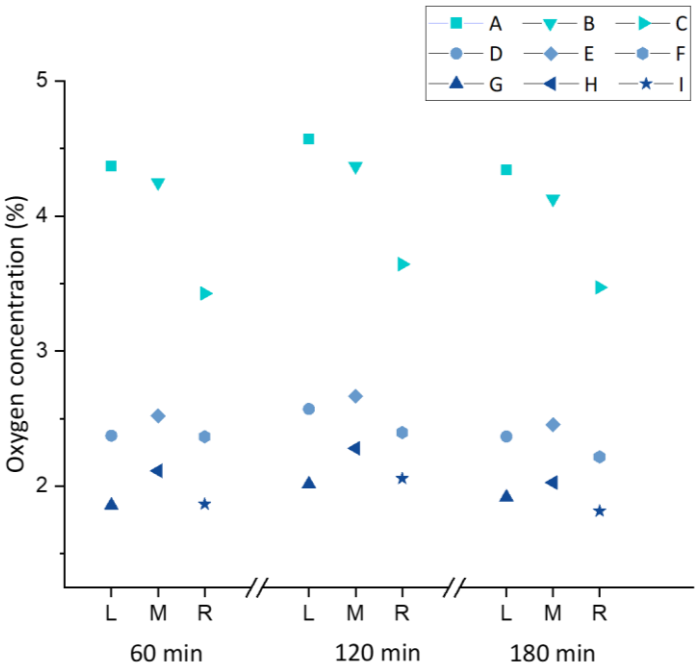

Figure 4.20: Oxygen concentrations in panels A – I for channel 4 from 50 µL/hour, data set 1, at 60, 120 and 180 minutes. L, M and R refer to the left, middle and right of the channel.

For channels 2, 3 and 4, oxygen concentrations are consistent over each of the time points at 60, 120 and 180 minutes. There is a gradient of oxygen observed in each channel which is larger on the left of the channel than the right. This can be seen as the oxygen concentration on the top side of the channel (panels A, B and C) decreases from left to right. It is unclear why the oxygen concentration at the bottom side of the channel does not increase at the same rate, as observed in the computational results in Figure 4.16.

For channel 3, the concentrations in the top (A, B, C), middle (D, E, F) and bottom (G, H, I) are more spread out compared to channels 2 and 4. In channels 2 and 4, the concentrations in the middle and bottom of the channel are close together, then there is a larger difference between the middle and the top of the channel. The computational results in Figure 4.16 show a narrower range of concentrations in each channel with an smooth and even oxygen gradient centred around the middle of the channel. It is possible that the microscopy results do not show as smooth and

consistent gradients because of variation in imaging depth due to movement of the chip during imaging or subtle inconsistencies in channel depth acquired during the fabrication process.

4.3 Summary

Oxygenated and deoxygenated solutions of $Ru(BPY)_3$ were used to create gradients in the chip at 25 µL/hour and 50 µL/hour. The solutions were imaged using a fluorescence microscope and the oxygen concentrations in the channels were calculated based on the measured MGVs and the Stern-Volmer equation.

It was found that there was some variation in the MGVs over time due to experimental factors such as potential movement of the chip during imaging, but these artefacts could be removed by normalising the data. The results at 25 µL/hour suggested a potential leak of oxygen into the system, but there was no evidence of oxygen getting into the system when the flow rate was increased 50 µL/hour.

The normalised results at 50 µL/hour showed trends in oxygen concentration in the chip that were similar to those produced by the calculations in COMSOL Multiphysics® discussed in Chapter 3. The agreement between the two data sets provides sufficient evidence that oxygen gradients can be created and maintained in the chip for time periods of a few hours.

Overall, the combination of computational and fluorescence techniques to measure oxygen concentration was effective. The fluorescence microscopy technique used was relatively easy and did not require any special modification to the chip as it had been designed in Chapter 2. The computational results aided understanding of the microscopy results and shed light on how gradients developed within the channels, which may have been more difficult to conclude from the microscopy experiments alone.

The next step was to culture cancer cells in the chip and study their responses to the different oxygen conditions. This is discussed in Chapter 5.

4.4 Materials and Methods

4.4.1 Experimental Set-Up

Chip system

The chip system was assembled as shown in Chapter 1, Figure 2.15 and washed through with 70% ethanol then water before filling with $Ru(BPY)_3$. Both syringes were fitted onto the dual syringe pump (Harvard Apparatus, 11 Plus, 70-2212) during flow experiments. The chip was secured onto the microscope stage with magnetic clips during measurements.

$Ru(BPY)_3$ Solutions

Solutions of $Ru(BPY)_3$ (4 µM) were prepared in PBS. Control solutions at 21% oxygen were equilibrated under atmospheric oxygen. Control solutions at 0% oxygen were prepared by dissolving Na_2SO_3 (50 mg/mL). Solutions at 0% oxygen for gradient measurements were prepared by bubbling with nitrogen gas for 1 hour.

Control Measurements for K_q Calculations

Two syringes of 21% control solution were connected to chip system. The system was washed through with solution then flow rate was set to same flow rate as used for the experiment (25 or 50 µL/hour) for both syringes. Measurements were taken in each channel 10 minutes apart for 30 minutes. This process was repeated for the 0% control solution.

Gradient Measurements

One syringe filled with 21% solution and one syringe filled with 0% (nitrogen bubbled) solution were connected to chip system. The 21% solution was connected to the top inlet and the 0% solution was connected to the bottom inlet of the chip as displayed in Figure 4.21. The system was washed through with a small amount of solution to displace the previous sample and then the flow rate was gradually reduced to the

desired flow rate. Measurements were taken every 15 minutes using the settings described in section 4.4.2. The total experiment time for the experiment at 25 µL/hour was 45 minutes, for the first experiment at 50 µL/hour was 180 minutes and for the second experiment at 50 µL/hour was 235 minutes.

4.4.2 Imaging

The chip was imaged using a Nikon Ti2 Live Imaging microscope with x40 air objective (CFI Plan Apochromat Lambda) and LED light source (Lumencor SPECTRA X Light Engine). The excitation and emission wavelengths for $Ru(BPY)_3$ are approximately 450 nm and 630 nm, hence a CFP (cyan fluorescent protein) excitation filter (414 nm – 462 nm) and a TxRed (Texas red) emission filter (566 nm – 716 nm) were used.[141] The exposure time was 170 ms and the light power was 10%. Large images were compiled from 3 × 3 individual images for each channel, as shown in Figure 4.21. The Nikon Elements 5.1 software was used to automate image acquisition. Imaging positions were saved on the software so that images were taken from the same positions in each channel at each time point on the set timing profile.

A representative image produced using the settings detailed in Section 4.4.2 is shown in Figure 4.22. ImageJ was used to measure the mean gray value in the centre of each individual image, as shown by the black boxes. Data was collated and analysed in Origin.

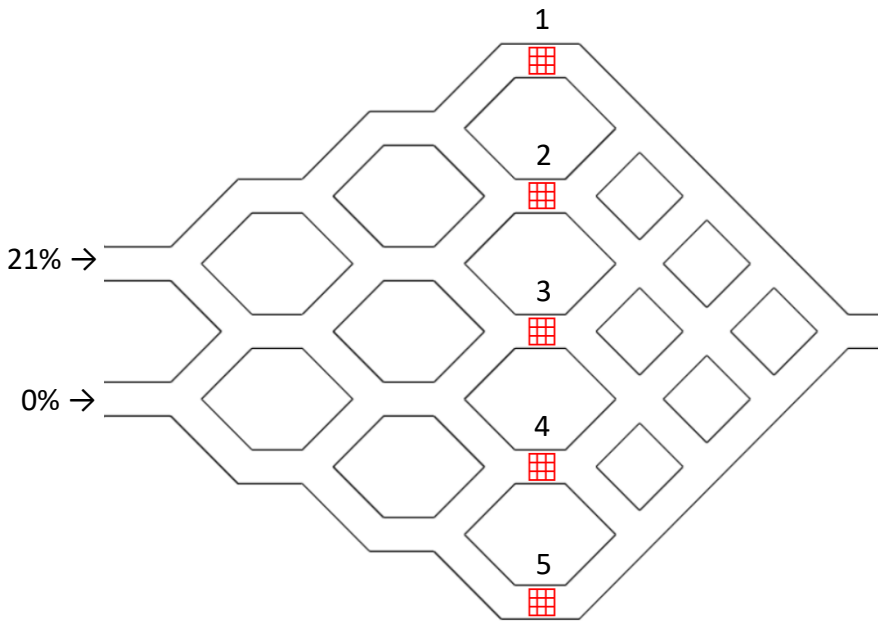

Figure 4.21: Image of channel network showing approximate position of 3 × 3 images in channels 1 – 5. Arrows indicate 21% oxygen solution feeding into the top inlet and 0% solution feeding into the bottom inlet for gradient generation in the chip.

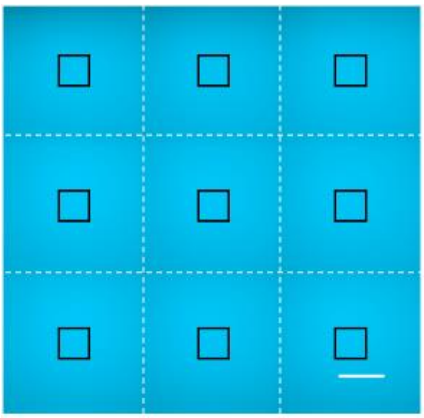

Figure 4.22: Representative 3 × 3 image produced using settings detailed in Section 4.4.2. One 3 × 3 image is taken for each of channels 1 – 5 at every time point. White dashed lines show the outline of each individual image. Each individual image is approximately 300 µm × 300 µm giving a total imaged area of approximately 900 µm × 900 µm in each channel. Black boxes show 68 µm × 68 µm area in the centre of each image where data is collected from. Solid white scale bar is 100 µm.

4.4.3 Data Analysis

Calculations of K_q

The average mean gray value measured over all channel and time points was calculated for 21% and 0% oxygen control solutions. The values are then assigned as follows: I_0 is the average value for the 0% solution, I_{21} is the average value for the 21% solution and $[O_2]$ is 21%. These values are then used in the Stern-Volmer equation to calculate K_q.

Calculations of Oxygen Concentration

The oxygen concentration for each MGV measurement (9 measurements per channel per time point) was calculated using the average I_0 value from the 0% oxygen control solution. For data collected at 25 µL/hour, oxygen concentrations overall time points were normalised 0:21. For data collected at 25 µL/hour and 50 µL/hour, the subsets of oxygen concentrations for each time point were normalised 0:21. Then the average oxygen concentration and standard deviation was calculated for each channel at each time point.

Chapter 5: In-Chip Cell Culture

5.1 Introduction

The aim of the work in this chapter was to investigate how to culture cells in the chip (fabricated in Chapter 2) under an oxygen gradient (characterised in Chapters 3 and 4). Culturing cells in the chip is different to standard cell culture methods using flasks and well plates in two major ways.

First, in standard cell culture the media is static (not moving), whereas media flow over the cells is required in the chip system to maintain the oxygen gradient. This imposes an additional stress on the cells and is given further consideration in Section 5.1.1. Second, cell culture systems are generally open to allow gas exchange between the air in the flask and the air in the cell culture incubator (5% CO_2), which is important for buffering the cell culture media at a physiological pH. However, the chip system is closed, which makes gas exchange between the contained cell culture media and the atmosphere not possible. This is discussed further in Section 5.1.2.

Survival of two prostate cancer cell lines, PC3 and DU145, and one liver cancer cell line, HepG2/C3A, were tested in the chip. The results are presented and discussed in Section 5.2.

5.1.1 Culturing Cells with Media Flow

In standard cell culture methods, cells are grown in flasks, petri dishes or well plates with media on top and stored in incubators such that the fluid does not constantly move around on top of the cells. However, the design for the chip presented here required constant media flow over the cells to maintain the oxygen gradient.

In some scenarios, media flow over the cells can be advantageous because it is a phenomenon that cells experience *in vivo*. Systems have been developed to investigate growth of cells under physiologically relevant shear stress, for example epithelial cells, cancer metastasis and lung models.[142–145] Constant media flow can also be beneficial for replenishing nutrients and removing waste in the culture.[92,146]

However, if the flow rate is too high, it can cause damage to cell membranes and result in detachment of adherent cell lines.[147]

There are various examples of cancer cells grown under shear stress reported in literature, some are summarised in Table 5.1. HepG2 cells have been reported to grow well under shear stress, with studies generally investigating shear stress levels below 1 dyn/cm^2. No examples of prostate cancer cell lines being cultured under shear stress were found during the course of this project. However, a paper by Liu *et al.* shows PC3 cells being cultured in a microfluidic device and becoming detached at shear stress levels over 1 dyn/cm^2.[147]

Table 5.1: Literature examples of cancer cell types grown under shear stress.

Organ	**Cell type**	**Shear stress** (dyn/cm^2)	**Reference**
Lung	A549	0.145	Wang *et al*.[148]
Cervix	HeLa	0.145	Wang *et al*.[148]
Liver	HepG2	0.7	Liu *et al*. [149]
Liver	HepG2	$1.7 \times 10^{-6} – 6.2 \times 10^{-6}$	Ke *et al*.[150]
Liver	HepG2/C3A	0.02 – 0.06	Baudoin *et al*.[146]
Endometrium	Ishikawa	0.03	Orcheston-Findlay *et al.*[59]

Calculations of shear stress in the channels in the chip designed in Chapter 2 were performed in COMSOL Multiphysics® based on results from the fluid flow calculations in Chapter 3. The calculated levels of shear stress in channels 1 – 5 with flow at both inlets at 50 µL/hour were between 0.0028 – 0.0065 dyn/cm^2 (Appendix 2). These levels are well below those reported in Table 5.1 (with the exception of the paper by Ke *et al*.) which suggests that it should be possible to maintain cancer derived cell lines in the chip with flow, particularly hepatocytes.

5.1.2 Culturing Cells without CO_2

In mammalian cell cultures, pH has to be regulated to a physiological level (usually around 7.2 – 7.4) to maintain cell health and function.[151] In two of the most common cell culture media types for mammalian cells, DMEM (Dulbecco's modified eagle medium) and RPMI (Roswell Park Memorial Institute) 1640 medium, the pH is controlled by a carbonate buffer system, as described by equation 5.1.[152–154] Cells are usually cultured under an atmosphere of 5 – 10% CO_2 and media is supplemented with sodium bicarbonate such that there is a sufficient supply of both CO_2 and bicarbonate to buffer the system.[152–154]

$$CO_2 + H_2O \rightleftharpoons HCO_3^- + H^+ \qquad 5.1$$

However, the chip system described in this work has been designed to be impermeable to oxygen and is, therefore, also impermeable to carbon dioxide. This means that the traditional carbonate buffer media system will likely be ineffective at maintaining a physiological pH because carbon dioxide cannot get into the system. Hence, alternative media that are not reliant on carbonate buffer were investigated.

L-15 (Leibovitz) medium and CO_2-Ind (carbon dioxide independent) medium both use phosphate buffer system to maintain physiological pH.[155,156] Monobasic and dibasic phosphate ions ($H_2PO_4^-$ and HPO_4^{2-}) are supplemented into the media as potassium or sodium salts and equilibria between the protonated and deprotonated phosphate ions forms the buffer system.[155,156] Additionally, L-15 is supplemented with 17 free base amino acids, of which L-arginine, L-histidine and L-cysteine in particular have been reported to contribute to pH regulation.[157–159]

5.2 Results

5.2.1 In-Chip Cell Culture – PC3 Cells

Media and Protein Screen

As explained in Section 5.1.2, the common cell culture media (DMEM and RPMI) rely on equilibration at 5-10% CO_2 so that the carbonate buffer can maintain a physiological pH. However, CO_2 equilibration is not possible in the chip because gases from the atmosphere are unable to permeate into the system. To investigate alternative media that rely on phosphate buffer instead of carbonate buffer, culture of PC3 cells was tested without CO_2 in CO_2-Ind and L-15 media.

For *in vitro* cell culture of adherent cell lines on plastic and glass materials, it is common to coat the surface with an extra-cellular matrix (ECM) protein to help the cells attach and grow on the surface. In this short screening experiment, cells were also seeded on two different proteins, collagen and fibronectin, to see if the cells performed better on either coating.

Experimental details of the screen are given in Section 5.4.3. The cells were seeded on 4 different surfaces in CO_2-Ind and L-15 media; glass cover slip coated in collagen, glass cover slip coated in fibronectin, control glass cover slip soaked in water or PBS and the plastic tissue-culture treated well plate surface (no cover slip). Triplicate samples of each condition were prepared and the cells were incubated without CO_2 for 3 days. Representative images of the cells in CO_2-Ind media and L-15 media are shown in Figure 5.1 and in Figure 5.2 respectively.

The cells in both CO_2-Ind media (Figure 5.1) and L-15 media (Figure 5.2) appeared to attach and grow on all surfaces tested. However, the cells in CO_2-Ind media showed even confluence whereas the cell in L-15 media showed patchy confluence with some areas much more densely populated than others. It is unlikely that the patchy confluence is due to quality of the protein coatings, as this trend was also observed in the control cover slip and well plate. This suggested that the cells preferred CO_2-Ind

medium to L-15 medium, but the cells showed no strong preference over collagen or fibronectin.

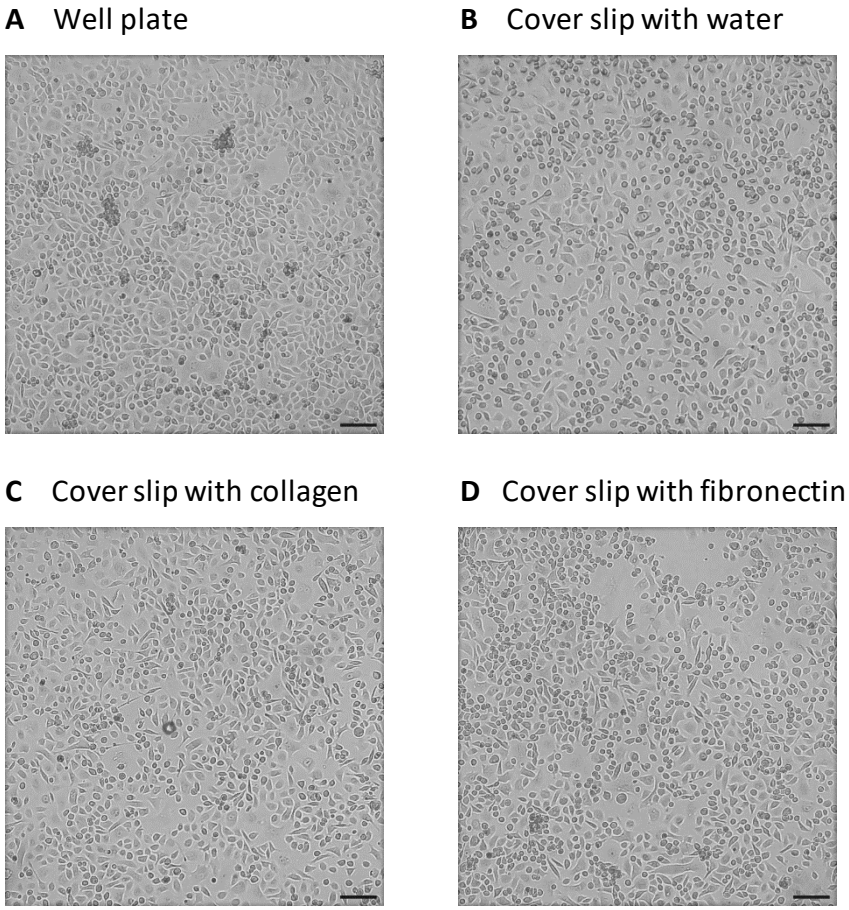

Figure 5.1: PC3 cells in CO_2-Ind media. ***A*** *Blank well plate control.* ***B*** *Cover slip with water control.* ***C*** *Cover slip coated with 100 µg/mL collagen.* ***D*** *Cover slip coated with 17 µg/mL fibronectin. All images taken on Motic AE200 microscope with x4 objective, scale bar is 150 µm.*

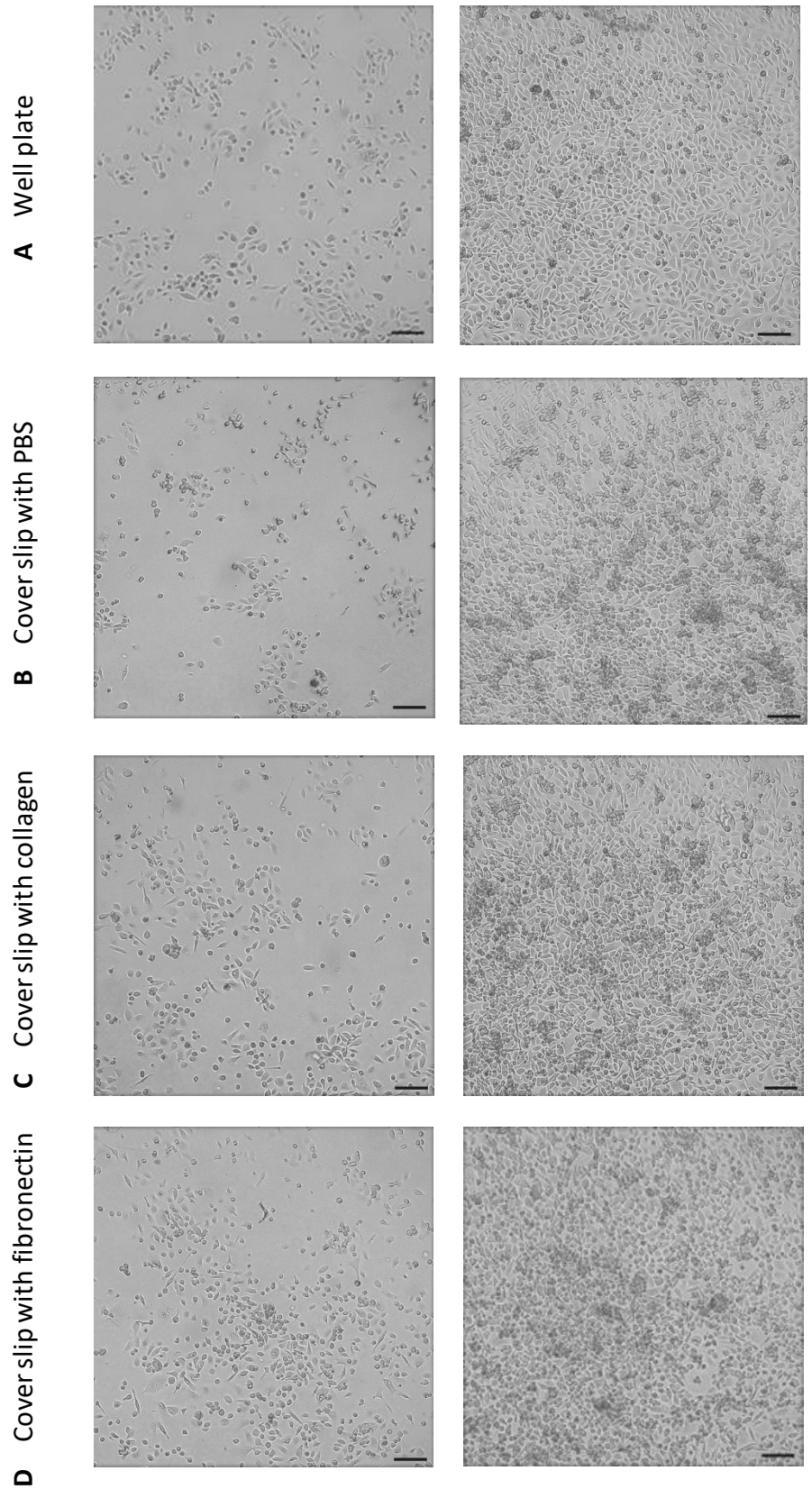

Figure 5.2: PC3 cells in L-15 media. Representative images of areas with low (left) and high (right) cell density are shown for each condition. ***A*** *Blank well plate control.*

***B** Cover slip with water control. **C** Cover slip coated with 100 µg/mL collagen. **D** Cover slip coated with 17 µg/mL fibronectin. All images taken on Motic AE200 microscope with x4 objective, scale bar is 150 µm.*

Seeding in Chip

Since PC3 cells were shown to survive without CO_2, seeding them into the chip was attempted. This work was carried out earlier in the project and the first iteration of the acrylic chip system was used as described in Section 2.2.3.

Full details of the seeding process are given in Section 5.4.4. Briefly, the chip was coated with collagen and PC3 cells were seeded into the chip in CO_2-Ind medium. The cells were incubated at 37° C for 3 hours, which was observed to be sufficient time to allow the cells to attach to the surface of the chip. A representative image is shown in Figure 5.3 A. The cells were then returned to the incubator and media flow was started by setting the syringe pump to withdraw at 30 µL/hour. After 30 minutes, it was observed that the cells had become detached from the surface (Figure 5.3 B). The cells were then incubated for a further 1 hour to see if the detached cells would recover and reattach to the surface. However, after the cells remained detached as shown in Figure 5.3 C.

This result was unexpected as 30 µL/hour was considered a slow flow rate that would impose minimum shear stress on the cells in the chip. However, the experiment was repeated and similar results were obtained. Over the course of this project, no literature examples of adherent PC3 cells being cultured under media flow were found. From these experiments, it was concluded that PC3 cells are very sensitive to shear stress and could not be cultured in this system and so other cancer cell lines were investigated.

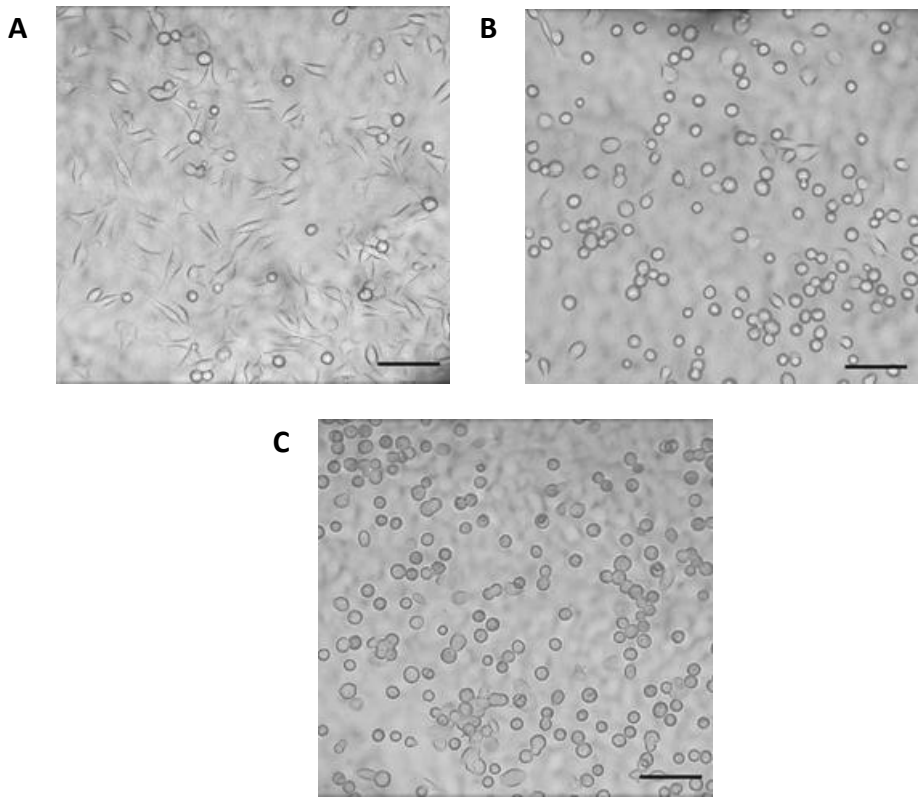

*Figure 5.3: PC3 cells in chip after **A** 3 hour incubation, **B** 30 minutes flow at 30 µL/hour and **C** 1 hour incubation post flow. All images taken on Motic AE200 microscope with x10 objective, scale bar is 100 µm.*

5.2.2 In-Chip Cell Culture - HepG2/C3A Cells

Unlike PC3 cells, human hepatocyte cell lines have been grown under flow in microfluidic devices and it has been demonstrated that they can survive moderate levels of shear stress, as discussed in Section 5.1.1. Therefore, HepG2/C3A cells were selected as the next cell type to try to seed in the chip.

Media Screen

First, HepG2/C3A cell survival was tested in CO_2-Ind and L-15 media. Approximately 1.2×10^6 cells were seeded in T25 culture flasks in each medium and incubated at 37° C and 0% CO_2. After 1 day, the cells in L-15 were all dead but the cells in CO_2-Ind were still alive.

Sometimes cells can take time to adapt to a new media. One approach to make the transition easier, is to gradually dilute the original media with the desired media at each cell passage. This was tried with HepG2/C3A cells and L-15. During a passage of the main culture, 1.2×10^6 cells were seeded in a T25 culture flask with 50% DMEM and 50% L-15 and placed in the incubator with 0% CO_2. However, the cells were again observed to be dead after 24 hours.

The cells in CO_2-Ind media were still alive and so were harvested and counted after 3 days. The cell density had increased from 1.2×10^6 cells to 1.5×10^6 cells. In the main DMEM culture, cell numbers approximately triple over 3 days. So although the cells do survive in CO_2-Ind and 0% CO_2, proliferation is much slower than in DMEM and 5% CO_2.

Since the cells survive in CO_2-Ind media, it was carried forward to use for seeding cells in the chip. In future work, optimisation of the media would be carried out to investigate the addition of nutrients, growth factors or additional buffers to sustain cell health and proliferation.

Seeding in Chip

Seeding of HepG2/C3A cells in the chip was carried out using the second iteration of the chip system as described in Section 2.2.4. The seeding process was similar to the process described for the PC3 cells and full details are given in Section 5.4.5.

In the first experiment, HepG2/C3A cells were seeded in a collagen coated chip and visually observed to be attached after 5 hours incubation, as shown in Figure 5.4 A. The cells were incubated without flow overnight (Figure 5.4 B) and it was observed that this resulted in a deterioration in cell health. Although some cells remained attached to the surface with characteristic cell morphology, many had become rounded and detached from the surface. Since there was still some live cells in the chip, media (21 % oxygen) flow through the chip was carried out at 50 µL/hour (both inlets) for 4 hours. Figure 5.4 C and D show cell quality was patchy after exposure to

media flow. In some areas there were live and attached cells (Figure 5.4 C), but other areas showed a higher proportion of rounded cells (Figure 5.4 D).

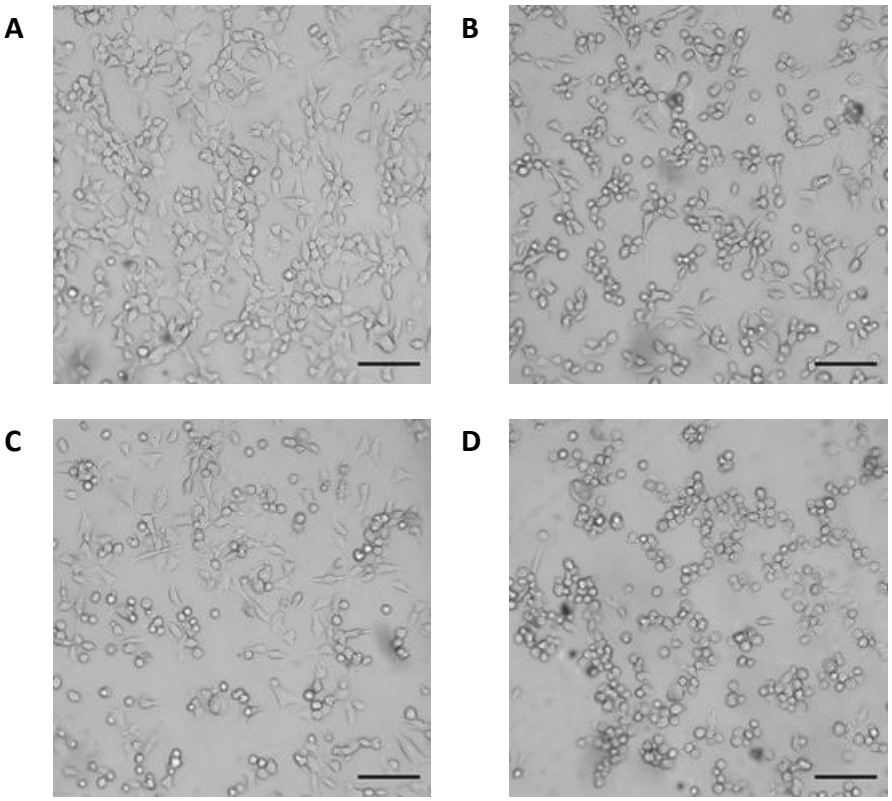

*Figure 5.4: HepG2/C3A cells in chip after **A** 5 hour incubation **B** overnight incubation without flow **C** and **D** after 4 hours with flow. All images taken on Motic AE200 microscope with x10 objective, scale bar is 100 µm.*

The presence of live cells indicated that it could be possible to culture HepG2/C3A cells in the chip under flow with some further optimisation of the process. It was hypothesised that the deterioration of cell health during the overnight incubation with no media flow may have been due to depletion of oxygen and nutrients in the small volume of media in the local environment of the cells. Hence, the experiment was repeated but the cells were incubated overnight with media flow at 50 µL/hour (both inlets).

The results in Figure 5.5 show images of the cells after 5 hours of incubation without flow to allow the cells to attach to the surface (Figure 5.5 A) and after media (21%

oxygen) flow overnight at 50 µL/hour (Figure 5.5 B). The image in panel B shows that there were many live cells remaining after the period of flow. Cell health appeared improved compared to the overnight incubation without flow (Figure 5.4 B) as there were more attached cells with characteristic morphology and fewer rounded cells. The cells were also more consistent throughout the chip.

The same cells were then exposed to hypoxic media flow at 50 µL/hour overnight. Media was deoxygenated as described in Section 5.4.6. As shown in Figure 5.5 C, the cells also appeared healthy and alive, demonstrating that the HepG2/C3A cells can be cultured in the device under flow for up to 2 days and can survive in hypoxic conditions.

To confirm that the cells that appeared healthy and attached to the surface were indeed alive, they were stained with Trypan blue. Trypan blue is a dye that cannot permeate live cell membranes but can accumulate in dead cells. Cells in the chip were stained by first removing all tubing and attachments, then pipetting 1:1 solution of CO_2-Ind:Trypan blue into the channels. The image in Figure 5.5 D shows most cells have excluded Trypan blue, and appear lighter against the blue background of the solution, whereas dead cells are highlighted as dark blue circles.

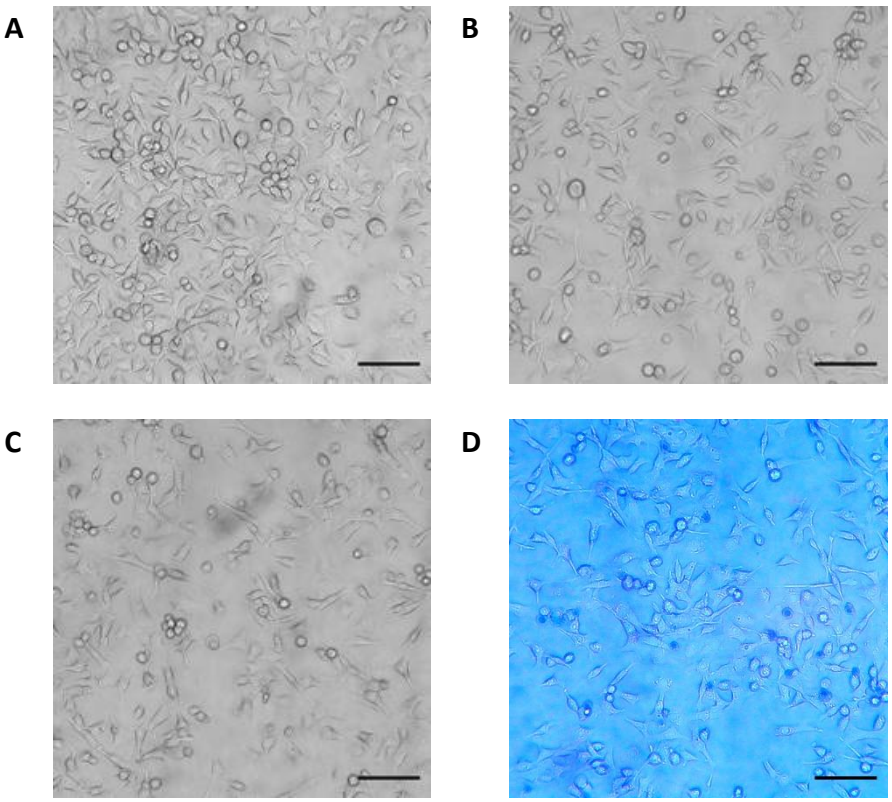

*Figure 5.5: HepG2/C3A cells in chip after **A** 5 hour incubation **B** overnight incubation with 21% O_2 media flow **C** overnight incubation with 0% O_2 media flow and **D** stained with trypan blue. All images taken on Motic AE200 microscope with x10 objective, scale bar is 100 µm.*

5.2.3 In-Chip Cell Culture - DU145 Cells

Following on from the successful method developed to culture HepG2/C3A cells in the chip, the same protocol was tested with an alternative prostate cancer cell line, DU145. The cells were tested in the chip using a similar method as was used for the HepG2/C3A cells (Section 5.4.5) to see if the DU145 cells were more resistant to shear stress compared to the PC3 cells.

Media Test

The DU145 cells were seeded in a T25 culture flask at a density of 0.5 × 10^6 cells/mL in CO_2-Ind medium and incubated without CO_2. After 3 days, the cells were harvested and counted and the cell numbers had increased to 0.7 × 10^6 cells/mL.

Similar to the HepG2/C3A cells, the DU145 cells grow slowly in CO_2-Ind medium. The medium is sufficient to culture cells without CO_2 and should be suitable for testing culture of the cells under media flow in the chip.

Seeding in Chip

The cells were seeded in a collagen coated chip at a density of 2.7 × 10^6 cells/mL and the cells appeared attached to the surface after 5 hours, as shown in Figure 5.6 A. The cells were exposed to media flow of 50 µL/hour at each inlet and cells were observed to be rounded and detached after 1.5 hours, as shown in Figure 5.6 B. The same cells were incubated in the chip overnight without flow and appeared to still be alive and reattached to the surface (Figure 5.6 C). The cells were exposed to media flow of 50 µL/hour at each inlet for 3 hours, but again the cells became rounded (Figure 5.6 D).

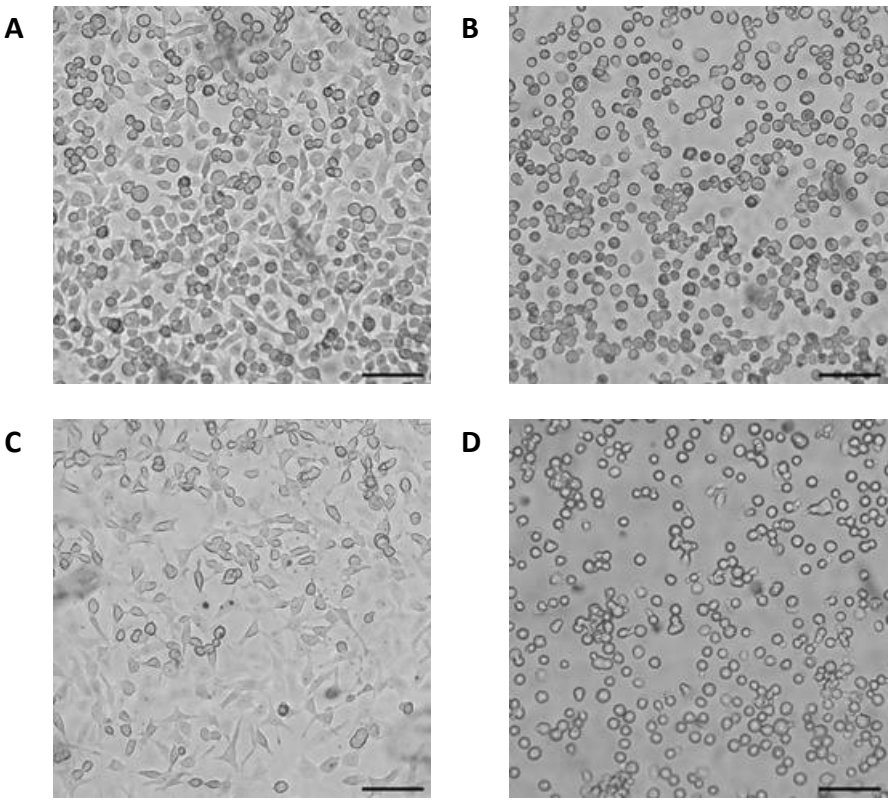

*Figure 5.6: DU145 cells in chip after **A** 5 hour incubation **B** 1.5 hours of media flow **C** overnight incubation without media flow and **D** 3 hours of media flow. All images taken on Motic AE200 microscope with x10 objective, scale bar is 100 µm.*

5.3 Summary

The experiments in this chapter tested the ability of two prostate cancer cell lines, PC3 and DU145, and one liver cancer cell line, HepG2/C3A, to survive inside the chip with media flow and without CO_2.

The ability of the cells lines to grow without CO_2 in CO_2-Ind and L-15 media was tested using standard cell culture flasks or well plates. PC3 and HepG2/C3A cells were shown to prefer CO_2-Ind over L-15 medium, however, growth of HepG2/C3A and DU145 cells was shown to be slower than in DMEM and RPMI respectively with 5% CO_2. Despite the slow growth, CO_2-Ind media was used to seed each cell type into the chip and test cell survival under flow.

The in-chip experiments demonstrated that both prostate cancer cell lines were very sensitive to shear stress and could therefore not survive the media flow inside the chip. On the other hand, HepG2/C3A cells did survive the flow and could be kept alive in the chip with media flow at 50 μL/hour for 2 days, including 24 hours with media at 0% oxygen.

Although CO_2-Ind media kept HepG2/C3A cells alive in the chip, the slow growth in the culture flask media tests suggested that the cells were not as healthy as they could be. This is something that could be investigated further in future work. For example, adding additional buffering agents, growth factors or proteins to the medium could make the environment even more suitable for maintaining cell health and proliferation.

Culture of HepG2/C3A cells in the chips is continued in the next chapter, where expression of hypoxia dependent proteins in the cells under hypoxic gradients is investigated.

5.4 Materials and Methods

5.4.1 Cell Culture Materials

All materials used for cell culture are listed in Table 5.2. DMEM, RPMI, L-15 and CO_2-Ind media were all supplemented with 10% FBS and 1% pen-strep (v/v) and CO_2-Ind medium was also supplemented with 5% L-glutamine (all v/v). All cell types were gifted from colleagues at the University of Edinburgh.

5.4.2 Routine Cell Culture

HepG2/C3A were cultured in DMEM and DU145 and PC3 cells were cultured in RPMI. Cells were maintained in flasks in cell culture incubators at 37° C, 95% humidity and 5% CO_2. Cells were fed as required and passaged when the flasks reached approximately 80% confluence. TripLE™ Express Enzyme was used to detach cells during passaging.

Table 5.2: Materials and Sources for Cell Culture

Material	**Supplier**	**Product code**
CO_2 Independent Medium	Gibco (Thermo Fisher Scientific)	18045088
Collagen, Type 1, Rat Tail	Corning	354249
Corning Costar Tissue Culture (TC)-Treated Flasks	Merck	CLS430641U, CLS430372
Corning Costar Tissue Culture (TC)-Treated Multiple Wells Plates	Merck	CLS3513
Dulbecco's modified eagle medium (DMEM)	Gibco (Thermo Fisher Scientific)	31885023
Dulbecco's phosphate buffered saline (PBS)	Sigma-Aldrich (Merck)	D8537
Fetal Bovine Serum	Sigma-Aldrich (Merck)	F7524
Fibronectin, bovine plasma	Sigma-Aldrich (Merck)	341631
Geltrex™ LDEV-free reduced growth factor basement membrane matrix	Gibco (Thermo Fisher Scientific)	A1413201
Leibovitz L-15 medium	Gibco (Merck)	L1518
L-Glutamine	Gibco (Thermo Fisher Scientific)	25030081
Millex-GP 0.22 µm syringe filter	Millipore (Merck)	SLGP033R
Penicillin-streptomycin (pen-strep)	Gibco (Thermo Fisher Scientific)	15140122
Roswell Park Memorial Institute (RPMI) 1640 medium	Gibco (Thermo Fisher Scientific)	21875034
TripLE™ Express Enzyme (1X)	Gibco (Thermo Fisher Scientific)	12605-010

5.4.3 PC3 Media and Protein Screen

Cover slips (18 mm) were sterilised in 70% ethanol and rinsed three times with water or PBS. Nine cover slips were placed into each of two 12-well plates; three were covered with fibronectin solution (17 µg/mL in PBS), three were covered with collagen solution (100 µg/mL in PBS), three were covered with water (CO_2-Ind well plate) or PBS (L-15 well plate) and the remaining 3 well were left empty. The plates were refrigerated at 4° C overnight then rinsed twice with PBS. PC3 cells were seeded at approximately 100,000 cells in 1.5 mL media in each well. CO_2-Ind media was used for one well plate and L-15 media was used for the other. Cells were incubated at 37° C, 95% humidity and 0% CO_2 for 3 days then imaged on a Motic AE200 microscope with x4 objective.

5.4.4 Seeding PC3 Cells into Chip

The first iteration of the acrylic chip system was used as described in Section 2.2.3. An image of the system from Figure 2.12 C is shown again here in Figure 5.7.

Figure 5.7: Image of first iteration of acrylic chip system (repeated from Figure 2.12 C). The image shows the chip sealed with glass cover slip inside the incubator, needles are attached at each inlet to the chip and inserted through septa into foil pouches containing media. The longer tube is connected to the chip outlet and a syringe which sits on the syringe pump outside of the incubator.

All components of the system were sterilised with 70% ethanol and washed with PBS. The channels of the chip were filled with 100 µg/mL collagen, refrigerated at 4° C overnight, washed with PBS and then washed with CO_2-Ind medium. Tubing and needles were filled with PBS and attached to the chip, the system was washed through with CO_2-Ind media via a syringe attached to the outlet tube. Foil pouches were then filled with CO_2-Ind medium and inlet needles were inserted through the septa. Cells were cultured in RPMI and resuspended in CO_2-Ind medium before injecting into chip. A suspension of 3×10^6 cells/mL was injected into the system by a syringe on the outlet tube. This syringe was then swapped for a syringe containing a small amount of media and the chip was incubated at 37° C for 3 hours.

Images of the cells inside the chip were taken with a Motic AE200 microscope with x10 objective. The chip was then returned to the incubator and the syringe pump was set to withdraw media through the system at 30 µL/hour for 30 minutes. The cells were imaged, returned to the incubator for 1 hour without flow and then imaged again.

5.4.5 Seeding HepG2/C3A Cells in Chip

The second iteration of the acrylic chip system was used as described in Section 2.2.4. An image of the system from Figure 2.15 A is shown again here in Figure 5.8.

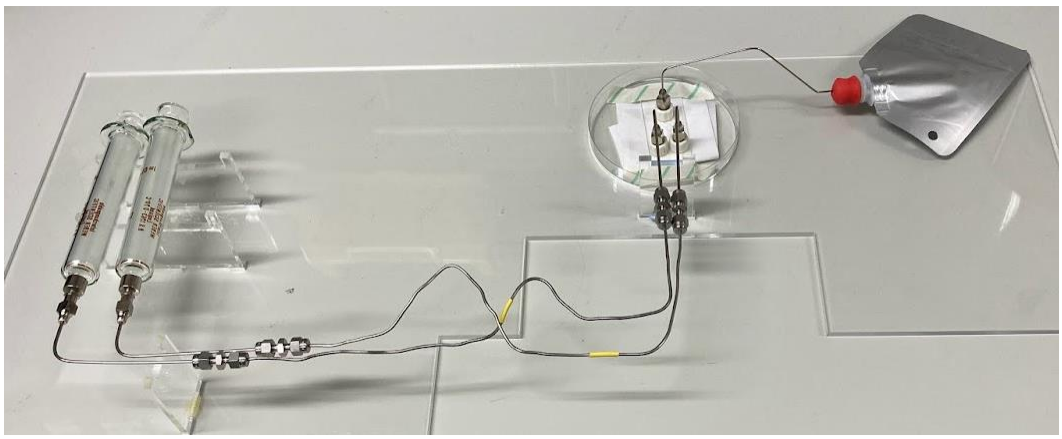

Figure 5.8: Image of second iteration of acrylic chip system (repeated from Figure 2.15 A). The image shows the chip sealed with a thin acrylic sheet, tubing is attached at each inlet to the chip and then connected to glass syringes which sit outside the incubator on a dual syringe pump. A needle is connected to the chip outlet and inserted through septa into a foil pouch which collects the outflow.

Tubing, needle, pouch and chip were sterilised with 70% ethanol and washed with PBS. Glass syringes and septa were sterilised by autoclave. The channels of the chip were filled with 100 µg/mL collagen, refrigerated at 4° C overnight, washed with PBS and then washed with CO_2-Ind medium. Tubing/needles were filled with PBS and attached to the chip, the system was washed through with CO_2-Ind media via two syringes connected to the inlets. The foil pouch was then filled 5-10 mL PBS and the outlet needle was inserted through the septum. Cells were cultured in DMEM and

then resuspended in CO_2-Ind medium before injecting into the chip. Approximately 0.5 mL cell suspension (4.0×10^6 - 4.5×10^6 cells/mL) was injected into the system through each syringe. The syringes were then swapped for syringes containing media and the chip was incubated at 37° C for 5 hours. Flow was set on the dual syringe pump at various flow rates for various lengths of time as specified in the main results text (Sections 5.2 and 6.2).

5.4.6 Preparation of Deoxygenated Cell Culture Media

An RBF and septum were sterilised by autoclave and a magnetic stirrer bar was sterilised in 70% ethanol and rinsed with PBS. In a sterile tissue culture hood, the desired volume of media was placed in the RBF with magnetic stirrer bar and sealed with the septum. Two sterile needles (21G, 4.75") were inserted through the septum and capped with 0.22 µm syringe filter. The RBF was then removed from the hood and placed on a stirrer plate. The solution was gently agitated and the needles were positioned above the level of the fluid. One needle was attached to a flow of nitrogen gas for approximately 1 hour.

The flow was then stopped, a balloon of nitrogen gas was attached over one filter and the other needle was removed. The RBF was placed back in the sterile tissue culture hood and syringes were filled with deoxygenated media. To confirm that the media was effectively deoxygenated, remaining media was decanted into a beaker via syringe and the oxygen level was measured using the Hach HQ40d Multimeter LDO Probe as described in Section 2.4.3.

Chapter 6: Immunofluorescence Staining of Hypoxic Markers in Cells In-Chip

6.1 Introduction

In Chapter 5, it was shown that HepG2/C3A cells can survive under flow in the chip at 21% oxygen and 0% oxygen. In this chapter, the aim was to culture HepG2/C3A cells in the chip under gradients of oxygen and then measure a metabolic marker to show that the cells in the hypoxic areas of the chip behave differently to the cells in the normoxic areas of the chip.

There are many established approaches for investigating and measuring cellular hypoxia *in vitro,* as summarised in a recent review by Godet *et al*.[19] Examples of techniques which involve direct measurements of intracellular oxygen, formation of oxygen dependent protein adducts, measurement of nitroreductase activity and detection of protein targets upregulated by hypoxia are discussed in Sections 6.1.1 - 6.1.4.

The approach chosen for the work in this chapter was to examine expression of two different proteins, HIF-1α and carbonic anhydrase 9 (CAIX), in cells in the chip using immunofluorescence (IF) staining. These markers were selected because HIF-1α accumulates in the nucleus and has a fast response to hypoxia, whereas CAIX is membrane associated and may take longer to accumulate. The hypothesis was that expression of both proteins should increase as oxygen concentration decreases across the chip.

6.1.1 Intracellular Oxygen Measurements

Fluorescent probes can be used to measure the intracellular oxygen concentration, using the same principles as discussed in Section 4.1.2. An oxygen sensitive metal-based complex is added to the cell culture, where it accumulates in the cells by crossing the cell membrane and is then imaged using fluorescence microscopy.

Where oxygen is present, fluorescence is quenched, therefore, higher fluorescence intensity/lifetime is used to identify hypoxic cells.[19,160]

Zhang *et al*. showed that an iridium based complex could be used to identify hypoxic environments of less than 5% oxygen in live *in vitro* cell cultures as shown in Figure 6.1.[160] Cell culture lines tested were Chinese hamster ovary (CHO), human cervical cancer (HeLa), mouse squamous cell carcinoma (SCC-7) and human glioblastoma (U251).

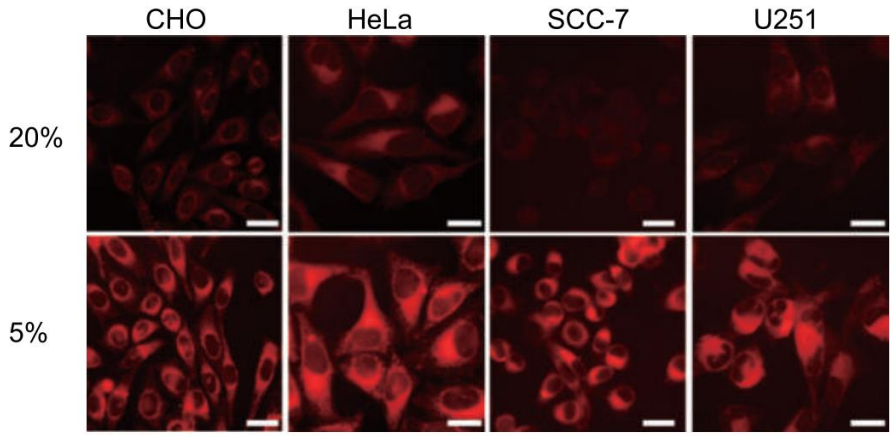

Figure 6.1: Iridium based fluorescent probe in CHO, HeLa, SCC-7 and U251 cells at 20% and 5% oxygen. Reproduced from Zhang et al. with permission from the American Association for Cancer Research.

There is also a commercially available range of intracellular oxygen probes, Image-IT Red and Green Hypoxia Reagents by Invitrogen. The red option is reversibly fluorescent and can be used to image oxygen concentration in real time. The green option is irreversible and fixable such that any cells that have been hypoxic can be identified, even if they become re-oxygenated.[161] Both red and green probes have been shown to be effective for measuring oxygen concentrations of less than 5% in bone (U2OS), lung (A549) and cervical (HeLa) cancer cell lines.[161]

6.1.2 Hypoxia Dependent Protein Adducts

Hypoxyprobe™ is a well-established commercially available product for measuring hypoxia in cells that has been in use for over 20 years.[19] The hypoxia dependent agent is pimonidazole, which enters the cells and becomes reduced (NO_2 to NH_2) when oxygen concentration is low. The reduced pimonidazole can then bind to thiol groups in amino acids via the imidazole ring, as shown in Figure 6.2, and the resulting adduct is stained with a fluorescent antibody.[162]

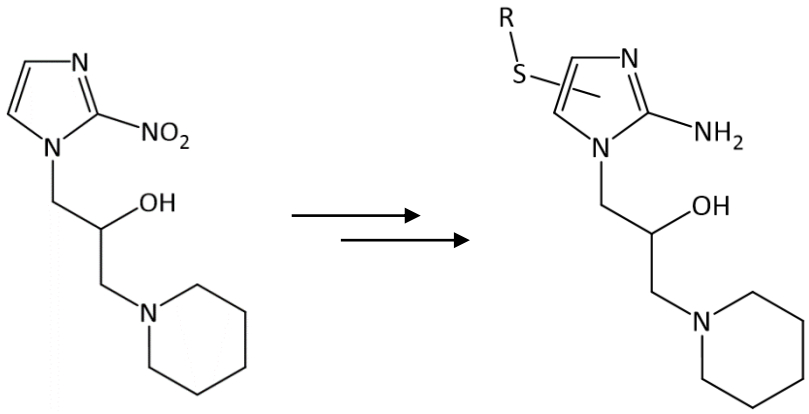

Figure 6.2: Structure of pimonidazole (left) and reduced pimonidazole bound to thiol group (right). R represents amino acid/peptide/protein.[19,162]

Recent examples by Kang *et al.* and Ando *et al.* show Hypoxyprobe™ being used in 2D cultures of primary hepatocytes and human breast cancer cells (MCF-7) respectively.[107,109] Both examples show that Hypoxyprobe™ can identify hypoxia below approximately 1.3% oxygen.[19,107,109]

6.1.3 Nitroreductase Activity Probes

In hypoxic cancer cells, the metabolic switch to glycolysis results in a more reductive intracellular environment and accumulation of nicotinamide adenine dinucleotide (phosphate) NAD(P)H.[163,164] Reductase enzymes, such as nitroreductase, are also upregulated and can catalyse the reduction of nitroaromatic compounds by NAD(P)H.[19,164,165]

Hence, fluorescent probes with nitroaromatic structures have been developed to detect hypoxic cells indirectly. The probes enter the cell in a non-fluorescent form, where they are reduced by nitroreductase and NAD(P)H to generate a fluorescent product in hypoxic cells. Higher fluorescence correlates to increased levels of nitroreductase and a more hypoxic intracellular environment.[19,164,165]

This method has an advantage over the others, as these probes can detect larger ranges of hypoxia and can be used in live cells (as opposed to fixed cells). Fan *et al*. demonstrated the use of a novel probe which detected nitroreductase activity in cervical cancer (HeLa) cells at 1, 5, 10 and 20% oxygen.[166] As expected, nitroreductase activity increased as oxygen concentration decreased, as shown in Figure 6.3.[166]

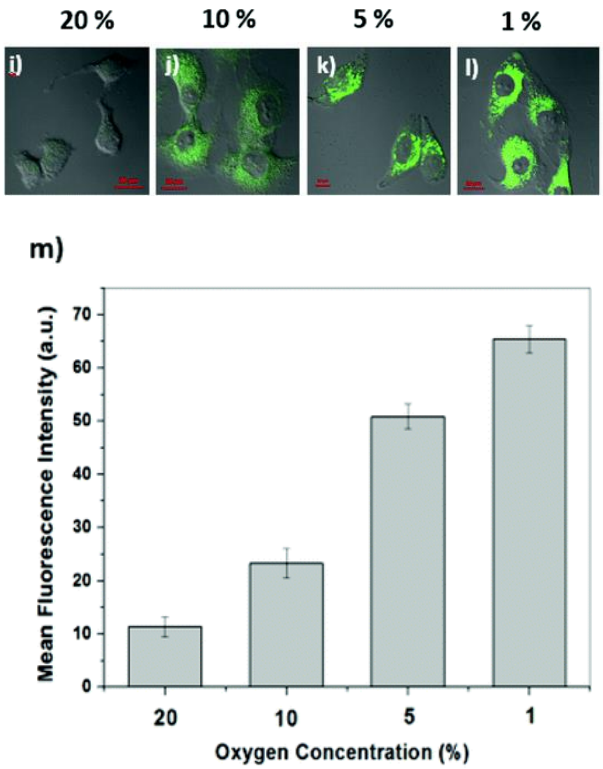

Figure 6.3: HeLa cells stained with a novel nitroreductase probe. Panels I – L show merged fluorescence and bright field images of the cells at 20, 10, 5 and 1% oxygen respectively. Panel M shows the mean fluorescence intensity in each fluorescence image. Reprinted from Fan et al. with permission from the Royal Society of Chemistry.

There is a diverse range of this style of probe presented in the literature and there is also a commercially available nitroreductase sensitive probe, Hypoxia Red, developed by Enzo.[164,167] Jing *et al*. used Hypoxia Red to effectively monitor development of hypoxia in lung cancer cells (A549) over time (6 hours).[164]

6.1.4 HIF-1α and Downstream Protein Targets

As discussed in Section 1.1.3, HIF-1α is stabilised in hypoxic cells resulting in transcription of many downstream protein targets that aid cancer cell survival and tumour growth. Many analytical techniques are available for looking at specific protein levels in cells including western blotting and flow cytometry.[168,169] However, immunofluorescence staining (IF) is a more appropriate technique for examining cells in microfluidic devices because the cells can be fixed (preserved) and stained *in situ* without removing them from the device.

Specific proteins within the cells can be stained by selective fluorescent antibodies, and then imaged using fluorescence microscopy.[170] Expression of the protein of interest can then be correlated to oxygen conditions within the cell. For example, Ando *et al.* used IF staining to observe an increase in GLUT-1 expression in MCF-7 cells cultured in a microfluidic device where hypoxia was generated by cellular consumption of oxygen.[109] Additionally, Kang *et al*. observed an increase in HIF-1α in hepatocytes cultured in a microfluidic device after only 2 hours exposure to hypoxic conditions generated by oxygen scavenging chemicals.[107]

6.1.5 Statistical Analysis

In this chapter, immunofluorescence images of cells stained for HIF-1α or CAIX were acquired. The mean gray values of the cells were analysed and compared when cells were exposed to hypoxic and non-hypoxic conditions. Statistical tests were performed on the data collected to highlight any significant differences between the cells in different environments.

Common methods used to mathematically compare the means of normal (Gaussian) distributions are t-tests (for two distributions) and analysis of variance (ANOVA) (for more than two distributions). ANOVA can identify statistically significant differences within a set of samples, but cannot report on which two samples are statistically different to each other. To do this, post-hoc analysis - usually a Tukey test - is done to compare each pair of samples.[171]

These methods consider the mean, sample size and standard deviation to determine if the distributions being compared are the same or different. Each test assumes a null hypothesis that the distributions are the same. The distributions are mathematically compared and a probability value (p) is reported between 0 and 1. If p is 1, the null hypothesis is true and distributions are considered the same. However, if p falls below a certain threshold, usually 0.05, the hypothesis is rejected and the distributions can be considered statistically different. Another way of phrasing this is if $p < 0.05$, the chance of observing a difference between the means when the distributions are the same is < 5%. So when p is very small, it is more likely that the distributions are truly different and the null hypothesis can be rejected.[171]

ANOVA and t-tests make some assumptions about the data sets, including that the sample sizes are similar and the distributions are Gaussian. However, these assumptions were not always true for the data presented in this chapter. The nonparametric equivalent to a t-test is the Mann-Whitney test and the equivalent to ANOVA with post-hoc Tukey test is the Kruskal-Wallis with post-hoc Dunn's test. These tests use mathematical methods to compare population medians and results are reported as p values. These nonparametric tests work best if the distribution of populations being compared is similar, although they make no assumptions about what that shape is. They are also more appropriate for comparing populations of different sample sizes.[171]

In general, Mann-Whitney and Kruskal-Wallis tests are less statistically powerful compared to t-test and ANOVA, which means that the mathematical methods may

be less effective at identifying true differences. However, they are used for the results presented in this chapter because the basic assumptions are more appropriate for the data sets.[171]

6.2 Results

6.2.1 HIF-1α and CAIX Screen

A short screen was carried out to investigate expression of HIF-1α and CAIX in HepG2/C3A and DU145 cells. It is known that HIF-1α and CAIX are expressed by prostate cancer and hepatocyte cell lines, however, this experiment tested if increases in protein levels could be measured by IF staining after a few hours of exposure to hypoxic conditions.[172–175] The results of this screen were then used to inform which protein to look for to measure a response from the cells cultured under different oxygen conditions in the chip, as discussed in Section 6.2.2.

To do the screen efficiently, cells were cultured on a 96-well plate and exposed to $CoCl_2$ (a hypoxia mimetic) for 3 hours. Treated and untreated samples were then stained for HIF-1α and CAIX and the cells were imaged using fluorescence microscopy as described in Section 6.4. Representative images of HIF-1α stained samples for each cell type are shown in Figure 6.4. One image was taken per sample (three samples per condition and stain) and the mean fluorescence intensity of all the cells in each image was measured using ImageJ. The mean gray values across all images for each conditions were combined into a single histogram, as shown in Figure 6.5. The figure shows that the combined histogram reflects the shape of the distributions from the individual images. The histograms for HepG2 cells and DU145 cells are plotted in Figure 6.6 and Figure 6.7 respectively. Since all of the histograms show a non-Gaussian distribution, Mann-Whitney tests were used to compare treated and untreated sample distributions (Appendix 5).

Both cell types showed an increase in HIF-1α after treatment with $CoCl_2$. However, the MGVs for the HepG2/C3A cells are lower suggesting that in general, HepG2/C3A cells express less HIF-1α than DU145 cells. The HepG2/C3A treated and untreated

cells showed similar CAIX expression over the short period of hypoxia. The untreated DU145 cells showed higher expression of CAIX in the untreated sample compared to the treated sample, which is the opposite of the hypothesised trend.

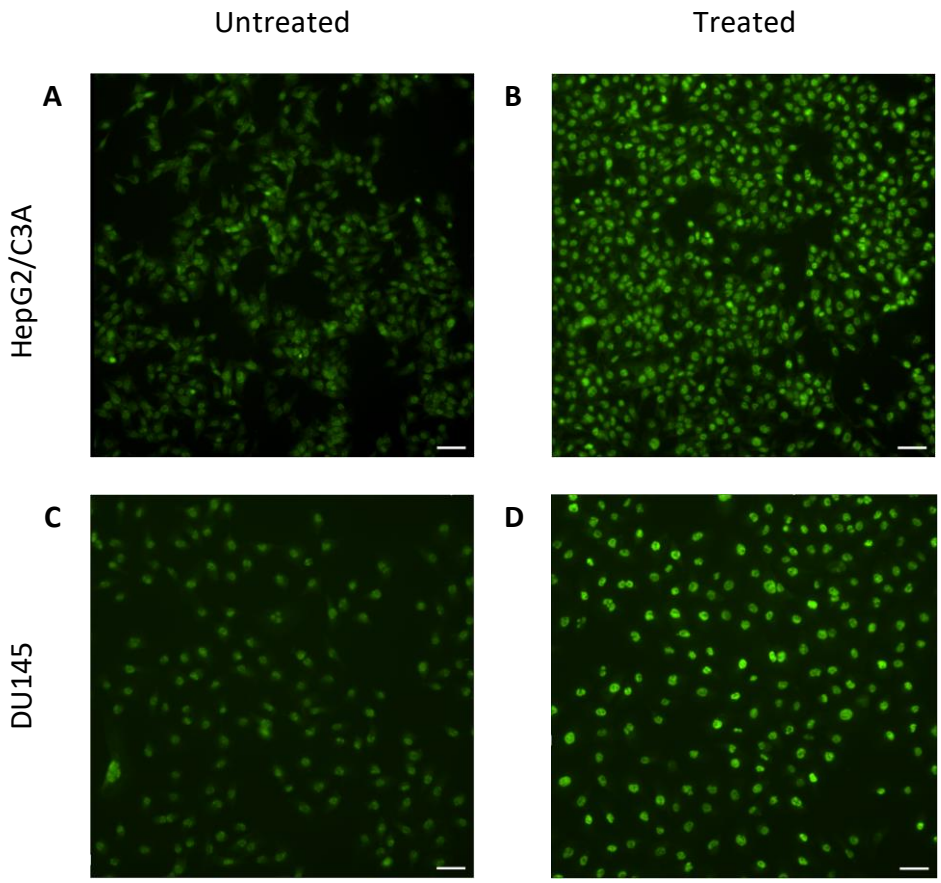

*Figure 6.4: Representative images of HepG2/C3A cells (**A** and **B**) and DU145 cells (**C** and **D**) untreated (**A** and **C**) or treated with 400 µM $CoCl_2$ for 3 hours (**B** and **D**). Scale bar is 50 µm.*

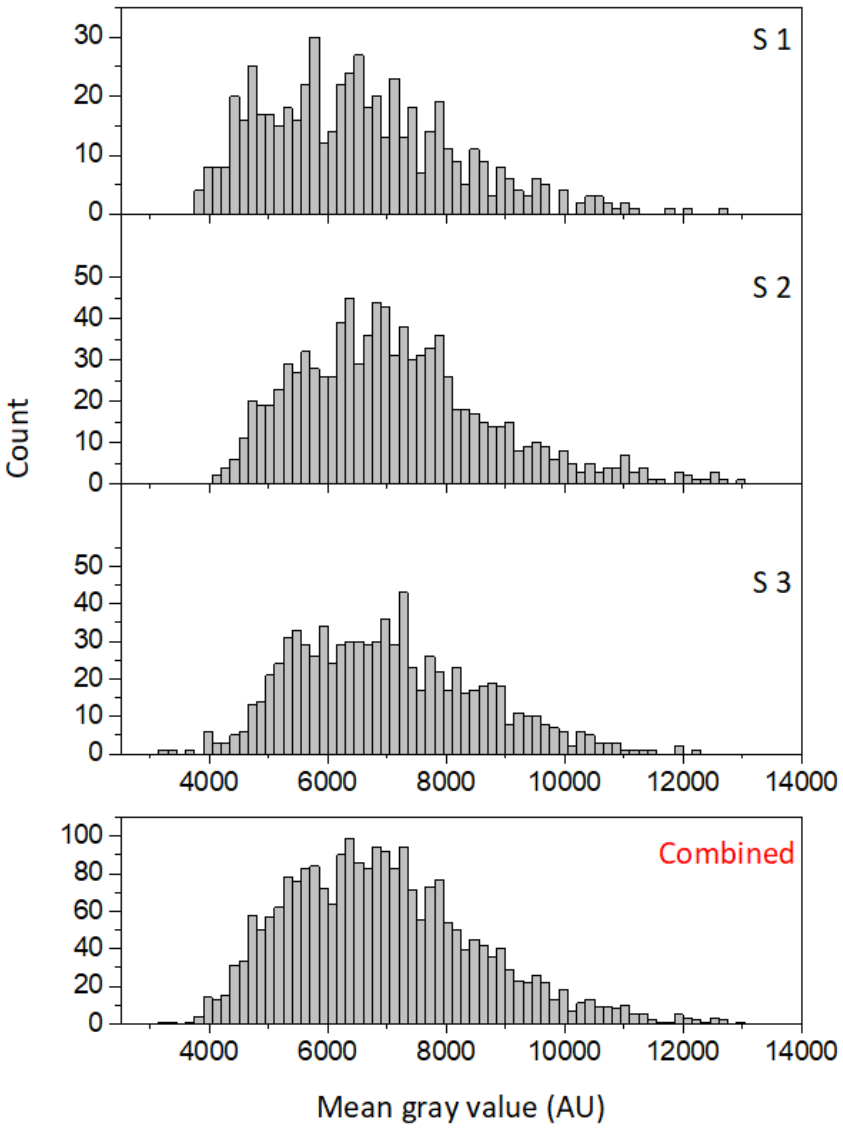

Figure 6.5: Histograms (bin width 150) of cells in three samples (S, one image per sample) and the same three histograms combined into one. All of the histograms show a similar shape, with the peak on the left side of the distribution and a longer tail to the right.

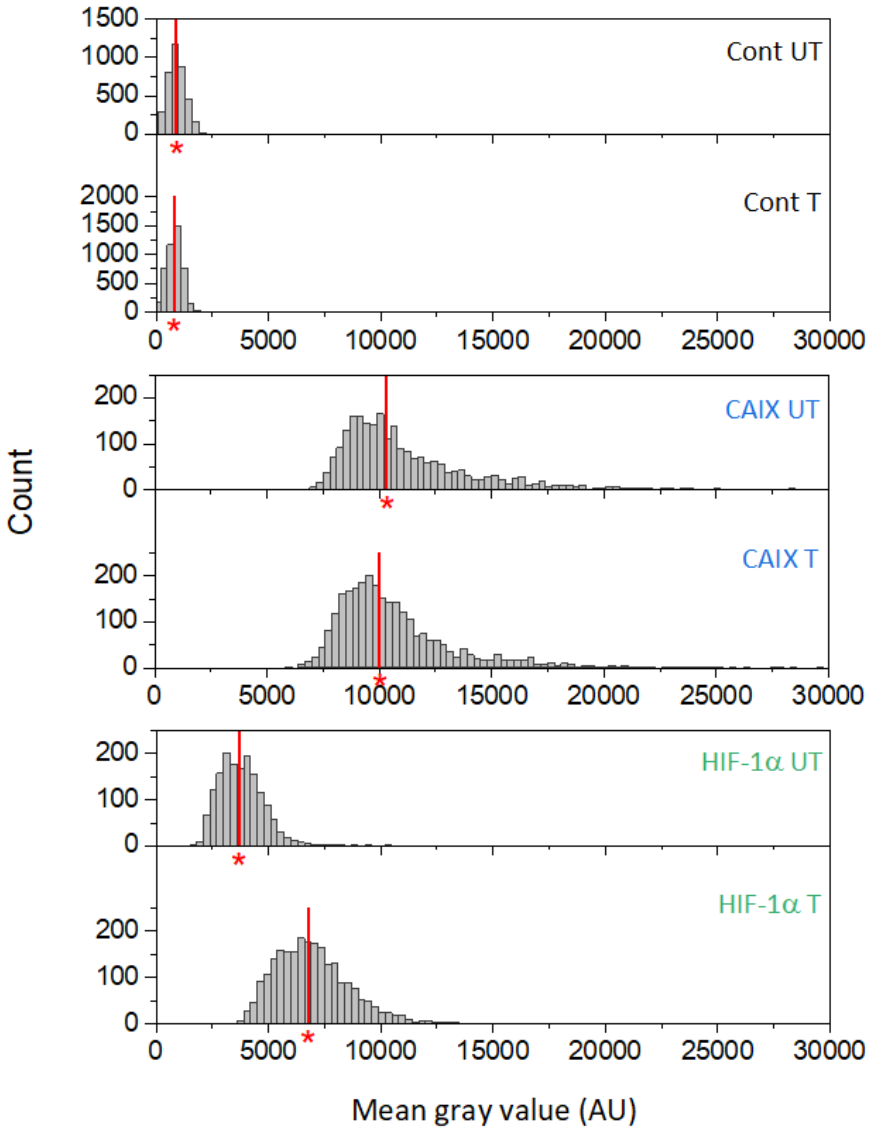

Figure 6.6: Histograms of HepG2/C3A cells treated (T) with 400 µM $CoCl_2$ or untreated (UT) and stained with for HIF-1α or CAIX. Control samples (Cont) were not incubated with a primary antibody but were stained with Alexa Fluor® 488. Histograms (bin width 300) show combined results from three samples, red line labelled with asterisk indicates the median. Differences between each set of treated and untreated distributions were significant ($p < 0.0001$) by a two-tailed Mann-Whitney test. Full statistical results are tabulated in Appendix 5.

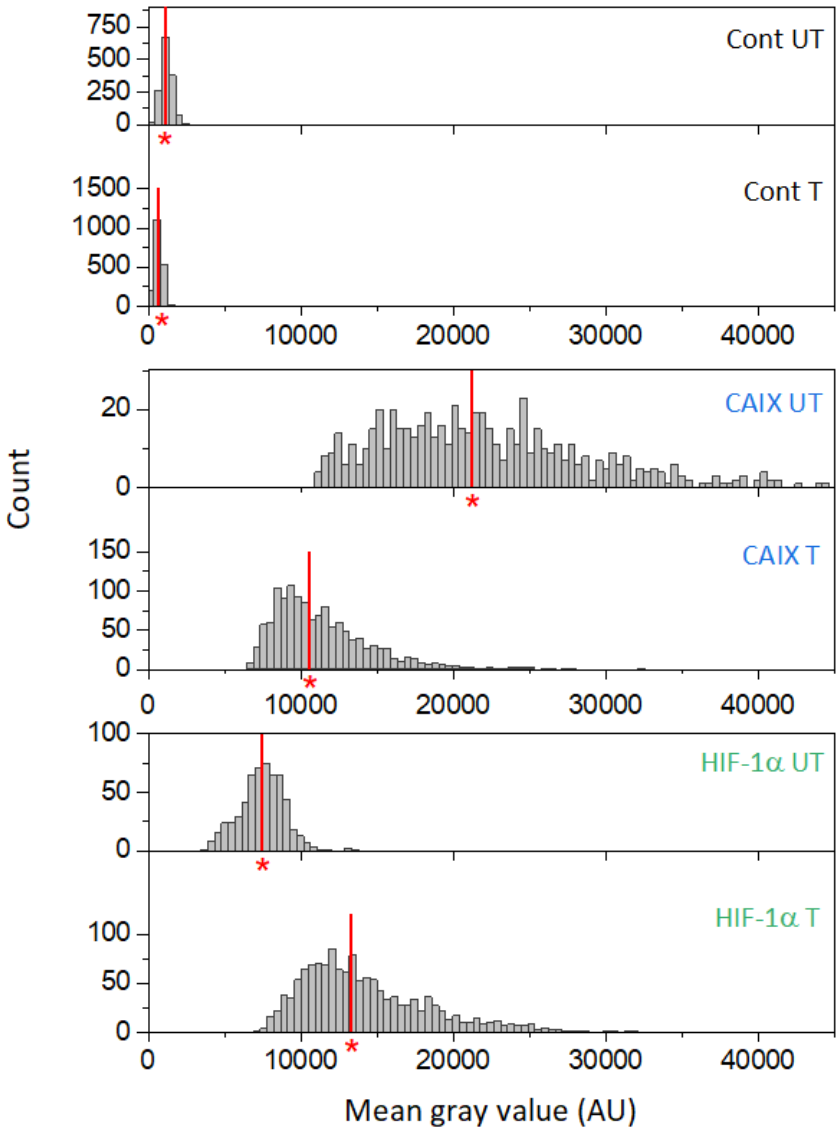

Figure 6.7: Histograms of DU145 cells treated (T) with 400 µM $CoCl_2$ or untreated (UT) and stained with for HIF-1α or CAIX. Control samples (Cont) were not incubated with a primary antibody but were stained with Alexa Fluor® 488. Histograms (bin width 450) show combined results from three samples, red line labelled with asterisk indicates the median. Differences between each set of treated and untreated distributions were significant ($p < 0.0001$) by a two-tailed Mann-Whitney test. Full statistical results are tabulated in Appendix 5.

In the standard IF staining technique, the cell membrane is disrupted (permeabilised) to allow antibodies and staining agents to enter the cell and tag onto the protein of interest. However, CAIX is a membrane-associated protein so it is possible that the protein could become damaged during this step. The screen was repeated but the membrane permeabilisation step of the staining protocol was skipped for a subset of the CAIX samples. The results for the HepG2/C3A and DU145 cells are shown in Figure 6.8 and Figure 6.9 respectively.

The trends for HIF-1α and CAIX expression were reproduced in both cell types. Trends in CAIX expression in both cell types were the same regardless of whether the membrane was permeabilised or not. Since the results showed a reproducible difference in HIF-1α expression between hypoxic and non-hypoxic conditions over 3 hours, HIF-1α was carried forward to study cells in the chip.

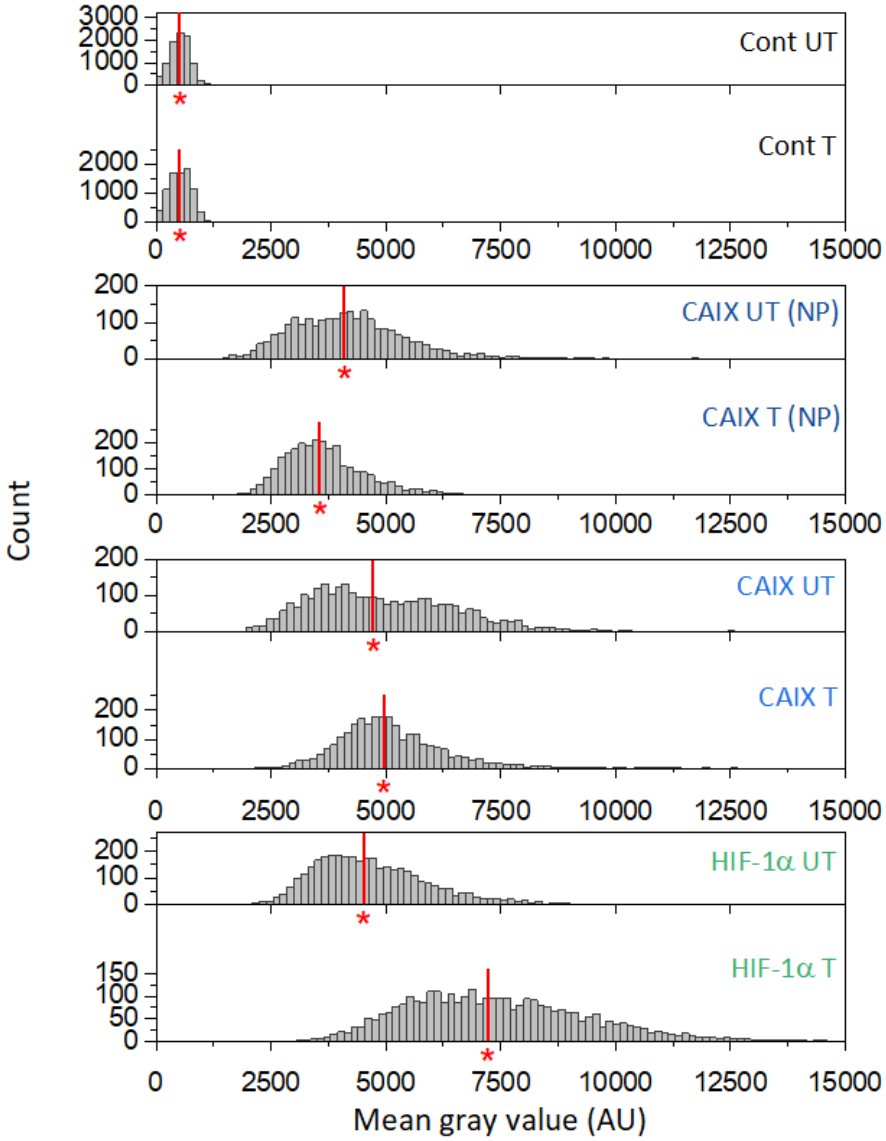

Figure 6.8: Histograms of HepG2/C3A cells treated (T) with 400 µM $CoCl_2$ or untreated (UT) and stained with for HIF-1α or CAIX. For one set of samples stained with CAIX, the cell membranes were not permeabilised (NP). Control samples (Cont) were not incubated with a primary antibody but were stained with Alexa Fluor® 488. Histograms (bin width 150) show combined results from three samples for HIF-1α and two samples for all others, red line labelled with asterisk indicates the median. Differences between each set of treated and untreated distributions were significant ($p < 0.0001$) by a two-tailed Mann-Whitney test. Full statistical results are tabulated in Appendix 5.

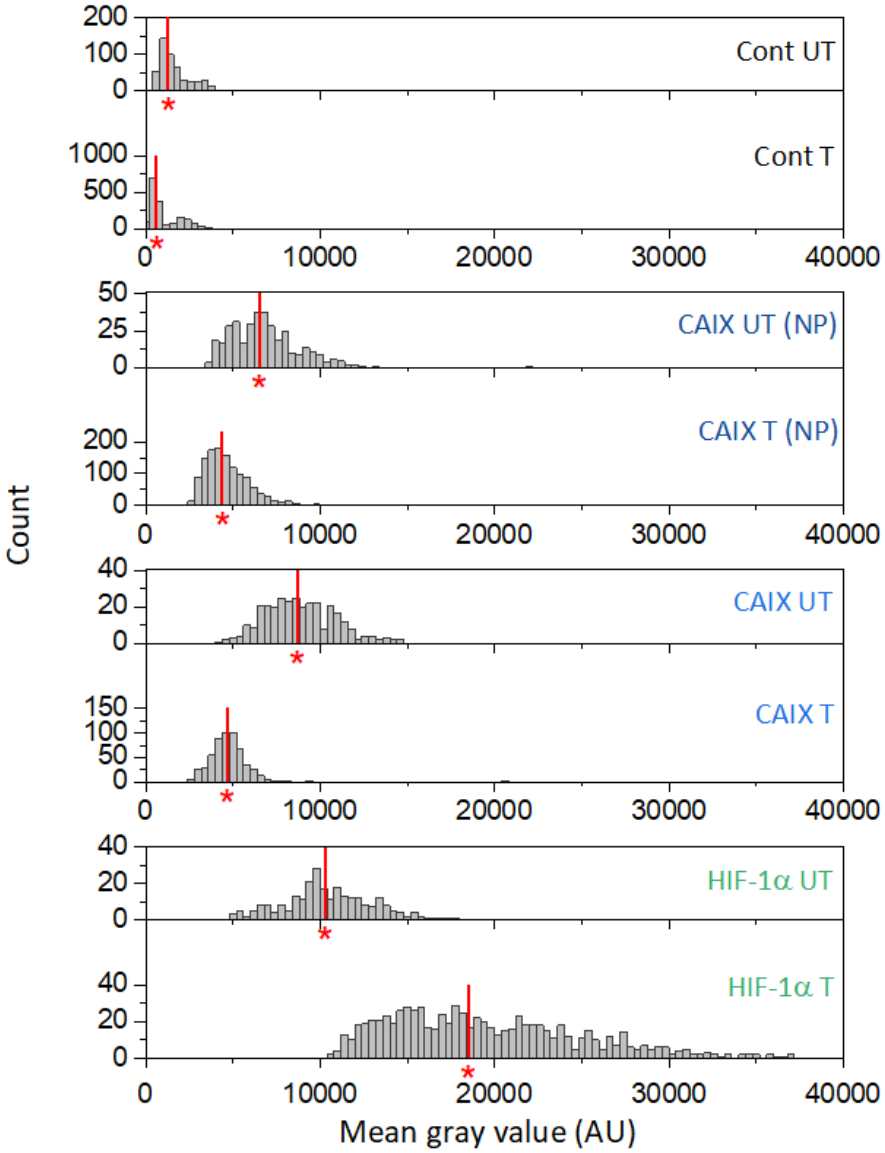

Figure 6.9: Histograms of DU145 cells treated (T) with 400 µM $CoCl_2$ or untreated (UT) and stained with for HIF-1α or CAIX. For one set of samples stained with CAIX, the cell membranes were not permeabilised (NP). Control samples (Cont) were not incubated with a primary antibody but were stained with Alexa Fluor® 488. Histograms (bin width 400) show combined results from three samples for HIF-1α and two samples for all others, red line labelled with asterisk indicates the median. Differences between each set of treated and untreated distributions were significant ($p < 0.0001$) by a two-tailed Mann-Whitney test. Full statistical results are tabulated in Appendix 5.

6.2.2 HIF-1α Expression in HepG2/C3A Cells In-Chip

The experiments discussed so far have shown that it is possible to culture HepG2/C3A cells in the chip under a flow rate of 50 µL/hour for up to 2 days. HepG2/C3A cells also show an increase in HIF-1α in a standard well plate in response to hypoxic conditions imposed by $CoCl_2$. Thus, the aim of the experiments discussed in this section was to grow HepG2/C3A cells in the chip, expose them to a gradient of oxygen and measure a higher HIF-1α expression in cells cultured in areas of the chip with lower oxygen concentration.

Experiment 1

The cells were seeded in the chip as described in Section 5.4.5 and then incubated overnight with a media (CO_2-Ind, 21% oxygen) flow rate of 50 µL/hour at each inlet. Syringes were arranged with oxygenated medium (21% oxygen) feeding into the channel 1 side of the chip and deoxygenated medium (0% oxygen, prepared as described in Section 5.4.6) feeding into the channel 5 side of the chip, as shown in Figure 6.10. The flow rate was set to 50 µL/hour, exposing the cells to the oxygen gradient overnight. The cells were then stained for HIF-1α as described in Sections 6.4.1 and 6.4.4.

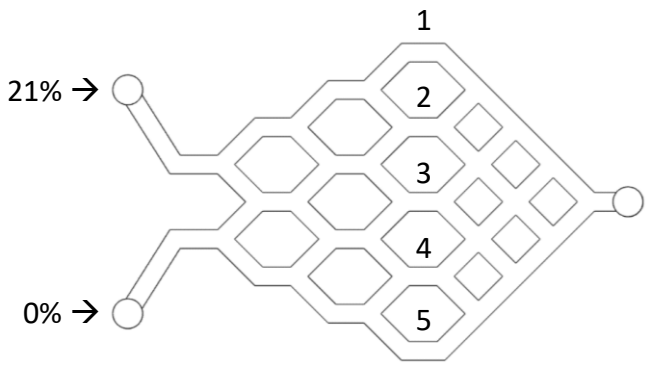

Figure 6.10: Channel network showing inlet arrangement of oxygenated (21% oxygen) and deoxygenated (0% oxygen) media with respect to numbered channels.

Five images of cells were taken in each channel, then the mean fluorescence intensity of every cell was measured using ImageJ. The mean gray values across all images were combined into a single histogram, as shown in Figure 6.11. The figure shows that the combined histogram reflects the shape of the distributions from the individual images. The histograms for each channel are plotted in Figure 6.12. Since all of the histograms show a non-Gaussian distribution, Kruskal-Wallis tests were used to statistically analyse the distributions.

It was expected that as hypoxia increased from channel 1 through to channel 5 the expression of HIF-1α would increase. The results do generally show this trend. The median MGV increases from channel 1 to 5 indicating increased expression of HIF-1α with the exception of channel 3. The Kruskal-Wallis and post-hoc Dunn's test indicated a significant difference between the distributions in channels 1 and 5, which suggests that the cells may be responding to the different levels of oxygen. However, the unexplained dip in the trend in channel 3 and the relatively small differences between the median MGVs with respect to the range of the distributions indicates that the results may be down to chance.

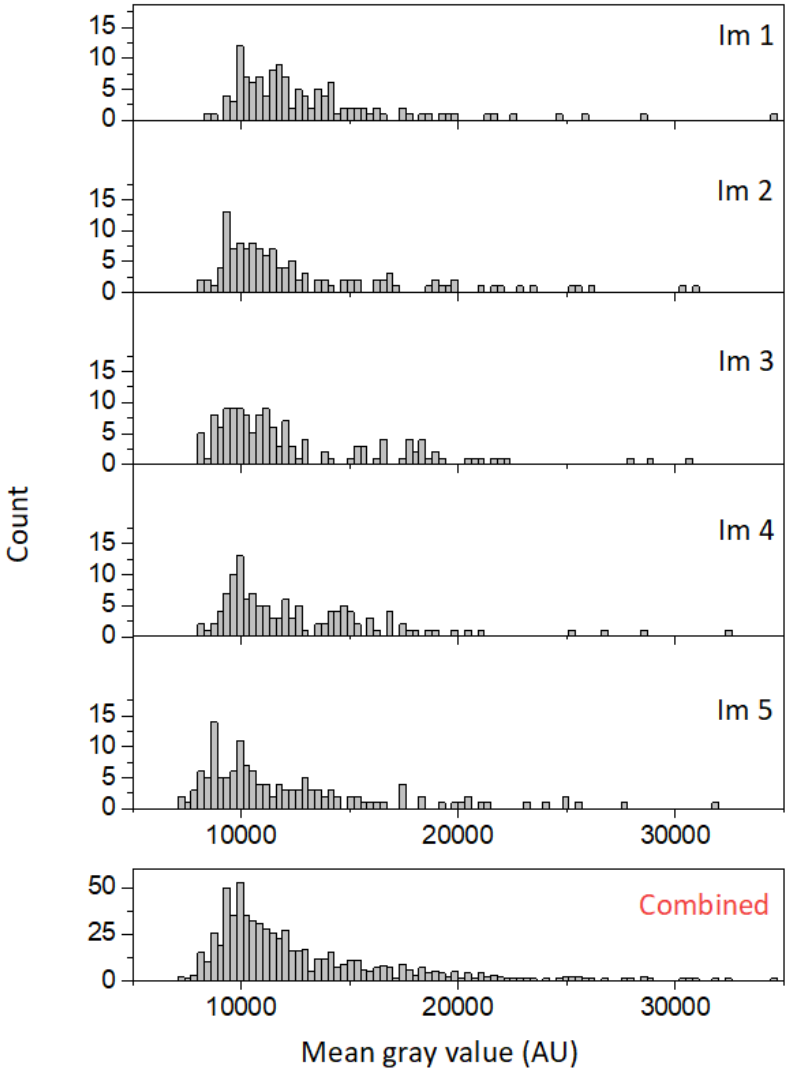

Figure 6.11: Histograms (bin width 300) of cells in five images (Im) of channel 1 and the same five histograms combined into one. All of the histograms show a similar shape, with the peak on the left side of the distribution and a longer tail to the right.

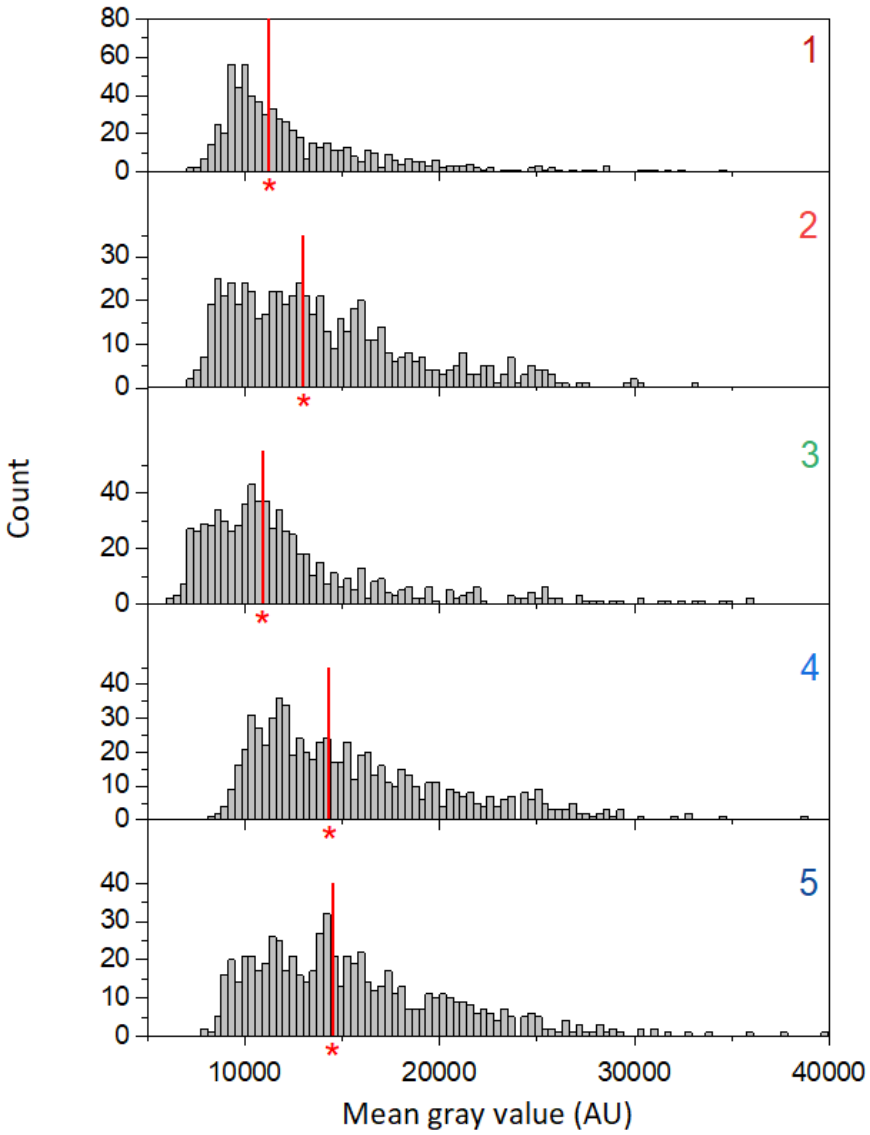

Figure 6.12: HIF-1α expression in HepG2/C3A cells cultured in the chip and exposed to an oxygen gradient for 24 hours. Images were taken with 5 s exposure and 80% light power. Histograms (bin width 350) show combined results from five images per channel, red line labelled with asterisk indicates the median. Differences between all channels were statistically significant ($p < 0.05$) except for differences between channels 1 and 3 and channels 4 and 5. Full statistical results are tabulated in Appendix 6.

Experiment 2

Experiment 1 was repeated but the cells in the chip were exposed to a gradient of $CoCl_2$ instead of a gradient of oxygen. It was thought that the $CoCl_2$ gradient may result in a larger difference in HIF-1α in cells across the chip since it has been shown to work in the well plate control experiments.

The experimental process was the same as for Experiment 1 except the deoxygenated medium was replaced with medium supplemented with 100 µM $CoCl_2$. A well plate control experiment was conducted to show that HepG2/C3A cells experience an increase in HIF-1α after incubation with 100 µM $CoCl_2$ overnight, as discussed in Appendix 4. The results, shown in Figure 6.13, show higher median MGVs for channels 1 and 2 compared to channels 3, 4 and 5. The results suggest that the cells in channel 1 (0 µM $CoCl_2$) show higher expression of HIF-1α compared to the cells in channel 5 (100 µM $CoCl_2$). The difference was statistically significant ($p = 0.014$), however, it contradicts the hypothesised result that cells in more hypoxic regions (higher $CoCl_2$) would show higher HIF-1α expression.

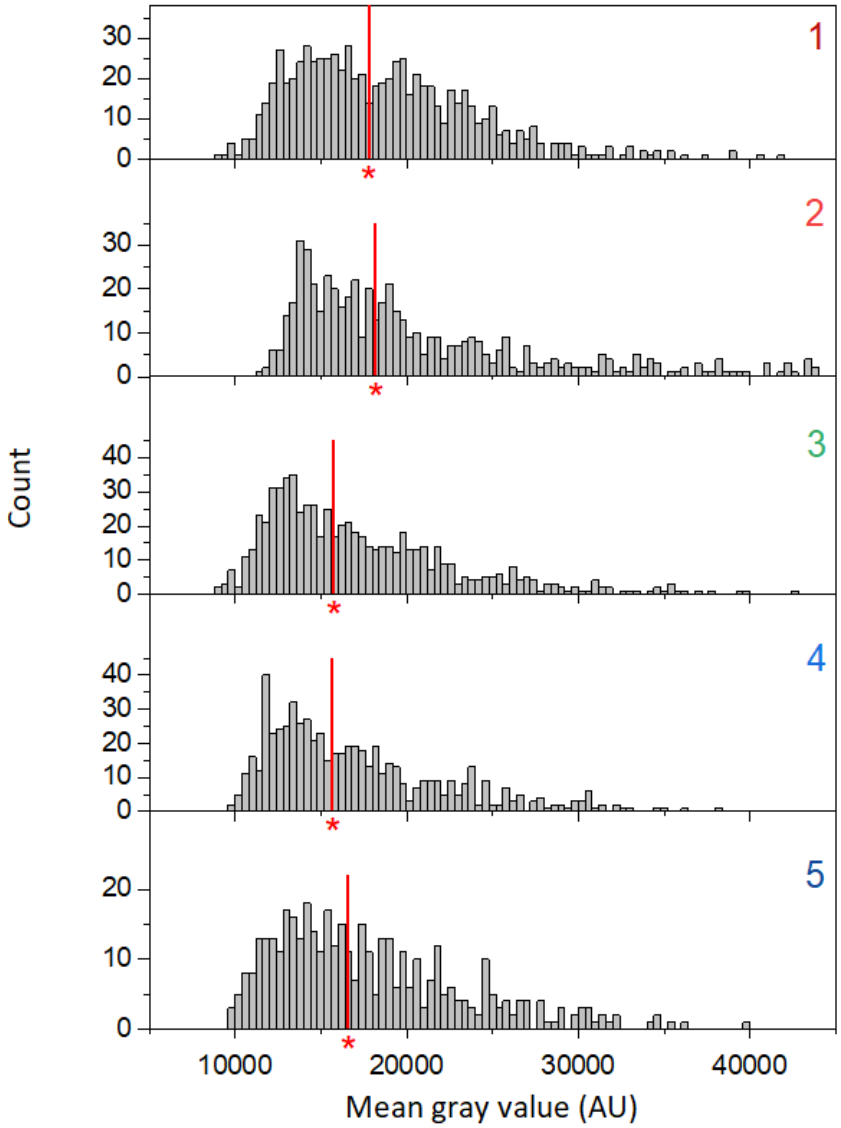

Figure 6.13: HIF-1α expression in HepG2/C3A cells cultured in the chip and exposed to a gradient of 0 µM (channel 1) - 100 µM $CoCl_2$ (channel 5) for 24 hours. Images were taken with 5 s exposure and 80% light power. Histograms (bin width 400) show combined results from five images per channel, red line labelled with asterisk indicates the median. Differences between all channels were statistically significant ($p < 0.05$) except for differences between channels 3, 4 and 5. Full statistical results are tabulated in Appendix 6.

One potential reason that the differences between channels are small and the trends are not as expected is that the cells are experiencing shear stress, which is causing an increase in HIF-1α unrelated to the hypoxic conditions. It may be possible that the cells do experience an increase in HIF-1α as a result of low oxygen or $CoCl_2$, but that this increase is small compared to the increase in HIF-1α as a result of shear stress Therefore, the difference in HIF-1α due to oxygen concentration is overwhelmed by the increase due to shear stress.

As discussed in Chapter 3 (Section 3.3 and Appendix 2), channels 1 and 5 experience the lowest shear stress (0.0028 dyn/cm^2) followed by channels 2 and 4 (0.0055 dyn/cm^2) and channel 3 (0.0065 dyn/cm^2). So, if the hypothesis that shear stress increases HIF-1α is true, a trend with a peak in HIF-1α expression for channel 3 would be expected, but this is not observed. Perhaps the variation in shear stress between the channels is insignificant – given that the values are all of the same order of magnitude – compared to the average level of shear stress experienced across the chip.

Feng *et al*. and Wu *et al*. have reported an increase in HIF-1α in human endothelial cells as a result of shear stress, but no reports of this occurring in cancer cells were found in literature over the course of this project.[176,177]

Experiment 3

In this experiment, the time that the cells were exposed to flow was reduced to minimise exposure to shear stress. Also, an additional protein coating was added on top of the cells to try to give them extra protection from the flow. The cells were coated with Geltrex™, which is a basement membrane matrix that contains proteins commonly found in the ECM including collagen, laminin and entactin.[178] Rather than incubating the cells overnight with the flow, the cells were then exposed to a gradient of $CoCl_2$ for 3 hours directly after seeding and coating with protein. The $CoCl_2$ concentration was increased from 100 µM to 400 µM so that the concentration and

time of exposure matched the conditions used for the screening experiments discussed in Section 6.2.1.

The cells were seeded as before, and after 3 hours, the channels were filled with a solution of 0.3 mg/mL Geltrex^{TM} in CO_2-Ind media. The cells were incubated for a further 1 hour to allow the proteins to settle into a thin layer on top of the seeded cells. As in Experiment 2, normal CO_2-Ind medium was inserted via the inlet close to the channel 1 side of the chip and medium supplemented with 400 µM was inserted via the inlet close to the channel 5 side of the chip. The flow was set to 50 µL/hour at both inlets, exposing the cells to the gradient for 3 hours before fixing, staining for HIF-1α and imaging.

The results are shown in Figure 6.14 and this time there is a slight increase in MGV from channel 1 (0 µM $CoCl_2$) to channel 5 (100 µM $CoCl_2$), indicating the cells in channel 5 have higher HIF-1α expression than the cells in channel 1. Differences between all channels were significantly different ($p < 0.0001$) except differences between channels 1 and 2 and channel 4 and 5. The results follow the expected trend, however, the difference is still relatively small compared to the range of the distributions, so this result could still be down to chance. The results suggest that reducing the amount of time the cells are exposed to flow and coating them with extra protein could be helpful for identifying differences in expression of HIF-1α due to hypoxic conditions.

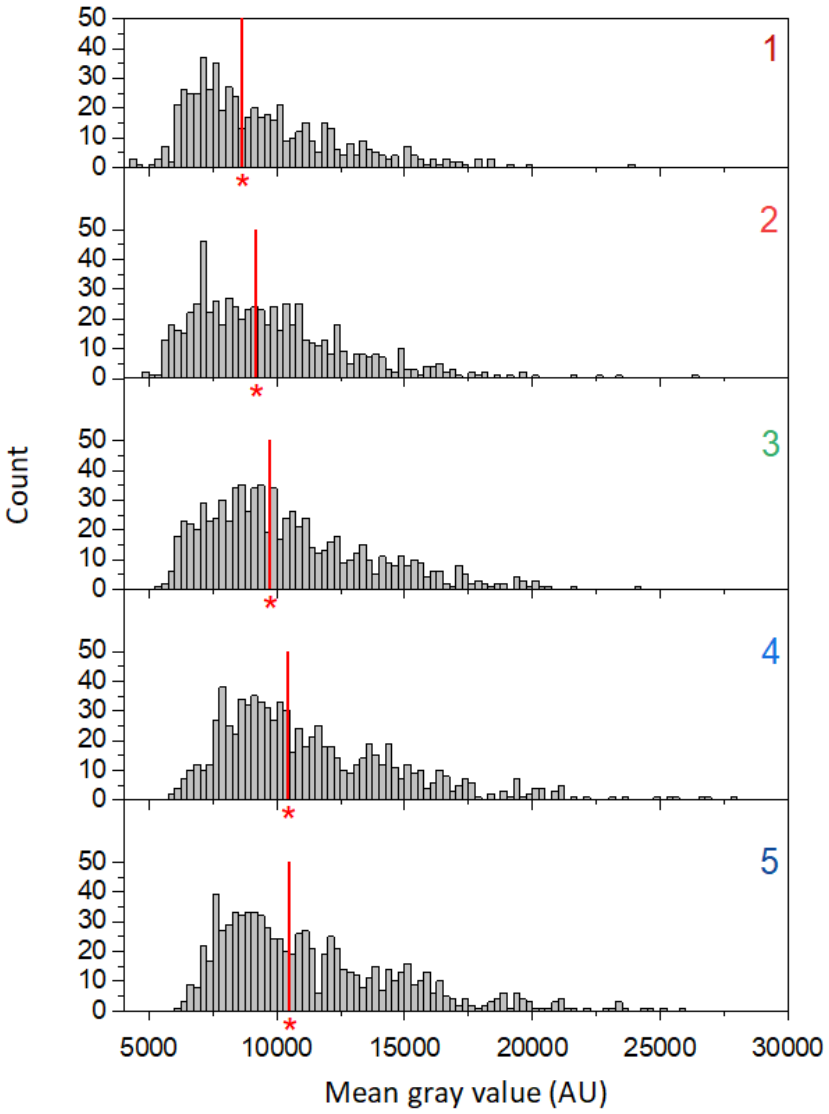

Figure 6.14: HIF-1α expression in HepG2/C3A cells cultured in the chip and exposed to a gradient of 0 µM (channel 1) - 400 µM $CoCl_2$ (channel 5) for 3 hours. Images were taken with 5 s exposure and 10% light power. Histograms (bin width 250) show combined results from five images per channel, red line labelled with asterisk indicates the median. Differences between all channels were statistically significant ($p < 0.0001$) except for differences between channels 1 and 2 and channels 4 and 5. Full statistical results are tabulated in Appendix 6.

Experiment 4

To build on the conclusions from Experiment 3 and try to increase the difference between the hypoxic and non-hypoxic regions of the chip, the time that cells were exposed to flow in this experiment was reduced further from 3 hours to 1.5 hours. The cells were seeded in the same way as described for Experiment 3 with the 0.3 mg/mL Geltrex^{TM} coating. The gradient was set up with 0 µM $CoCl_2$ feeding into the channel 1 side and 400 µM $CoCl_2$ feeding into the channel 5 side of the chip.

It was expected that the cells in channels 4 and 5 exposed to higher concentration of $CoCl_2$ would have higher expression of HIF-1α than cells in channels 1 and 2 where the concentration of $CoCl_2$ is zero. However, the results in Figure 6.15 show the opposite, with channels 1 and 2 showing slightly higher median MGVs than cells in channels 4 and 5.

This experiment concludes that reducing the time that the cells are exposed to media flow was not helpful for increasing the difference in expression of HIF-1α in cells across the $CoCl_2$ gradient in the chip. It is possible that the expected trend in HIF-1α expression was not observed here because the time of exposure to the gradient was reduced too far. The cells may require 3 hours as a minimum, as used in well plate experiment and Experiment 3, to respond to hypoxic conditions and significantly increase levels of HIF-1α.

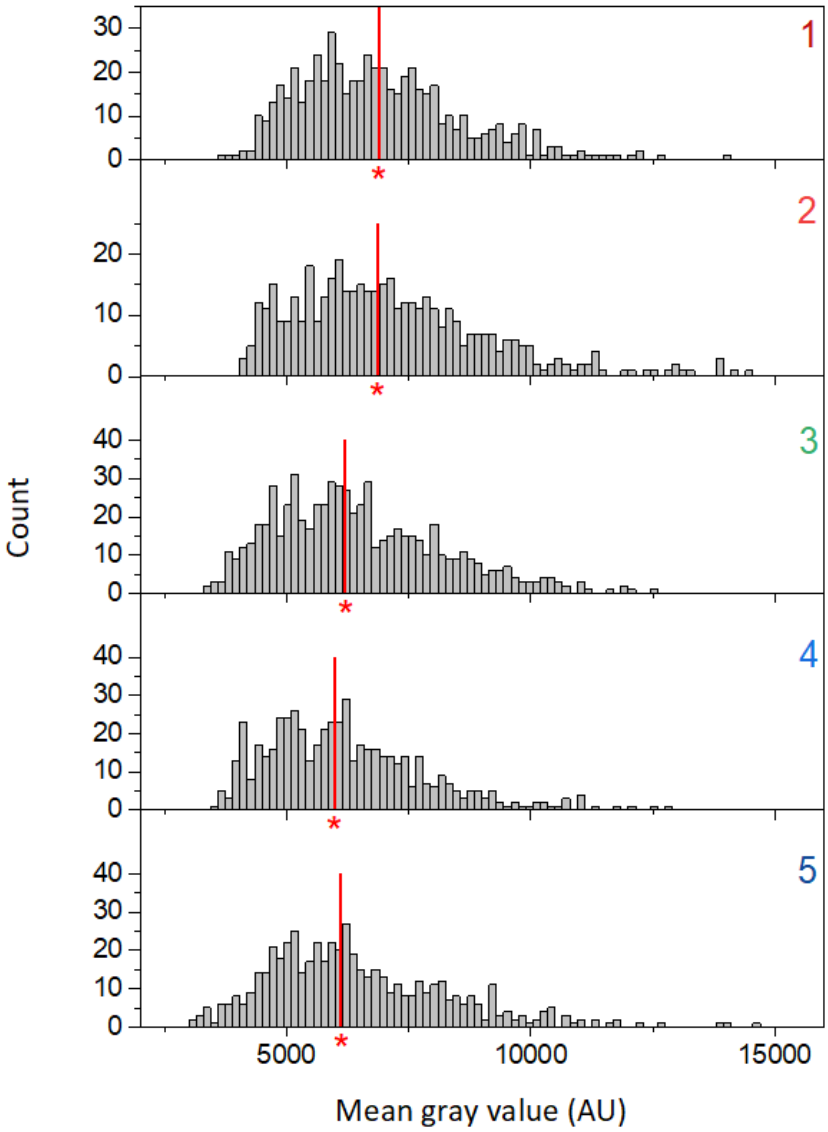

Figure 6.15: HIF-1α expression in HepG2/C3A cells cultured in the chip and exposed to a gradient of 0 µM (channel 1) - 400 µM $CoCl_2$ (channel 5) for 1.5 hours. Images were taken with 5 s exposure and 10% light power. Histograms (bin width 150) show combined results from five images per channel, red line labelled with asterisk indicates the median. Differences between channels 1 and 2 and channels 3, 4 and 5 were not significant. Differences between channels 1 or 2 and channels 3, 4 or 5 were significant ($p < 0.0001$). Full statistical results are tabulated in Appendix 6.

Interestingly, these results do support the hypotheses that exposure to shear stress increases HIF-1α expression in HepG2/C3A cells. The cells in Experiment 3 were exposed to 50 µL/hour flow for 3 hours and showed median MGVs of around 9000 – 11,000, whereas the cells in Experiment 4 were exposed to 50 µL/hour flow for 1.5 hours and showed medain MGVs of around 6000 – 7000. So it appears that reducing the time that cells are exposed to flow may reduce HIF-1α expression produced as a response to shear stress. Unfortunately, these experiments cannot be directly compared to Experiments 1 and 2 because the light power used for imaging was higher. There may be contributions to the MGV in Experiments 1 and 2 from the longer exposure to flow but also the higher light power used for imaging.

Experiment 5

In this experiment the time that cells were exposed to the flow was increased back to 3 hours, but the flow rate was reduced from 50 µL/hour to 30 µL/hour. The experimental set up was consistent with those described for Experiments 3 and 4 with the Geltrex^{TM} coating and 400 µM $CoCl_2$ gradient.

The results in Figure 6.16 show a similar trend to Experiment 4, with the median MGVs in channels 4 and 5 slightly lower than the median MGVs in channels 1, 2 and 3. Again, this is the opposite of the anticipated trend and the reason, if not chance, is unclear. The largest difference in median MGV between the channels in this experiment and in Experiment 3 – which did show an increase in median MGV from channel 1 to channel 5 – is approximately 2000 units. So, if the results of this experiment are down to chance, then it is also likely that the trend observed in Experiment 3 is down to chance even though it agreed with the hypothesised trend.

The median MGVs over the experiment range from around 7500 – 9500, which overlaps with ranges reported for Experiment 3 (50 µL/hour, 3 hours, median MGVs 9500 – 11,000) and Experiment 4 (50 µL/hour, 1.5 hours, median MGVs 6000 – 7000). It was expected that the reduction in flow rate would reduce levels of shear stress in the chip and that, if the hypotheses that shear stress increases HIF-1α expression is

true, then median MGVs in this experiment would be lower than those for Experiment 3 at 50 µL/hour. The values are slightly lower, but reducing the time that cells were exposed to flow appeared to have a larger impact than reducing the flow rate.

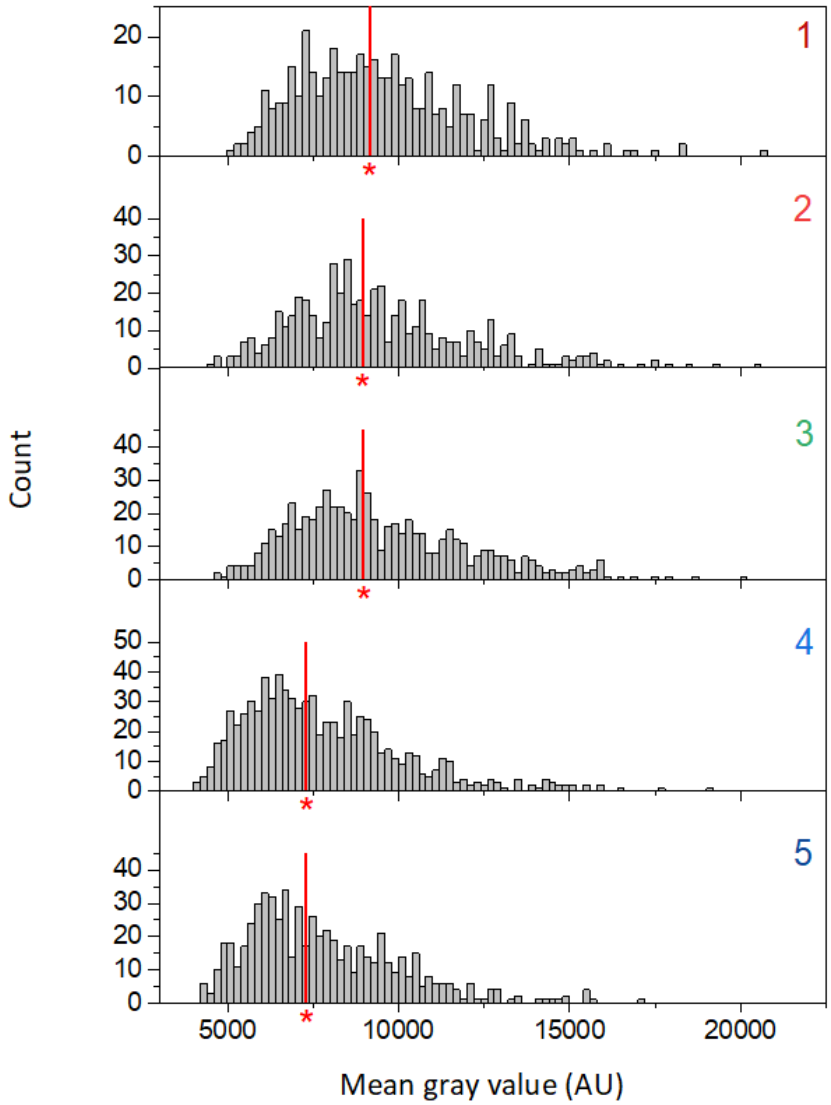

Figure 6.16: HIF-1α expression in HepG2/C3A cells cultured in the chip and exposed to a gradient of 0 µM (channel 1) - 400 µM $CoCl_2$ (channel 5) for 3 hours with flow rate of 30 µL/hour. Images were taken with 5 s exposure and 10% light power. Histograms (bin width 200) show combined results from five images per channel, red line labelled with asterisk indicates the median. Differences between channels 1, 2 and 3 and channels 4 and 5 were not significant. Differences between channels 1, 2 or 3 and

channels 4 or 5 were significant ($p < 0.0001$). Full statistical results are tabulated in Appendix 6.

Experiment 6

To further study the impact that media flow was having on cells in the chip, the next experiment was to culture cells in the chip but without any flow. Cells were seeded in 4 individual chips and coated with Geltrex™ as described previously but without any inlet tubing. A pipette was used to transfer solutions into the channels and luer lock stoppers were used to seal the chip. After seeding and protein coating, the medium was replaced in all chips but the medium for two chips was supplemented with 400 µM $CoCl_2$. The chips were then incubated for 3 hours, as shown in Figure 6.17, before fixing, staining for HIF-1α and imaging. Since this experiment did not require any flow, it was also completed with DU145 cells (seeding density 2.3×10^6 cells/mL) for comparison. It was expected that cells in chips with $CoCl_2$ would show higher HIF-1α expression than those in chips without $CoCl_2$.

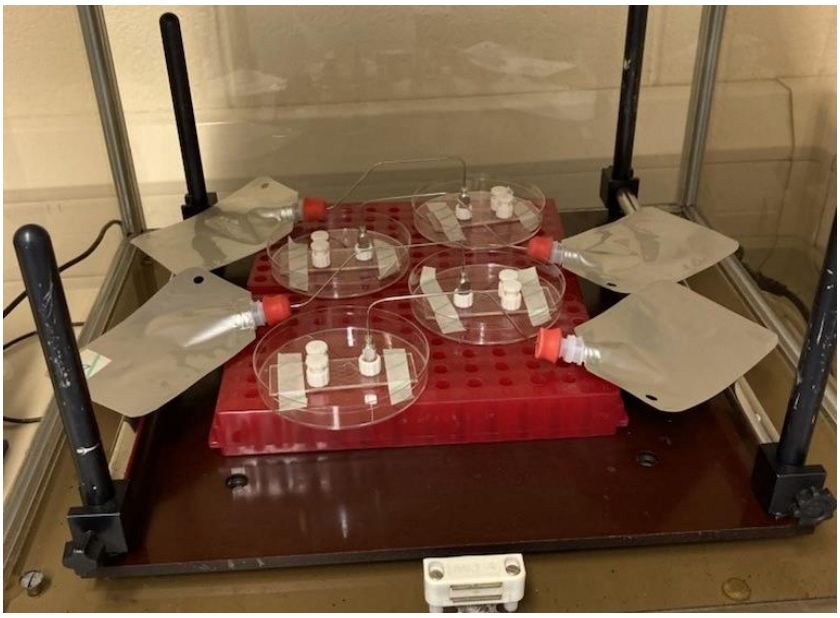

Figure 6.17: Image of 4 chips in a cell culture incubator with inlets sealed with luer lock stoppers and outlet connected to foil pouch via stainless steel needle.

The results for HepG2/C3A and DU145 cells are shown in Figure 6.18 and Figure 6.19 respectively. The median and range are plotted for each channel in multiple chips on the same graph to make visual comparison between the chips easier. Full histograms for each channel are shown in Appendix 7. In well plate experiments, both cell types had shown an increase in HIF-1α when treated with $CoCl_2$, however, here the cells show similar levels of HIF-1α expression in chips with and without $CoCl_2$. This may be because the cells in the chips without $CoCl_2$ also experience hypoxia during the 3-hour incubation due to depletion of oxygen from the available media by cellular consumption.

In the example by Ando *et al.* (Figure 3.2 and Figure 4.3), breast cancer cells consumed oxygen quickly such that a hypoxic environment was created within only 10 minutes of culture in the device.[109] Hepatocyte cell lines are also known consume oxygen quickly due to their high metabolic rate.[179] Zirath *et al.* showed that lung cancer cells consume oxygen from available media over 3 hours when the cell density is high.[134] However, when cell density is lower, oxygen depletion is less severe.[134] So if this experiment was to be repeated, it may be more successful to seed the cells at a much lower density to prevent cells in the 'non-hypoxic' chips from experiencing hypoxia.

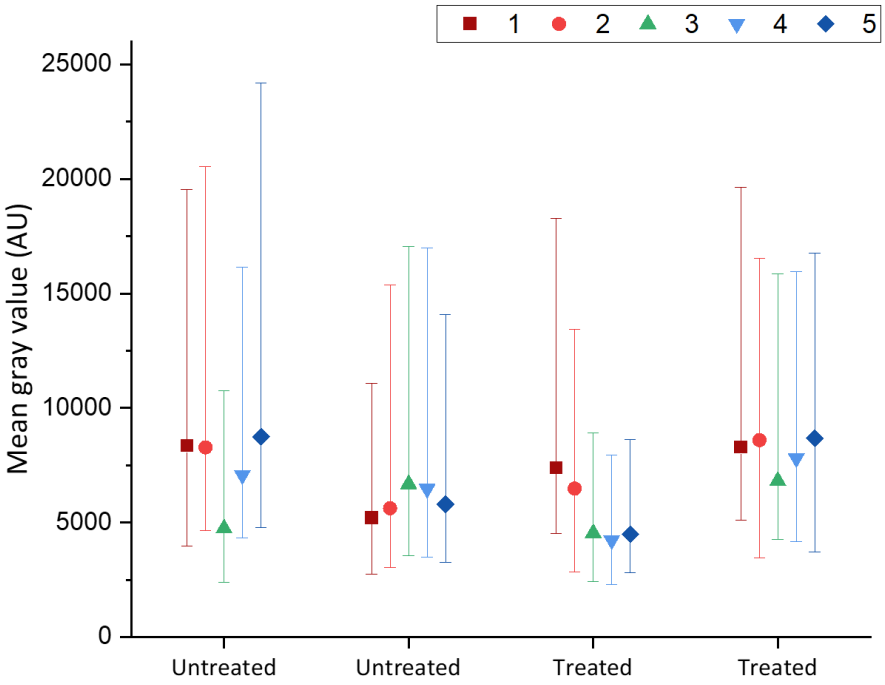

Figure 6.18: HIF-1α expression in HepG2/C3A cells in chips without media flow. Chips were incubated with media (untreated) or media supplemented with 400 µM $CoCl_2$ media for 3 hours (treated). Images were taken with 5 s exposure and 10% light power. Each data point shows the median and range of three combined images per channel, full histograms are shown in Appendix 7. Full statistical results for each chip are tabulated in Appendix 6.

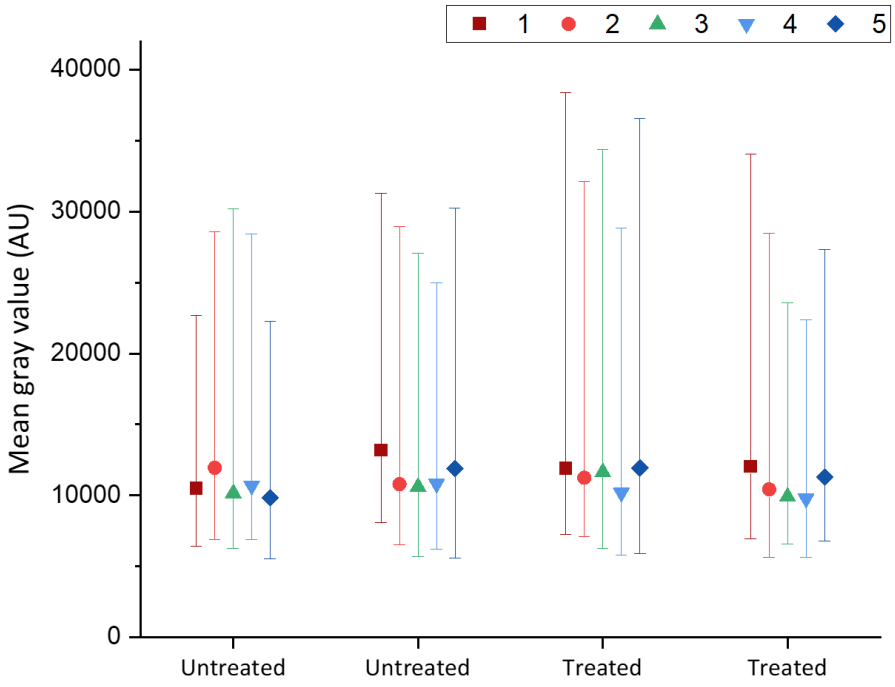

Figure 6.19: HIF-1α expression in DU145 cells in chips without media flow. Chips were incubated with media (untreated) or media supplemented with 400 µM $CoCl_2$ media for 3 hours (treated). Images were taken with 5 s exposure and 10% light power. Each data point shows the median and range of three combined images per channel, full histograms are shown in Appendix 7. Full statistical results for each chip are tabulated in Appendix 6.

The intention for this experiment was for the cells in each chip to show consistent HIF-1α across all channels, since there were no oxygen/$CoCl_2$ gradients or media flow involved. However, the results show a high degree of variability in HIF-1α expression in HepG2/C3A cells. The trends in HIF-1α expression across channels 1 – 5 varies between each chip and in each pair of untreated and treated chips, there is one chip with a slightly higher range of MGVs than the other. The variability observed here confirms that any trends observed in previous experiments are likely not real and produced by chance.

Experiments 7 and 8

These final two experiments continued to investigate the effects of flow on HIF-1α expression in HepG2/C3A cells by increasing the flow rate to 100 µL/hour (Experiment 7) and 150 µL/hour (Experiment 8). The cells were seeded with Geltrex™ as described previously and then the cells were exposed to flow of CO_2-Ind medium (21% oxygen and no $CoCl_2$) from both syringes for 3 hours. Results at 100 µL/hour and 150 µL/hour are shown in Figure 6.20 and Figure 6.21 respectively.

Since there were no oxygen or $CoCl_2$ gradients used in this experiment, MGVs should be consistent across the channels. However, even at high flow rates with no gradients, variability in median MGV between the channel is still observed. The unpredictable nature of the trends throughout the experiments could be down to chance, or due to a subtle experimental feature, such as slight variation between individual chips.

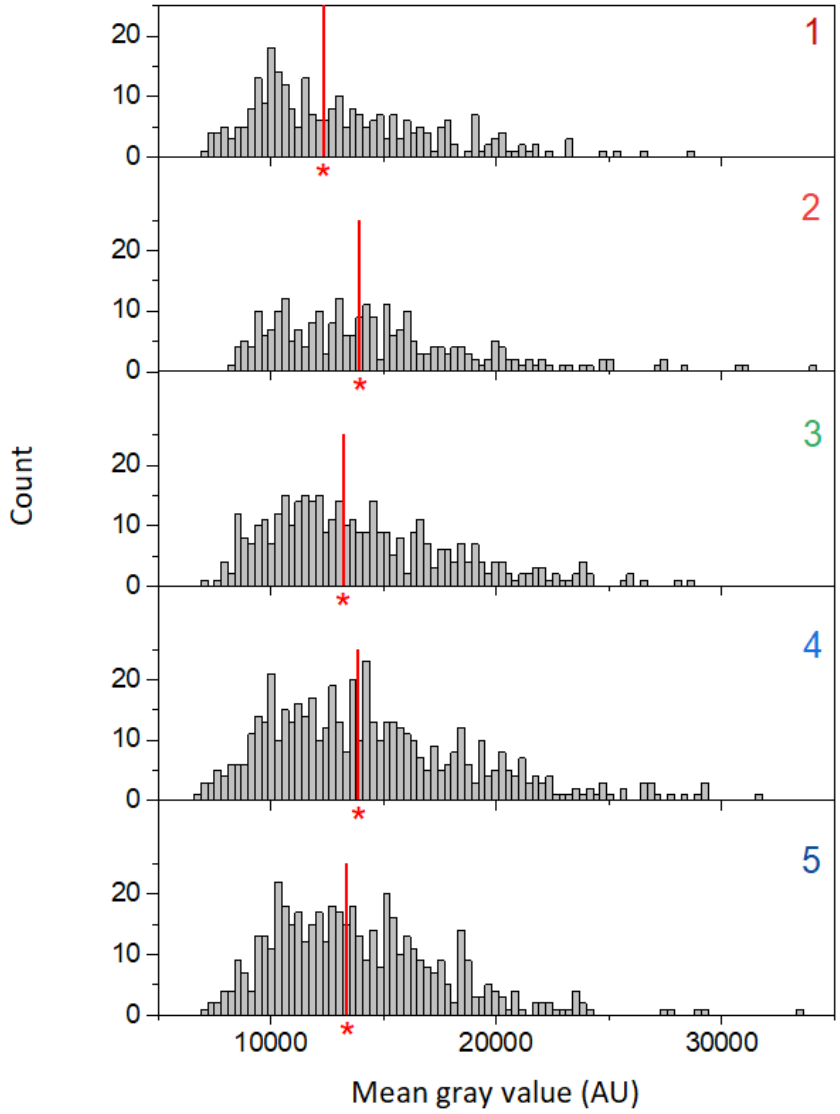

Figure 6.20: HIF-1α expression in HepG2/C3A cells cultured in chips and exposed to flow rates of 100 µL/hour at each inlet for 3 hours with normal CO_2-Ind medium and no gradient. Images were taken with 5 s exposure and 10% light power. Histograms (bin width 300) show combined results from three images per channel, red line labelled with asterisk indicates the median. Full statistical results for each chip are tabulated in Appendix 6.

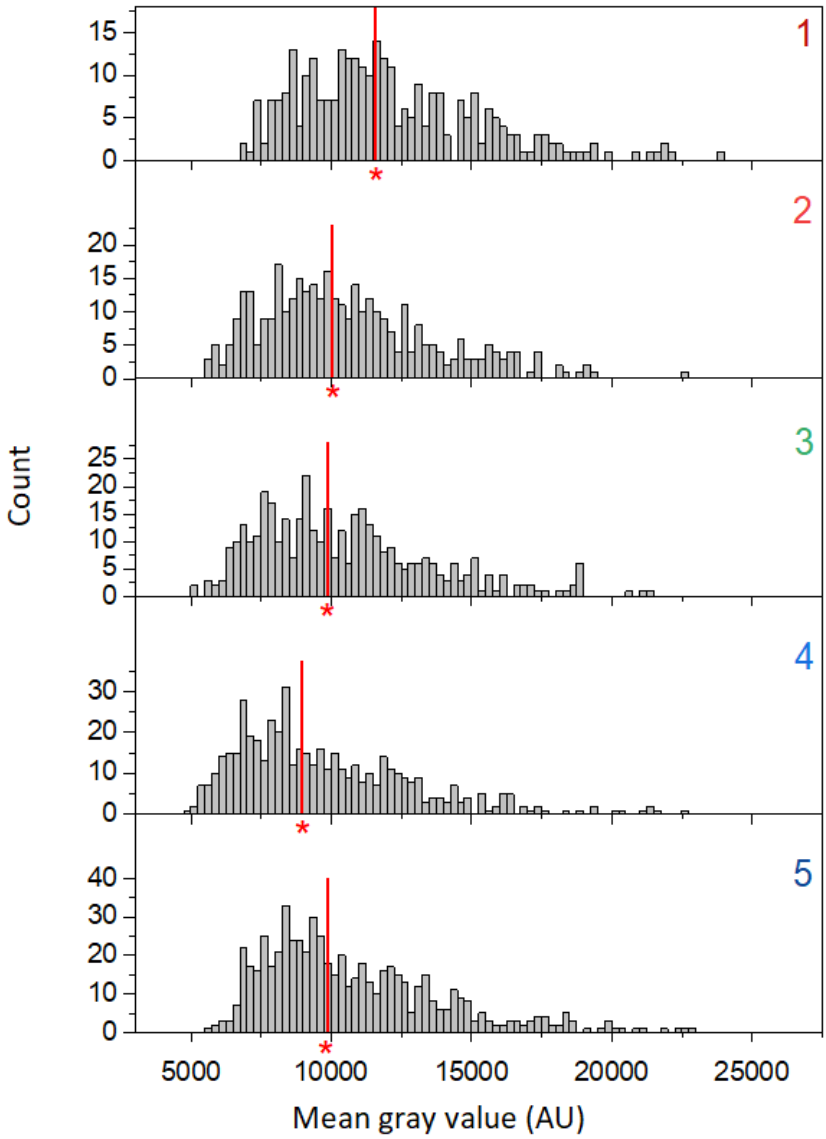

Figure 6.21: HIF-1α expression in HepG2/C3A cells cultured in chips and exposed to flow rates of 150 µL/hour at each inlet for 3 hours with normal CO_2-Ind medium and no gradient. Images were taken with 5 s exposure and 10% light power. Histograms (bin width 300) show combined results from three images per channel, red line labelled with asterisk indicates the median. Full statistical results for each chip are tabulated in Appendix 6.

The graph in Figure 6.22 shows a comparison of the MGV distributions over all channels in each chip at the various flow rates tested. One hypothesis discussed throughout this set of experiments is that differences in HIF-1α induced by gradients of oxygen or $CoCl_2$ were being obscured by increases in HIF-1α expression caused by shear stress across the chip. The data in the graph shows that there is a statistically significant ($p < 0.0001$) increase in HIF-1α from 0 – 100 µL/hour, which supports the hypothesis. However, the results at 150 µL/hour drop down to a similar level to the results at 50 µL/hour, spoiling the trend, which could mean that the trend is not real and was observed by chance.

It is possible that the trend is real but non-linear if HIF-1α expression in HepG2/C3A cells peaks at around the levels observed at 50 – 150 µL/hour. In general, the MGV at higher flow rates (50 – 150 µL/hour) are higher than at the lower flow rates (0 – 30 µL/hour or 50 µL/hour for a shorter time). Variation in each subset of cells at the lower and higher flow rates could be due to natural variation between the individual samples.

It is not appropriate to make conclusive statements from this series of experiments because there was only one sample per experiment. The experiments were limited to one chip at a time as there was only one dual syringe pump available. This is a big disadvantage of the designed system and should be taken into consideration for future designs.

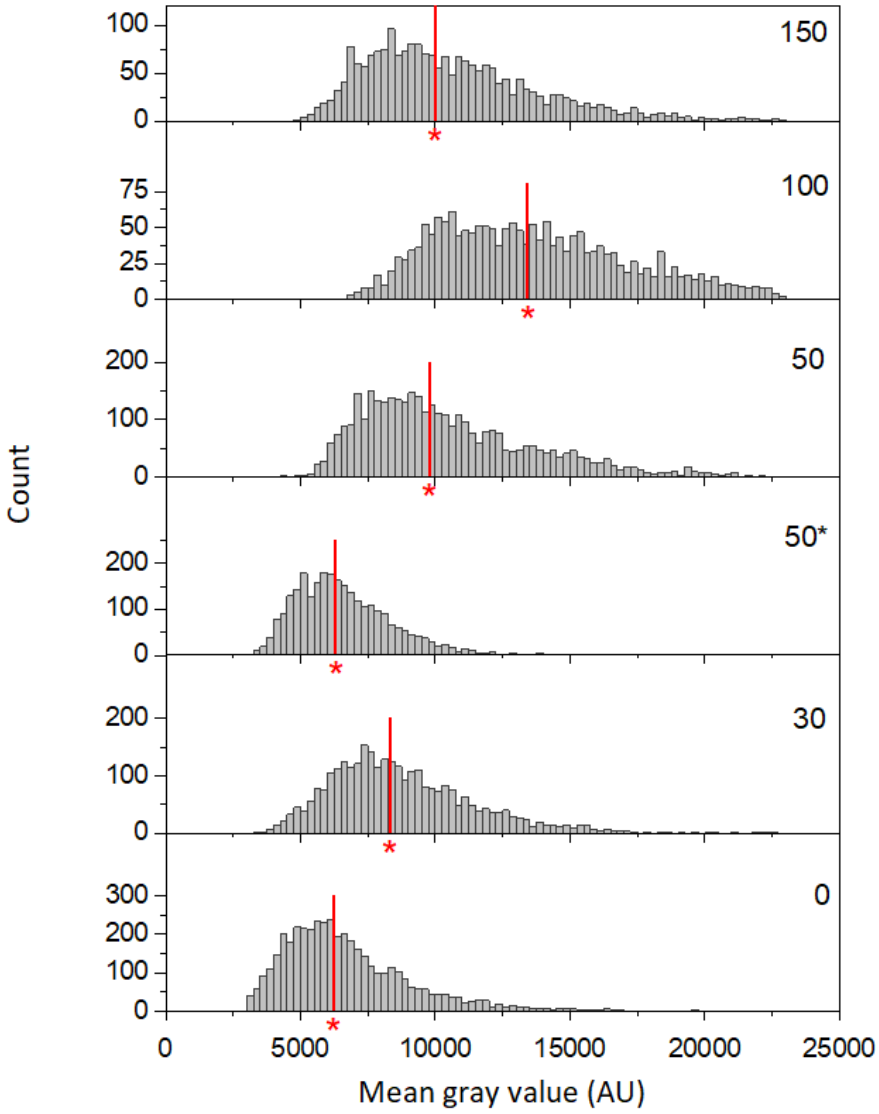

Figure 6.22: HIF-1α expression in HepG2/C3A cells cultured in chips at various flow rates. All experiments exposed cells to flow for 3 hours, except 50 which was 1.5 hours, and cells were imaged with the same microscope settings (5 s exposure and 10% light power). Histograms (bin width 250) show combined results from channel 1 – 5 from each experiment, red line labelled with asterisk indicates the median. Differences between chips at all flow rates were statistically significant ($p < 0.0001$) except between 0 and 50* µL/hour and 50 and 150 µL/hour. Full statistical results for each chip are tabulated in Appendix 6. 0 µL/hour: Experiment 6, 30 µL/hour: Experiment 5, 50* µL/hour: Experiment 4, 50 µL/hour: Experiment 3, 100 and 150 µL/hour: Experiment 7.*

6.3 Summary

The aim of the work in this chapter was to culture HepG2/C3A cells in the chip under gradients of oxygen and show that the cells in the hypoxic areas of the chip behave differently to the cells in the non-hypoxic areas of the chip by measuring expression of a hypoxia dependent protein.

An experiment was carried out to see if hypoxia dependent proteins HIF-1α and CAIX were upregulated in HepG2/C3A and DU145 cells after a short incubation with $CoCl_2$ (hypoxia mimetic). It was found that HIF-1α was upregulated in both cell types, however, CAIX was not upregulated in HepG2/C3A cells. It is possible that HepG2/C3A cells require longer incubation before increases in CAIX can be measured. In DU145 cells, the cells incubated with $CoCl_2$ showed lower expression of CAIX compared to the cells incubated with normal medium. This was an unexpected result that was reproduced in a repeat experiment but is not well understood.

The results from Chapter 5 showed that of the 3 cell types studied, HepG2/C3A cells were the most suitable for culturing in the chip. So, in the final set of experiments, HepG2/C3A cells were seeded in chips, exposed to gradients of oxygen or $CoCl_2$ and then the cells were fixed and stained for HIF-1α. The series of experiments is summarised in the Table 6.1.

Table 6.1: Summary of in-chip experiments conducted with HepG2/C3A cells in Section 6.2.2.

Experiment	Gradient	Flow rate (µL/hour)	Time (hours)
1	0% oxygen – 21% oxygen	50	24
2	0 µM $CoCl_2$ – 100 µM $CoCl_2$	50	24
3	0 µM $CoCl_2$ – 400 µM $CoCl_2$	50	3
4	0 µM $CoCl_2$ – 400 µM $CoCl_2$	50	1.5
5	0 µM $CoCl_2$ – 400 µM $CoCl_2$	30	3
6	0 µM $CoCl_2$ – 400 µM $CoCl_2$	0	3
7	0 µM $CoCl_2$ – 400 µM $CoCl_2$	100	3
8	0 µM $CoCl_2$ – 400 µM $CoCl_2$	150	3

It was expected that the cells in the more hypoxic regions of the chips would show higher expression of HIF-1α. However, none of the conditions tested produced a large increase in HIF-1α in the hypoxic area of the chip compared to the non-hypoxic areas of the chip. Experiments 1 and 3 showed a statistically significant increase in HIF-1α from non-hypoxic to hypoxic channels of the chip, but the differences were small with respect to range of the distributions. The rest of the experiments showed variable and inconsistent trends in HIF-1α expression across the chip and highlighted the likelihood that the trends observed in Experiments 1 and 3 were down to chance. Over all of the experiments, HIF-1α expression was found to be independent of the imposed gradient.

It was proposed that the expression of HIF-1α increased across all cells in the chip due to shear stress. It may be possible that HIF-1α can be induced in HepG2/C3A cells as a result of hypoxic stress and shear stress, and that the impact of shear stress overwhelms any more subtle differences induced by hypoxic stress. The results

generally support this hypothesis, but it is not possible to make firm conclusions based on the experiments conducted.

As discussed previously, shear stress is highest in channel 3. Therefore, if the correlation between shear stress and HIF-1α expression is true, it would be expected that channel 3 would also show higher HIF-1α expression compared to other channels. This trend is not observed in the data, possibly because the differences in shear stress between the channels is insignificant compared to the overall level of shear stress. However, it is possible that the variation in velocity and shear stress across the channels is adding additional complexity to the results.

A quantitative live/dead cell count for each channel may have been useful to highlight inconsistencies in the chip and to help understand the relationship between shear stress and HIF-1α. In future work, it would be beneficial to redesign the chip – as suggested in Chapter 3 – to have consistent flow characteristics across the chip. This would help to make the channels more consistent and comparable to one another.

6.4 Materials and Methods

6.4.1 Immunofluorescence Staining and Imaging

Staining

Anti-HIF-1α antibody (rabbit, ab51608), anti-carbonic anhydrase 9 (CAIX) antibody (rabbit, ab184006) and Alexa Fluor® 488 (goat anti-rabbit, ab15007) were purchased from Abcam.

Between each step of the staining process, cells were washed 3 times with PBS. Cells were fixed with 4% formaldehyde for 10 minutes, permeabilised with 0.1% Triton X100 (Sigma-Aldrich) for 30 minutes and then blocked with blocking buffer (5% FBS in PBS) for 1 hour at room temperature. Cells were incubated with the primary antibody, anti-HIF-1α or anti-CAIX diluted 1:500 in blocking buffer, at 4° C overnight and then with Alexa Fluor® 488 diluted 1:200 in blocking buffer for 2 hours at room temperature. Cell were washed 3 times with PBS and stored in PBS for imaging.

Imaging

Stained cells were imaged using a Nikon Ti2 Live Imaging microscope with x20 or x40 air objective (CFI Plan Apochromat Lambda) and LED light source (Lumencor SPECTRA X Light Engine). The excitation and emission wavelengths for Alexa Fluor® 488 are 495 nm and 519 nm, hence a GFP (green fluorescent protein) excitation filter (448 - 500 nm) and a Cy3 emission filter (513 – 679 nm) were used.

6.4.2 Data Analysis

Fluorescence images of cells were analysed in ImageJ. The 'Analyse particles' function was used to select each fluorescent cell as a region of interest. The average and standard deviation MGV in each cell was measured. The average MGV was measured in 5 different small areas of background across the image. All values were recorded and processed in Origin. The mean and standard deviation of MGV values for all cells in each image was calculated and the average background MGV was subtracted.

Statistical analysis was performed in GraphPad Prism 9. Kruskal-Wallis tests were used to compare the 5 channels in each chip, followed by a Dunn's multiple comparisons test. In experiment 6, a Mann-Whitney test was used to compare populations of treated and untreated cells.

6.4.3 HIF-1α and CAIX Screen

Wells in two 96-well plates (Greiner bio-one, 655090) were coated with 100 µg/mL collagen for 1 hour at 37° C then washed twice with PBS. HepG2/C3A and DU145 cells were seeded in 18 wells (separate well plates) at a density of 20,000 cells per well in 200 µL of DMEM or RPMI medium respectively. Cells were incubated for 2 days and then 9 wells were treated with 400 µM $CoCl_2$ in the respective medium for 3 hours.

In each set of the 9 $CoCl_2$ treated wells and 9 untreated wells, 3 were stained for HIF-1α and 3 were stained for CAIX according to the protocol in Section 6.4.1. The remaining 3 wells in each set were controls and went through the same staining

protocol but were incubated with blocking buffer instead of a primary antibody. Cells were imaged with a x20 objective, 5 second exposure time and 10% light power.

6.4.4 Staining HepG2/C3A Cells in Chip

To prepare for staining, syringes were used to gently wash the system through with PBS and to the fill the channels with 4% formaldehyde solution. After 10 minutes, the system was washed through with PBS and the tubing was removed from the chip. Staining for HIF-1α and imaging were completed as described in Section 6.4.1, using a pipette to transfer the reagents into the channels. Images were taken with a x40 objective with 5 s exposure and 80% or 10% light power.

Chapter 7: Summary

7.1 Conclusions

Microfluidic technologies offer methods to design and create physiologically relevant *in vitro* models of human tissues and organs. Often the designs can offer increased complexity compared to standard 2D culture models by incorporating additional features of the *in vivo* environment. However, the potential of microfluidics has not been fully realised in radiotherapy research. As discussed in Chapter 1, hypoxia is an important physiological feature of solid cancer tumours that is associated with aggressive growth and resistance to radiotherapy and other treatments. Hence, the aim of this project was to work towards developing a microfluidic model of tumour hypoxia that could be used to study the relationship between hypoxia and resistance to radiotherapy and combination therapies.

The first objective for the project was to design and create a microfluidic chip that was relatively simple to make and use. The final design for the chip was a branching network of channels, such that a range of oxygen concentrations could be produced from only two input solutions of different oxygen concentrations (Figure 7.1 A). The chip was made from acrylic and the rest of the system consisted of stainless steel tubes, glass syringes and an aluminium foil pouch, all of which were selected to isolate the system from atmospheric oxygen (Figure 7.1 C).

Fluid dynamics and the distribution of oxygen in the chip were studied using CFD simulations in COMSOL Multiphysics®. The simulations showed that mixing of solutions at 21% and 0% oxygen produced a range of intermediate oxygen concentrations across the chip. With a flow rate of 50 µL/hour at each inlet, the concentrations in channels 1 – 5 were approximately 21, 17, 10, 4 and 0% oxygen respectively (Figure 7.1 B). This provided an interesting range of values where channels 1 and 2 were representative of oxygen concentrations used in standard cell culture methods and channels 3 – 5 represented oxygen concentrations found in well oxygenated to hypoxic tumour regions.

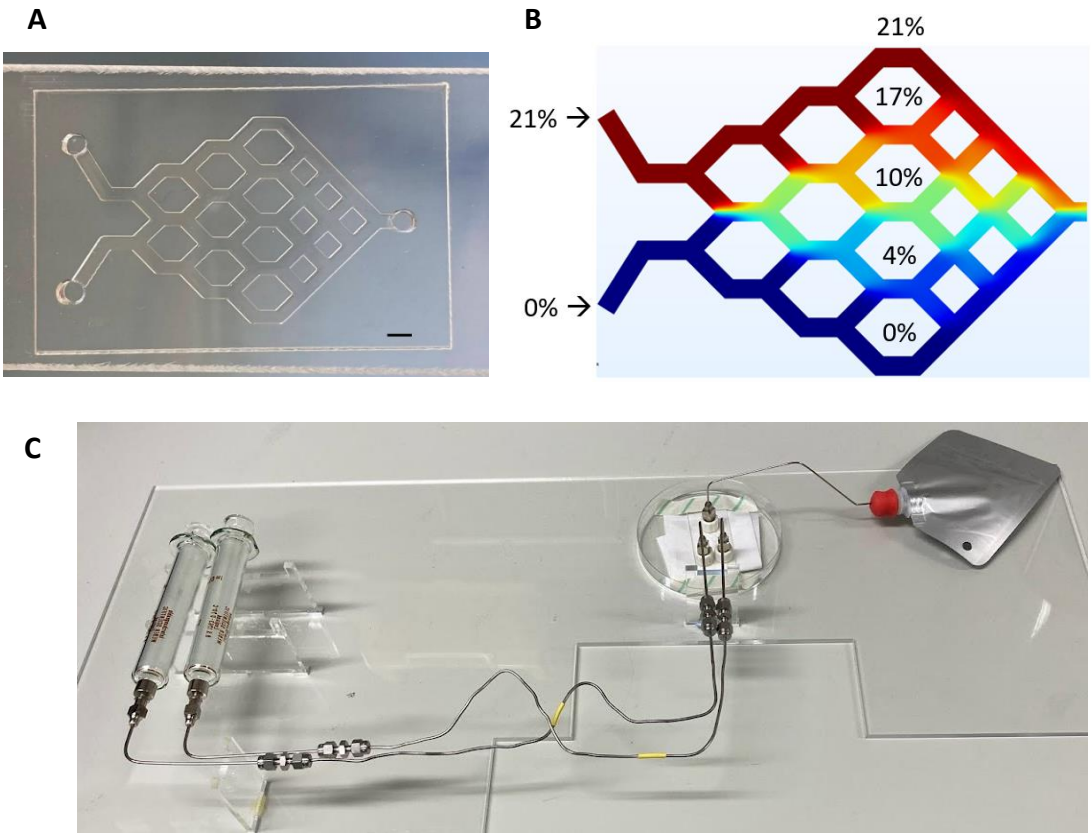

Figure 7.1: Oxygen gradient on a microfluidic chip. ***A*** *Image of the chip made from acrylic. Scale bar is 2 mm.* ***B*** *Oxygen profile in the chip with media flow from the inlets at 50 µL/hour.* ***C*** *Image of full system.*

Oxygen concentrations in the channels were also measured using fluorescence microscopy. The channels were filled with solutions of the oxygen sensitive fluorophore $Ru(BPY)_3$ at 21% and 0% oxygen and fluorescence intensity in each channel was used to calculate oxygen concentration. The normalised results correlated well with the computational results and demonstrated a stable oxygen gradient across the chip.

The next step was to culture cells in the chip. However, it was found that prostate cancer cell lines PC3 and DU145 could not survive in the chip, likely due to the shear stress imposed by the flowing culture media. Literature examples suggested that hepatocytes were more resistant to shear stress, so the liver cancer cell line HepG2/C3A was tested in the chip as an alternative. A successful method for seeding

HepG2/C3A cells in the chip was established and it was shown that the cells could survive in the chip for up to two days with media flow.

The HepG2/C3A cells were then grown under gradients of hypoxia and stained for the hypoxic marker HIF-1α. First, cells were exposed to a gradient of oxygen, but differences in HIF-1α expression between hypoxic and non-hypoxic regions of the chips were considerably small and inconsistent. Cells were then exposed to gradients of the hypoxia mimetic agent $CoCl_2$, which had been shown to induce HIF-1α expression in well-plate control experiments. However, these experiments – conducted at various flow rates – also did not produce consistent trends in HIF-1α between areas of high and low $CoCl_2$ concentration.

It is known that HIF-1α can be stabilised by stresses and experimental factors other than oxygen, therefore it was proposed that shear stress due to media flow was causing an increase in HIF-1α across all cells in the chip. If true, this effect could be overwhelming any more subtle differences in HIF-1α expression induced by the hypoxic gradients. Each of the cell culture experiments with HepG2/C3A cells in the chip was conducted only once, meaning that it is not possible to draw any firm conclusions.

Overall, the design and fabrication method for the microfluidic device used in this work present a potentially useful way to study ranges of hypoxia in human cancer cells. The chip offers advantages over traditional monolayer cultures because it enables a range of oxygen concentration to be studied at the same time and offers a simpler and less expensive alternative to animal models. Spheroid models grow to produce natural gradients of oxygen from the outer surface to the core of the sphere. But correlating cell behaviour and oxygen concentration can be difficult in the 3D environment and the cells cannot easily be separated and analysed according to their oxygen content. Additionally, controlling the size and shape of spheroids is not straightforward, resulting in sample inhomogeneity and challenging data analysis. The chip can overcome some of these issues by allowing homogeneous cell

monolayers to be studied in individual channels with different oxygen concentrations which can be analysed on-chip by fluorescence microscopy.

The development of human-based biological models is a rapidly expanding and developing field. The examples presented in this work are sophisticated and show that there is a balance to be reached between model simplicity and biological complexity. Compared to the other devices presented, the chip designed in this work was advantageous because it didn't require clean room technology to make and the design and system set-up were relatively simple. The chip offered a platform to study cells in isolated fluidic channels with different oxygen concentrations. This potentially allows more straightforward correlation between oxygen concentration and biological observation compared to the device by Orcheston-Findlay *et al*. with an oxygen gradient across a single channel. The chip was more compact than the 96-well plate device presented by Yao *et al*. and did not require bulky gas cylinders or expensive gas control systems, like the devices presented by Menolascina *et al*. and Rexius-Hall *et al*.

The oxygen profiles in the chip were created by controlling the dissolved oxygen concentration in the cell culture media and the flow rate through the chip. This allows for precise control of the oxygen environment in the chip without relying on chemicals that could potentially be toxic to the cells, as used by Sun *et al* and Sleeboom *et al*. It is also proposed that the gradients formed in the chip may be more reliable and reproducible compared to gradients generated in chips by cellular consumption of oxygen, for example in the device by Ando *et al.* The hypoxic conditions in these devices are reliant on cell seeding density and cell type, so although the gradients are formed naturally, they may be difficult to control and reproduce between experiments.

7.2 Future Work

In order to unlock the full potential of the chip, further optimisation is required to make the chip more suitable for culturing cells. Suggestions for future work include

trying different protein coatings on the channel surface and testing different cell lines. In the experiments presented in this work, collagen was used to coat the channel surface and Geltrex was deposited on top of the cells to provide the cells with extra-cellular matrix support and protect them from the media flow. It is possible that alternative proteins, such as fibronectin or gelatin, or combinations of proteins below and on top of the cells would optimise attachment to the channel surface and prevent them from detaching under flow. There is also variation between each individual cancer cell line, different cell lines could be cultured in the chip to find a cell type that can survive under the media flow and respond to the hypoxic gradient. Suggestions of cell types that may be more compatible with culture in the chip are fibroblast and epithelial lines, as these cell types are often exposed to shear stress environments *in vivo*.

It was found that the cell types used did not grow as well in the CO_2-Ind medium without CO_2 used in the chip experiments as they did in normal DMEM or RPMI with 5% CO_2. This could potentially be improved by adding growth factors or supplements to the CO_2-Ind medium to make it more suitable for the cells. Alternatively, the cells could be cultured in the chip with DMEM or RPMI that is pre-equilibrated at 5% CO_2. Medium at 21% oxygen could be prepared by equilibrating in a standard cell culture incubator and deoxygenated medium could be prepared by bubbling with 95% N_2 and 5% CO_2 rather than pure nitrogen gas.

The fabrication method for the chip should allow rapid prototyping of further iterations of the design, allowing the chip itself to be optimised. In the current design, there is variation in shear stress across the channels which may have introduced complexity and inconsistency in the cell culture experiments. One approach could be to adjust the geometry of the channels to produce constant velocity and shear stress across the channel network, making results from individual channels more consistent and comparable to one another. In future experiments, quantitative live/dead cell counting in each channel may be helpful for understanding the relationships between

cell health, flow rate and shear stress as well as highlighting any inconsistencies in the chip culture.

A second approach could be to rearrange the structure and design of the chip to isolate the cell culture from the flow. Two copies of the channel network could be sandwiched together with a permeable membrane between them. This would allow cells to be cultured in the bottom layer with static culture media and on the other side of the membrane, oxygenated and deoxygenated solutions could be purged through the channels to control the oxygen content of the static media below. Alternatively, the same channel pattern could be made in a glass device, although this would require a different fabrication method. Since glass is impermeable to oxygen, it might be possible to use a very similar set-up but reduce the flow rate even further to minimise shear stress on the cells and optimise cell growth and survival whilst maintaining an oxygen gradient.

References

1. Ferlay, J. *et al.* Global Cancer Observatory: Cancer Today. Lyon, France: International Agency for Research on Cancer. https://gco.iarc.fr/today (2020).
2. Cancer Research UK. Worldwide cancer statistics. https://www.cancerresearchuk.org/health-professional/cancer-statistics/worldwide-cancer#heading-Zero.
3. Cancer Research UK. What is Cancer? https://www.cancerresearchuk.org/about-cancer/what-is-cancer.
4. McKeown, S. R. Defining normoxia, physoxia and hypoxia in tumours - Implications for treatment response. *British Journal of Radiology* **87**, 1–12 (2014).
5. Muz, B., Puente, P. de la, Azab, F. & Azab, A. K. The role of hypoxia in cancer progression angiogenesis metastasis and resistance to therapy. *Hypoxia* **3**, 83–92 (2015).
6. Horsman, M. R. & Vaupel, P. Pathophysiological Basis for the Formation of the Tumor Microenvironment. *Front. Oncol.* **6**, (2016).
7. Graham, K. & Unger, E. Overcoming tumor hypoxia as a barrier to radiotherapy, chemotherapy and immunotherapy in cancer treatment. *IJN* **13**, 6049–6058 (2018).
8. Sørensen, B. S. & Horsman, M. R. Tumor Hypoxia: Impact on Radiation Therapy and Molecular Pathways. *Front. Oncol.* **10**, 562 (2020).
9. Hanahan, D. & Weinberg, R. A. The Hallmarks of Cancer. *Cell* **100**, 57–70 (2000).

10. Hanahan, D. Hallmarks of Cancer: New Dimensions. *Cancer Discovery* **12**, 31–46 (2022).

11. Ruan, K., Song, G. & Ouyang, G. Role of hypoxia in the hallmarks of human cancer. *J. Cell. Biochem.* **107**, 1053–1062 (2009).

12. Bartrons, R. & Caro, J. Hypoxia, glucose metabolism and the Warburg's effect. *J Bioenerg Biomembr* **39**, 223–229 (2007).

13. Fadaka, A. *et al.* Biology of glucose metabolization in cancer cells. *Journal of Oncological Sciences* **3**, 45–51 (2017).

14. Courtnay, R. *et al.* Cancer metabolism and the Warburg effect: the role of HIF-1 and PI3K. *Mol Biol Rep* **42**, 841–851 (2015).

15. DeBerardinis, R. J. & Chandel, N. S. Fundamentals of cancer metabolism. *Sci. Adv.* **2**, 1–18 (2016).

16. Lee, S.-H. & Griffiths, J. R. How and Why Are Cancers Acidic? Carbonic Anhydrase IX and the Homeostatic Control of Tumour Extracellular pH. *Cancers* **12**, 1616–1631 (2020).

17. Pastorekova, S. & Gillies, R. J. The role of carbonic anhydrase IX in cancer development: links to hypoxia, acidosis, and beyond. *Cancer and Metastasis Reviews* **38**, 65–77 (2019).

18. Masoud, G. N. & Li, W. HIF-1α pathway: Role, regulation and intervention for cancer therapy. *Acta Pharmaceutica Sinica B* **5**, 378–389 (2015).

19. Godet, I., Doctorman, S., Wu, F. & Gilkes, D. M. Detection of Hypoxia in Cancer Models: Significance, Challenges, and Advances. *Cells* **11**, 686 (2022).

20. Dengler, V. L., Galbraith, M. D. & Espinosa, J. M. Transcriptional regulation by hypoxia inducible factors. *Critical Reviews in Biochemistry and Molecular Biology* **49**, 1–15 (2014).

21. Albanese, A., Daly, L. A., Mennerich, D., Kietzmann, T. & Sée, V. The role of hypoxia-inducible factor post-translational modifications in regulating its localisation, stability, and activity. *International Journal of Molecular Sciences* **22**, 1–18 (2021).

22. Yang, M., Su, H., Soga, T., Kranc, K. & Pollard, Patrick. Prolyl hydroxylase domain enzymes: important regulators of cancer metabolism. *Hypoxia* **2**, 127-142 (2014).

23. Iyer, N. G., Özdag, H. & Caldas, C. p300/CBP and cancer. *Oncogene* **23**, 4225–4231 (2004).

24. Pavlacky, J. & Polak, J. Technical Feasibility and Physiological Relevance of Hypoxic Cell Culture Models. *Frontiers in Endocrinology* **11**, 57 (2020).

25. Jampasri, S., Reabroi, S., Tungmunnithum, D., Parichatikanond, W. & Pinthong, D. Plumbagin Suppresses Breast Cancer Progression by Independent Pathway under Hypoxic Condition. *Molecules* **27**, 5716 (2022).

26. Triantafyllou, A. *et al.* Cobalt induces hypoxia-inducible factor-1α (HIF-1α) in HeLa cells by an iron-independent, but ROS-, PI-3K- and MAPK-dependent mechanism. *Free Radical Research* **40**, 847–856 (2006).

27. Cancer Research UK. Treatment for Cancer. https://www.cancerresearchuk.org/about-cancer/cancer-in-general/treatment.

28. Cancer Research UK. Cancer treatment statistics. https://www.cancerresearchuk.org/health-professional/cancer-statistics/treatment.

29. Public Health England. Official Statistics. Chemotherapy, Radiotherapy and Surgical Tumour Resections in England. https://www.gov.uk/government/statistics/chemotherapy-radiotherapy-and-surgical-tumour-resections-in-england/chemotherapy-radiotherapy-and-surgical-tumour-resections-in-england (2020).

30. Cancer Research UK. What is radiotherapy? https://www.cancerresearchuk.org/about-cancer/cancer-in-general/treatment/radiotherapy/about.

31. Gong, L., Zhang, Y., Liu, C., Zhang, M. & Han, S. Application of Radiosensitizers in Cancer Radiotherapy. *IJN* **16**, 1083–1102 (2021).

32. Azzam, E. I., Jay-Gerin, J. P. & Pain, D. Ionizing radiation-induced metabolic oxidative stress and prolonged cell injury. *Cancer Letters* **327**, 48–60 (2012).

33. Hegedűs, C. *et al.* Redox control of cancer cell destruction. *Redox Biology* **16**, 59–74 (2018).

34. Cancer Research UK. How chemotherapy works. https://www.cancerresearchuk.org/about-cancer/cancer-in-general/treatment/chemotherapy/how-chemotherapy-works.

35. Cancer Research UK. What is chemotherapy? https://www.cancerresearchuk.org/about-cancer/cancer-in-general/treatment/chemotherapy/what-chemotherapy-is.

36. Oronsky, B. T., Knox, S. J. & Scicinski, J. Six Degrees of Separation: The Oxygen Effect in the Development of Radiosensitizers. *Translational Oncology* **4**, 189–198 (2011).

37. Marcu, L. & Olver, I. Tirapazamine: From Bench to Clinical Trials. *CCP* **1**, 71–79 (2006).

38. Mistry, I. N., Thomas, M., Calder, E. D. D., Conway, S. J. & Hammond, E. M. Clinical Advances of Hypoxia-Activated Prodrugs in Combination With Radiation Therapy. *Int J of Radiation Oncol Biol Phys* **98**, 1183–1196 (2017).

39. Mohs, R. C. & Greig, N. H. Drug discovery and development: Role of basic biological research. *Alzheimer's & Dementia: Translational Research & Clinical Interventions* **3**, 651–657 (2017).

40. Austin, D. *et al. Research and Development in the Pharmaceutical Industry*. Congressional Budget Office Report. https://www.cbo.gov/publication/57126 (2021).

41. Atkins, J. T. *et al.* Pre-clinical animal models are poor predictors of human toxicities in phase 1 oncology clinical trials. *Br J Cancer* **123**, 1496–1501 (2020).

42. Festing, S. & Wilkinson, R. The ethics of animal research: Talking Point on the use of animals in scientific research. *EMBO Rep* **8**, 526–530 (2007).

43. National Centre for the Replacement Refinement & Reduction of Animals in Research. The 3Rs. https://www.nc3rs.org.uk/who-we-are/3rs.

44. Van Norman, G. A. Limitations of Animal Studies for Predicting Toxicity in Clinical Trials. Is it Time to Rethink Our Current Approach? *JACC: Basic to Translational Science* **4**, 845–854 (2019).

45. Rand, P. *et al.* S.5002 - FDA Modernization Act 2.0. https://www.congress.gov/bill/117th-congress/senate-bill/5002 (2022).

46. Hernandez, J. The FDA no longer requires all drugs to be tested on animals before human trials. *NPR* https://www.npr.org/2023/01/12/1148529799/fda-animal-testing-pharmaceuticals-drug-development (2023).

47. Amez-Droz, E. How Animal Testing Harms Humans. *The Wall Street Journal* (2022).

48. Onaciu, A. *et al.* Spontaneous and Induced Animal Models for Cancer Research. *Diagnostics* **10**, 660–696 (2020).

49. Workman, P. *et al.* Guidelines for the welfare and use of animals in cancer research. *Br J Cancer* **102**, 1555–1577 (2010).

50. De Bruycker, S., Vangestel, C., Staelens, S., Van den Wyngaert, T. & Stroobants, S. How to Modulate Tumor Hypoxia for Preclinical In Vivo Imaging Research. *Contrast Media & Molecular Imaging* **2018**, 1–17 (2018).

51. Mortensen, L. S. *et al.* Accessing radiation response using hypoxia PET imaging and oxygen sensitive electrodes: A preclinical study. *Radiotherapy and Oncology* **99**, 418–423 (2011).

52. Hong, S. H. *et al.* In Vivo Model for Testing Effect of Hypoxia on Tumor Metastasis. *J. Vis. Exp.* **118** (2016).

53. Jensen, C. & Teng, Y. Is It Time to Start Transitioning From 2D to 3D Cell Culture? *Front. Mol. Biosci.* **7**, 33 (2020).

54. Strese, S., Fryknäs, M., Larsson, R. & Gullbo, J. Effects of hypoxia on human cancer cell line chemosensitivity. *BMC Cancer* **13**, 331 (2013).

55. Kim, M. H., Green, S. D., Lin, C. & Konig, H. Engineering Tools for Regulating Hypoxia in Tumour Models. *J Cell Mol Med* **25**, 7581–7592 (2021).

56. Yao, M., Walker, G. & Gamcsik, M. P. A multiwell plate-based system for toxicity screening under multiple static or cycling oxygen environments. *Sci Rep* **11**, 4020 (2021).

57. Yao, M. *et al.* Flow-Encoded Oxygen Control to Track the Time-Dependence of Molecular Changes Induced by Static or Cycling Hypoxia. *Anal. Chem.* **91**, 15032–15039 (2019).

58. Yao, M. *et al.* Mixing and delivery of multiple controlled oxygen environments to a single multiwell culture plate. *American Journal of Physiology-Cell Physiology* **315**, 766–775 (2018).

59. Orcheston-Findlay, L., Hashemi, A., Garrill, A. & Nock, V. A microfluidic gradient generator to simulate the oxygen microenvironment in cancer cell culture. *Microelectronic Engineering* **195**, 107–113 (2018).

60. Sun, W. *et al.* Interaction study of cancer cells and fibroblasts on a spatially confined oxygen gradient microfluidic chip to investigate the tumor microenvironment. *Analyst* **143**, 5431–5437 (2018).

61. Bhattacharya, S., Calar, K. & Puente, P. de la. Mimicking tumor hypoxia and tumor-immune interactions employing three-dimensional in vitro models. *Journal of Experimental & Clinical Cancer Research* **39**, 75–91 (2020).

62. Ziółkowska-Suchanek, I. Mimicking Tumor Hypoxia in Non-Small Cell Lung Cancer Employing Three-Dimensional In Vitro Models. *Cells* **10**, 141 (2021).

63. Close, D. A. Detection and impact of hypoxic regions in multicellular tumor spheroid cultures formed by head and neck squamous cell carcinoma cells lines. *SLAS Discovery* **27**, 39-54 (2022).

64. Han, S. J., Kwon, S. & Kim, K. S. Challenges of applying multicellular tumor spheroids in preclinical phase. *Cancer Cell International* **21**, 152–171 (2021).

65. Simon, K. A. *et al.* Metabolic response of lung cancer cells to radiation in a paper-based 3D cell culture system. *Biomaterials* **95**, 47–59 (2016).

66. Camci-Unal, G., Newsome, D., Eustace, B. K. & Whitesides, G. M. Fibroblasts Enhance Migration of Human Lung Cancer Cells in a Paper-Based Coculture System. *Adv. Healthcare Mater.* **5**, 641–647 (2016).

67. Refet-Mollof, E. *et al.* Hypoxic Jumbo Spheroids On-A-Chip (HOnAChip): Insights into Treatment Efficacy. *Cancers* **13**, 4046–4066 (2021).

68. Chermat, R. *et al.* Radiotherapy on-chip: microfluidics for translational radiation oncology. *Lab Chip* **22**, 2065–2079 (2022).

69. Cancer Research UK. Prostate cancer treatment statisics. https://www.cancerresearchuk.org/health-professional/cancer-statistics/statistics-by-cancer-type/prostate-cancer/diagnosis-and-treatment.

70. Niculescu, A.-G., Chircov, C., Bîrcă, A. C. & Grumezescu, A. M. Fabrication and Applications of Microfluidic Devices: A Review. *International Journal of Molecular Sciences* **22**, (2011).

71. Nielsen, J. B. *et al.* Microfluidics: innovations in materials and their fabrication and functionalization. *Analytical Chemistry* **92**, 150–168 (2020).

72. Shakeri, A., Khan, S. & Didar, T. F. Conventional and emerging strategies for the fabrication and functionalization of PDMS-based microfluidic devices. *Lab on a Chip* **21**, 3053–3075 (2021).

73. Lee, B. & Lee, B. K. Surfactant-added hydrophilic polydimethylsiloxane (PDMS) as mold material for thermoplastic hot embossing process. *AIP Advances* **10**, (2020).

74. Villegas, M., Cetinic, Z., Shakeri, A. & Didar, T. F. Fabricating smooth PDMS microfluidic channels from low-resolution 3D printed molds using an omniphobic lubricant-infused coating. *Analytica Chimica Acta* **1000**, 248–255 (2018).

75. Wu, C. C., Yuan, C. Y. & Ding, S. J. Effect of polydimethylsiloxane surfaces silanized with different nitrogen-containing groups on the adhesion progress of epithelial cells. *Surface and Coatings Technology* **205**, 3182–3189 (2011).

76. Burklund, A., Tadimety, A., Nie, Y., Hao, N. & Zhang, J. X. J. Advances in diagnostic microfluidics. in *Advances in Clinical Chemistry* vol. 95 1–72 (Elsevier, 2020).

77. Whitesides, G. M. & Stroock, A. D. Flexible Methods for Microfluidics. *Physics Today* **54**, 42–48 (2001).

78. Rexius-Hall, M. L., Rehman, J. & Eddington, D. T. A microfluidic oxygen gradient demonstrates differential activation of the hypoxia-regulated transcription factors HIF-1α and HIF-2α. *Integrative Biology* **9**, 742–750 (2017).

79. Menolascina, F. *et al.* Logarithmic sensing in Bacillus subtilis aerotaxis. *npj Systems Biology and Applications* **3**, 1–8 (2017).

80. Gencturk, E., Mutlu, S. & Ulgen, K. O. Advances in microfluidic devices made from thermoplastics used in cell biology and analyses. *Biomicrofluidics* **11**, 051502 (2017).

81. Guzzi, F. *et al.* A Disposable Passive Microfluidic Device for Cell Culturing. *Biosensors* **10**, 18 (2020).

82. Chen, Y., Zhang, L. & Chen, G. Fabrication, modification, and application of poly(methyl methacrylate) microfluidic chips. *Electrophoresis* **29**, 1801–1814 (2008).

83. Wan, A. M. D., Moore, T. A. & Young, E. W. K. Solvent bonding for fabrication of PMMA and COP microfluidic devices. *J. of Vis. Exp* **119** (2017).

84. Peñaherrera, A. *et al.* Evaluation of cell culture in microfluidic chips for application in monoclonal antibody production. *Microelectronic Engineering* **158**, 126–129 (2016).

85. Samuel, R., Thacker, C. M., Maricq, A. V. & Gale, B. K. Simple and cost-effective fabrication of microvalve arrays in PDMS using laser cut molds with application to *C. elegans* manipulation in microfluidics. *J. Micromech. Microeng.* **24**, (2014).

86. eurolaser. Cutting and Routing of PVC. https://www.eurolaser.com/materials/polyvinyl-chloride-pvc.

87. Lotus Laser Systems, Laser Marking. CO_2 vs. Fiber vs. UV Lasers - What's the difference? https://www.lotuslaser.com/laser-marking/uv-co2-fiber-laser-difference/.

88. Lotus Laser Systems, Laser Marking. Meta-C UV - UV Laser Marking Machine. https://www.lotuslaser.com/machine/uv-laser-marking-machine/.

89. Bovatsek, J., Kaiser, J. & Strugala, L. High-power UV lasers for precision micromachining. *Laser Focus World, Industrial Laser Solutions* https://www.laserfocusworld.com/industrial-laser-

solutions/article/14221734/highpower-uv-lasers-for-precision-micromachining (2020).

90. Alicat Scientific. Flow Controllers & Meters. https://www.alicat.com/products/flow/.

91. Young, E & Beebe, D. Fundamentals of microfluidic cell culture in controlled microenvironments. *Chem Soc Rev* **39**, 1036-1048 (2010).

92. Kim, L., Toh, Y. C., Voldman, J. & Yu, H. A practical guide to microfluidic perfusion culture of adherent mammalian cells. *Lab on a Chip* **7**, 681–694 (2007).

93. Skelley, A. M. & Voldman, J. An active bubble trap and debubbler for microfluidic systems. *Lab on a Chip* **8**, 1733–1737 (2008).

94. Sung, J. H. & Shuler, M. L. Prevention of air bubble formation in a microfluidic perfusion cell culture system using a microscale bubble trap. *Biomedical Microdevices* **11**, 731–738 (2009).

95. Karlsson, J. M. *et al.* Active liquid degassing in microfluidic systems. *Lab on a Chip* **13**, 4366–4373 (2013).

96. Wood, D. K., Soriano, A., Mahadevan, L., Higgins, J. M. & Bhatia, S. N. A biophysical marker of severity in sickle cell disease. *Sci. Translat. Med.* **123**, 15 (2012).

97. Grist, S. M., Schmok, J. C., Andy Liu, M. C., Chrostowski, L. & Cheung, K. C. Designing a microfluidic device with integrated ratiometric oxygen sensors for

the long-term control and monitoring of chronic and cyclic hypoxia. *Sensors* **15**, 20030–20052 (2015).

98. ThermoFisher. Physical Properties Table. https://static.thermoscientific.com/images/D20826~.pdf.

99. Darwin Microfluidics. Tygon ND 100-80 Tubing. https://darwin-microfluidics.com/collections/microfluidic-tubings/products/tygon-nd-100-80-micro-tubing (2022).

100. Jiang, X. *et al.* Biocompatibility of Tygon® tubing in microfluidic cell culture. *Biomedical Microdevices* **17**, 20 (2015).

101. Liga, A., Morton, J. A. S. & Kersaudy-Kerhoas, M. Safe and cost-effective rapid-prototyping of multilayer PMMA microfluidic devices. *Microfluidics and Nanofluidics* **20**, 164 (2016).

102. Fabrication. *Perspex Design Guide & Technical Manual* 4–21.

103. Sharma, A. *Introduction to Computational Fluid Dynamics: Development, Application and Analysis*. (Springer Nature Switzerland, 2022).

104. Technology Evaluation Centers. Top Computational Fluid Dynamics (CFD) Software. https://www.technologyevaluation.com/c/computational-fluid-dynamics-cfd.

105. COMSOL Multiphysics®. Introduction to Microfluidics Module. (2018).

106. Chen, Y. *et al.* Generation of oxygen gradients in microfluidic devices for cell culture using spatially confined chemical reactions. *Lab on a Chip* **11**, 3626 - 3633 (2011).

107. Kang, Y. B., Eo, J., Bulutoglu, B., Yarmush, M. L. & Usta, O. B. Progressive hypoxia-on-a-chip: An in vitro oxygen gradient model for capturing the effects of hypoxia on primary hepatocytes in health and disease. *Biotechnology and Bioengineering* **117**, 763–775 (2020).

108. Sleeboom, J. J. F., Toonder, J. M. J. den & Sahlgren, C. M. MDA-MB-231 Breast Cancer Cells and Their CSC Population Migrate Towards Low Oxygen in a Microfluidic Gradient Device. *International Journal of Molecular Sciences* **19**, 3047 (2018).

109. Ando, Y. *et al.* A microdevice platform recapitulating hypoxic tumor microenvironments. *Scientific Reports* **7**, 1–12 (2017).

110. Grant, J. *et al.* Establishment of physiologically relevant oxygen gradients in microfluidic organ chips. *Lab on a Chip* **22**, 1584–1593 (2022).

111. Lauga, E. Chapter 2: Viscosity. in *Fluid Mechanics: A Very Short Introduction* 18–31 (Oxford University Press, 2022).

112. COMSOL Multiphysics®. Navier-Stokes Equations. *Multiphysics Cyclopedia* https://www.comsol.com/multiphysics/navier-stokes-equations (2017).

113. Oh, K. W., Lee, K., Ahn, B. & Furlani, E. P. Design of pressure-driven microfluidic networks using electric circuit analogy. *Lab on a Chip* **12**, 515–545 (2012).

114. COMSOL Multiphysics®. What is Diffusion? *Multiphysics Cyclopedia* https://www.comsol.com/multiphysics/what-is-diffusion? (2018).

115. COMSOL Multiphysics®. Fluid Flow: Conservation of Momentum, Mass and Energy. *Multiphysics Cyclopedia* https://www.comsol.com/multiphysics/fluid-flow-conservation-of-momentum-mass-and-energy (2018).

116. COMSOL Multiphysics®. Chapter 12: Theory for Transport of Diluted Species. in *COMSOL Multiphysics Reference Manual 5.5* 842–856 (2019).

117. COMSOL Multiphysics®. Diffusion Equation. *Multiphysics Cyclopedia* https://www.comsol.com/multiphysics/diffusion-equation (2017).

118. COMSOL Multiphysics® v. 5.6. Material Library - Water. (2020).

119. Dertinger, S. K. W., Chiu, D. T., Noo Li Jeon & Whitesides, G. M. Generation of gradients having complex shapes using microfluidic networks. *Analytical Chemistry* **73**, 1240–1246 (2001).

120. Lauga, E. Chapter 3: Pipes. in *Fluid Mechanics: A Very Short Introduction* 32–52 (Oxford University Press, 2022).

121. Hsu, M. N., Tan, G. D. S., Tania, M., Birgersson, E. & Leo, H. L. Computational fluid model incorporating liver metabolic activities in perfusion bioreactor. *Biotechnology and Bioengineering* **111**, 885–895 (2014).

122. Emerson, D. R., Cieślicki, K., Gu, X. & Barber, R. W. Biomimetic design of microfluidic manifolds based on a generalised Murray's law. *Lab Chip* **6**, 447–454 (2006).

123. Pettersen, E. O., Larsen, L. H., Ramsing, N. B. & Ebbesen, P. Pericellular oxygen depletion during ordinary tissue culturing, measured with oxygen microsensors. *Cell Proliferation* **38**, 257–267 (2005).

124. Azimzadeh, M. *et al.* Microfluidic-based oxygen sensors for on-chip monitoring of cell, tissue and organ metabolism. *Biosensors* **12**, (2022).

125. Grist, S. M., Bennewith, K. L. & Cheung, K. C. Oxygen Measurement in Microdevices. *Annual Review of Analytical Chemistry* **15**, 221–246 (2022).

126. Brennan, M. D., Rexius-Hall, M. L., Elgass, L. J. & Eddington, D. T. Oxygen control with microfluidics. *Lab Chip* **14**, 4305–4318 (2014).

127. Hsueh, A. J. *et al.* Microdevice with an Integrated Clark-Type Oxygen Electrode for the Measurement of the Respiratory Activity of Cells. *Analytical Chemistry* **93**, 5577–5585 (2021).

128. Yamagishi, A. *et al.* Microfluidic device coupled with a microfabricated oxygen electrode for the measurement of bactericidal activity of neutrophil-like cells. *Analytica Chimica Acta* **985**, 1–6 (2017).

129. Luo, J., Dziubla, T. & Eitel, R. A low temperature co-fired ceramic based microfluidic Clark-type oxygen sensor for real-time oxygen sensing. *Sensors and Actuators, B: Chemical* **240**, 392–397 (2017).

130. Borisov, S. M. Chapter 1: Fundamentals of Quenched Phosphorescence Oxygen Sensing and Rational Design of Sensor Materials. in *Quenched-phosphorescence Detection of Molecular Oxygen: Applications in Life Sciences* (eds. Papkovsky, D. B. & Dmitriev, R. I.) 1–18 (Royal Society of Chemistry, 2018).

131. Lakowicz, J. R. Principles of fluorescence spectroscopy, 3rd Edition*, Springer,* New York, USA. (2006).

132. Berezin, M. Y. & Achilefu, S. Fluorescence Lifetime Measurements and Biological Imaging. *Chem. Rev.* **110**, 2641–2684 (2010).

133. Ungerböck, B., Charwat, V., Ertl, P. & Mayr, T. Microfluidic oxygen imaging using integrated optical sensor layers and a color camera. *Lab on a Chip* **13**, 1593–1601 (2013).

134. Zirath, H. *et al.* Every Breath You Take: Non-invasive Real-Time Oxygen Biosensing in Two- and Three-Dimensional Microfluidic Cell Models. *Front. Physiol.* **9**, 815 (2018).

135. Adler, M., Erickstad, M., Gutierrez, E. & Groisman, A. Studies of bacterial aerotaxis in a microfluidic device. *Lab on a Chip* **12**, 4835 (2012).

136. Mehta, G. *et al.* Quantitative measurement and control of oxygen levels in microfluidic poly(dimethylsiloxane) bioreactors during cell culture. *Biomedical Microdevices* **9**, 123–134 (2007).

137. Khanal, G., Hiemstra, S. & Pappas, D. Probing hypoxia-induced staurosporine resistance in prostate cancer cells with a microfluidic culture system. *Analyst* **139**, 3274–3280 (2014).

138. Adler, M., Polinkovsky, M., Gutierrez, E. & Groisman, A. Generation of oxygen gradients with arbitrary shapes in a microfluidic device. *Lab Chip* **10**, 388–391 (2010).

139. Chen, Y. A. *et al.* Generation of oxygen gradients in microfluidic devices for cell culture using spatially confined chemical reactions. *Lab on a Chip* **11**, 3626–3633 (2011).

140. Vohra, A., Schlingman, K., Carmichael, R. S. & Carmichael, T. B. Membrane-Interface-Elastomer Structures for Stretchable Electronics. *Chem* **4**, 1673–1684 (2018).

141. Sciuto, E. L. *et al.* Photo-physical characterization of fluorophore $Ru(bpy)_3^{2+}$ for optical biosensing applications. *Sensing and Bio-Sensing Research* **6**, 67–71 (2015).

142. Song, J. W. *et al.* Computer-controlled microcirculatory support system for endothelial cell culture and shearing. *Analytical Chemistry* **77**, 3993–3999 (2005).

143. Fois, C. A. M., Schindeler, A., Valtchev, P. & Dehghani, F. Dynamic flow and shear stress as key parameters for intestinal cells morphology and polarization in an organ-on-a-chip model. *Biomed Microdevices* **23**, 55 (2021).

144. Huang, Q. *et al.* Fluid shear stress and tumor metastasis. *Am J Cancer Res* **8**, 763–777 (2018).

145. Trieu, D., Waddell, T. K. & McGuigan, A. P. A microfluidic device to apply shear stresses to polarizing ciliated airway epithelium using air flow. *Biomicrofluidics* **8**, 064104 (2014).

146. Baudoin, R., Griscom, L., Prot, J. M., Legallais, C. & Leclerc, E. Behavior of HepG2/C3A cell cultures in a microfluidic bioreactor. *Biochemical Engineering Journal* **53**, 172–181 (2011).

147. Liu, L. *et al.* A microfluidic device for continuous cancer cell culture and passage with hydrodynamic forces. *Lab on a Chip* **10**, 1807–1813 (2010).

148. Wang, L. *et al.* Construction of oxygen and chemical concentration gradients in a single microfluidic device for studying tumor cell–drug interactions in a dynamic hypoxia microenvironment. *Lab Chip* **13**, 695–705 (2013).

149. Liu, W. *et al.* An integrated microfluidic system for studying cell-microenvironmental interactions versatilely and dynamically. *Lab on a Chip* **10**, 1717–1724 (2010).

150. Ke, M. *et al.* A microfluidic device for study of the effect of tumor vascular structures on the flow field and HepG2 cellular flow behaviors. *Biochemical and Biophysical Research Communications* **496**, 238–243 (2018).

151. Yang, Z. & Xiong, H.-R. Culture Conditions and Types of Growth Media for Mammalian Cells. in *Biomedical Tissue Culture* Intech Open, London (2012).

152. Gibco. Product Information Sheet - DMEM (Dulbecco's Modified Eagle Medium), Revision 4.0. (2022).

153. Gibco. Product Information Sheet - RPMI 1640 Medium, Revision 2.0. https://assets.thermofisher.com/TFS-Assets%2FLSG%2Fmanuals%2FMAN0018935_RPMI_1640Medium_IFU.pdf (2022).

154. Michl, J., Park, K. C. & Swietach, P. Evidence-based guidelines for controlling pH in mammalian live-cell culture systems. *Commun Biol* **2**, 144–156 (2019).

155. Gibco. Product Information Sheet - Leibovitz's L-15 Medium, Revision 2.0. https://assets.thermofisher.com/TFS-Assets%2FLSG%2Fmanuals%2FMAN0018899_LeibovitzL-15Medium_IFU.pdf (2022).

156. Life Technologies. CO_2 Independent Medium, Revision 1.0. https://assets.thermofisher.com/TFS-Assets%2FLSG%2Fmanuals%2F3347.pdf (2014).

157. Gibco. Media Formulation - Leibovitz's L-15. https://www.thermofisher.com/uk/en/home/technical-resources/media-formulation.80.html.

158. Riedl, S. A. B. *et al.* In vitro cultivation of primary intestinal cells from Eisenia fetida as basis for ecotoxicological studies. *Ecotoxicology* **31**, 221–233 (2022).

159. Leibovitz, A. The Growth and Maintenance of Tissue-Cell Cultures in Free Gas Exchange with the Atmosphere. *American Journal of Hygiene* **78**, 173–180 (1963).

160. Zhang, S. *et al.* Phosphorescent light-emitting iridium complexes serve as a hypoxia-sensing probe for tumor imaging in living animals. *Cancer Research* **70**, 4490–4498 (2010).

161. Invitrogen. User Guide: Image-iT™ Hypoxia Reagents. (2018).

162. Raleigh, J. A., Chou, S. C., Arteel, G. E. & Horsman, M. R. Comparisons among pimonidazole binding, oxygen electrode measurements, and radiation response in C3H mouse tumors. *Radiation Research* **151**, 580–589 (1999).

163. Xiao, W. & Loscalzo, J. Metabolic Responses to Reductive Stress. *Antioxidants and Redox Signaling* **32**, 1330–1347 (2020).

164. Jiang, J., Auchinvole, C., Fisher, K. & Campbell, C. J. Quantitative measurement of redox potential in hypoxic cells using SERS nanosensors. *Nanoscale* **6**, 12104–12110 (2014).

165. Yang, D. *et al.* Hypoxia imaging in cells and tumor tissues using a highly selective fluorescent nitroreductase probe. *Scientific Reports* **7**, 9174 (2017).

166. Fan, L. *et al.* Hypoxia imaging in living cells, tissues and zebrafish with a nitroreductase-specific fluorescent probe. *Analyst* **145**, 5657–5663 (2020).

167. Sarkar, S. *et al.* A Study on Hypoxia Susceptibility of Organ Tissues by Fluorescence Imaging with a Ratiometric Nitroreductase Probe. *ACS Sensors* **6**, 148–155 (2021).

168. ThermoFisher Scientific. Overview of Western Blotting. https://www.thermofisher.com/uk/en/home/life-science/protein-biology/protein-biology-learning-center/protein-biology-resource-library/pierce-protein-methods/overview-western-blotting.html.

169. ThermoFisher Scientific. How a Flow Cytometer Works. https://www.thermofisher.com/uk/en/home/life-science/cell-analysis/cell-analysis-learning-center/molecular-probes-school-of-fluorescence/flow-cytometry-basics/flow-cytometry-fundamentals/how-flow-cytometer-works.html.

170. ThermoFisher Scientific. Antibodies for Immunofluorescence (IF). https://www.thermofisher.com/uk/en/home/life-science/antibodies/primary-antibodies/antibodies-applications/antibodies-immunofluorescence.html.

171. Motulsky, H. J. GraphPad Statistics Guide. https://www.graphpad.com/guides/prism/latest/statistics/stat_learn-about-analyses-with-pris.htm.

172. Ravenna, L. *et al.* Distinct Phenotypes of Human Prostate Cancer Cells Associate with Different Adaptation to Hypoxia and Pro-Inflammatory Gene Expression. *PLoS ONE* **9**, (2014).

173. Quero, L., Dubois, L., Lieuwes, N. G., Hennequin, C. & Lambin, P. miR-210 as a marker of chronic hypoxia, but not a therapeutic target in prostate cancer. *Radiotherapy and Oncology* **101**, 203–208 (2011).

174. Hyuga, S. *et al.* Expression of carbonic anhydrase IX is associated with poor prognosis through regulation of the epithelial-mesenchymal transition in hepatocellular carcinoma. *International Journal of Oncology* **51**, 1179–1190 (2017).

175. Li, X. *et al.* Sinensetin suppresses angiogenesis in liver cancer by targeting the VEGF/VEGFR2/AKT signaling pathway. *Experimental and Therapeutic Medicine* **23**, 1–11 (2022).

176. Feng, S. *et al.* Mechanical Activation of Hypoxia-Inducible Factor 1α Drives Endothelial Dysfunction at Atheroprone Sites. *ATVB* **37**, 2087–2101 (2017).

177. Wu, D. *et al.* HIF-1α is required for disturbed flow-induced metabolic reprogramming in human and porcine vascular endothelium. *eLife* **6**, 25217 (2017).

178. Gibco. User Guide - Geltrex™ LDEV-Free Reduced Growth Factor Basement Membrane Matrix, Revision 3.0. https://assets.thermofisher.com/TFS-Assets%2FLSG%2Fmanuals%2FGeltrex_LDEVfree_PI.pdf (2021).

179. Metzen, E., Wolff, M., Fandrey, J. & Jelkmann, W. Pericellular P_{O2} and O_2 consumption in monolayer cell cultures. *Respiration Physiology* **100**, 101–106 (1995).

Appendix

1 Computational Oxygen Measurements at 100 µL/hour and 500 µL/hour

Graph: Oxygen concentrations in the centre of channels 1 – 5 with 100 µL/hour flow rate at both inlets.

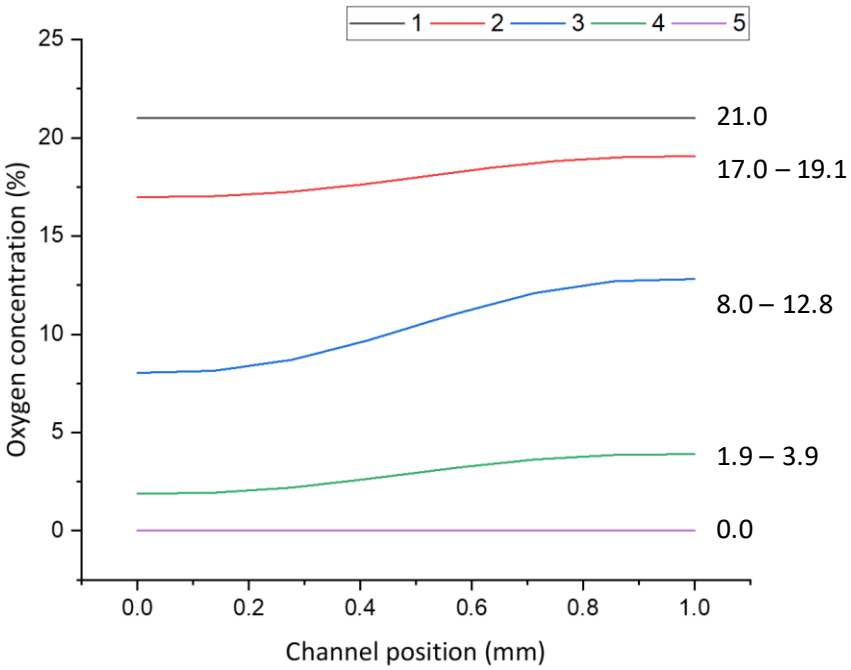

Graph: Oxygen concentrations at the left, middle and right of channel 3 with 100 µL/hour flow rate at both inlets.

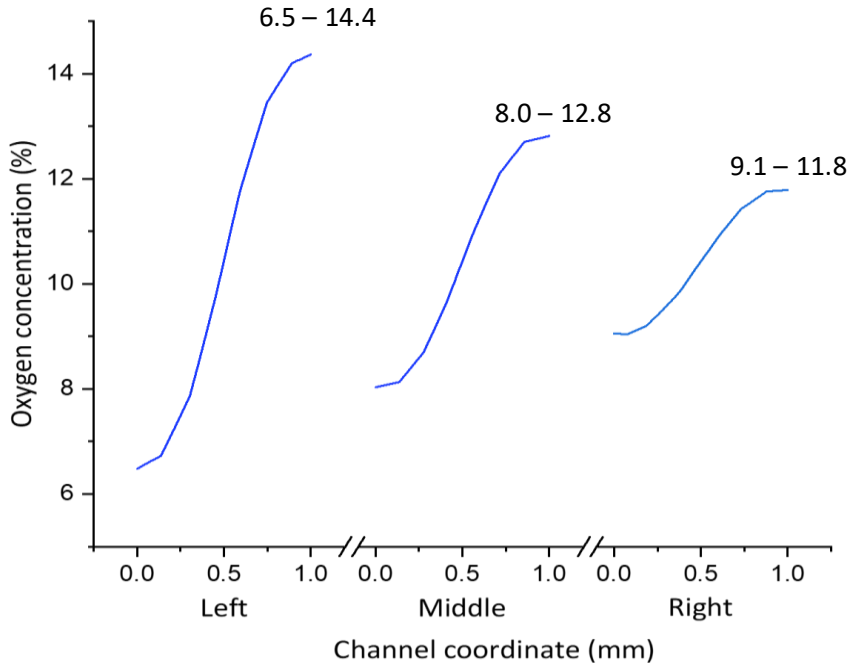

Graph: Oxygen concentrations in the centre of channels 1 – 5 with 500 µL/hour flow rate at both inlets.

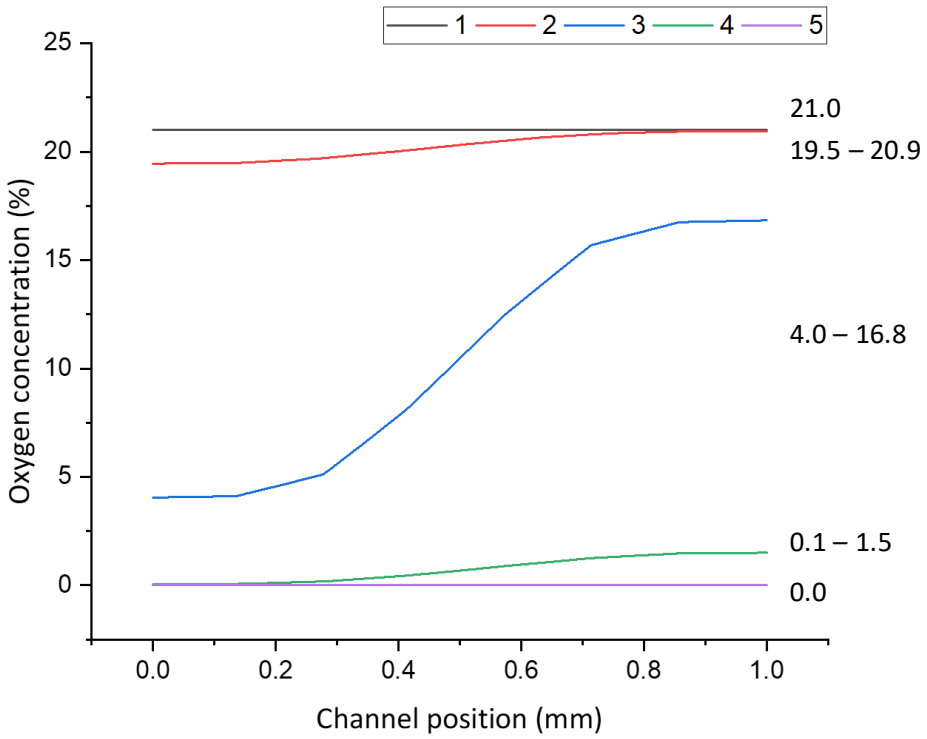

Graph: Oxygen concentrations at the left, middle and right of channel 3 with 500 µL/hour flow rate at both inlets.

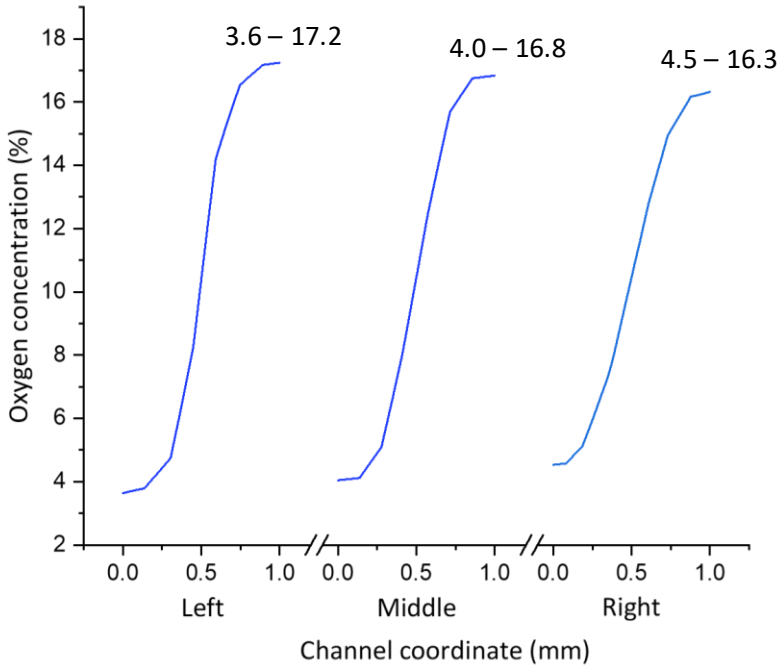

2 Shear Stress in Chip

Table: Shear stress in channels 1 – 5 calculated based on fluid flow simulation at various flow rates. Data points were collected from the base surface in the middle of each channel.

Channel	**Shear Stress** (x 10^{-4} dyn/cm^2)			
	25 µL/hour	**50 µL/hour**	**100 µL/hour**	**500 µL/hour**
1	14	28	56	280
2	27	55	110	550
3	32	65	130	650
4	27	55	110	550
5	14	28	56	280

Table: Oxygen concentration (%) for 9 images (A-I) for channels 1 – 5 at 60 minutes for data set 1.

		Channel				
		1	2	3	4	5
Image	A	20.6	19.9	14.4	4.3	0.7
	B	20.7	19.6	13.6	4.1	0.7
	C	20.5	18.7	12.6	3.5	0.5
	D	19.9	17.3	10.1	2.4	0.0
	E	20.2	17.4	10.1	2.5	0.3
	F	20.2	17.1	9.5	2.2	0.3
	G	20.8	16.8	7.4	1.9	1.6
	H	21.0	16.9	7.4	2.0	1.9
	I	20.7	16.6	7.2	1.8	1.8

Table: Oxygen concentration (%) for 9 images (A-I) for channels 1 – 5 at 60 minutes for data set 2.

		Channel				
		1	2	3	4	5
Image	A	21.0	20.0	13.7	5.5	0.8
	B	21.0	19.7	12.9	5.3	1.2
	C	20.7	18.5	12.0	4.8	1.0
	D	18.6	17.0	9.7	3.2	0.0
	E	19.2	17.3	9.7	3.5	0.3
	F	18.8	16.9	9.3	3.5	0.3
	G	19.1	16.2	7.5	2.8	0.7
	H	19.4	16.4	7.8	3.5	0.6
	I	18.8	16.0	7.6	3.6	0.9

4 HIF-1α Expression in HepG2/C3A Cells Induced by $CoCl_2$ and DFO

HepgG2/C3A cells were seeded on 25 mm collagen coated cover slips in a 6 well plate at a density of 1×10^6 cells per well in 1.5 mL of DMEM. Cells were incubated overnight and then treated with media supplemented with 100 µM $CoCl_2$, 200 µM $CoCl_2$ or 300 µM DFO for 24 hours. The untreated sample was incubated with normal DMEM. The cells were then washed, stained for HIF-1α and imaged as described in Section 6.4.3. The images were taken with a x40 objective with 500 ms exposure and 50% light power. There was one sample per condition and 5 images per sample were combined into one histogram, as shown on the following pages. Red line labelled with asterisk indicates the median.

Results demonstrated an increase in HIF-1α in all treated samples compared to the untreated sample. The largest increase in HIF-1α was induced by DFO. Doubling the concentration of $CoCl_2$ from 100 µM to 200 µM increased the expression of HIF-1α only slightly.

Histograms of HepG2/C3A cells stained for HIF-1α (bin width 25):

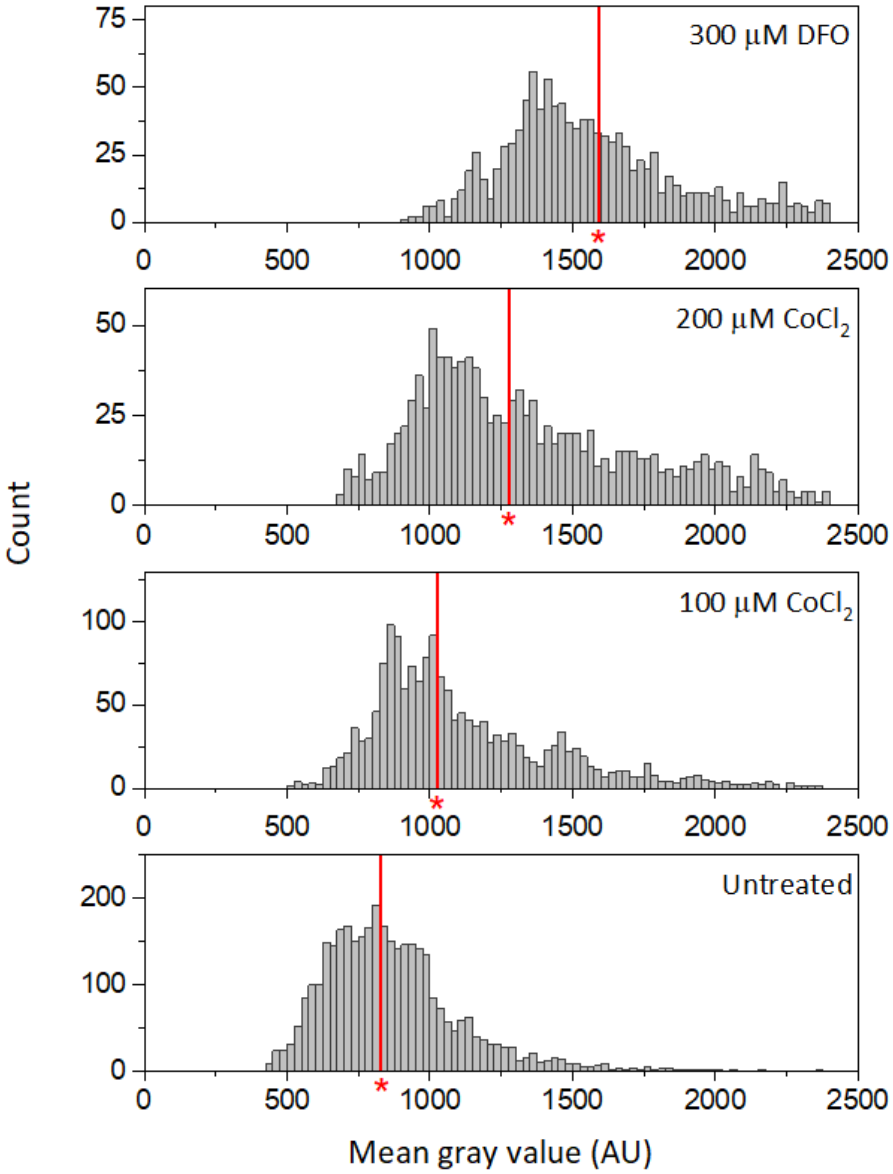

Condition	Sample count	Median	Mean	Standard Deviation
Untreated	3485	830	866	237
100 µM $CoCl_2$	1703	1027	1127	347
200 µM $CoCl_2$	1208	1279	1387	444
300 µM DFO	1369	1592	1823	650

Differences between all conditions were significant by Kruskal-Wallis test ($P < 0.0001$) and post-hoc Dunn's multiple comparisons tests ($P < 0.0001$).

Histograms of HepG2/C3A cells not treated with primary antibody (bin width 25):

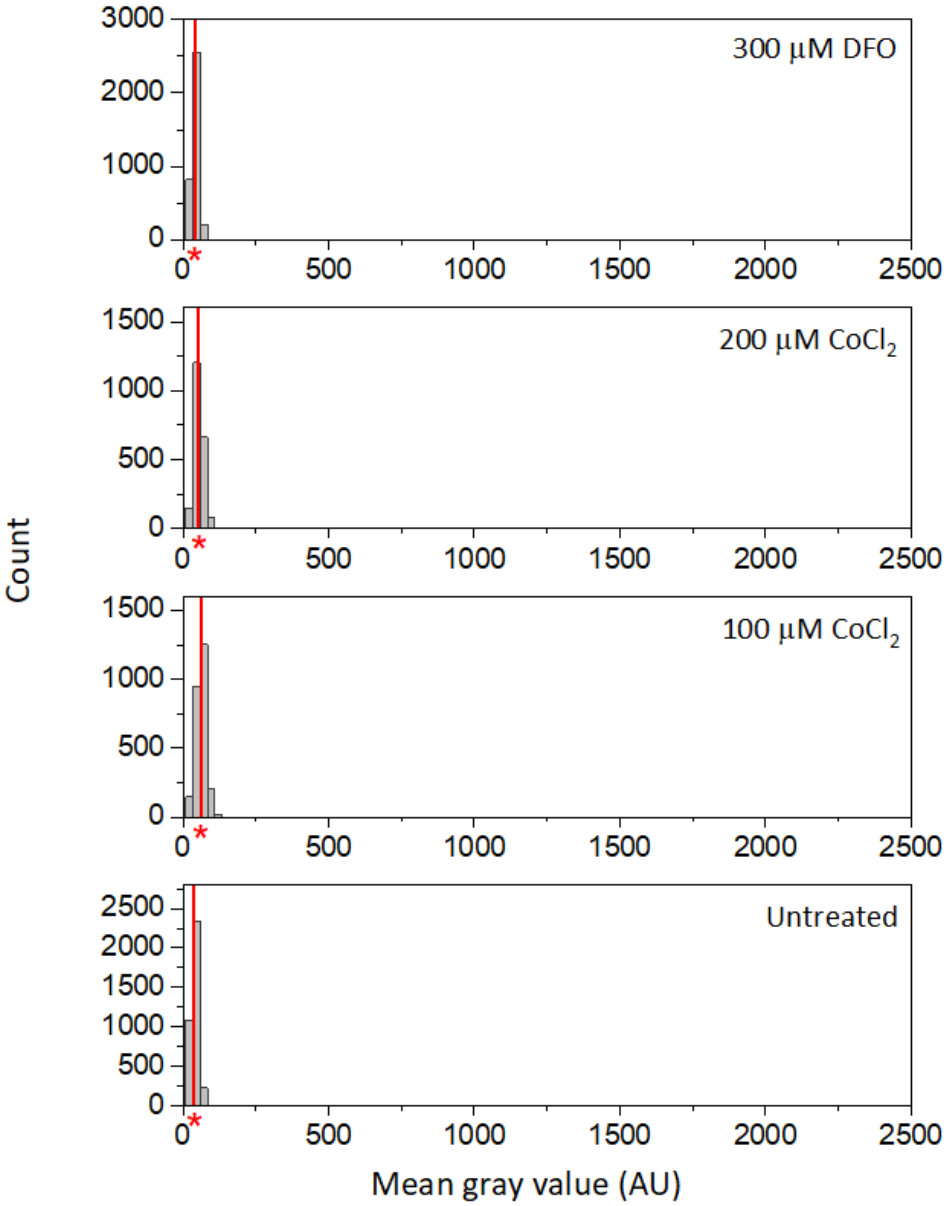

5 Statistical Analysis of Well Plate Control Experiments

The results of two-tailed Mann Whitney tests on distributions of MGV from cell samples in well plates untreated or treated with $CoCl_2$ and stained for HIF-1α or CAIX.

HepG2/C3A Cells Treated with 400 µM $CoCl_2$ and Stained for HIF-1α and CAIX

Stain	$CoCl_2$	Sample count	Median	Mean	Standard Deviation	Significant?	P value
HIF-1α	Untreated	2356	6800	6944	1629	Yes	<0.0001
HIF-1α	Treated	1597	3705	3798	1000		
CAIX	Untreated	2356	10364	11256	3119	Yes	<0.0001
CAIX	Treated	2745	10041	10760	2874		
Unstained	Untreated	3797	913	932	384	Yes	<0.0001
Unstained	Treated	4558	840	815	353		

DU145 Cells Treated with 400 µM $CoCl_2$ and Stained for HIF-1α and CAIX

Stain	$CoCl_2$	Sample count	Median	Mean	Standard Deviation	Significant?	P value
HIF-1α	Untreated	572	7531	7480	1478	Yes	<0.0001
HIF-1α	Treated	1354	13384	14225	4131		
CAIX	Untreated	603	21264	22188	6978	Yes	<0.0001
CAIX	Treated	1309	10639	11410	3292		
Unstained	Untreated	1411	1165	1192	377	Yes	<0.0001
Unstained	Treated	1872	677	680	246		

HepG2/C3A Cells Treated with 400 µM $CoCl_2$ and Stained for HIF-1α and CAIX, Repeated without Permeabilisation for CAIX Samples

Stain	Permeabilised	$CoCl_2$	Sample count	Median	Mean	Standard Deviation	Significant?	P value
HIF-1α	Yes	Untreated	3581	4529	4705	1258	Yes	<0.0001
HIF-1α	Yes	Treated	3373	7237	7465	2035		
CAIX	Yes	Untreated	2964	4740	4987	1689	Yes	<0.0001
CAIX	Yes	Treated	2639	4963	5122	1194		
CAIX	No	Untreated	2385	4110	4189	1246	Yes	<0.0001
CAIX	No	Treated	2670	3563	3715	1052		
Unstained	Yes	Untreated	9147	529	523	214	Yes	<0.0001
Unstained	Yes	Treated	8328	526	524	236		

DU145 Cells Treated with 400 µM $CoCl_2$ and Stained for HIF-1α and CAIX, Repeated without Permeabilisation for CAIX Samples

Stain	Permeabilised	$CoCl_2$	Sample count	Median	Mean	Standard Deviation	Significant?	P value
HIF-1α	Yes	Untreated	261	10320	10479	2549	Yes	<0.0001
HIF-1α	Yes	Treated	792	18519	19584	5610		
CAIX	Yes	Untreated	313	8732	8864	2011	Yes	<0.0001
CAIX	Yes	Treated	563	4718	4775	1188		
CAIX	No	Untreated	354	6549	6803	2018	Yes	<0.0001
CAIX	No	Treated	1247	4433	4690	1309		
Unstained	Yes	Untreated	482	1332	1636	1007	Yes	0.0078
Unstained	Yes	Treated	1737	638	1064	888		

6 Statistical Analysis of Chip Experiments 1 – 8

For experiment 6, a Mann Whitney test between treated (2 chips) and untreated (2 chips) was carried out for each cells type. This is similar to the more commonly used t-test for comparing two samples, but is more suitable for populations with different numbers of samples and non-Gaussian distributions.

Details – Experiment 6 HepG2/C3A Cells Mann Whitney						
Condition	**Sample count**	**Median**	**Mean**	**Standard Deviation**	**Significant?**	**P value**
Untreated	4328	6229	6732	2417	Yes	<0.0001
Treated	1942	6901	7238	2744		
Details – Experiment 6 DU145 Cells Mann Whitney						
Condition	**Sample count**	**Median**	**Mean**	**Standard Deviation**	**Significant?**	**P value**
Untreated	1973	11,119	12,145	4286	No	0.2051
Treated	2824	11,061	11,997	4255		

Kruskal-Wallis tests showed significant differences in each chip in experiments 1 – 8. The tables show a summary of the values and post-hoc Dunn's multiple correction tests for each experiment.

Details – Experiments 1, 2, 3							Post-Hoc Dunn's multiple comparison tests				
Experiment	**Channel**	**Sample count**	**Median**	**Mean**	**Standard deviation**	**Channels**	**Significant?**	**P value**	**Channels**	**Significant?**	**P value**
1	1	675	11277	13000	5781	1 vs 2	Yes	<0.0001	2 vs 4	Yes	<0.0001
1	2	619	13027	14077	4826	1 vs 3	No	0.2188	2 vs 5	Yes	<0.0001
1	3	735	10954	12787	6627	1 vs 4	Yes	<0.0001	3 vs 4	Yes	<0.0001
1	4	716	14373	15647	4999	1 vs 5	Yes	<0.0001	3 vs 5	Yes	<0.0001
1	5	679	14544	15639	5103	2 vs 3	Yes	<0.0001	4 vs 5	No	>0.9999
2	1	758	17835	18680	5338	1 vs 2	Yes	0.0123	2 vs 4	Yes	<0.0001
2	2	558	18200	20694	7771	1 vs 3	Yes	<0.0001	2 vs 5	Yes	<0.0001
2	3	683	15799	17307	5631	1 vs 4	Yes	<0.0001	3 vs 4	No	>0.9999
2	4	613	15691	17055	5235	1 vs 5	Yes	0.014	3 vs 5	No	0.3611
2	5	423	16602	17914	5699	2 vs 3	Yes	<0.0001	4 vs 5	No	0.0933
3	1	581	8665	9412	2909	1 vs 2	No	0.3363	2 vs 4	Yes	<0.0001
3	2	674	9205	9740	3046	1 vs 3	Yes	<0.0001	2 vs 5	Yes	<0.0001
3	3	809	9755	10451	3216	1 vs 4	Yes	<0.0001	3 vs 4	Yes	<0.0001
3	4	830	10453	11401	3648	1 vs 5	Yes	<0.0001	3 vs 5	Yes	<0.0001
3	5	831	10520	11450	3843	2 vs 3	Yes	0.0001	4 vs 5	No	>0.9999

Details – Experiments 4, 5, 7, 8							Post-Hoc Dunn's multiple comparison tests				
Experiment	**Channel**	**Sample count**	**Median**	**Mean**	**Standard deviation**	**Channels**	**Significant?**	**P value**	**Channels**	**Significant?**	**P value**
4	1	564	6701	6907	1657	1 vs 2	No	>0.9999	2 vs 4	Yes	<0.0001
4	2	457	6868	7205	2105	1 vs 3	Yes	<0.0001	2 vs 5	Yes	<0.0001
4	3	670	6214	6473	1711	1 vs 4	Yes	<0.0001	3 vs 4	No	0.0789
4	4	538	5997	6235	1680	1 vs 5	Yes	<0.0001	3 vs 5	No	>0.9999
4	5	543	6127	6482	1914	2 vs 3	Yes	<0.0001	4 vs 5	No	0.3819
5	1	451	9178	9565	2550	1 vs 2	No	>0.9999	2 vs 4	Yes	<0.0001
5	2	530	8975	9458	2614	1 vs 3	No	>0.9999	2 vs 5	Yes	<0.0001
5	3	639	8997	9527	2694	1 vs 4	Yes	<0.0001	3 vs 4	Yes	<0.0001
5	4	809	7326	7796	2381	1 vs 5	Yes	<0.0001	3 vs 5	Yes	<0.0001
5	5	643	7315	7783	2314	2 vs 3	No	>0.9999	4 vs 5	No	>0.9999
7	1	281	12368	13201	3996	1 vs 2	Yes	0.0005	2 vs 4	No	>0.9999
7	2	266	13971	14649	4484	1 vs 3	Yes	0.031	2 vs 5	No	>0.9999
7	3	388	13245	14092	4130	1 vs 4	Yes	0.0001	3 vs 4	No	>0.9999
7	4	522	13910	14567	4595	1 vs 5	Yes	0.0189	3 vs 5	No	>0.9999
7	5	488	13396	13973	3862	2 vs 3	No	>0.9999	4 vs 5	No	>0.9999
8	1	308	11600	12198	3464	1 vs 2	Yes	<0.0001	2 vs 4	Yes	<0.0001
8	2	370	10063	10598	3037	1 vs 3	Yes	<0.0001	2 vs 5	No	>0.9999
8	3	396	9877	10519	3219	1 vs 4	Yes	<0.0001	3 vs 4	Yes	0.0008
8	4	501	8989	9771	3196	1 vs 5	Yes	<0.0001	3 vs 5	No	>0.9999
8	5	611	9883	10769	3188	2 vs 3	No	>0.9999	4 vs 5	Yes	<0.0001

Details – Experiment 6 HepG2/C3A cells						Post-Hoc Dunn's multiple comparison tests					
Condition	**Channel**	**Sample count**	**Median**	**Mean**	**Standard deviation**	**Channels**	**Significant?**	**P value**	**Channels**	**Significant?**	**P value**
Untreated 1	1	309	8351	8746	2533	1 vs 2	No	>0.9999	2 vs 4	Yes	<0.0001
Untreated 1	2	190	8276	8993	2922	1 vs 3	Yes	<0.0001	2 vs 5	No	>0.9999
Untreated 1	3	188	4749	5095	1630	1 vs 4	Yes	<0.0001	3 vs 4	Yes	<0.0001
Untreated 1	4	189	7074	7526	2064	1 vs 5	No	0.2276	3 vs 5	Yes	<0.0001
Untreated 1	5	375	8753	9365	2874	2 vs 3	Yes	<0.0001	4 vs 5	Yes	<0.0001
Untreated 2	1	877	5212	5422	1539	1 vs 2	Yes	<0.0001	2 vs 4	Yes	<0.0001
Untreated 2	2	717	5619	5978	1879	1 vs 3	Yes	<0.0001	2 vs 5	No	0.3337
Untreated 2	3	472	6681	6992	1935	1 vs 4	Yes	<0.0001	3 vs 4	No	>0.9999
Untreated 2	4	408	6469	6917	2047	1 vs 5	Yes	<0.0001	3 vs 5	Yes	<0.0001
Untreated 2	5	603	5802	6087	1617	2 vs 3	Yes	<0.0001	4 vs 5	Yes	<0.0001
Treated 1	1	246	7386	8005	2454	1 vs 2	Yes	<0.0001	2 vs 4	Yes	<0.0001
Treated 1	2	197	6484	6675	2086	1 vs 3	Yes	<0.0001	2 vs 5	Yes	<0.0001
Treated 1	3	192	4540	4665	1421	1 vs 4	Yes	<0.0001	3 vs 4	No	0.848
Treated 1	4	212	4229	4354	1174	1 vs 5	Yes	<0.0001	3 vs 5	No	>0.9999
Treated 1	5	101	4498	4761	1276	2 vs 3	Yes	<0.0001	4 vs 5	No	0.6595
Treated 2	1	225	8294	8898	2488	1 vs 2	Yes	<0.0001	2 vs 4	No	0.1009
Treated 2	2	205	8599	8839	2379	1 vs 3	No	>0.9999	2 vs 5	No	>0.9999
Treated 2	3	142	6819	7216	2104	1 vs 4	No	0.1647	3 vs 4	Yes	0.0002
Treated 2	4	185	7810	8266	2322	1 vs 5	Yes	<0.0001	3 vs 5	Yes	<0.0001
Treated 2	5	237	8684	8880	2473	2 vs 3	No	>0.9999	4 vs 5	No	0.0613

Details – Experiment 6 DU145 Cells						Post-Hoc Dunn's multiple comparison tests					
Condition	**Channel**	**Sample count**	**Median**	**Mean**	**Standard deviation**	**Channels**	**Significant?**	**P value**	**Channels**	**Significant?**	**P value**
Untreated 1	1	216	10512	11219	3365	1 vs 2	Yes	<0.0001	2 vs 4	Yes	0.0028
Untreated 1	2	231	11946	13213	4617	1 vs 3	No	>0.9999	2 vs 5	Yes	<0.0001
Untreated 1	3	213	10148	11157	3762	1 vs 4	No	>0.9999	3 vs 4	No	>0.9999
Untreated 1	4	182	10688	11675	3893	1 vs 5	No	0.1216	3 vs 5	No	0.6978
Untreated 1	5	247	9834	10473	3428	2 vs 3	Yes	<0.0001	4 vs 5	Yes	0.0129
Untreated 2	1	191	13183	14516	4820	1 vs 2	Yes	<0.0001	2 vs 4	No	>0.9999
Untreated 2	2	180	10790	12176	4416	1 vs 3	Yes	<0.0001	2 vs 5	Yes	0.003
Untreated 2	3	134	10599	12032	4115	1 vs 4	Yes	<0.0001	3 vs 4	No	>0.9999
Untreated 2	4	171	10814	11618	3724	1 vs 5	No	0.1509	3 vs 5	Yes	0.0053
Untreated 2	5	208	11904	13633	4801	2 vs 3	No	>0.9999	4 vs 5	Yes	0.0004
Treated 1	1	250	11909	13781	5163	1 vs 2	Yes	0.005	2 vs 4	Yes	0.04
Treated 1	2	259	11241	12205	4005	1 vs 3	No	0.2847	2 vs 5	No	>0.9999
Treated 1	3	238	11635	12848	4744	1 vs 4	Yes	<0.0001	3 vs 4	Yes	0.0008
Treated 1	4	188	10189	11204	3909	1 vs 5	No	0.6912	3 vs 5	No	>0.9999
Treated 1	5	230	11937	12830	4617	2 vs 3	No	>0.9999	4 vs 5	Yes	0.0002
Treated 2	1	294	12025	13454	4837	1 vs 2	Yes	<0.0001	2 vs 4	No	0.2529
Treated 2	2	357	10425	11097	3810	1 vs 3	Yes	<0.0001	2 vs 5	Yes	0.0005
Treated 2	3	328	9911	10807	3014	1 vs 4	Yes	<0.0001	3 vs 4	No	0.8534
Treated 2	4	358	9772	10538	3345	1 vs 5	Yes	0.0137	3 vs 5	Yes	<0.0001
Treated 2	5	322	11293	12180	3890	2 vs 3	No	>0.9999	4 vs 5	Yes	<0.0001

Details – Flow rate comparison					
Experiment	**Flow rate** (µL/hour)	**Sample count**	**Median**	**Mean**	**Standard deviation**
6	0	4328	6229	6732	2417
5	30	3028	8332	8769	2680
4	50*	2772	6315	6638	1835
3	50	3725	9800	10595	3487
7	100	1945	13456	14137	4249
8	150	2186	10021	10667	3289

Post-Hoc Dunn's multiple comparison tests – Flow rate comparison		
Flow rate (µL/hour)	**Significant?**	**P value**
0 vs. 30	Yes	<0.0001
0 vs. 50*	No	>0.9999
0 vs. 50	Yes	<0.0001
0 vs. 100	Yes	<0.0001
0 vs. 150	Yes	<0.0001
30 vs. 50*	Yes	<0.0001
30 vs. 50	Yes	<0.0001
30 vs. 100	Yes	<0.0001
30 vs. 150	Yes	<0.0001
50* vs. 50	Yes	<0.0001
50* vs. 100	Yes	<0.0001
50* vs. 150	Yes	<0.0001
50 vs. 100	Yes	<0.0001
50 vs. 150	No	>0.9999
100 vs. 150	Yes	<0.0001

* All flow rate experiments were run for 3 hours except 50* which was run for 1.5 hours.

7 Histograms for each Channel in Experiment 6

Each histogram shows combined results from three images per channel and red line labelled with asterisk indicates the median.

HepG2/C3A Cells, Untreated Chip 1, bin width 250:

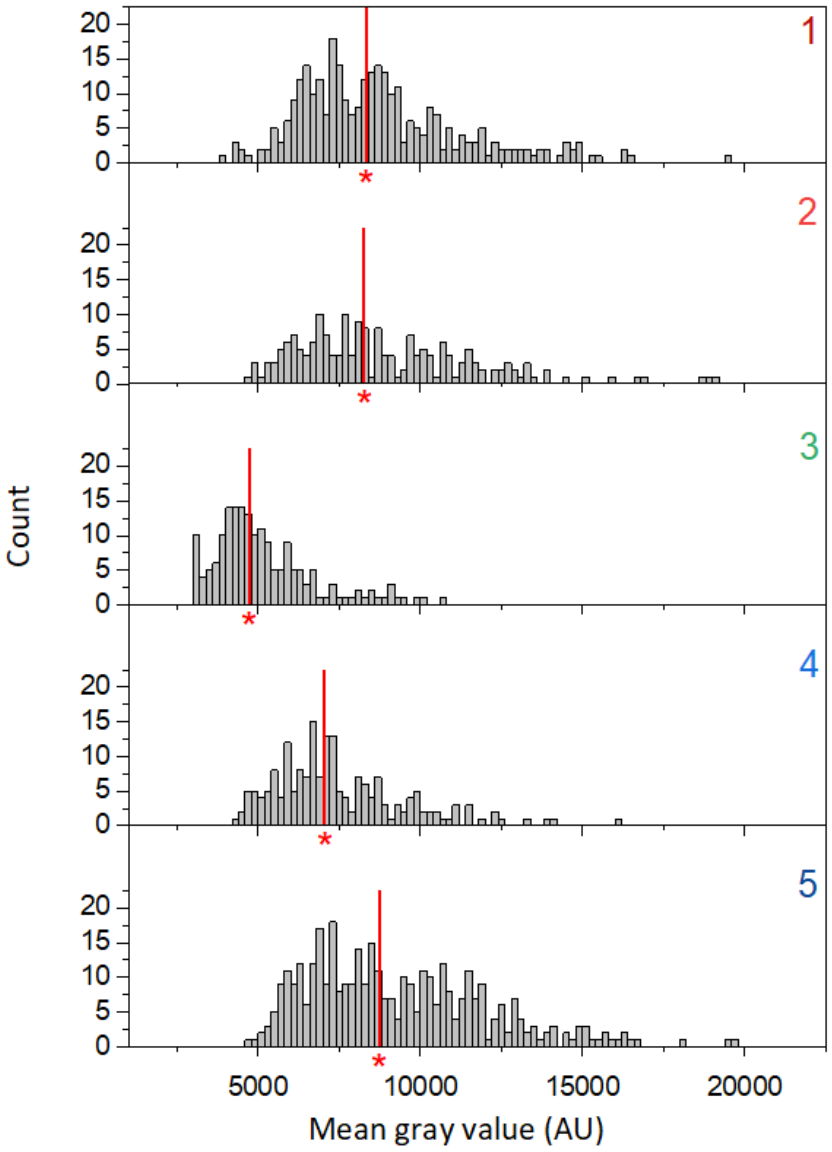

HepG2/C3A Cells, Untreated Chip 2, bin width 150:

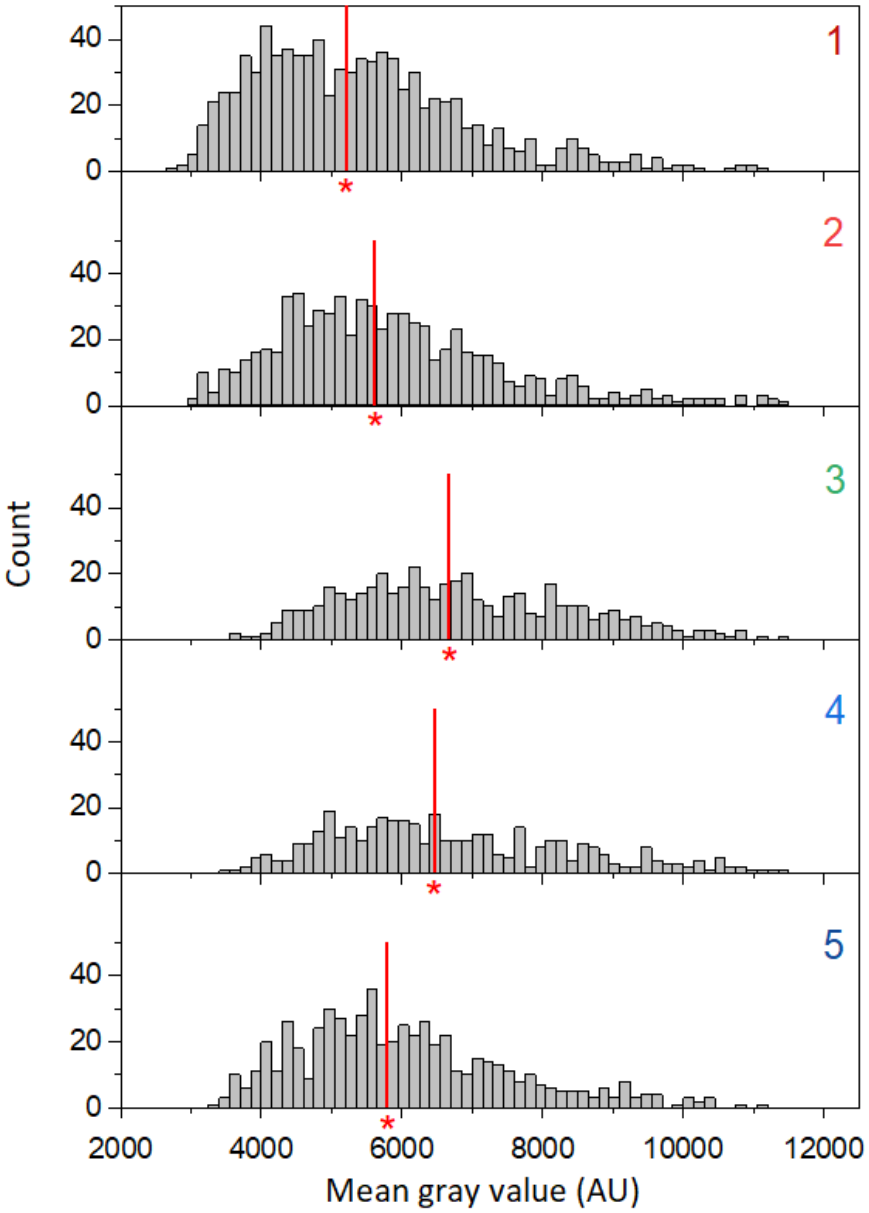

HepG2/C3A Cells, Treated Chip 1, bin width 150:

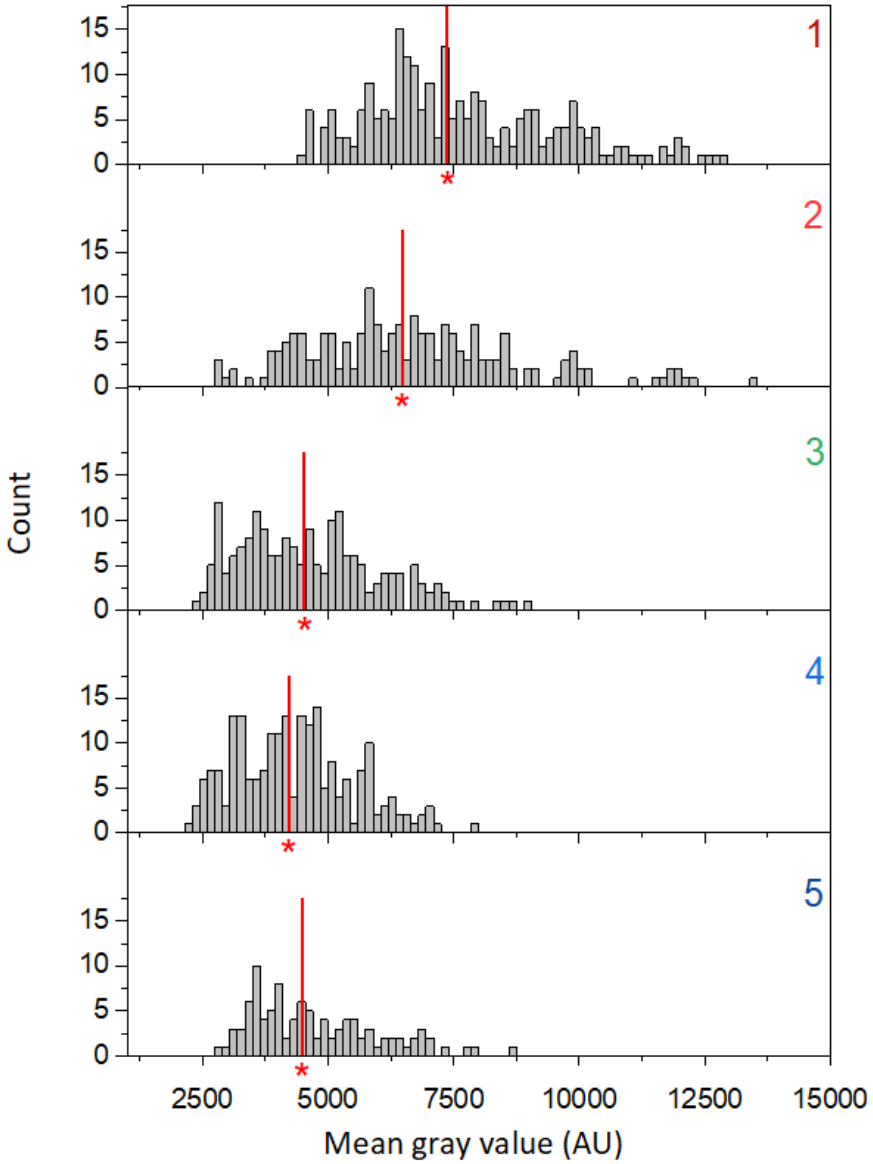

HepG2/C3A Cells, Treated Chip 2, bin width 200:

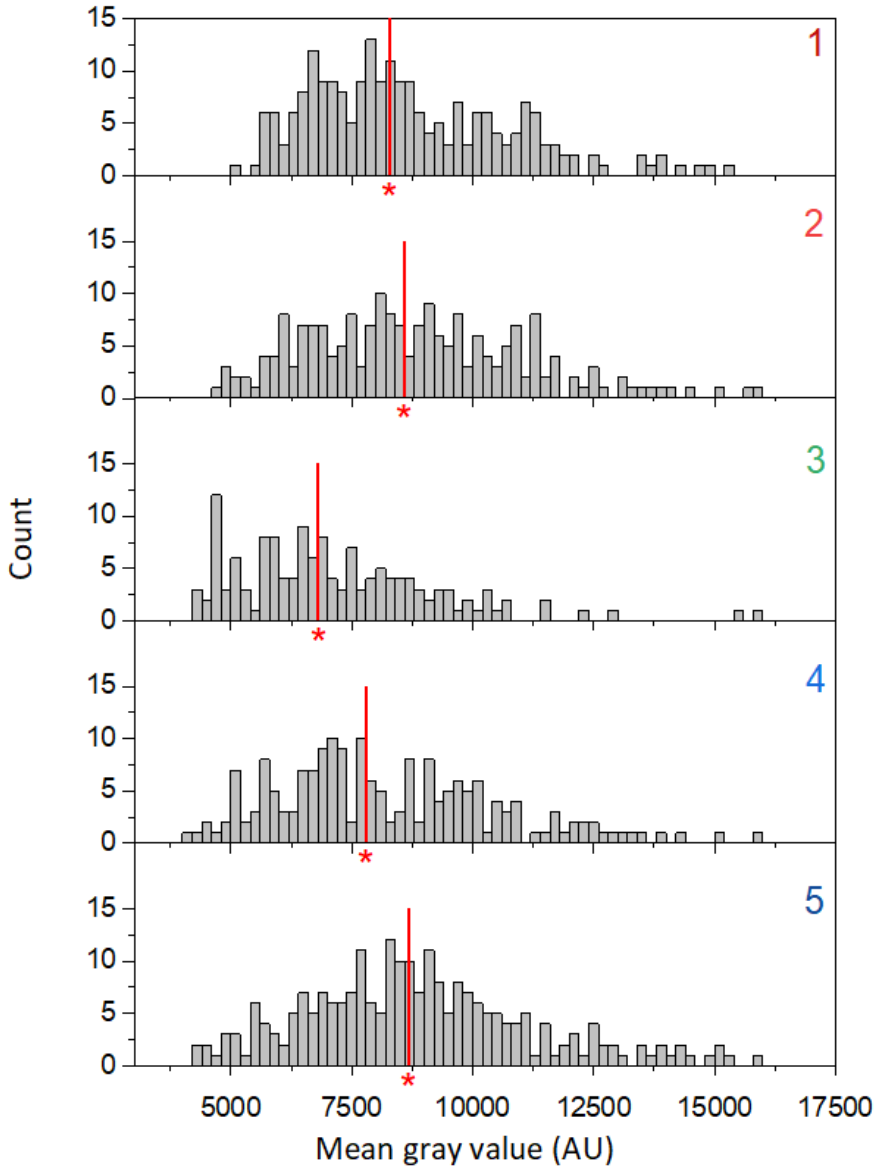

DU145 Cells, Untreated Chip 1, bin width 200:

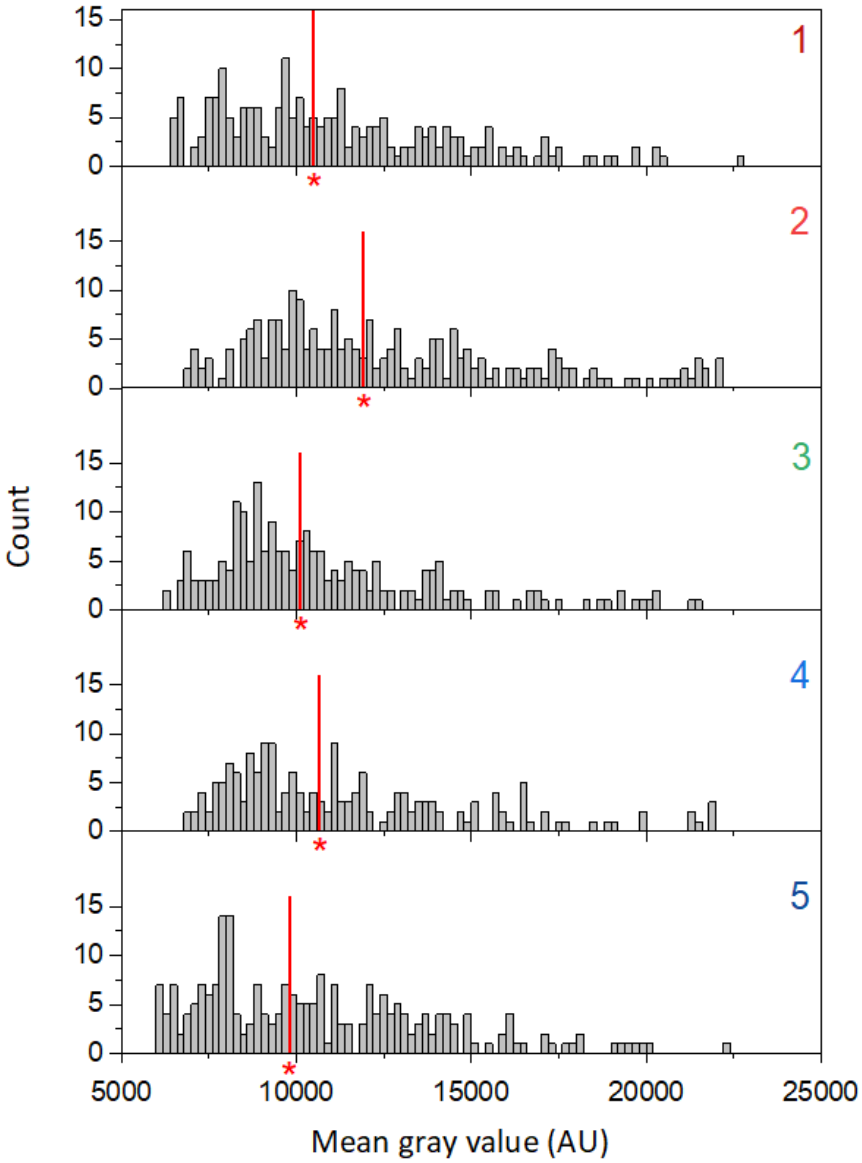

DU145 Cells, Untreated Chip 2, bin width 300:

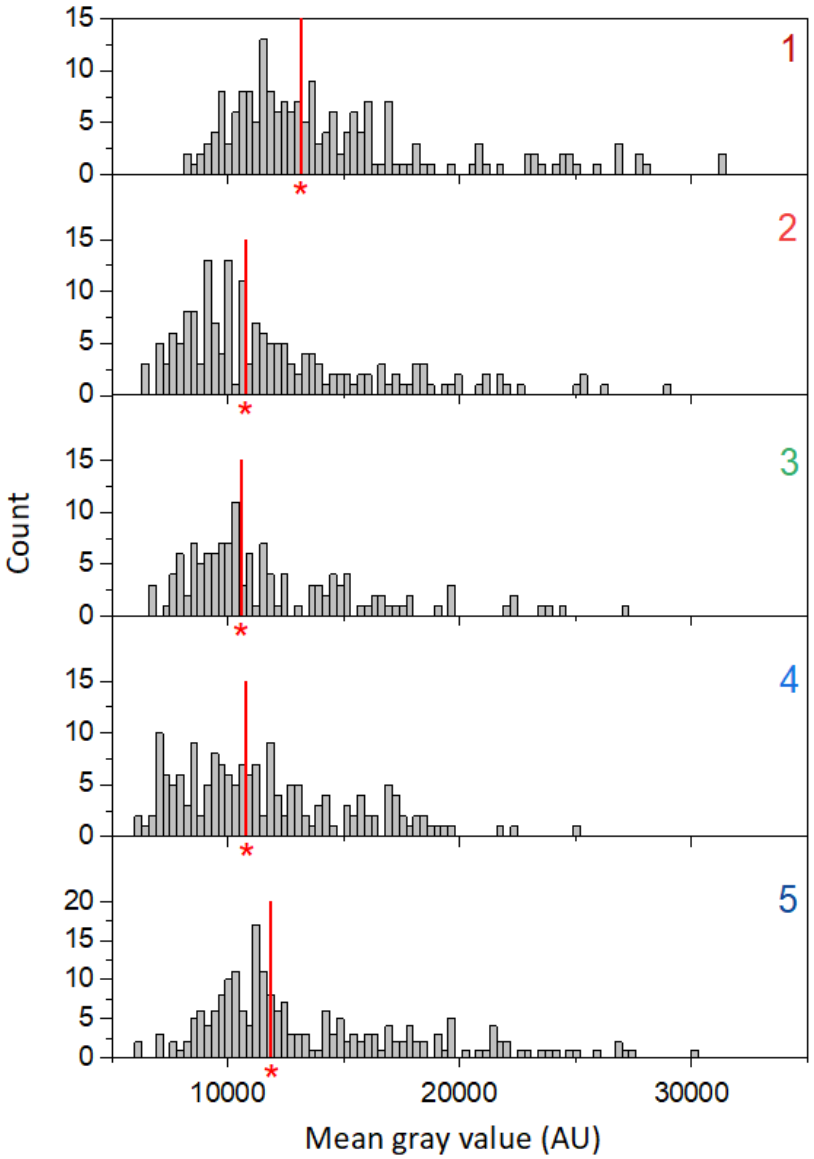

DU145 Cells, Treated Chip 1, bin width 350:

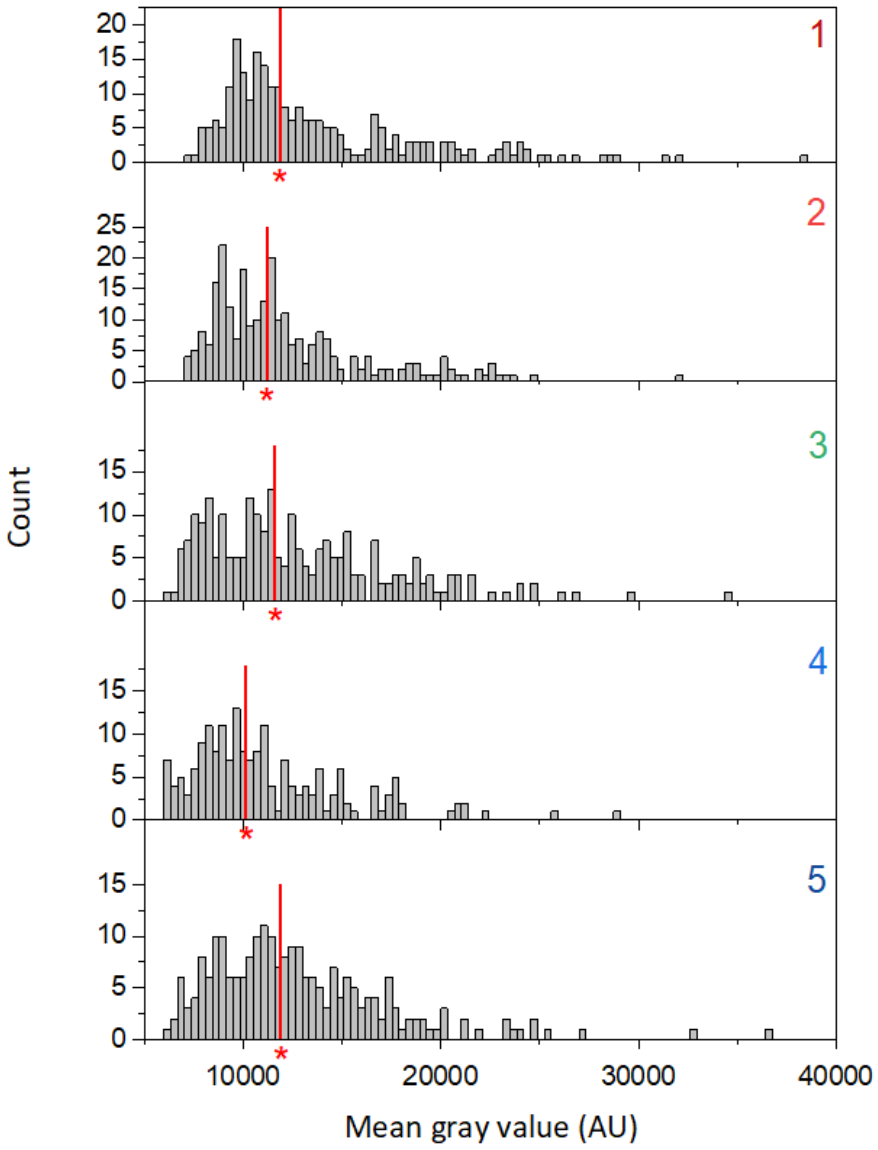

DU145 Cells, Treated Chip 2, bin width 300: